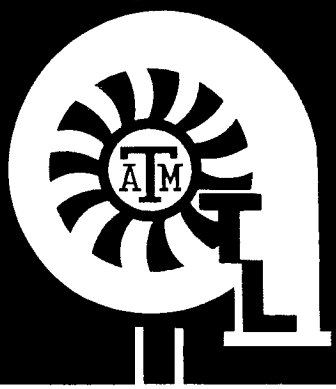

A Comparison Of Experimental And Theoretical Results For Labyrinth Gas Seals

by

Joseph Kirk Scharrer

February 1987

TRC-SEAL-3-87

Turbomachinery Laboratories
Mechanical Engineering Department

A COMPARISON OF EXPERIMENTAL AND THEORETICAL RESULTS FOR LABYRINTH GAS SEALS

by

JOSEPH KIRK SCHARRER

Texas A&M University

Turbomachinery Laboratories

Mechanical Engineering Department

College Station, Texas 77843

February 1987

TRC-SEAL-3-87

ABSTRACT

A Comparison of Experimental and Theoretical Results for Labyrinth Gas Seals. (May 1987)

Joseph K. Scharrer, B.S., Northern Arizona University; M.S., Texas A&M University

Chairman of Advisory Committee: Dr. Dara Childs

The basic equations are derived for a two-control-volume model for compressible flow in a labyrinth seal. The flow is assumed to be completely turbulent and isoenergetic. The wall friction factors are determined using the Blasius formula. Jet flow theory is used for the calculation of the recirculation velocity in the cavity. Linearized zeroth and first-order perturbation equations are developed for small motion about a centered position by an expansion in the eccentricity ratio. The zeroth-order pressure distribution is found by satisfying the leakage equation. The circumferential velocity distribution is determined by satisfying the momentum equations. The first order equations are solved by a separation of variable solution. Integration of the resultant pressure distribution along and around the seal defines the reaction force developed by the seal and the corresponding dynamic coefficients. The results of this analysis are compared to experimental test results presented in this report. The results presented are for three teeth-on-rotor and three teeth-on-stator labyrinth seals with different radial clearances. The theory

compares well with the cross-coupled stiffness data for both seal types and with the direct damping data for a teeth-on-rotor labyrinth seal. For a teeth-on-stator labyrinth seal, the test results show a decrease in direct damping for an increase in radial seal clearance, while the theory shows the opposite.

ACKNOWLEDGEMENT

This project would not have been possible without the hard work and dedication of Dr. Dara Childs, Keith Hale, David Elrod, Anne Owens, and Dean Nunez. This project was supported in part by NASA Grant NAS8-33716 from NASA Lewis Research Center and AFOSR Contract F49620-82-K-0033.

TABLE OF CONTENTS

LIST OF TABLES

LIST OF FIGURES

Page

Page

Page

NOMENCLATURE

A_i Cross sectional area of control volume (L^2); illustrated in figures (9) and (14)

B_i Height of labyrinth seal strip (L); illustrated in figure (6)

C Direct damping coefficient (Ft/L)

C_r Nominal radial clearance (L); illustrated in figure (6)

D_h Hydraulic diameter of cavity (L); introduced in equation (44)

H Local radial clearance (L)

K Direct stiffness coefficient (F/L)

L Pitch of seal strips (L); illustrated in figure (6)

NT Number of seal strips

NC=NT-1 Number of cavities

P Pressure (F/L^2)

R Gas constant (L^2/Tt^2)

Rs_1 Radius of control volume I (L); illustrated in figure (6)

Rs_2 Radius of control volume II (L); illustrated in figure (6)

$Rs\omega$ Surface velocity of rotor (L/t)

T Temperature (T)

Tp Tooth tip width (L); illustrated in figure (6)

U_1 Average axial velocity for control volume I (L/t); illustrated in figure (7)

U_2 Average axial velocity for control volume II (L/t); illustrated in figure (7)

W_{i1} Average circumferential velocity for control volume I (L/t); illustrated in figure (7)

W_{2i} Average circumferential velocity for control volume II (L/t); illustrated in figure (7)

Wo_i Average circumferential velocity in the interface between control volumes I and II (L/t); introduced in equation (40)

a,b Radial seal displacement components due to elliptical whirl (L); introduced in equation (73)

ar Dimensionless length upon which shear stress acts on rotor; introduced in equation (42)

as Dimensionless length upon which shear stress acts on stator; introduced in equation (42)

c Cross coupled damping coefficient (Ft/L); in equation (41)

e_o Displacement of the seal rotor from centered position (L)

k Cross coupled stiffness coefficient (F/L); in equation (41)

$\dot{m}$ Leakage mass flow rate per circumferential length (M/Lt)

mr, nr, ms, ns Coefficients for friction factor; introduced in equation (43)

t Time (t)

v Total velocity (L/t); introduced in equation (48)

ω Shaft angular velocity (1/t)

Ω Shaft precessional velocity (1/t)

ρ Density of fluid (M/L^3)

ν Kinematic viscosity (L^2/t)

$\varepsilon = e_o/C_r$ Eccentricity ratio

e Turbulent viscosity (Ft/L^2);introduced in equation (9)

$\pi = 3.141592$

γ Ratio of specific heats

Subscripts

o Zeroth-order component

1 First-order component, control volume I value

2 Control volume II value

i i-th chamber value

j Value along the dividing streamline

x X-direction

y Y-direction

r Reservoir value

s Sump value

CHAPTER I

INTRODUCTION

The problems of instability and synchronous response in turbomachines have arisen recently because of the trends in design toward greater efficiency with higher performance. To achieve these design goals, the machines are designed for higher speeds, larger loadings, and tighter clearances. In order to achieve the higher speeds, rotors frequently traverse several critical speeds (speeds which coincide with the rotor's damped natural frequency). The characteristics of synchronous reponse, when the rotor vibrates at a frequency coincident with the running speed, are such that the vibrational amplitude reaches a maximum at each critical speed. In order to limit the peak synchronous vibration levels, damping must be introduced into the rotor system. As loadings are increased and clearances decreased, fluid forces increase and can lead to unstable or self-excited vibrations. This motion is typically subsynchronous, which means that the rotor whirls at a frequency less than the rotating speed, and occurs with large amplitudes which grow as running speed increases. This situation can also be improved by adding damping to the rotor system, which would help curb the growth of the amplitudes. One of the rotordynamic force mechanisms which plays a role in self-excited vibration and synchronous response is that of the forces developed by labyrinth seals.

Journal Model: ASME Journal of Tribology

A limited amount of experimental data has been published to date on the determination of stiffness and damping coefficients for labyrinth gas seals. The first published results for stiffness coefficients were those of Wachter and Benckert [1,2,3]. They investigated the following three types of seals: a) teeth-on-stator, b) teeth on the rotor and stator, and c) teeth on the stator and steps or grooves on the rotor. These results were limited in that the pressure drop was small, much of the data were for nonrotating seals, no data were presented for seals with teeth on the rotor, the rotor speed was limited, and tests where rotation and inlet tangential velocity existed simultaneously were very scarce.

The next investigation was carried out by Wright [4], who measured an equivalent radial and tangential stiffness for single-cavity seals with teeth on the stator. Although for a very limited and special case, Wright's results do give insight into the effect of pressure drop, convergence or divergence of the clearance, and forward or backward whirl of a seal. These results could be reduced to direct and cross-coupled stiffness and damping, hence, they are the first published damping coefficients for teeth-on-stator labyrinth seals.

Brown and Leong [5] investigated the same seal configurations as Wachter and Benckert, in an effort to verify and extend their work. Their results include variations of pressure, geometry, rotor speed, and inlet tangential velocity. Although the investigation was extensive, the published results are limited because of the lack of information concerning operating conditions for the various tests.

Childs and Scharrer [6] investigated geometrically similar teeth-on-rotor and teeth-on-stator labyrinth seals for stiffness and damping

coefficients up to speeds of 8000 cpm. Kanemitsu and Ohsawa [7] investigated multistage teeth-on-stator and interlocking labyrinth seals up to speeds of 2400 cpm. They measured an effective radial and tangential stiffness while varying the whirl frequency of the rotor. These data could be reduced to stiffness and damping coefficients. Hisa et al. [8] investigated teeth-on-stator seals with 2-4 teeth and a teeth-on-stator seal with steps on the rotor up to speeds of 6000 cpm. These data only included static tests for direct and cross-coupled stiffness using steam.

In the area of theoretical analysis of labyrinth seals, there is much more published information. The first steps toward the analysis of a labyrinth seal were taken by Alford [9], who neglected circumferential flow and Spürk et al [10] who neglected rotation of the shaft. Vance and Murphy [11] extended the Alford analysis by introducing a more realistic assumption of choked flow.

Kostyuk [12] performed the first comprehensive analysis, but failed to include the change in area due to eccentricity which is responsible for the relationship between cross-coupled forces and parallel rotor displacements. Iwatsubo [13,14] refined the Kostyuk model by including the time dependency of area change but neglected the area derivative in the circumferential direction. Kurohashi [15] incorporated dependency of the flow coefficient on eccentricity into his analysis, but assumed that the circumferential velocity in each cavity was the same. Gans [16] improved on the Iwatsubo model by introducing the area derivative in the circumferential direction. Martinez-Sanchez et al. [17] produced results similar to Gans, but used

empirical flow coefficients to improve their results. Childs and Scharrer [18] improved the Iwatsubo solution by using a modified set of reduced governing equations and an efficient solution technique. However, their solution continued to neglect axial velocities.

Hauck [19] introduced the use of multi-control-volume analysis in the study of labyrinth seals by applying the equations of impulse and "balance of moments" to a three-control-volume model. These equations were written in the axial direction only and neglected the effects of rotor speed. Fujikawa et al. [20] introduced the use of two control volumes into the analysis of labyrinth seals, but their analysis, which neglects the axial velocity components, was heavily dependent on empirical information which is not customarily available. Finally, Jenny et al. [21] used the two-control-volume approach in conjunction with a two dimensional solution to the Navier-Stokes equations to account for the free shear stress between the jet flow and the cavity flow. However, they neglected the recirculation velocity in the cavity, assumed the flow to be incompressible, and their free shear stress relation required a correction factor to fit the experimental data. Further, the present author obtains different signs in the expansion of the continuity equation and different perturbation equations. These discrepancies are explained in detail in the following section.

The most extensive comparison of analytical predictions and experimental results was carried out by Scharrer [22] using the theory of Childs and Scharrer [18] and the results of Childs and Scharrer [6]. This comparison showed that the theory [18] predicts cross-coupled

stiffness reasonably well, but underpredicts direct stiffness, direct damping, and cross-coupled damping.

In reviewing the state of the art in labyrinth seal experimentation and analysis, it becomes clear that there is a need for (a) an improved theory for the prediction of damping coefficients, (b) more extensive testing of teeth-on-rotor seals, and (c) test results showing the effects of change of radial seal clearance and higher speeds on stiffness and damping coefficients. This report will describe the revised test facility and program designed to measure the forces developed in a gas labyrinth seal. Some results, showing the effect of radial clearance change and higher rotor speed on teeth-on-rotor and teeth-on-stator labyrinth seals, will be presented. Also, a new analysis, which more accurately describes the physics of the flow field, will be presented and a comparison made between the theoretical and experimental mass flow rate, pressure distribution, and seal coefficients for the new results presented here.

The major contribution of this report is a new analysis which incorporates the recirculating velocity in the cavity into the shear stress calculations. In addition, the analysis is based on a close comparison with the CFD results of Rhode [23,24]. The CFD results were reinforcement for the assumptions and modelling of the shear stresses and velocity profiles. Stoff [25] carried out a comparison of CFD and experimental results for incompressible flow in a labyrinth seal. However, not enough data was provided in the paper to use the results for a comparison in this report.

CHAPTER II

THEORETICAL DEVELOPMENT

SEAL ANALYSIS OVERVIEW

As related to rotordynamics, seal analysis has the objective of determining the reaction forces acting on the rotor arising from shaft motion within the seal. There are two linearized seal models, expressed in terms of dynamic coefficients, which have been suggested for the force-motion relationship. For small motion about an eccentric position, as shown in figure 1, the relations of equation (1) have been proposed.

$$-\begin{Bmatrix} F_x \\ F_y \end{Bmatrix} = \begin{bmatrix} K_{xx}(\varepsilon_o) & K_{xy}(\varepsilon_o) \\ K_{yx}(\varepsilon_o) & K_{yy}(\varepsilon_o) \end{bmatrix} \begin{Bmatrix} X \\ Y \end{Bmatrix} + \begin{bmatrix} C_{xx}(\varepsilon_o) & C_{xy}(\varepsilon_o) \\ C_{yx}(\varepsilon_o) & C_{yy}(\varepsilon_o) \end{bmatrix} \begin{Bmatrix} \dot{X} \\ \dot{Y} \end{Bmatrix} \qquad (1)$$

where the dynamic coefficients {Kxx,Kyy,Cxx,Cyy} and {Kxy,Kyx, Cxy,Cyx} represent the direct stiffness and damping and the cross-coupled stiffness and damping, respectively. These coefficients are functions of the equilibrium eccentricity ratio, $\varepsilon_o = e_o/C_r$, where e_o is the displacement of the rotor from the centered position and C_r is the nominal radial clearance. The cross-coupling terms result when motion in one plane results in a reaction in a plane orthogonal to it. These cross-coupling terms depend on the magnitude and direction (with respect to the rotor's rotation) of the fluid's circumferential velocity. This velocity may exist at entry to the seal or may develop as the fluid passes through the seal. The cross-coupled stiffness term

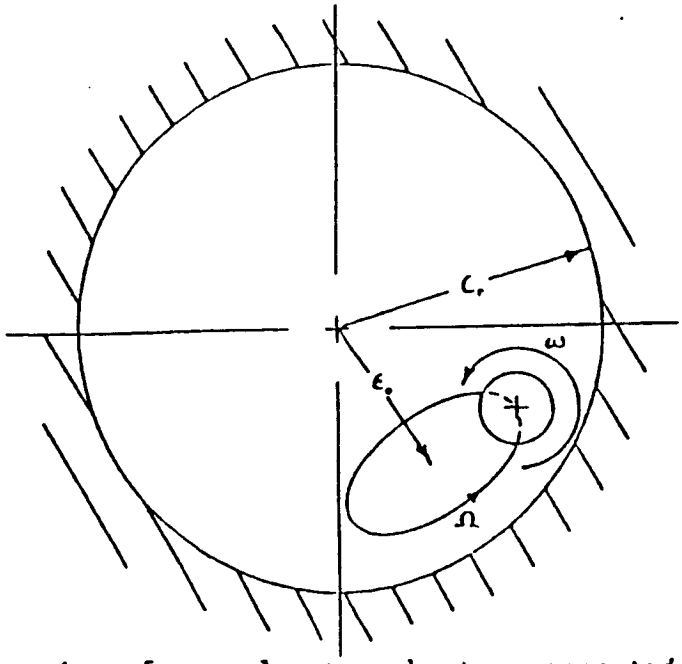

Fig. 1 Small motion of a seal rotor about an eccentric position. ω is the rotor spin speed, Ω is the precessional orbit frequency.

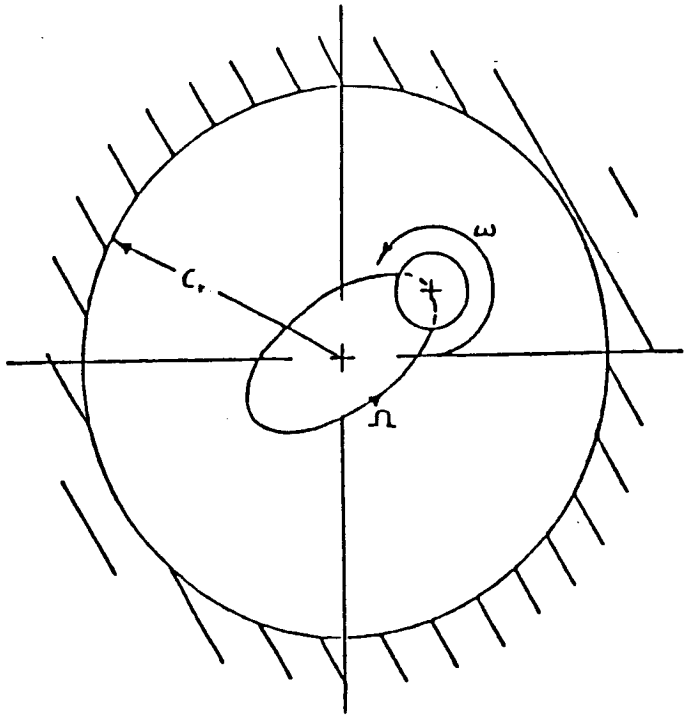

Fig. 2 Small motion of a seal rotor about a centered position. ω is the rotor spin speed, Ω is the precessional orbit frequency.

usually produces a destabilizing force component, and is therefore of considerable interest. The cross-coupled damping term is generally much less significant than the cross-coupled stiffness term with respect to stability. The second linearized seal model is applicable for small motion about a centered position, as shown in figure 2. The form of the model is

$$-\begin{Bmatrix} F_x \\ F_y \end{Bmatrix} = \begin{bmatrix} K & k \\ -k & K \end{bmatrix} \begin{Bmatrix} X \\ Y \end{Bmatrix} + \begin{bmatrix} C & c \\ -c & C \end{bmatrix} \begin{Bmatrix} \dot{X} \\ \dot{Y} \end{Bmatrix} \tag{2}$$

where the dynamic coefficient matrices are skew-symmetric. This model is used in the analysis which follows.

Preamble

The flow in a labyrinth seal has been shown by experiment [14] and calculation [23] to be comprised of two flow regimes: a jet flow region in the leakage path and a recirculating velocity region in the cavity itself(see figure 3). The first attempts at analysis of this system neglected the axial velocity components in the flow and concentrated on the circumferential components. This was the single control volume approach, used in refs [9-18]. In an attempt to improve upon the results of these analyses the two-control-volume approach was introduced, see refs [20,21]. These analyses incorporated the axial velocity of the jet flow into the solution but not the recirculating velocity component of the cavity flow. The results from Jenny et al. [21] showed substantial improvement in the prediction of stiffness and damping coefficients, but, in the end, correction factors had to be incorporated into the calculation of the shear stress to improve the correlation with test data.

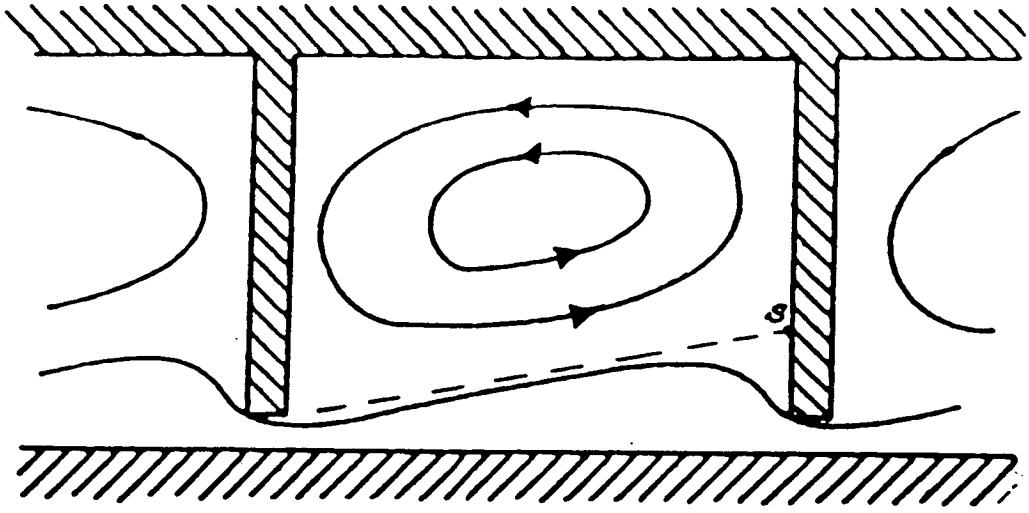

Fig. 3 Flow pattern in a labyrinth seal cavity.

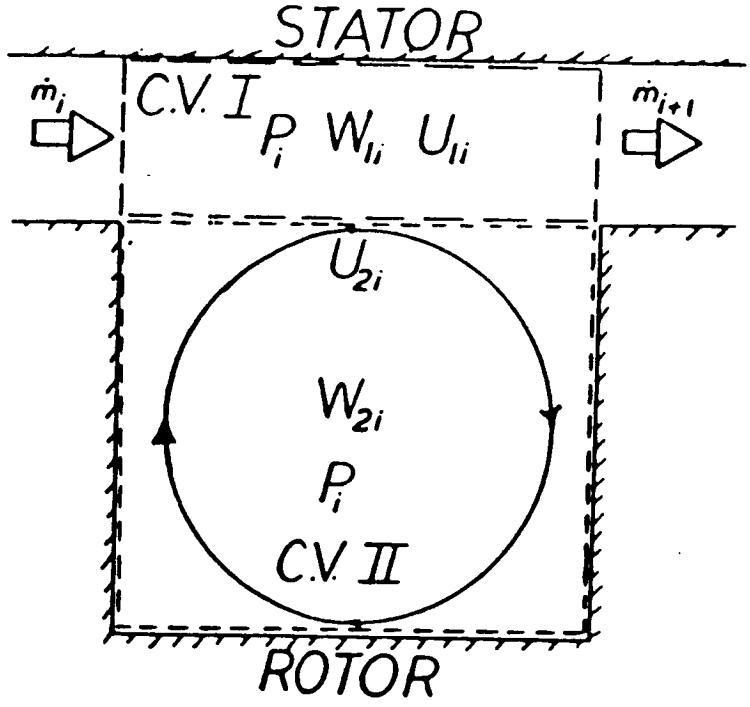

Fig. 4 Two-control-volume model with recirculation velocity, U_2.

This report introduces the calculation of the recirculation velocity into the analysis. The model for the recirculation velocity, U_2, used here is illustrated in figure 4. This velocity component is important in the calculation of the cavity shear stresses. The focus is on the shear stresses, because experimental results [6] have shown that the stiffness and damping coefficients are very sensitive to the circumferential velocity in the seal. In the control volume analysis to be presented, the solution to the circumferential momentum equation yields the circumferential velocity in the seal. An improvement in the shear stress calculation will yield an improvement in the calculation of the stiffness and damping coefficients.

Before proceeding with the solution development, the approach taken in modelling the flow will be discussed. As mentioned previously, the flow in a labyrinth seal is known to have two distinct regions: a jet flow region in the leakage path and a recirculating flow region in the cavity itself(see figure 3). Therefore, a two-control-volume model seems appropriate. The choice is between the "box-in-a-box" model(see figure 5) of Jenny et al [21] or a more conventional model with a control volume for the jet flow and one for the recirculating flow in the cavity, as shown in figure 4. The two-separate-control-volume model was chosen, since it is suggested by the known physics of the flow. The flow enters the seal and separates into two distinct flow regions which are separated by the dividing streamline.

The final question is whether the control volumes should be defined using a geometric boundary or using the dividing streamline as

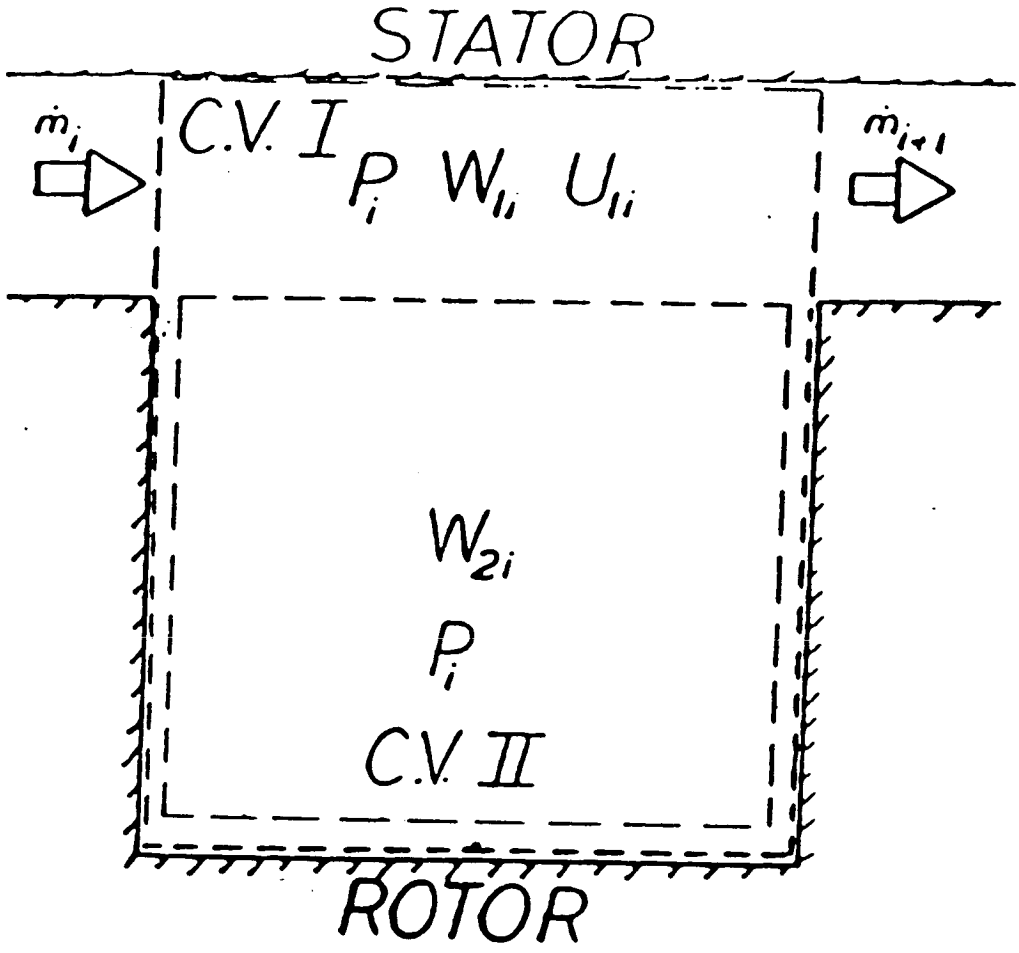

Fig. 5 The "box-in-a-box" control volume model of ref.[21]

the boundary. The dividing streamline approach seems, at first, to be the obvious choice. The governing equations would be simplified by the restriction of no flow across a streamline, the free shear stress relations are derived for flow along the dividing streamline, and the solution for the velocity of the recirculating flow may be derived for flow along the dividing streamline. Despite these advantages, the dividing streamline approach was not used, however, it will now be reviewed and a method of solution discussed. The geometric boundary approach and solution is provided in the following section.

DIVIDING STREAMLINE APPROACH

Assumptions

The following assumptions are used in deriving the governing equations:

1) The fluid is considered to be an ideal gas.
2) Pressure variations within a chamber are small compared to the pressure difference across a seal strip.
3) The lowest frequency of acoustic resonance in the cavity is much higher than that of the rotor speed.
4) The eccentricity of the rotor is small compared to the radial seal clearance.
5) Although the shear stress is significant in the determination of the flow parameters (velocity etc.), the contribution of the shear stress to the forces on the rotor are negligible when compared to the pressure forces.
6) The cavity flow is turbulent and isoenergetic.
7) The recirculation velocity, U_2, is unchanged by viscous stresses as it swirls within a cavity.

Procedure

The following analysis is developed for the teeth-on-rotor "see-through" labyrinth seal shown in figure 6. The continuity and circumferential momentum equations are derived for the two-control-volume model shown in figures 7 through 11. A procedure is discussed for determining the approximate location of the dividing streamline and the perturbation of the dividing streamline for small motion about a centered position.

Continuity Equations

Figures 7 and 8 show the control volumes defined by the dividing streamline. These control volumes have a unity circumferential width. Their continuity equations are:

$$\text{I:} \qquad \frac{\partial \rho A_1}{\partial t} + \frac{\partial \rho W_1 A_1}{Rs_1 \partial \theta} + \dot{m}_{i+1} - \dot{m}_i = 0 \tag{3}$$

$$\text{II:} \qquad \frac{\partial \rho A_2}{\partial t} + \frac{\partial \rho W_2 A_2}{Rs_2 \partial \theta} = 0 \tag{4}$$

where the control volume areas, A_1 and A_2, are shown in figure 9 and are defined by

$$A_1 = LCr + \int_0^L y\,dx \quad ; \quad A_2 = LB - \int_0^L y\,dx \tag{5}$$

The following momentum equations for control volumes I and II are derived using figures 10 and 11 which show the pressure forces and shear stresses acting on the control volumes. It is important to note that the recirculation velocity, U_2, is included in the shear stress definitions used in equations (6) and (7). These definitions are developed in a subsequent section of this chapter.

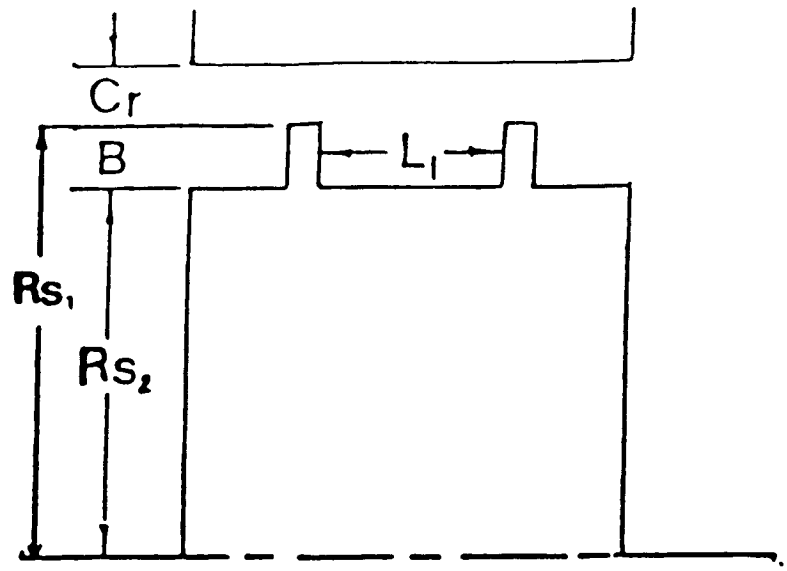

Fig. 6 A typical cavity.

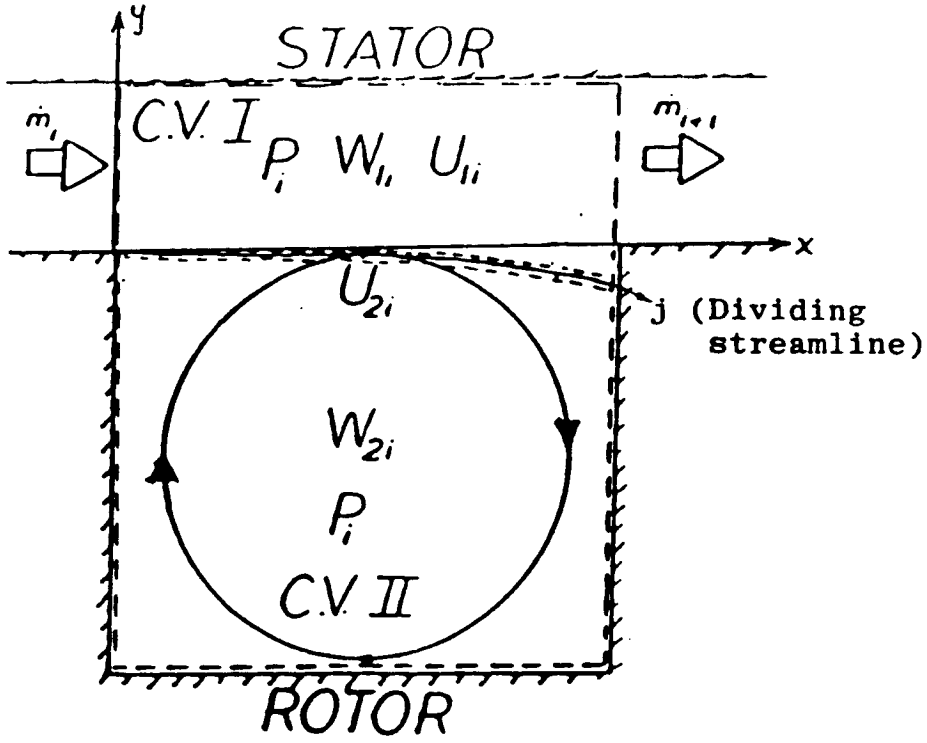

Fig. 7 Control volumes separated by dividing streamline.

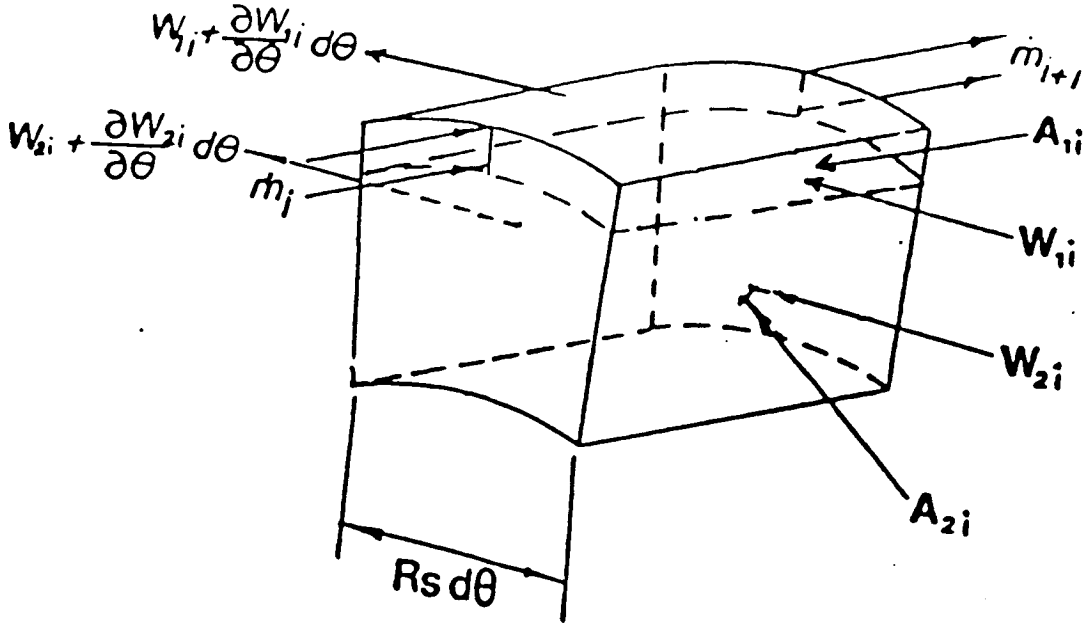

Fig. 8 Isometric view of control volumes.

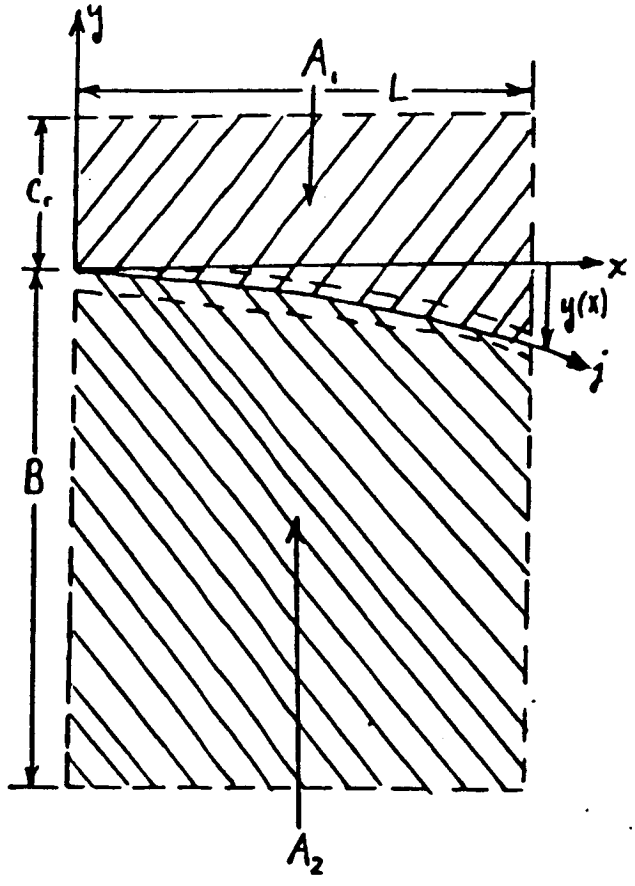

Fig. 9 Control volume areas.

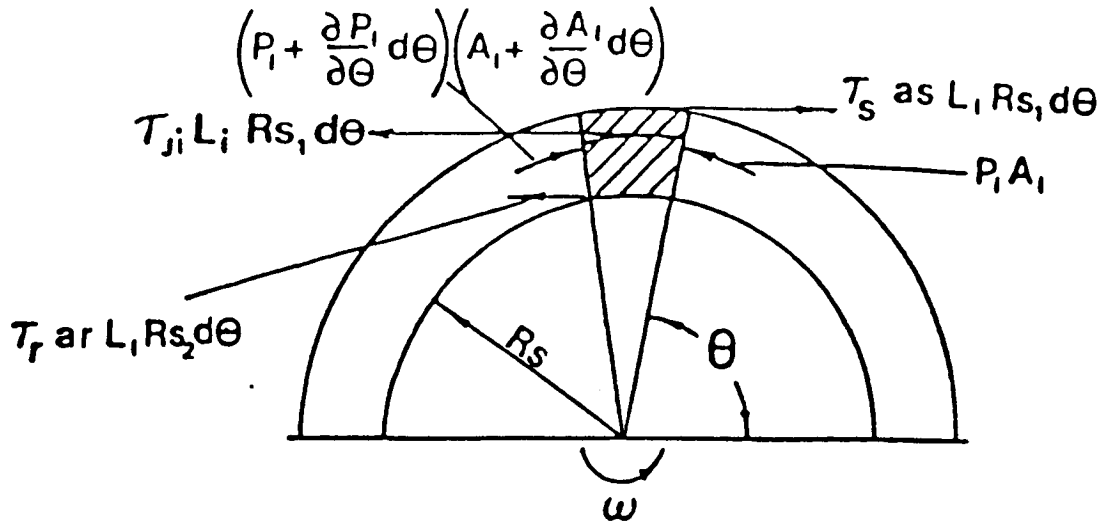

Fig.10 Forces on control volumes

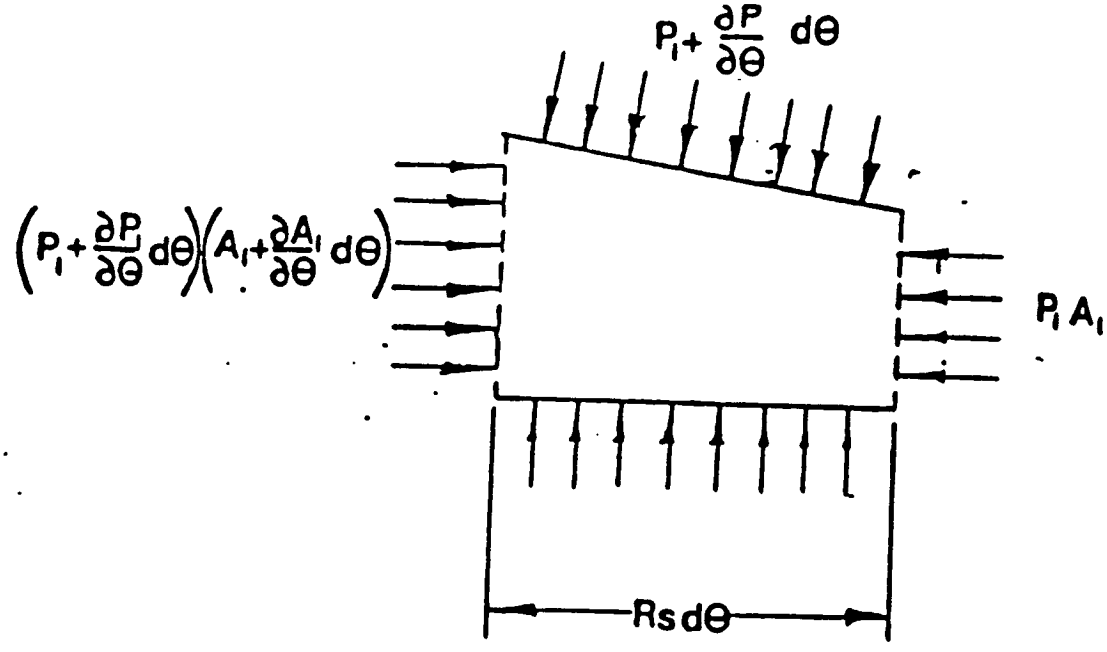

Fig.11 Pressure forces on control volume I

$$\text{I:}\quad \frac{\partial \rho W_1 A_1}{\partial t} + \frac{2\rho W_1 A_1}{Rs_1}\frac{\partial W_1}{\partial \theta} + \frac{\rho W_1}{Rs_1}\frac{\partial A_1}{\partial \theta} + \frac{W_1 A_1}{Rs_1}\frac{\partial \rho}{\partial \theta} \tag{6}$$

$$+ \dot{m}_{i+1} W_{1i} - \dot{m}_i W_{1i-1} = -\frac{A_1}{Rs_1}\frac{\partial P_i}{\partial \theta} + \tau_{jiLi} - \tau_{siasiLi}$$

$$\text{II:}\quad \frac{\partial \rho W_2 A_2}{\partial t} + \frac{2\rho W_2 A_2}{Rs_2}\frac{\partial W_2}{\partial \theta} + \frac{\rho W_2}{Rs_2}\frac{\partial A_2}{\partial \theta} + \frac{W_2 A_2}{Rs_2}\frac{\partial \rho}{\partial \theta} \tag{7}$$

$$= -\frac{A_2}{Rs_2}\frac{\partial P_i}{\partial \theta} - \tau_{jiLi} + \tau_{riariLi}$$

Streamline Location

The main difficulty in obtaining a solution to the above equations (3) through (7) is in the determination of the location of the dividing streamline. The streamline definition, $y(x)$, must be found to determine the control-volumes areas, A_1 and A_2, defined in equations 5. There is no known solution for the location of a dividing streamline for the three dimensional flow field found in a labyrinth cavity. An approximation for the location of the dividing streamline can be obtained using the theory for the flow of a two-dimensional, turbulent, isoenergetic, half-infinite jet. Figure 12 shows the model for this theory. The flow is assumed to enter with one velocity component, in the x-direction, and spread into the cavity, developing a y-component of velocity. This model does not account for the circumferential velocity component, which is the same order of magnitude as the axial velocity, in a labyrinth seal flowfield. The solution procedure involves solving the infinitessimal form of the x-momentum equation for the dimensionless velocity profile and then solving the integral form of the continuity and momentum equations for the location of the dividing

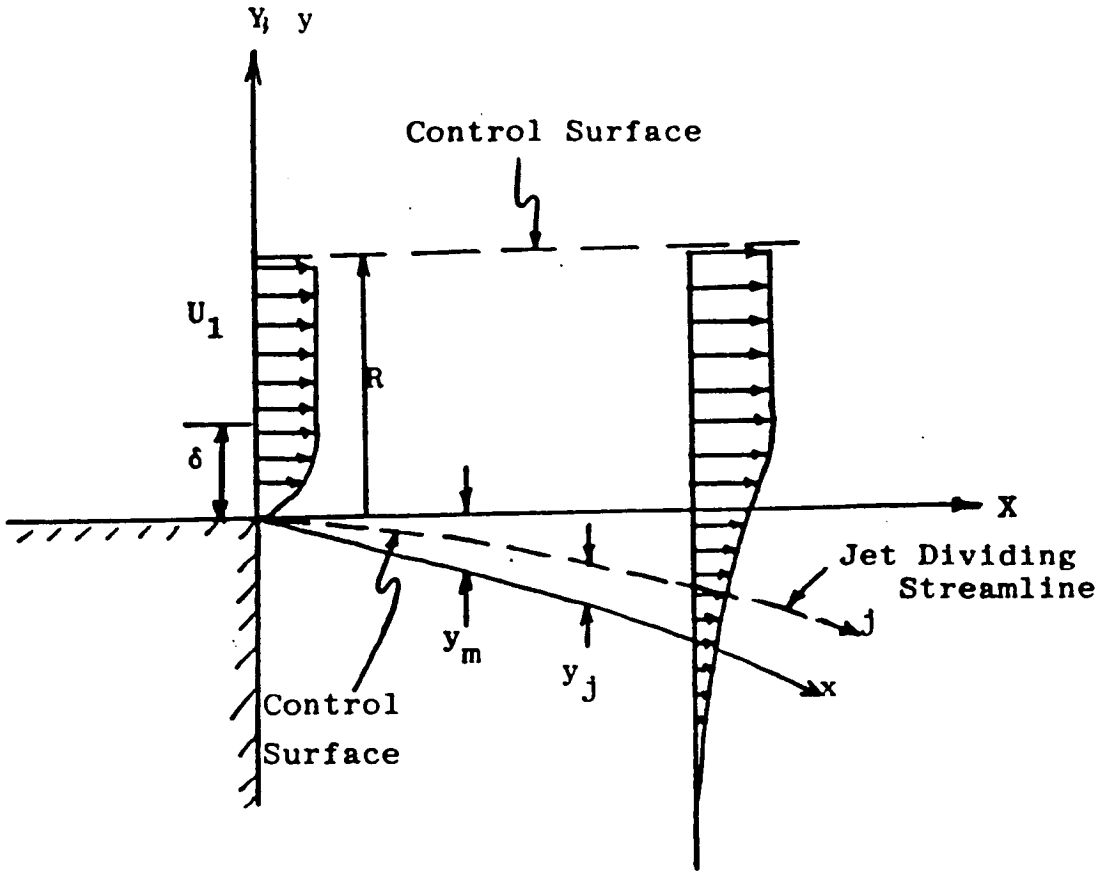

Fig. 12 Half-infinite jet model.

streamline. A complete discussion of this theory can be found in Korst et al. [26].

The following is a derivation of the equations necessary to determine the location of the jet dividing streamline. The following derivation uses the assumption that the curvature in the dividing streamline is small. The infinitessimal form of the continuity equation for the flow illustrated in figure 12 is:

$$\partial(\rho u)/\partial x + \partial(\rho v)/\partial y = 0 \tag{8}$$

where the x and y velocity components, u and v, respectively, are time averaged. The infinitessimal x-momentum equation, which has been reduced using equation (8), is:

$$\rho u\ \partial u/\partial x + \rho v\ \partial u/\partial y = \partial(e\rho\partial u/\partial y)/\partial y \tag{9}$$

where e is the apparent(turbulent) kinematic viscosity. Since the flow illustrated in figure 12 is a quasi-one-dimensional jet flow where there is little or no initial vertical velocity component, equation (9) can be linearized using the following perturbation method:

$$u = U_1 + u'' \ ; \quad v = v'' \ ; \ \rho = \rho_1 + \rho'' \tag{10}$$

where $|v''| << |U_1|$ and $|u''| << |U_1|$. The resultant equation is:

$$\rho_1 U_1\ \partial u''/\partial x + \rho_1 V_1\ \partial u''/\partial y = e\rho_1\ \partial^2 u''/\partial^2 y \tag{11}$$

where $e=e(x)$ and the second term (V_1 term) is considered small. The final form of the equation is:

$$U_1\ \partial u''/\partial x = e\ \partial^2 u''/\partial y^2 \tag{12}$$

The following dimensionless variables are introduced:

$$\begin{aligned} \phi &= U/U_1 = 1+u''/U_1 \\ \zeta &= y/\delta \\ \psi &= x/\delta \\ \xi &= \int_0^{\psi} e\ d\psi/(U_1\delta) \end{aligned} \tag{13}$$

where δ is the initial boundary layer thickness shown in figure 12.

Equation (12) becomes:

$$\partial\phi/\partial\xi = \partial^2\phi/\partial\zeta^2 \qquad (14)$$

with the initial conditions:

$$\phi = \phi(0,\zeta) = 0 \quad \text{for } -\infty < \zeta < 0$$
$$\phi = \phi(0,\zeta) = \phi_0(\zeta) \quad \text{for } 0 < \zeta < 1.0$$
$$\phi = \phi(0,\zeta) = 1.0 \quad \text{for } 1.0 < \zeta < \infty$$

and boundary conditions:

$$\phi = \phi(\xi,-\infty) = 0 \quad \text{for } \xi > 0$$
$$\phi = \phi(\xi,\infty) = 1.0 \quad \text{for } \xi > 0$$

The solution to equation (14) for the above initial and boundary conditions is:

$$\phi = 0.5[1-\text{erf}(\eta_p-\eta)] + 1/\sqrt{\pi} \int_{\eta-\eta_p}^{\eta} \phi[(\eta-\beta)/\eta_p] e^{-\beta^2} d\beta \qquad (15)$$

where

$$\eta_p = 1/(2\sqrt{\xi}) \; ; \; \eta = \zeta\eta_p$$
$$\text{erf}(x) = 2/\sqrt{\pi} \int_0^x \exp(-\beta^2)d\beta$$
$$\text{erf}(-x) = -\text{erf}(x)$$

The apparent viscosity, e, can be expressed in terms of the apparent viscosity far from the mixing region, e_1:

$$e = e_1 f(\psi) \qquad (16)$$

where

$$f(\psi) \dashrightarrow 1.0 \text{ as } \psi \dashrightarrow \infty$$

According to Prandtl, this can be rewritten as:

$$e_1 = \kappa b(x)[U_{max} - Umin] \qquad (17)$$

with

$$\partial e/\partial y = 0$$

For a half-infinite jet, equation (17) is:

$$e_1 = \kappa b(x) U_1 \qquad (18)$$

where b(x) is the width of the mixing region. Assuming that the mixing increases linearly, i.e.

$$b(x) = cx = c\psi\delta \qquad (19)$$

where c is a constant, equation (16) becomes:

$$e = c\psi\delta U_1 f(\psi) \qquad (20)$$

Substituting this into ξ, from equation (13) yields:

$$\xi = c \int_0^{\psi} \psi f(\psi)\, d\psi \qquad (21)$$

Looking at a limiting case of equation (21):

as $x/\delta \rightarrow \infty$

then $\psi \rightarrow \infty$

$\xi \rightarrow \infty$

$$\eta_p = 1/2\sqrt{\xi} \rightarrow 0$$

This limiting case is for either no initial boundary layer, which is a good assumption for labyrinth seals, or fully developed velocity profiles. Since $\eta_p \rightarrow 0$, the variable η is now undefined. Liepman and Laufer [27] have defined η for this limiting condition using the following development. By definition:

$$\text{as } \psi \rightarrow \infty \text{ then } f(\psi) \rightarrow 1.0$$

Inserting this into equation (21) yields:

$$\xi = c\psi^2/2$$

By definition:

$$\eta = \zeta\eta_p = \zeta/2\sqrt{\xi} = \zeta/(\psi\sqrt{2c}) = y/(x\sqrt{2c})$$

Letting $c = 1/(2\sigma^2)$, yields the desired result:

$$\eta = \sigma y/x \qquad (22)$$

where σ is the jet spreading parameter. Korst and Tripp [28] used experimental data to find the following relation for σ:

$$\sigma = 12.0 + 2.758M_1 \text{ (for air)} \qquad (23)$$

Goertler [29] has shown that the dimensionless velocity, ϕ, follows directly from equation (15) when $\eta_p \rightarrow 0$:

$$\phi = 0.5(1+\text{erf}(\eta)) \qquad (24)$$

Equations (24) is a solution for the dimensionless velocity profile, ϕ, at any dimensionless position, η. The goal of this development is to

determine the dimensionless dividing streamline position, η_j. η_j can be obtained by solving the integral form of the continuity and x-momentum equations for the system shown in figure 12.

Control Volume Analysis

The coordinate systems and definition of the control surface are shown in figure 12. The (x,y) coordinate system is the intrinsic coordinate system while the (X,Y) coordinate system is the reference system. Equations (22) and (24) are approximate relations; exact relationships, if known, would provide for conservation of momentum for the constant pressure mixing region. The reference coordinate system is the coordinate system in which momentum is conserved. The intrinsic coordinate system is located with respect to the reference coordinate system by a control volume analysis utilizing the conservation of momentum principle for this constant pressure mixing region. The relationship between the coordinate systems normal to the jet is:

$$y_m(x) = y - Y$$

with

$$y_m(0) = 0.$$

X-Momentum Equation

The steady flow x-momentum equation for the jet flow shown in figure 12, written for the reference coordinate system and expressed in the previously defined dimensionless variables is:

$$\int_0^R \rho U^2 \, dY \Big|_{X=0} = \int_{-\infty}^R \rho U^2 \, dY \Big|_{X=X} \qquad (25)$$

For the momentum equation, the lower control surface is located at $-\infty$. This equation contains no surface forces. This is realistic for a labyrinth seal if location R is far from of the stator wall. Rewriting equation (25) for the intrinsic coordinate system:

$$\int_0^{\delta} \rho U^2 \, dy \Big|_{x=0} + \int_{\delta}^{R} \rho U^2 \, dy \Big|_{x=0} = \int_0^{R+y_m} \rho U^2 \, dy \Big|_{x=x} \tag{26}$$

Introducing the previously defined dimensionless variables, equations (13) and (22), equation (26) becomes:

$$\eta_p \int_0^{1.0} (\rho/\rho_1)\phi_o^2 \, d\zeta + \eta R - \eta p = \int_{-\infty}^{\eta_R - \eta_m} (\rho/\rho_1)\phi^2 \, d\eta \tag{27}$$

Distance R is chosen such that:

$$1 - \phi(\eta_R) <<< 1.0$$

Equation (27) becomes:

$$\eta_p \int_0^{1.0} (\rho/\rho_1)\phi_o^2 \, d\zeta + \eta R - \eta p = \int_{-\infty}^{\eta_R} (\rho/\rho_1)\phi^2 \, d\eta + \eta_m \tag{28}$$

Applying the condition of no initial boundary condition (η_p --> 0), equation (28) is:

$$\eta_m = \eta R - \int_{-\infty}^{\eta_R} (\rho/\rho_1)\phi^2 \, d\eta \tag{29}$$

Continuity Equation

The steady flow continuity equation, written for the reference coordinate system, is:

$$\int_0^{R} \rho U \, dY \Big|_{X=0} = \int_{y_j - y_m}^{R} \rho U \, dY \Big|_{X=X} \tag{30}$$

For the continuity equation, the lower control surface is coincident with the jet dividing streamline. Rewriting equation (30) for the intrinsic coordinate system:

$$\int_0^{\delta} \rho U \, dy \Big|_{x=0} + \int_{\delta}^{R} \rho U \, dy \Big|_{x=0} = \int_{y_j}^{R+y_m} \rho U \, dy \Big|_{x=x} \tag{31}$$

Introducing the previously defined dimensionless coordinates and multiplying equation (31) by $\eta_{p/\delta}$:

$$\eta_p \int_0^{1.0} (\rho/\rho_1)\phi_o \, d\zeta + \eta_R - \eta_p = \int_{\eta_j}^{\eta_R} (\rho/\rho_1)\phi \, d\eta + \eta_m \qquad (32)$$

Substituting the results of the momentum equation, equation (29), into equation (32) yields:

$$\int_{\eta_j}^{\eta_R} (\rho/\rho_1)\phi \, d\eta = \int_0^{1.0} (\rho/\rho_1)(1-\phi)_o \, d\zeta + \int_{-\infty}^{\eta_R} (\rho/\rho_1)\phi^2 \, d\eta \qquad (33)$$

Making the assumption of no initial boundary layer ($\eta_p \rightarrow 0$), equation (33) becomes:

$$\int_{\eta_j}^{\eta_R} (\rho/\rho_1)\phi \, d\eta = \int_{-\infty}^{\eta_R} (\rho/\rho_1)\phi^2 \, d\eta \qquad (34)$$

The density ratio, (ρ/ρ_1), for isoenergetic flow (constant temperature) is given as:

$$\rho/\rho_1 = (1-Ca^2)/(1-Ca^2\phi^2) \qquad (35)$$

The final form of the continuity equation becomes:

$$\int_{\eta_j}^{\eta_R} (\phi/[1-Ca^2\phi^2]) \, d\eta = \int_{-\infty}^{\eta_R} (\phi^2/[1-Ca^2\phi^2]) \, d\eta \qquad (36)$$

Where Ca is the Crocco number. The Crocco number is defined as:

$$Ca^2 = (\gamma-1)M^2/(2+(\gamma-1)M^2) \qquad (37)$$

The Crocco number is a dimensionless velocity similar to the Mach number. The Crocco number uses the maximum isentropic speed of a gas while the Mach number uses the local speed of sound. The Mach number varies between 0 and ∞ while the Crocco number has a range of 0 to 1.

The solution to equation (36),the location of the dividing streamline, can be obtained by the following steps:

0) Calculate the Mach number using the zeroth-order leakage value. The zeroth-order leakage is discussed in the next section.

1) Calculate the Crocco number using equation (37).

2) Substitute equation (24) into equation (36) and integrate the error function. The value of the error function at the limits R and $-\infty$ is 1.0, leaving an equation in η_j only. This is solved for η_j, which is the dimensionless location of the dividing streamline.

3) Use the straight line approximation, equation (22), to find y as a function of x.

4) Insert y(x) from step 3 into equation (5) and calculate the areas of the control volumes.

The above procedure yields the zeroth-order (centered) value for the areas. The problem is to find the values for a perturbation analysis. Since equation (24) is an error function, an explicit equation for the change in area for a perturbation in clearance cannot be obtained. However, the above procedure could be carried out for a range of clearances in the neighborhood of the nominal clearance and an approximation for the change in area and a final result could be obtained.

As noted at the beginning of this discussion, the advantages of the dividing streamline approach are that the free shear stress and recirculating velocity equations may be derived along the dividing streamline, and the governing equations are simplified by the condition of no mass flow across a streamline. The above solution procedure yields only an approximation for the location of the dividing streamline for a simplified (two-dimensional) flow while increasing the difficulty in obtaining a solution. Therefore, the advantages of the dividing streamline approach are outweighed by the difficulty in obtaining a solution. The geometric boundary approach and a complete solution will now be presented.

GEOMETRIC BOUNDARY APPROACH

Procedure

The analysis presented here is developed for the teeth-on-rotor "see-through" labyrinth seal shown in figure 5. The equivalent equations for the teeth-on-stator labyrinth seal are given in Appendix A. The continuity and circumferential momentum equations will be derived for the two-control-volume model shown in figures 13,14,15, and 16. A leakage model will be employed to account for the axial flow. The governing equations are linearized using perturbation analysis for small motion about a centered position. The zeroth-order continuity and momentum equations will be solved to determine the steady state pressure, axial and circumferential velocity for each cavity. The first-order continuity and momentum equations will be reduced to linearly independent, algebraic equations by assuming an elliptical orbit for the shaft and a corresponding harmonic response for the pressure and velocity perturbations. The force coefficients for the seal are found by integration of the first-order pressure perturbation along and around the shaft.

Continuity Equations

The control volumes of figures 13 and 14 have a unity circumferential width. Their continuity equations are:

$$\text{I:} \qquad \frac{\partial \rho A_1}{\partial t} + \frac{\partial \rho W_1 A_1}{Rs_1 \partial \theta} + \dot{m}_{i+1} - \dot{m}_i + \dot{m}_r = 0 \tag{38}$$

$$\text{II:} \qquad \frac{\partial \rho A_2}{\partial t} + \frac{\partial \rho W_2 A_2}{Rs_2 \partial \theta} - \dot{m}_r = 0 \tag{39}$$

For the teeth-on-rotor case, A_1=LCr, A_2=LB, Rs_2=Rs, and Rs_1=Rs+B.

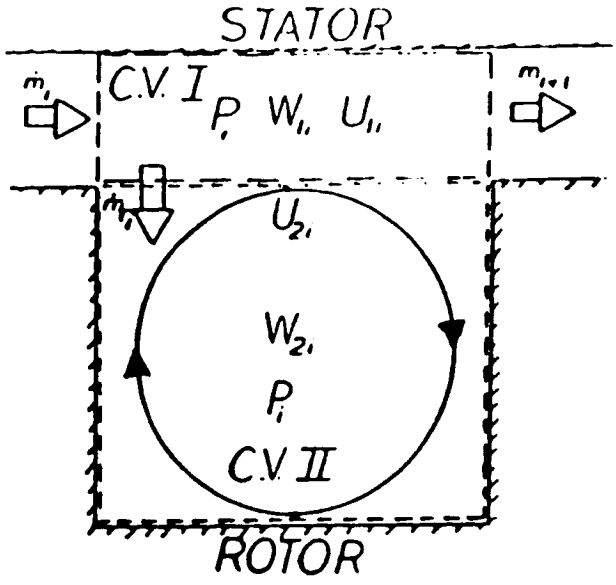

Fig. 13 Control Volumes with geometric boundary.

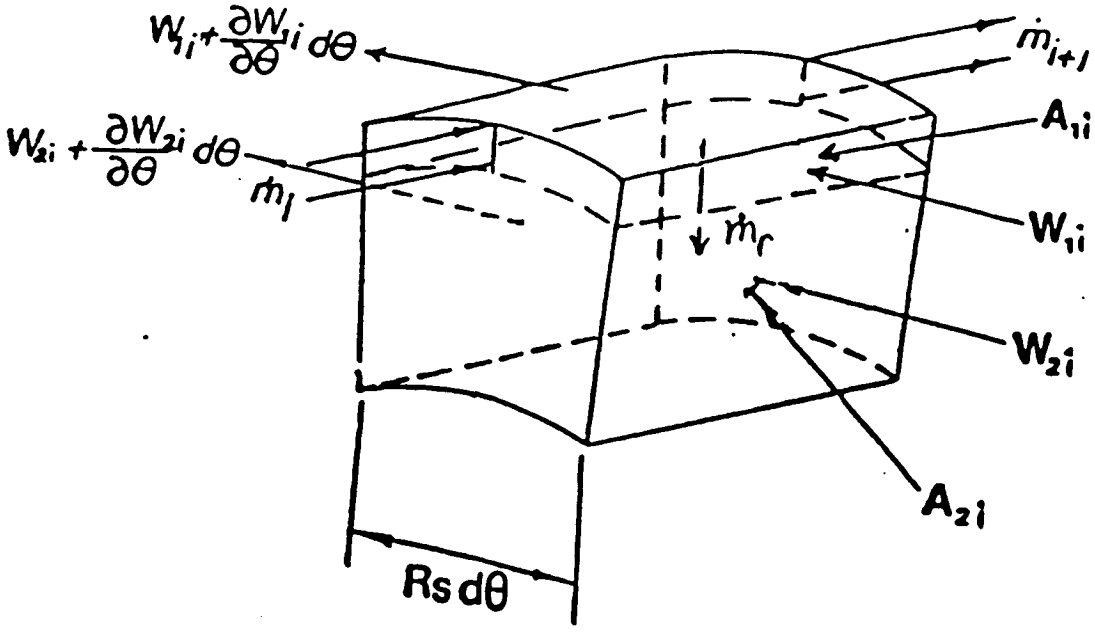

Fig. 14 Isometric view of Control Volumes with geometric boundary.

Momentum Equations

The following momentum equations for control volumes I and II are derived using figures 15 and 16 which show the pressure forces and shear stresses acting on the control volumes.

$$\text{I:}\quad \frac{\partial \rho W_1 A_1}{\partial t} + \frac{2\rho W_1 A_1}{Rs_1}\frac{\partial W_1}{\partial \theta} + \frac{\rho W_1}{Rs_1}\frac{\partial A_1}{\partial \theta} + \frac{W_1 A_1}{Rs_1}\frac{\partial \rho}{\partial \theta} + \dot{m}_{rWoi} \tag{40}$$

$$+ \dot{m}_{i+1}W_{1i} - \dot{m}_i W_{1i-1} = -\frac{A_1}{Rs_1}\frac{\partial P_i}{\partial \theta} + \tau_{jiLi} - \tau_{siasiLi}$$

$$\text{II:}\quad \frac{\partial \rho W_2 A_2}{\partial t} + \frac{2\rho W_2 A_2}{Rs_2}\frac{\partial W_2}{\partial \theta} + \frac{\rho W_2}{Rs_2}\frac{\partial A_2}{\partial \theta} + \frac{W_2 A_2}{Rs_2}\frac{\partial \rho}{\partial \theta} \tag{41}$$

$$- \dot{m}_{rWoi} = -\frac{A_2}{Rs_2}\frac{\partial P_i}{\partial \theta} - \tau_{jiLi} + \tau_{riariLi}$$

where ar and as are the dimensionless length upon which the shear stresses act and are defined for the teeth-on-rotor labyrinth by

$$as_i = 1 \qquad ar_i = (2B_i + L_i)/L_i \,. \tag{42}$$

W_o is the circumferential velocity between the control volumes.

Various models for the stator wall shear stress were evaluated by comparison to CFD results of Rhode [23]. For a teeth-on-rotor labyrinth seal, the optimum model for the stator shear stress (rotor shear stress for a teeth-on-stator seal) was obtained by using the equation of Glauert [30] for wall shear stress of a plane jet issuing fom a slot. However, this relation requires knowledge of the maximum axial velocity and its displacement from the wall. This information is not available in a control volume analysis. The next best model, by comparison to [23], is Colebrook's formula [31], but this equation is not explicit in the friction factor and cannot be perturbed. Experience [32] has shown that the perturbation of the friction factor is important in stiffness

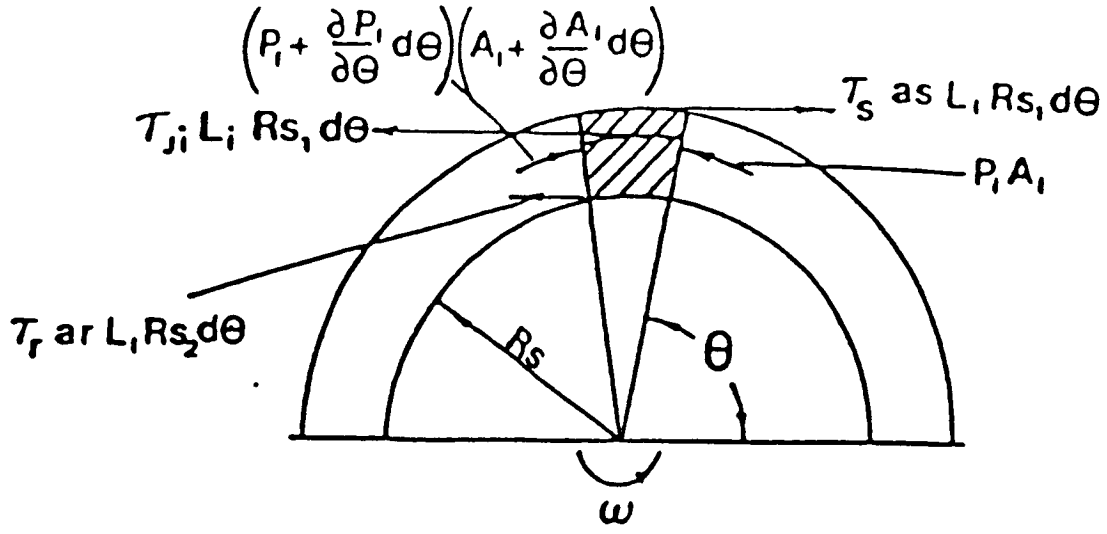

Fig. 15 Forces on control volumes with geometric boundary.

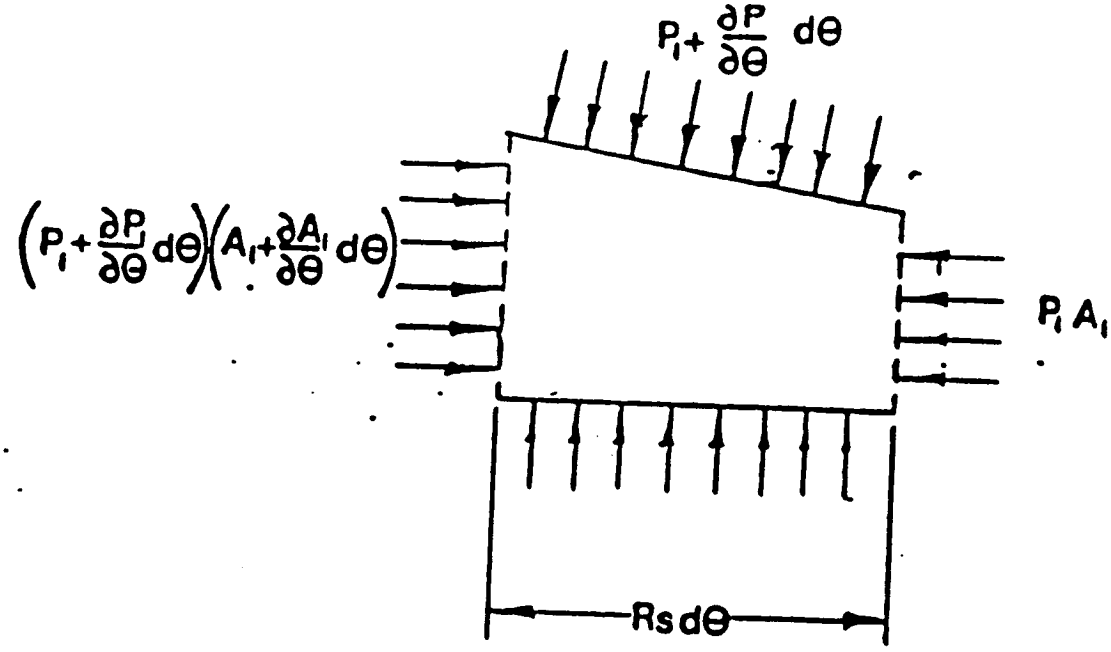

Fig. 16 Pressure forces on control volume I of geometric boundary model.

calculations. The next best shear stress model is based on the assumption that the shear stresses (for rotor and stator surfaces) are similar to those found in the pipe analysis of Blasius [33]. Blasius determined that the shear stresses for turbulent flow in a smooth pipe could be written as

$$\tau = \frac{1}{2}\,\rho U_m^2\ no\left(\frac{UmDh}{\nu}\right)^{mo}$$

where Um is the mean flow velocity relative to the surface upon which the shear stress is acting. The constants mo and no can be empirically determined for a given surface from pressure flow experiments. However, for smooth surfaces the coefficients given by Yamada [34] for turbulent flow between annular surfaces are:

$$mo = -0.25 \qquad no = 0.079$$

Applying Blasius' equation to the labyrinth rotor surfaces yields the following definitions for the rotor shear stress in the circumferential direction. Note that the recirculation velocity, U_2, is included in the definition of the total velocity acting on the rotor.

$$\tau_r = \frac{1}{2}\,\rho\sqrt{(Rs_2\omega-W_2)^2+U_2^2}\,(Rs_2\omega-W_2)\ nr\left(\frac{\sqrt{(Rs_2\omega-W_2)^2+U_2^2}\ Dhi}{\nu}\right)^{mr} \qquad (43)$$

where Dh_{2i} is the hydraulic diameter of control volume II, defined by

$$Dh_{2i} = 2BL/(B+L) \qquad (44)$$

Similarly, the stator shear stress in the circumferential direction is:

$$\tau_s = \frac{1}{2}\,\rho\sqrt{W_1^2+U_1^2}\ W_1\ \ ns\left(\frac{\sqrt{W_1^2+U_1^2}\ Dhi}{\nu}\right)^{ms} \qquad (45)$$

where Dh_{1i} is the hydraulic diameter of control volume I, defined by

$$Dh_{1i} = 2CrL/(Cr+L) \qquad (46)$$

and the axial velocity U_1 is

$$U_1 = \dot{m}/\rho Cr \qquad (47)$$

Figure 17 shows a comparison of the predictions from equation (45) and CFD results for stator wall shear stress for seal A of table 1. The recirculation velocity, U_2, is undefined at this point. It will be discussed in the following section. Table 1 shows the seal geometries calculated by Rhode [23]. The figure shows that the comparison is very good. Similar results are obtained for the other seals of table 1. Figure 18 shows a comparison of rotor wall-shear-stress predictions from equation (43), CFD, and averaged CFD results for rotor wall shear stress for seal A of table 1. The averaged CFD result is used here for comparison since the bulk flow model yields a single averaged result for cavity shear stress and is not capable of modelling the complex flowfield. The figure shows that the prediction of equation (43) is close to the CFD results. The dips in the CFD results are the lower corners of the cavity. Similar results are obtained for the other seals of table 1.

The flow across a labyrinth tooth is very similar to the flow of a turbulent jet issuing from a slot. The problem with using jet-flow results for labyrinth seals is that current jet-flow theory only considers the flow of a jet with a coflowing stream or a crossflowing stream, not both. In the following derivation, the relations given by Abramovich [35] for the velocity profile of a semi-contained, one-dimensional, turbulent jet with a coflowing stream are assumed to apply for the two-dimensional labyrinth seal flow. According to Abramovich [35], the velocity profile for such a flow can be shown to fit the following function when compared to experimental results:

$$v = v_1 + (v_2 - v_1)\left[1-\left(\frac{y+y_2}{b}\right)^{1.5}\right]^2 \qquad (48)$$

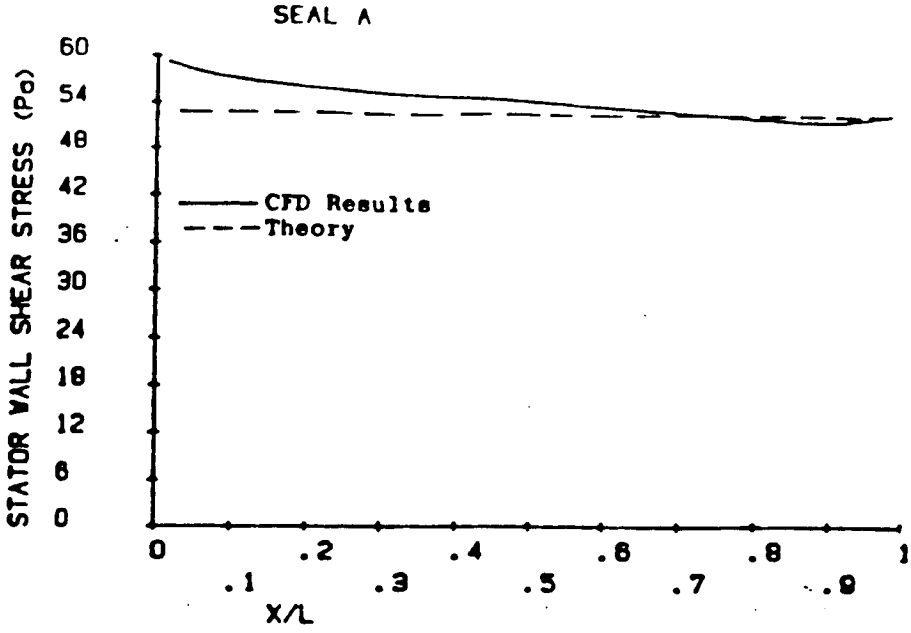

Fig. 17 A comparison of Theoretical and CFD results for stator wall shear stress. See table 1 for seal geometry.

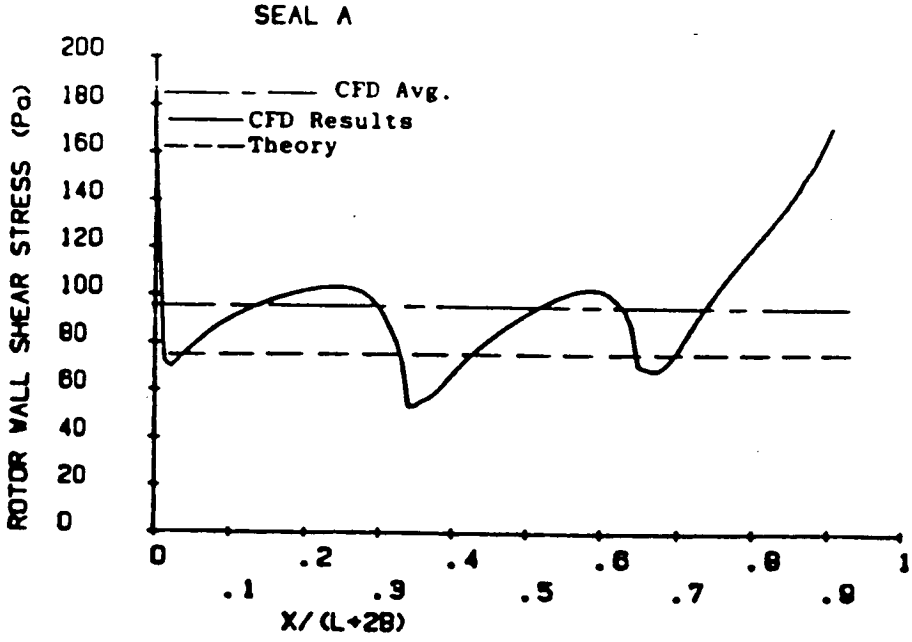

Fig. 18 A comparison of Theoretical and CFD results for rotor wall shear stress. See table 1 for seal geometry.

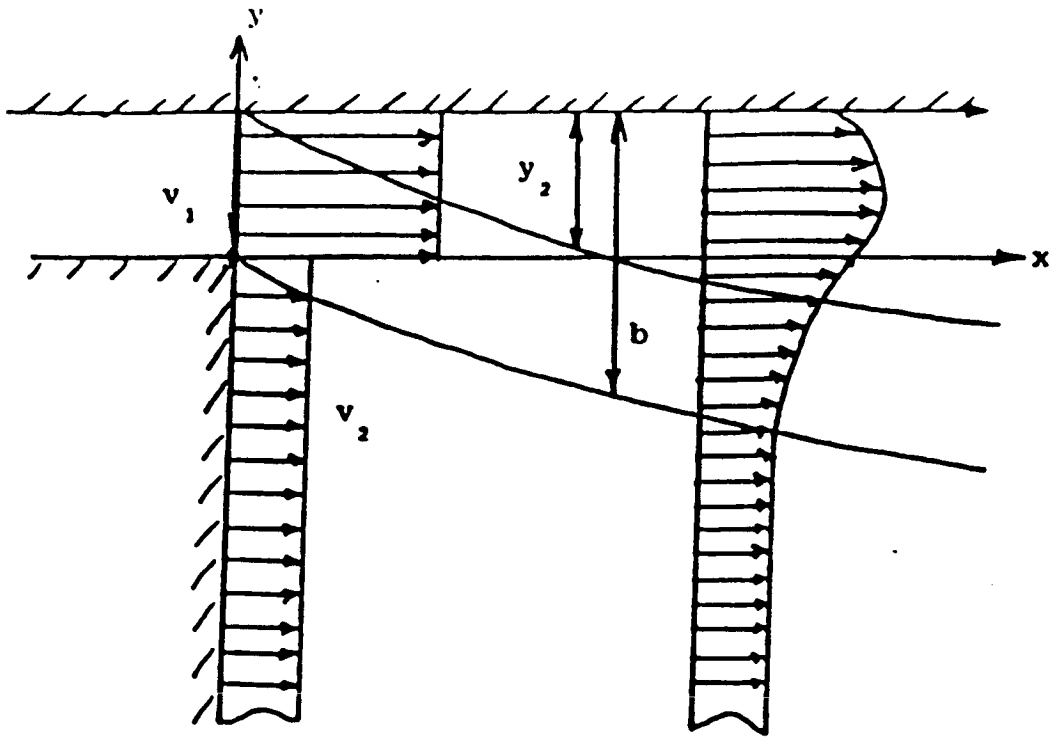

Fig. 19 Model of semi-contained turbulent jet.

Table 1. Seal geometries calculated by Rhode.

	Seal			
	A	B	C	D
Rs	72.0543mm	72.0543mm	72.0543mm	41.780mm
B	3.175mm	3.175mm	3.175mm	0.889mm
L	3.175mm	3.175mm	3.969mm	0.8585mm
Tp	0.35mm	0.35mm	0.35mm	0.15mm
Cr	0.4064mm	0.508mm	0.508mm	0.2159mm

where the coordinate y, the mixing thickness b, and the boundary layer thickness y_2 are defined in figure 19. The relationship between the boundary layer thickness and the mixing thickness was found [35] by comparison to experiment to be:

$$y_2/b = 0.584 - 0.134(v_2/v_1) \tag{49}$$

Once the velocity ratio across the dividing streamline, v_2/v_1, is found, equation (49) reduces to a constant. The total free shear stress is found using Prandtl's mixing length hypothesis [36]:

$$\tau_{jt} = \rho \ell^2 \left|\partial v/\partial y\right| (\partial v/\partial y) \tag{50}$$

where the mixing length, ℓ, for a labyrinth seal, has been determined from the calculations of Rhode [23] to be:

$$\ell = 0.275b \tag{51}$$

Table 1 shows the seal geometries calculated by Rhode [22]. The mixing length, ℓ, given in equation (51) is the most sensitive factor in this solution. The large magnitude of the mixing length shows the high turbulence level of the labyrinth flow as compared to similar flows. The typical values given for the mixing lengths of rectangular and round jet flows, in one dimension, are in the range of 0.07 to 0.09. Without the CFD results, one of these values would have to be used and the results of using ℓ in the range [0.07,0.09] would have been disappointing.

Jenny et al. [21] used a 2-D CFD code to obtain a correlation for ℓ/b as a function of clearance and tooth geometry. Their relation is shown below for the teeth-on-rotor case:

$$\ell/b = 0.055(1+1.03Cr/L+0.08\sqrt{Rs/L}) \tag{52}$$

However, their shear stress relation neglected the recirculating velocity component, U_2. Upon comparison with the data of Rhode [23],

the mixing length ratio, ℓ/b, was found to be relatively constant when the shear stress is calculated using all velocity components.

Substituting the differentiated version of equation (48) and equation (51) into equation (50) yields an expression for the total free shear stress. At the interface of the two control volumes (y=0), the total free shear stress is:

$$\tau_{jt} = 0.68\ \rho|v_2-v_1|(v_2-v_1)[1-(y_2/b)^{.5}]^2(y_2/b) \qquad (53)$$

The circumferential component of the free shear stress is:

$$\tau_j = 0.68\ \rho\sqrt{(W_2-W_1)^2+(U_2-U_1)^2}\ (W_2-W_1)[1-(y_2/b)^{.5}]^2(y_2/b) \qquad (54)$$

The circumferential component of the velocity at the interface, W_{oi}, is obtained from equation (48).

$$W_{oi} = W_1 + (W_2-W_1)[1-(y_2/b)^{.5}]^2(y_2/b) \qquad (55)$$

Equations (53,54,55) are all valid along the dividing streamline. Since the control volumes are defined geometrically and not by the dividing streamline, the shear stress calculated using the above equations is assumed to be close to that existing along the geometric boundary line. This is a good assumption considering that the angle of the dividing streamline from the horizontal has been found experimentally to be on the order of 6 degrees by several investigators [37,38].

The analysis to this point is incomplete in that the recirculation velocity, U_2, and the relationship between the mixing thickness and the boundary layer thickness, y_2/b, are undefined. In order to determine the recirculation velocity, U_2, and subsequently y_2/b, the analysis presented in the previous section dealing with the DIVIDING STREAMLINE APPROACH is used. Again, this analysis is valid along the dividing streamline, but is considered close enough to the values along the

geometric boundary line. The final form of the continuity equation, equation (36), is rewritten here:

$$\int_{\eta_j}^{\eta_R} (\phi/[1-Ca^2\phi^2])\, d\eta = \int_{-\infty}^{\eta_R} (\phi^2/[1-Ca^2\phi^2])\, d\eta \qquad (56)$$

where Ca is the Crocco number, η is the dimensionless coordinate, and ϕ is the velocity ratio U/U_1. The solution to this equation is obtained by substituting equation (24) into equation (56) and solving for the dividing streamline coordinate, η_j, for a given Crocco number. This is then inserted back into equation (24) and a value of ϕ_j is obtained. The results of this solution procedure are tabulated in table 2, for air. For air (γ=1.4) flowing in a labyrinth seal, the maximum possible Mach number is 1.0. Therefore, the maximum possible Crocco number is 0.408 or Ca^2=0.167. The range of solutions is:

$$0.61632 < \phi_j < 0.6263$$

Using an average solution of $\phi_j = 0.62$ gives a maximum error of less than ± 1%. The recirculation velocity at the interface is:

$$U_{2j} = 0.62U_1 \qquad (57)$$

The only remaining problem is the numerical definition of y_2/b. Looking back, equations (48) and (24) both describe the axial velocity profile in the jet flowfield. If the following observation is made

$$v_2/v_1 = \phi_j$$

then equation (57) can be substituted back into equation (49) yielding the following numerical definition for y_2/b:

$$y_2/b = 0.584-0.134\phi_j = 0.50$$

It is interesting to note that Jenny et al. [21] assumed that y_2/b=0.5.

Figure 20 shows a plot of the dimensionless axial velocity profile in the recirculation region for seal A of table 1 as calculated by

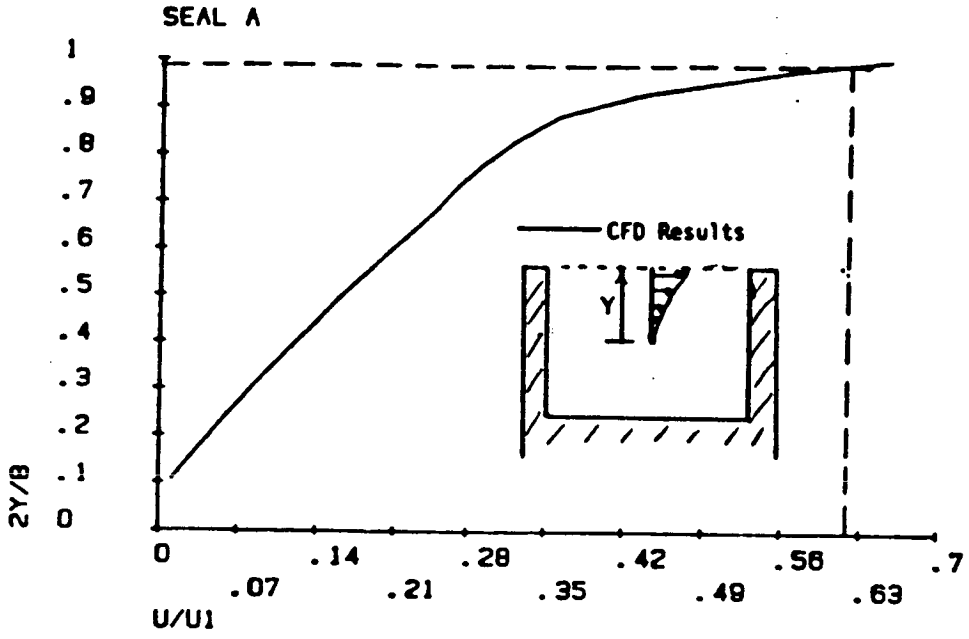

Fig. 20 CFD calculation of dimensionless recirculation velocity.

Table 2. Tabulated solution to equation (56).

Ca^2	ϕ_j	Ca^2	ϕ_j
0.00000	0.61632	0.68000	0.67553
0.05000	0.61915	0.72000	0.68188
0.10000	0.62211	0.76000	0.68903
0.15000	0.62523	0.80000	0.69724
0.20000	0.62848	0.84000	0.70689
0.24000	0.63129	0.86490	0.713944
0.28000	0.63405	0.88360	0.719944
0.32000	0.63725	0.90250	0.726834
0.36000	0.64047	0.92160	0.734949
0.40000	0.64387	0.94090	0.744883
0.44000	0.64748	0.96040	0.757869
0.48000	0.65132	0.98010	0.777432
0.52000	0.65543	0.992016	0.798766
0.56000	0.65979	0.998001	0.823427
0.60000	0.66462	1.000000	1.000000
0.64000	0.66982		

Rhode [23]. This profile is for the center of the recirculation region to the top of the labyrinth tooth. The intersection of the two dashed lines is the location and value of the theoretical recirculation velocity as calculated using equation (57) and the assumption that the dividing streamline makes an angle of 6° with the horizontal. The agreement is excellent. Equation (57) is actually the velocity at the interface of the two control volumes. The velocity components used in the shear stress equations are all average velocity components. To be consistent, the average recirculation velocity must be used. The CFD results show that the velocity distribution is parabolic in nature. Integrating this yields:

$$U_2 = 0.206U_1 \tag{58}$$

Reduced Equations

The solution of the governing equations can be simplified by reducing the number of equations by one. This reduction is accomplished by using equation (39) to eliminate $\dot{m}_r$ from the other equations. The continuity equation for control volume I becomes:

$$\frac{\partial \rho A_1}{\partial t} + \frac{\partial \rho W_1 A_1}{Rs_1 \partial \theta} + \dot{m}_{i+1} - \dot{m}_i + \frac{\partial \rho A_2}{\partial t} + \frac{\partial \rho W_2 A_2}{Rs_2 \partial \theta} = 0 \tag{59}$$

If equation (59) times the circumferential velocity, W_1, is now subtracted from equation (40), the following reduced form of the momentum equation for control volume I is obtained:

$$\rho A_1 \frac{\partial W_1}{\partial t} + \frac{\rho W_1 A_1}{Rs_1} \frac{\partial W_1}{\partial \theta} + \left[\frac{\partial \rho A_2}{\partial t} + \frac{\partial W_2 A_2 \rho}{Rs_2 \partial \theta}\right](W_{oi} - W_1 i) \tag{60}$$

$$+ \dot{m}_i(W_1 i - W_1 i-1) = -\frac{A_1}{Rs_1}\frac{\partial P_i}{\partial \theta} + \tau_{jiLi} - \tau_{siasiLi}$$

Similarly, if equation (39) times the circumferential velocity, W_2, is

subtracted from equation (41), the reduced momentum equation for control volume II is obtained.

$$\rho A_2 \frac{\partial W_2}{\partial t} + \frac{\rho W_2 A_2}{Rs_2} \frac{\partial W_2}{\partial \theta} + \left[\frac{\partial \rho A_2}{\partial t} + \frac{\partial \rho W_2 A_2}{Rs_2 \partial \theta}\right](W_{2i} - W_{oi}) \qquad (61)$$

$$= - \frac{A_2}{Rs_2} \frac{\partial P_i}{\partial \theta} + \tau_{jiLi} - \tau_{riariLi}$$

The number of variables is reduced by using the ideal gas law to eliminate the density terms.

$$P_i = \rho_i RT \qquad (62)$$

This concludes the development of the governing equations for the new analysis presented in this report. The following is a discussion of the analysis of Jenny et al. [21].

The theory of Jenny et al. [21]

The theory of Jenny et al. [21] has shown consistently good agreement with measured test results [39] in predictions of cross-coupled stiffness and direct damping. The author had hoped to program their solution and make direct comparison to the present theory; however, as outlined below, unresolvable difficulties arose in deriving the published equations of [21].

The theory of Jenny et al. [21] was derived for the "box-in-a-box" control volume configuration illustrated in figure 5. Thus, a direct comparison of their equations with those presented in this report is not feasible. However, a review of the development of their governing equations is of interest.

The following convention will be used for the control volumes in figure 5: the large control volume is control volume I and the small

control volume is control volume II. The continuity equations for the control volumes shown in figure 5 are:

Continuity I

$$\frac{\partial \rho W_2 A_2}{Rs\partial\theta} + \frac{\partial \rho W_1 A_1}{Rs\partial\theta} + \frac{\partial \rho (A_1+A_2)}{\partial t} + \dot{m}_{i+1} - \dot{m}_i = 0 \qquad (J1)$$

Continuity II

$$\frac{\partial \rho W_2 A_2}{Rs\partial\theta} + \frac{\partial \rho A_2}{\partial t} - \dot{m}_{ri} = 0 \qquad (J2)$$

The following assumptions are used by Jenny et al. [21] to simplify equations (J1) and (J2):

a) the flow is incompressible (ρ = constant),

b) $\dot{m}_{i+1} = \dot{m}_i$, and

c) the area of the control volume II is constant.

The first assumption seems questionable, since this is a compressible flow solution, and quite often the flow in a labyrinth seal achieves Mach 1 at the exit. Assumption (b) is a valid assumption for the zeroth-order, steady flow solution, but it is questionable for the first-order, unsteady flow solution for an orbiting rotor. Using the chain rule for the expansion of partial derivatives and the above assumptions, equations (J1) and (J2) become:

Continuity I

$$A_2 \frac{\partial W_2}{\partial\theta} + A_1 \frac{\partial W_1}{\partial\theta} + W_1 L \frac{\partial Cr}{\partial\theta} + Rs \frac{\partial (A_1+A_2)}{\partial t} = 0 \qquad (J3)$$

Continuity II

$$\rho A_2 \frac{\partial W_2}{\partial\theta} - Rs\dot{m}_{ri} = 0 \qquad (J4)$$

The equations given by Jenny et al. [21] are:

Continuity I

$$A_2 \frac{\partial W_2}{\partial\theta} + A_1 \frac{\partial W_1}{\partial\theta} - W_1 L \frac{\partial Cr}{\partial\theta} - Rs \frac{\partial (A_1+A_2)}{\partial t} = 0 \qquad (J5)$$

Continuity II

$$\rho A_2 \frac{\partial W_2}{\partial \theta} - \dot{m}_{ri} = 0 \qquad (J6)$$

The difference between equations (J3) and (J5) is in the sign of the third and fourth terms. The second and third terms in equations (J3) and (J5) originate from the same partial derivative, but have opposite signs. This author could not arrive at the same conclusion using the chain rule. The difference between equations (J4) and (J6) is the radius, Rs, in the second term. This may or may not be a problem since the radial mass flow term, $\dot{m}_{ri}$, is not defined by Jenny et al. [21].

The author agreed with the derivation of the momentum equations for the control volumes shown in figure 5 except for the aforementioned assumptions and the following discrepancies:

(a) the axial velocity component is incorporated into the definition of the stator wall shear stress, but neglected in the definition of the Reynold's number which is used to calculate the friction factor term in the shear stress relation.

(b) the perturbation of the friction factor is ignored. This term has been shown [32] to be important in the solution for rotordynamic coefficients.

(c) the leakage equation is a global leakage equation. This means that local perturbations for a cavity can not be found from this equation. Jenny et al. [21] perturb this global equation for clearance.

(d) the carryover coefficient definition used in the leakage equation is a global equation and cannot be perturbed.

(e) the flow coefficient used in the leakage equation was obtained from a plot of empirical data. No explanation was given for the method

used to obtain the dervatives of the flow coefficient used in the perturbation equations.

The aforementioned problems prevented the author from obtaining a solution based on the theory of Jenny et al. [21]. Regrettably, no direct comparison between it and the theory presented in this paper was possible. This completes the discussion of the theory of Jenny et al. [21]. The following is a discussion of the solution procedure for the new analysis presented in this report.

Leakage Equation

To account for the leakage mass flow rate in the continuity and momentum equations, the following model was chosen.

$$\dot{m}_i = \mu_{1i}\,\mu_2\,H_i\sqrt{\frac{P_{i-1}^2 - P_i^2}{RT}} \tag{63}$$

where the kinetic energy carryover coefficient μ_2 is defined by Vermes [40] for straight through seals as:

$$\mu_2 = 1/[1-\alpha]^{1/2} \tag{64}$$

where

$$\alpha = 8.52/((L_i-Tp_i)/Cr+7.23)$$

and is unity, by definition, for the first tooth of any seal and all the teeth in interlocking and combination groove seals. This definition of the carryover coefficient is a local coefficient which can be perturbed in the clearance. The previous analyses by Childs and Scharrer [6] and Jenny et al. [21] used a global definition which could not be perturbed.

The flow coefficient is defined by Chaplygin [41] as:

$$\mu_{1i} = \frac{\pi}{\pi+2-5s_i+2s_i^2} \qquad \text{where,} \quad s_i = \left(\frac{P_{i-1}}{P_i}\right)^{\frac{\gamma-1}{\gamma}} - 1 \tag{65}$$

This flow coefficient yields a different value for each tooth along the seal as has been shown to be the case by Egli [42]. For choked flow, Fliegner's formula [43] will be used for the last seal strip. It is of the form:

$$\dot{m}_{NC} = \frac{0.510\mu_2}{\sqrt{RT}} P_{NC} H_{NC} \qquad (66)$$

PERTURBATION ANALYSIS

For cavity i, the continuity equation (59), momentum equations (60,61) and leakage equation (63) are the governing equations for the variables W_{1i}, W_{2i}, P_i, $\dot{m}_i$. A perturbation analysis of these equations is to be developed with the eccentricity ratio, $\varepsilon = e_o/Cr$, selected to be the perturbation parameter. The governing equations are expanded in the perturbation variables

$$P_i = P_{oi} + \varepsilon P_{1i} \qquad H_i = C_{ri} + \varepsilon H_1$$

$$W_{1i} = W_{1oi} + \varepsilon W_{11i} \qquad A_i = A_o + \varepsilon LH_1$$

$$W_{2i} = W_{2oi} + \varepsilon W_{21i}$$

where $\varepsilon = e_o/Cr$ is the eccentricity ratio. The zeroth-order equations define the leakage mass flow rate and the circumferential velocity distribution for a centered position. The first-order equations define the perturbations in pressure and circumferential velocity due to a radial position perturbation of the rotor. Strictly speaking, results of a first order analysis are only valid for small motion about a centered position.

Zeroth-Order Solution

The zeroth-order leakage equation is

$$\dot{m}_{i+1} = \dot{m}_i = \dot{m}_o \qquad (67)$$

and is used to determine both the leakage-rate $\dot{m}_o$ and pressure

distribution for a centered position. The leakage-rate and cavity pressures are determined iteratively, in the following manner. First, determine whether the flow is choked or not by assuming that the Mach number at the last tooth is one. Then, knowing the pressure ratio for flow at sonic conditions, the pressure in the last cavity is found. The mass flow can be calculated using equation (66). Working backwards towards the first tooth, the rest of the pressures can be found using equation (63). The final pressure calculation will result in the reservoir pressure necessary to produce the sonic condition at the last tooth. If the actual reservoir pressure is less than this value, then the flow is unchoked. Otherwise, it is choked. If the flow is choked, a similar procedure is followed, but now the pressure in the last cavity is guessed and a mass flow rate calculated using equation (66). The remaining pressures are calculated using equation (63). This is repeated until the calculated reservoir pressure equals the actual reservoir pressure. If the flow is unchoked, the pressure in the first cavity is guessed and a mass flow rate calculated using equation (63). The remaining pressures are calculated with the same equation. This procedure is repeated until the calculated sump pressure equals the actual sump pressure.

The zeroth-order circumferential-momentum equations are

$$\dot{m}_o(W_{1oi}-W_{1oi-1}) = (\tau_{jio}-\tau_{sio}\ a_{si})L_i \tag{68}$$

$$\tau_{joi}L_i = \tau_{roi}\ a_{ri}L_i \tag{69}$$

From calculated pressures, the densities can be calculated at each cavity from equation (62), and the only unknowns remaining in equations (68) and (69) are the circumferential velocities W_{1oi} and W_{2oi}. Given an inlet tangential velocity, a Newton-root-finding approach can be

used to solve equations (68) and (69) for the i-th velocities, one cavity at a time; starting at the first cavity and working downstream.

First-Order Solution

The governing first-order equations (70,71,72), define the pressure and velocity fluctuations resulting from the seal clearance function. The continuity and momentum equations follow in order:

$$G_{1i}\frac{\partial P_{1i}}{\partial t} + G_{2i}\frac{\partial P_{1i}}{\partial \theta} + G_{3i}\frac{\partial W_{1,i}}{\partial \theta} + G_{4i}\frac{\partial W_{2,i}}{\partial \theta} + G_{5i}P_{1i} + G_{6i}P_{1,i-1} + G_{7i}P_{1,i+1} = -G_{8i}H_{1i} - G_{9i}\frac{\partial H_{1i}}{\partial t} - G_{10i}\frac{\partial H_{1i}}{\partial \theta} \tag{70}$$

$$X_{1i}\frac{\partial W_{1,i}}{\partial t} + \frac{X_{1i}W_{10i}}{Rs_1}\frac{\partial W_{1,i}}{\partial \theta} + \left[X_{2i} + \frac{X_{3i}W_{20i}}{Rs_2}\right]\frac{\partial P_{1i}}{\partial \theta} + X_{3i}\frac{\partial P_{1i}}{\partial t} + \frac{X_{3i}P_{0i}}{Rs_2}\frac{\partial W_{2,i}}{\partial \theta} + X_{4i}P_{1i} + X_{5i}P_{1,i-1} + X_{6i}W_{1,i} + X_{7i}W_{2,i} - \dot{m}W_{1,i-1} = X_{8i}H_{1i} \tag{71}$$

$$Y_{1i}\frac{\partial W_{2,i}}{\partial t} + \left[\frac{Y_{2i}P_{0i}}{Rs_2} + \frac{Y_{1i}W_{20i}}{Rs_2}\right]\frac{\partial W_{2,i}}{\partial \theta} + \left[Y_{3i} + \frac{Y_{2i}W_{20i}}{Rs_2}\right]\frac{\partial P_{1i}}{\partial \theta} + Y_{2i}\frac{\partial P_{1i}}{\partial t} + Y_{4i}P_{1i} + Y_{5i}W_{2,i} + Y_{6i}P_{1,i-1} + Y_{7i}W_{1,i} = Y_{8i}H_{1i} \tag{72}$$

where the X_i's, Y_i's, and G_i's are defined in Appendix B. These perturbation equations are very different from those of Jenny et al. [21], because their analysis neglects pressure perturbations in the leakage and shear stress equations and assumes that the density is constant.

If the shaft center moves in an elliptical orbit, then the seal clearance function can be defined as:

$$\begin{aligned} \varepsilon H_1 &= -a\cos\omega t\cos\theta - b\sin\omega t\sin\theta \\ &= -\frac{a}{2}[\cos(\theta-\omega t) + \cos(\theta+\omega t)] - \frac{b}{2}[\cos(\theta-\omega t) - \cos(\theta+\omega t)] \end{aligned} \tag{73}$$

The pressure and velocity fluctuations can now be stated in the associated solution format:

$$P_{1i} = P^{+}_{ci}\cos(\theta+\omega t) + P^{+}_{si}\sin(\theta+\omega t) + P^{-}_{ci}\cos(\theta-\omega t) + P^{-}_{si}\sin(\theta-\omega t) \quad (74)$$

$$W_{1i} = W^{+}_{1ci}\cos(\theta+\omega t)+W^{+}_{1si}\sin(\theta+\omega t)+W^{-}_{1ci}\cos(\theta-\omega t)+W^{-}_{1si}\sin(\theta-\omega t) \quad (75)$$

$$W_{2i} = W^{+}_{2ci}\cos(\theta+\omega t)+W^{+}_{2si}\sin(\theta+\omega t)+W^{-}_{2ci}\cos(\theta-\omega t)+W^{-}_{2si}\sin(\theta-\omega t) \quad (76)$$

Substituting equations (73), (74), (75) and (76) into equations (70), (71) and (72) and grouping like terms of sines and cosines (as shown in Appendix C) eliminates the time and theta dependency and yields twelve linear algebraic equations per cavity. The resulting system of equations for the i-th cavity can be stated:

$$[A_{i-1}]\,(X_{i-1}) + [A_i]\,(X_i) + [A_{i+1}]\,(X_{i+1}) = \frac{a}{\varepsilon}\,(B_i) + \frac{b}{\varepsilon}\,(C_i) \quad (77)$$

where

$$(X_{i-1}) = (P^{+}_{si-1},\ P^{+}_{ci-1},\ P^{-}_{si-1},\ P^{-}_{ci-1},\ W^{+}_{1si-1},\ W^{+}_{1ci-1},\ W^{-}_{1si-1},\ W^{-}_{1ci-1},\ W^{+}_{2si-1},\ W^{+}_{2si-1},\ W^{-}_{2si-1},\ W^{-}_{2ci-1})^{T}$$

$$(X_i) = (P^{+}_{si},\ P^{+}_{ci},\ P^{-}_{si},\ P^{-}_{ci},\ W^{+}_{1si},\ W^{+}_{1ci},\ W^{-}_{1si},\ W^{-}_{1ci},\ W^{+}_{2si},\ W^{+}_{2ci},\ W^{-}_{2si},\ W^{-}_{2ci})^{T}$$

$$(X_{i+1}) = (P^{+}_{si+1},\ P^{+}_{ci+1},\ P^{-}_{si+1},\ P^{-}_{ci+1},\ W^{+}_{1si+1},\ W^{+}_{1ci+1},\ W^{-}_{1si+1},\ W^{-}_{1ci+1},\ W^{+}_{2si+1},\ W^{+}_{2ci+1},\ W^{-}_{2si+1},\ W^{-}_{2ci+1})^{T}$$

The A matrices and column vectors B and C are given in Appendix C. To use equation (77) for the entire seal solution, a system matrix can be formed which is block tridiagonal in the A matrices. The size of this resultant matrix is (12NC X 12NC) since pressure and velocity perturbations at the inlet and the exit are assumed to be zero. This system is easily solved by various linear equation algorithms, and yields a solution of the form:

$$
\begin{aligned}
P^{+}_{si} &= \frac{a}{\epsilon} F^{+}_{asi} + \frac{b}{\epsilon} F^{+}_{bsi} \\
P^{-}_{si} &= \frac{a}{\epsilon} F^{-}_{asi} + \frac{b}{\epsilon} F^{-}_{bsi} \\
P^{+}_{ci} &= \frac{a}{\epsilon} F^{+}_{aci} + \frac{b}{\epsilon} F^{+}_{bci} \\
P^{-}_{ci} &= \frac{a}{\epsilon} F^{-}_{aci} + \frac{b}{\epsilon} F^{-}_{bci}
\end{aligned}
\tag{78}
$$

Determination of Dynamic Coefficient

The force-motion equations for a labyrinth seal are assumed to be of the form:

$$
-\begin{Bmatrix} F_x \\ F_y \end{Bmatrix} = \begin{bmatrix} K & k \\ -k & K \end{bmatrix} \begin{Bmatrix} X \\ Y \end{Bmatrix} + \begin{bmatrix} C & c \\ -c & C \end{bmatrix} \begin{Bmatrix} \dot{X} \\ \dot{Y} \end{Bmatrix} \tag{79}
$$

The solution of equation (79) for the stiffness and damping coefficients is the objective of the current analysis. For the assumed elliptical orbit of equation (73), the X and Y components of displacement and velocity are defined as:

$$
\begin{aligned}
X &= a\cos\omega t & \dot{X} &= -a\omega \sin\omega t \\
Y &= b\sin\omega t & \dot{Y} &= b\omega \cos\omega t
\end{aligned}
$$

Substituting these relations into equation (79) yields:

$$
\begin{aligned}
F_x &= -Ka\cos\omega t - kb\sin\omega t + Ca\omega \sin\omega t - cb\omega \cos\omega t \\
F_y &= -ka\cos\omega t - Kb\sin\omega t - ca\omega \sin\omega t - Cb\omega \cos\omega t
\end{aligned}
\tag{80}
$$

Redefining the forces, Fx and Fy, as:

$$
\begin{aligned}
F_x &= F_{xc}\cos\omega t + F_{xs}\sin\omega t \\
F_y &= F_{yc}\cos\omega t + F_{ys}\sin\omega t
\end{aligned}
\tag{81}
$$

and substituting back into equation (78) yields the following relations:

$$
\begin{aligned}
-F_{xc} &= Ka + cb\omega & -F_{xs} &= -Ca\omega + kb \\
-F_{yc} &= ka + Cb\omega & -F_{ys} &= Kb + ca\omega
\end{aligned}
\tag{82}
$$

The X and Y components of force can be found by integrating the pressure around the seal as follows:

$$Fx = -Rs\varepsilon \sum_{i=1}^{NC} \int_{0}^{2\pi} P_{1i} L_i \cos\theta \, d\theta \tag{83}$$

$$Fy = Rs\varepsilon \sum_{i=1}^{NC} \int_{0}^{2\pi} P_{1i} L_i \sin\theta \, d\theta \tag{84}$$

Only one of these components needs to be expanded in order to determine the dynamic coefficients. For this analysis, the X component was chosen. Substituting equation (74) into (83) and integrating yields:

$$Fx = -\varepsilon\pi Rs \sum_{i=1}^{NC} L_i [(\overset{+}{P}_{si} - \overset{-}{P}_{si}) \sin\omega t + (\overset{+}{P}_{ci} + \overset{-}{P}_{ci}) \cos\omega t] \tag{85}$$

substituting from equations (78) and (80) into equation (85) and equating coefficients of $\sin\omega t$ and $\cos\omega t$ yields:

$$\begin{aligned} F_{xs} &= -\pi Rs \sum_{i=1}^{NC} L_i [a(\overset{+}{F}_{asi} - \overset{-}{F}_{asi}) + b (\overset{+}{F}_{bsi} - \overset{-}{F}_{bsi})] \\ F_{xc} &= -\pi Rs \sum_{i=1}^{NC} L_i [a(\overset{+}{F}_{aci} + \overset{-}{F}_{aci}) + b (\overset{+}{F}_{bci} + \overset{-}{F}_{bci})] \end{aligned} \tag{86}$$

Equating the alternative definitions for F_{xs} and F_{xc} provided by equations (82) and (86) and grouping like terms of the linearly independent coefficients a and b yields the final solutions to the stiffness and damping coefficients:

$$\begin{aligned} K &= \pi R \sum_{i=1}^{NC} (\overset{+}{F}_{aci} + \overset{-}{F}_{aci}) L_i \\ k &= \pi R \sum_{i=1}^{NC} (\overset{+}{F}_{bsi} - \overset{-}{F}_{bsi}) L_i \\ C &= \frac{-\pi Rs}{\omega} \sum_{i=1}^{NC} (\overset{+}{F}_{asi} - \overset{-}{F}_{asi}) L_i \\ c &= \frac{\pi Rs}{\omega} \sum_{i=1}^{NC} (\overset{+}{F}_{bci} + \overset{-}{F}_{bci}) L_i \end{aligned} \tag{87}$$

Data Requirements and Solution Procedure Summary

The required input for the analysis presented is as follows:

a) Reservoir pressure, temperature, and kinematic viscosity.

b) Sump pressure.

c) Gas constant and ratio of specific heats.

d) Inlet circumferential velocity and rotor speed.

e) Seal radius, radial clearance, tooth pitch, height and tip width.

f) Rotor and stator friction coefficients (mr,nr,ms,ns).

g) Number of teeth.

In review, the solution procedure uses the following sequential steps:

a) Determination of whether flow is choked or not using equations (63) and (66).

b) The steady-state pressure distribution and leakage are found using equation (63)and/or (66).

c) The steady-state circumferential velocity distribution is determined using equation (68).

d) A system equation is formed for the first-order perturbation variables and solved using the cavity equation (77).

e) Results of this first-order perturbation solution, as defined in equations (78), are inserted into equation (87) to define the rotordynamic coefficients.

CHAPTER III

TEST APPARATUS AND FACILITY

TESTING APPROACH

The testing method employed at the TAMU facility is the same as that used by Iino and Kaneko [44]. An external hydraulic shaker is used to impart translatory motion to the rotating seal, while rotor motion relative to the stator and the reaction force components acting on the stator are measured.

Figure 21 shows the manner in which the rotor could be positioned and oscillated in order to identify the dynamic coefficients of the seal for small motion about an eccentric position, e_o. Equation (1) is rewritten here

$$-\begin{Bmatrix} F_X \\ F_Y \end{Bmatrix} = \begin{bmatrix} K_{XX}(\varepsilon_o) & K_{XY}(\varepsilon_o) \\ K_{YX}(\varepsilon_o) & K_{YY}(\varepsilon_o) \end{bmatrix} \begin{Bmatrix} X \\ Y \end{Bmatrix} + \begin{bmatrix} C_{XX}(\varepsilon_o) & C_{XY}(\varepsilon_o) \\ C_{YX}(\varepsilon_o) & C_{YY}(\varepsilon_o) \end{bmatrix} \begin{Bmatrix} \dot{X} \\ \dot{Y} \end{Bmatrix} \tag{88}$$

First, harmonic horizontal motion of the rotor is assumed, where

$$X = e_o + A \sin(\Omega t) + B \cos(\Omega t)$$

$$\dot{X} = A\Omega \cos(\Omega t) - B\Omega \sin(\Omega t)$$

$$Y = \dot{Y} = 0$$

This yields small motion parallel to the static eccentricity vector, where Ω is the shaking frequency. In a similar fashion, the X and Y-direction force components can be expressed

$$\begin{aligned} F_X &= FXS \sin(\Omega t) + FXC \cos(\Omega t) \\ F_Y &= FYS \sin(\Omega t) + FYC \cos(\Omega t) \end{aligned} \tag{89}$$

Substituting these expressions into equation (88) and equating coefficients of constant, sine, and cosine terms yields the following four equations for the dynamic coefficients

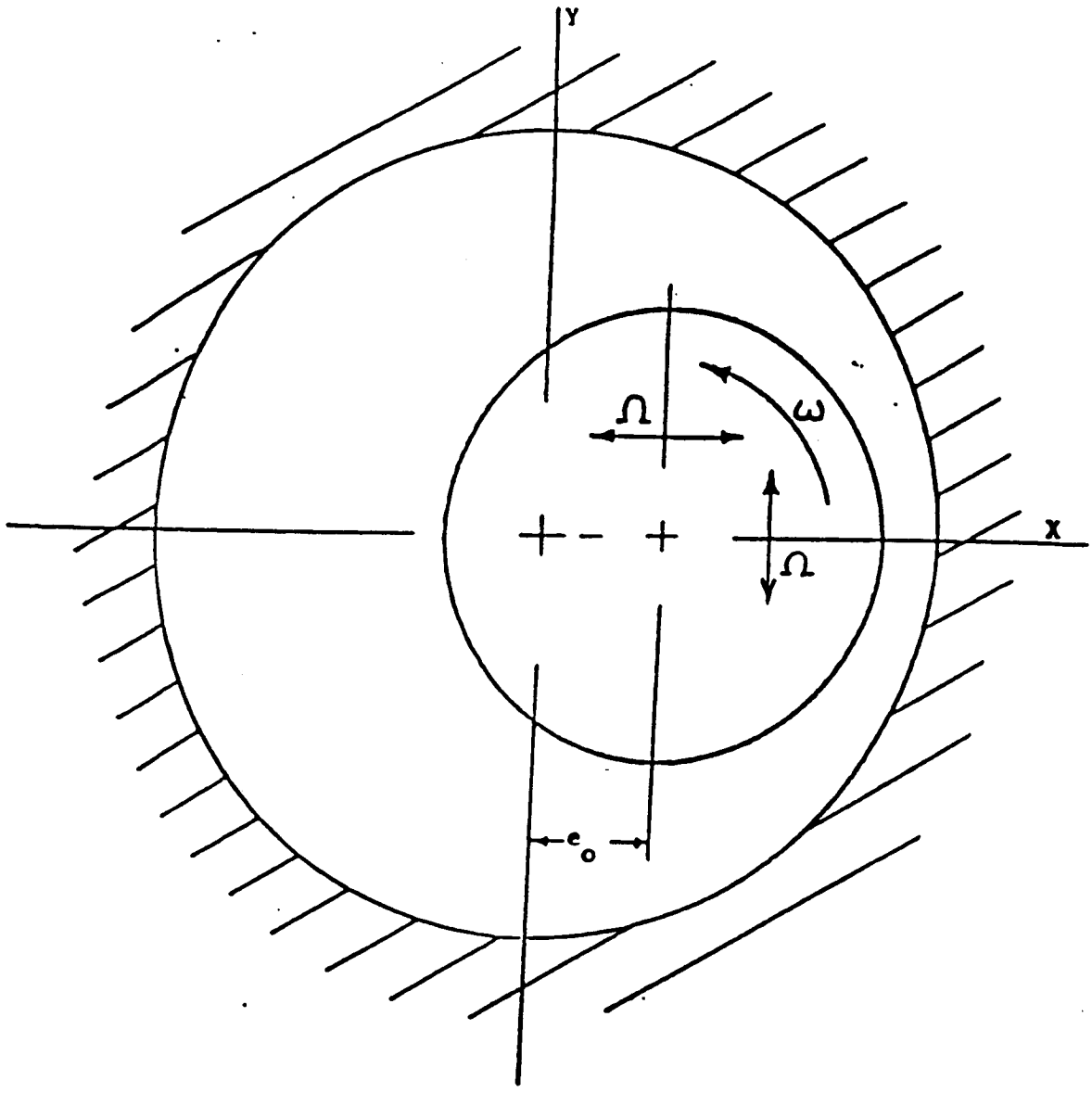

Fig. 21 External shaker method used for coefficient identification.

$$
\begin{aligned}
F_{XS} &= K_{XX}\, A - C_{XX}\, B \\
F_{XC} &= K_{XX}\, B + C_{XX}\, A \\
F_{YS} &= K_{YX}\, A - C_{YX}\, B \\
F_{YC} &= K_{YX}\, B + C_{YX}\, A.
\end{aligned}
\tag{90}
$$

Solving this system of four equations in four unknowns defines the dynamic coefficients as

$$
\begin{aligned}
K_{XX}(\epsilon_o) &= (F_{XC}\, B + F_{XS}\, A) \,/\, (A^2 + B^2) \\
K_{YX}(\epsilon_o) &= (F_{YS}\, A + F_{YC}\, B) \,/\, (A^2 + B^2) \\
C_{XX}(\epsilon_o) &= (F_{XC}\, A - F_{XS}\, B) \,/\, \Omega(A^2 + B^2) \\
C_{YX}(\epsilon_o) &= (F_{YC}\, A - F_{YS}\, B) \,/\, \Omega(A^2 + B^2)
\end{aligned}
\tag{91}
$$

Therefore, by measuring the reaction forces due to known rotor motion, determining the Fourier coefficients ($A, B, F_{XS}, F_{XC}, F_{YS}, F_{YC}$), and substituting into the above definitions, the indicated dynamic coefficients can be identified. If the rotor is shaken about a centered position (e_o=0), the process is complete. Since the linearized model has skew-symmetric stiffness and damping matrices, all of the coefficients are identified. If, however, the rotor is shaken about an eccentric position as initially postulated, then it must be shaken vertically about that same point in order to complete the identification process.

Assuming harmonic vertical motion of the rotor, as defined by

$$X = e_o,\ \dot{X} = 0,$$

$$Y = A \sin(\Omega t) + B \cos(\Omega t), \text{ and}$$

$$\dot{Y} = A\Omega \cos(\Omega t) - B\Omega \sin(\Omega t),$$

yields oscillatory motion that is perpendicular to the assumed static eccentricity vector. A similar process as before results in the

coefficient definitions

$$K_{YY}(\varepsilon_o) = (F_{XS}\,A + F_{XC}\,B) / (A^2 + B^2)$$

$$K_{XY}(\varepsilon_o) = -(F_{YC}\,B + F_{YS}\,A) / (A^2 + B^2)$$

$$C_{YY}(\varepsilon_o) = (F_{XC}\,A - F_{XS}\,B) / \Omega(A^2 + B^2) \qquad (92)$$

$$C_{XY}(\varepsilon_o) = (F_{YS}\,B - F_{YC}\,A) / \Omega(A^2 + B^2).$$

All eight dynamic coefficients are thus determined by alternately shaking the rotor at one frequency Ω in directions which are parallel and perpendicular to the static eccentricity vector.

APPARATUS OVERVIEW

Detailed design of the TAMU gas seal apparatus was carried out by J.B. Dressman of the University of Louisville. It is of the external shaker configuration, with the dynamic-coefficient-identification process described in the preceding section.

Considering both the coefficient identification process and the analysis, some objectives for the design of the test apparatus are apparent. First, to determine the dynamic coefficients, the apparatus must provide for (a) the necessary rotor motion within the seal, and (b) measurement of the reaction-force components due to this motion. Secondly, it would be advantageous (for purposes of comparison) if the apparatus could provide the same variable seal parameters afforded by the analysis (i.e., pressures, seal geometry, rotor rotational speed, fluid prerotation, and rotor/stator surface roughness). With this capability, the influence of each independent parameter could be examined and compared for correlation between theoretical predictions and experimental results.

With these design objectives in mind, the discussion of the test

apparatus is presented in three sections. The first section, Test Hardware, describes how the various seal parameters are physically executed and controlled. For example, the manner in which the dynamic "shaking" motion of the seal rotor is achieved and controlled is described in this section. The second section, Instrumentation, describes how these controlled parameters, such as rotor motion, are measured. Finally, the Data Acquisition and Reduction section explains how these measurements are used to provide the desired information.

TEST HARDWARE

This section deals only with the mechanical components and operation of the test apparatus. It provides answers for the following questions:

1) How is the static position of the seal rotor controlled?
2) How is the dynamic motion of the rotor executed and controlled?
3) How is compressed air obtained and supplied to the apparatus, and how is the pressure ratio across the seal controlled?
4) How is the incoming air prerotated before it enters the seal?
5) How are the seal rotor and stator mounted and replaced?
6) How is the seal rotor driven (rotated)?

Recalling the rotordynamic-coefficient-identification process described earlier, the external shaker method requires that the seal rotor be set in some static position and then oscillated about that point. The test apparatus meets those requirements by providing independent static and dynamic displacement control, which are described below.

Static Displacement Control.

The test apparatus is designed to provide control over the static eccentricity position both horizontally and vertically within the seal. The rotor shaft is suspended pendulum-fashion from an upper, rigidly mounted pivot shaft, as shown in figures 22 and 23. This arrangement allows a side-to-side (horizontal) motion of the rotor, and a cam within the pivot shaft allows vertical positioning of the rotor.

The cam which controls the vertical position of the rotor is driven by a remotely-operated DC gearhead motor, allowing accurate positioning of the rotor during testing. Horizontal positioning of the rotor is accomplished by a Zonic hydraulic shaker head and master controller, which provide independent static and dynamic displacement or force control. The shaker head is mounted on an I-beam support structure, and can supply up to 4450 N (1000 lbf) static and 4450 N dynamic force at low frequencies. The dynamic force decreases as frequency is increased. As illustrated in figure 22, the shaker head output shaft acts on the rotor shaft bearing housing, and works against a return spring mounted on the opposite side of the bearing housing. The return spring maintains contact between the shaker head shaft and the bearing housing, thereby preventing hammering of the shaker shaft and the resulting loss of control over the horizontal motion of the rotor.

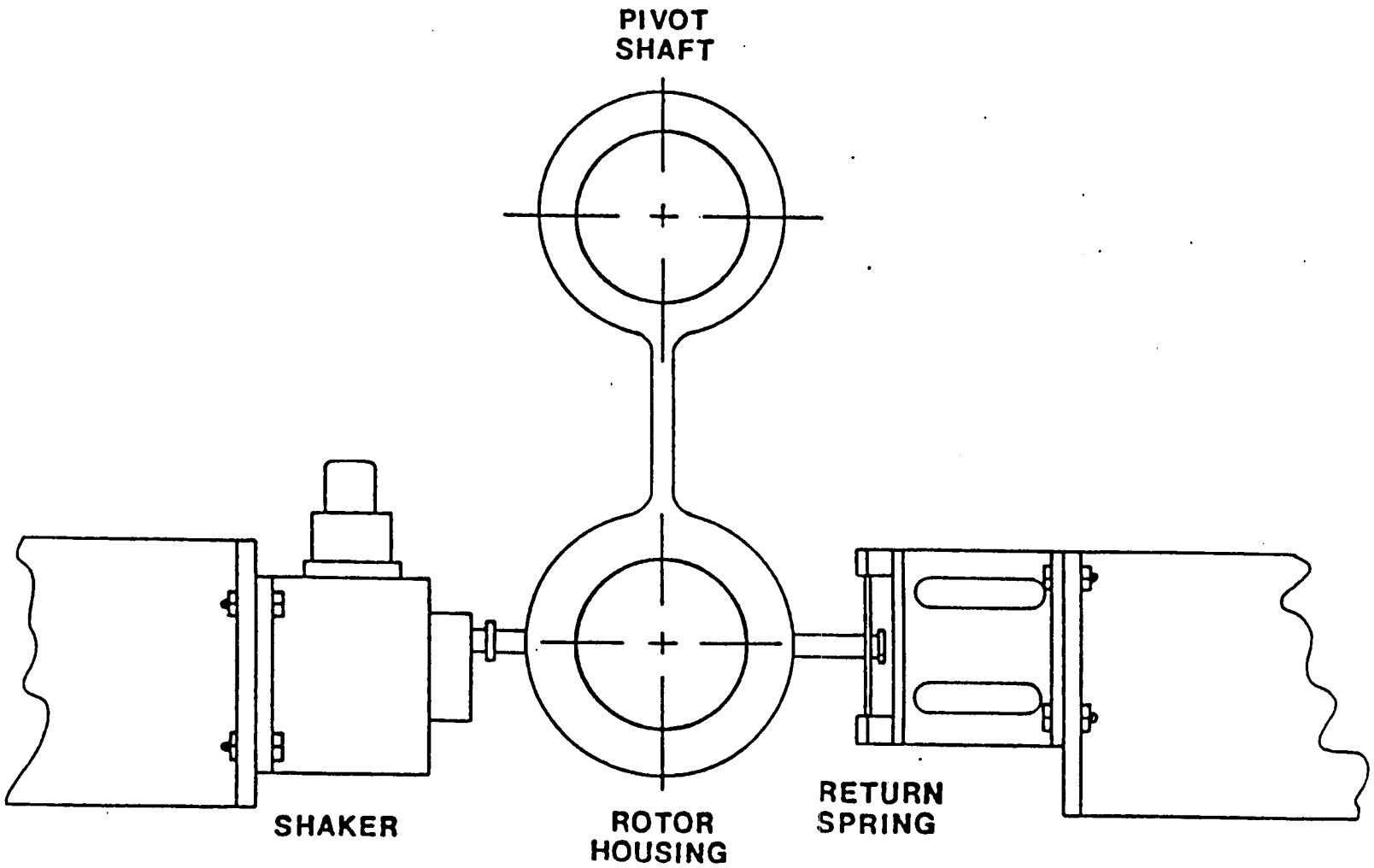

Fig. 22 Components used for static and dynamic displacement of seal rotor.

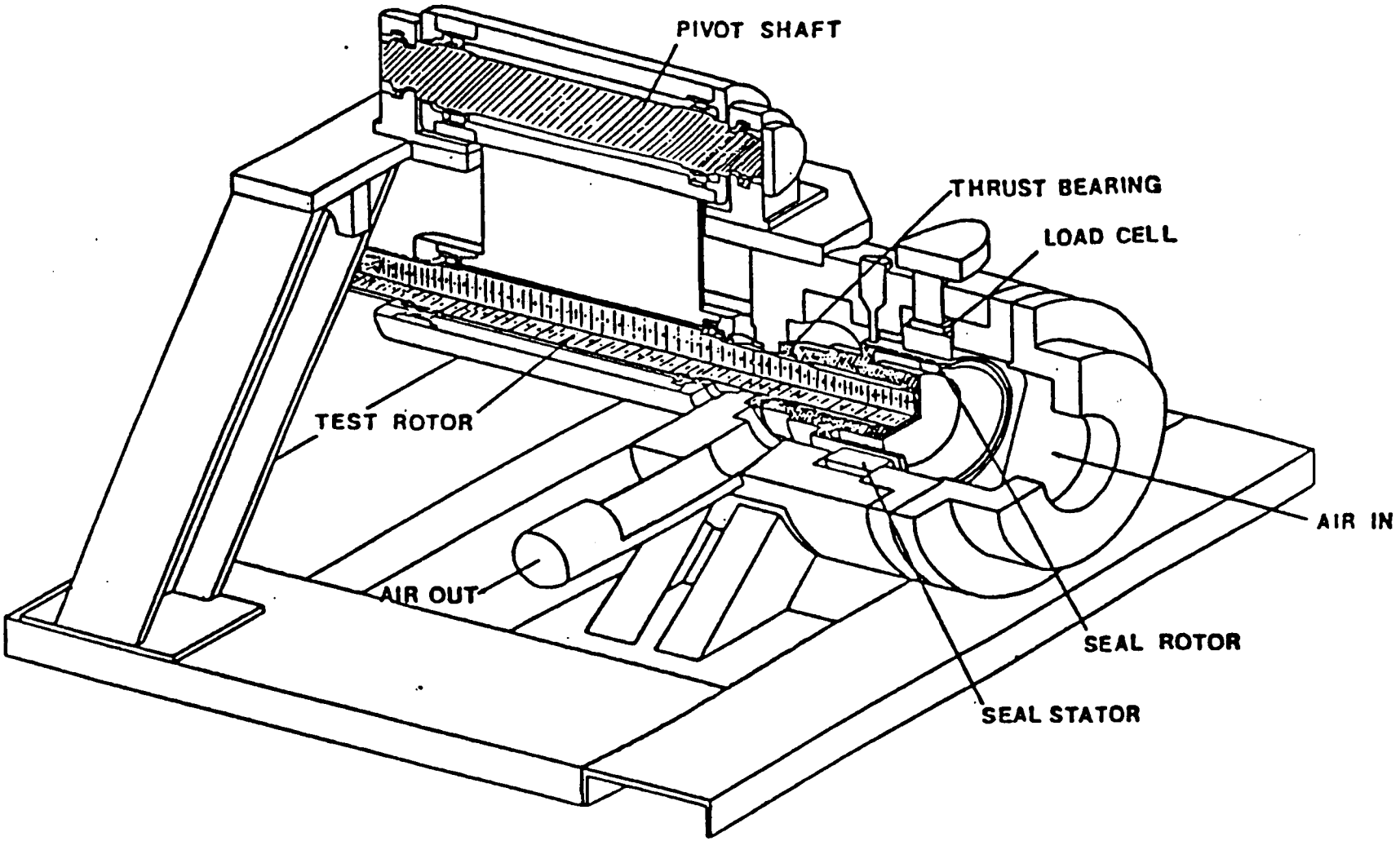

Fig.23 Test apparatus.

Dynamic Displacement Control.

The dynamic motion of the seal rotor within the stator is horizontal. In addition to controlling the static horizontal position of the rotor, the Zonic shaker head moves the rotor through horizontal harmonic oscillations as the test is run. A Wavetek function generator provides the sinusoidal input signal to the Zonic controller, and both the amplitude and frequency of the rotor oscillations are controlled.

Although the test-rig design provides for dynamic motion of the rotor only in the horizontal X-direction, all of the coefficients for either seal model (equation (1) or (2)) can still be determined. As figure 24 shows, the required rotor motion perpendicular to the static eccentricity vector can be accomplished in an equivalent manner by statically displacing it the same amount (e_o) in the vertical direction and continuing to shake horizontally.

In addition to providing control over the rotor's static position and dynamic motion, the test apparatus allows other seal parameters to be controlled independently, providing insight into the influence these parameters have on seal behavior. These parameters coincide with the variable input parameters for the analysis, and they include:

1) pressure ratio across the seal,
2) prerotation of the incoming fluid,
3) seal configuration, and
4) rotor rotational speed.

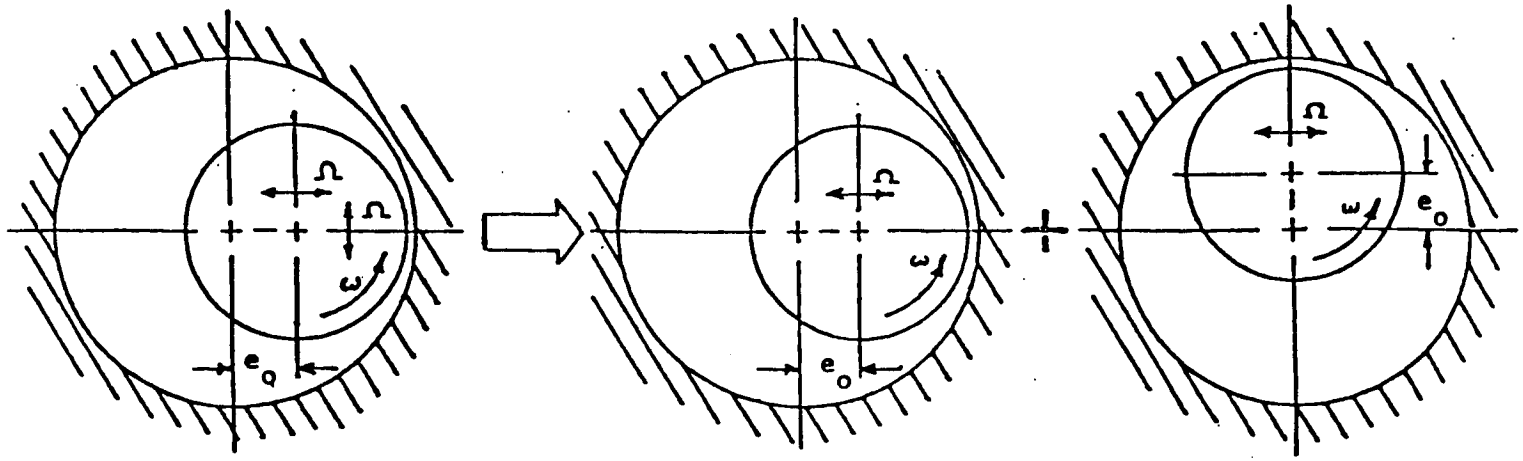

Fig. 24 Shaking motion used for rotordynamic coefficient identification.

Pressure Ratio.

The inlet air pressure and attendant mass flow rate through the seal are controlled by an electric-over-pneumatically actuated Masoneilan Camflex II flow control valve located upstream of the test section. An Ingersoll-Rand SSR-2000 single stage screw compressor rated at 34 m^3/min @ 929 kPa (1200 scfm @ 120 psig) provides compressed air, which is then filtered and dried before entering a surge tank. Losses through the dryers, filters, and piping result in an actual maximum inlet pressure to the test section of approximately 825 kPa (105 psig) and a maximum flow rate of 10 m^3/min (350 scfm). A four-inch inlet pipe from the surge tank supplies the test rig, and after passing through the seal, the air exhausts to atmosphere through a manifold with muffler.

Inlet Circumferential Velocity Control.

In order to determine the effects of fluid rotation on the rotordynamic coefficients, the test rig design also allows for prerotation of the incoming air as it enters the seal. This prerotation introduces a circumferential component to the air flow direction, and is accomplished by guide vanes which direct and accelerate the flow towards the annulus of the seal. Figure 25 illustrates the vane configuration. Five sets of guide vanes are available; two rotate the flow in the direction of rotor rotation at different speeds , another introduces no fluid rotation, and two rotate the flow opposite the direction of rotor rotation at different speeds. The important difference between the vanes is the gap height, A. The vanes with a small gap height produce the highest inlet tangential velocity.

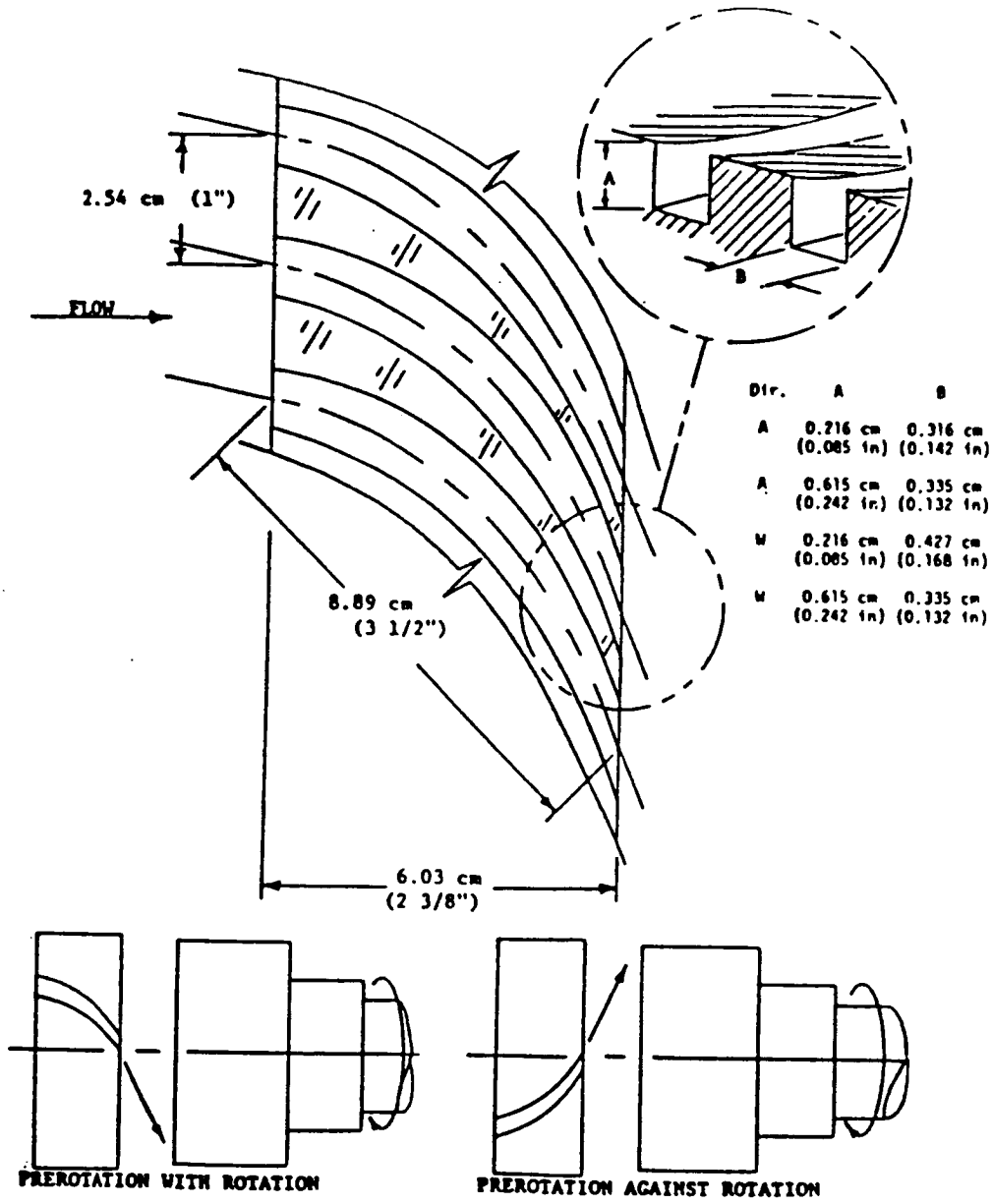

Fig. 25 Inlet guide vane detail.

Seal Configuration.

The design of the test rig, figure 26, permits the installation of various rotor/stator combinations. The stator is supported in the test section housing by three Kistler quartz load cells in a trihedral configuration, as shown in figure 27. Different seal stator designs are obtained by the use of inserts. The smooth and labyrinth inserts used for the .4mm (.016 in.) radial clearance seal tests are shown in figure 28. The labyrinth rotor and the tooth detail are shown in figures 29 and 30. Seals with different geometries (i.e., clearances, tapers, lengths) can be tested, as well as seals with different surface roughnesses.

Rotational Speed.

A Westinghouse 50-hp variable-speed electric motor drives the rotor shaft through a belt-driven jackshaft arrangement. This shaft is supported by two sets of Torrington hollow-roller bearings [45]. These bearings are extremely precise, radially preloaded, and have a predictable and repeatable radial stiffness. The shaft bearings are lubricated by a positive-displacement gear-type oil pump.

Different jackshaft drive-pulleys can be fitted to provide up to a 4:1 speed increase from motor to rotor shaft, which would result in a rotor shaft speed range of 0-21,200 cpm. Previously, the maximum possible test speed was 8500 cpm. High bearing temperatures and the reduction of interference in the rotor-shaft fitment with increasing speed had served to limit shaft speed. These problems have been addressed by some specific design modifications which are discussed below.

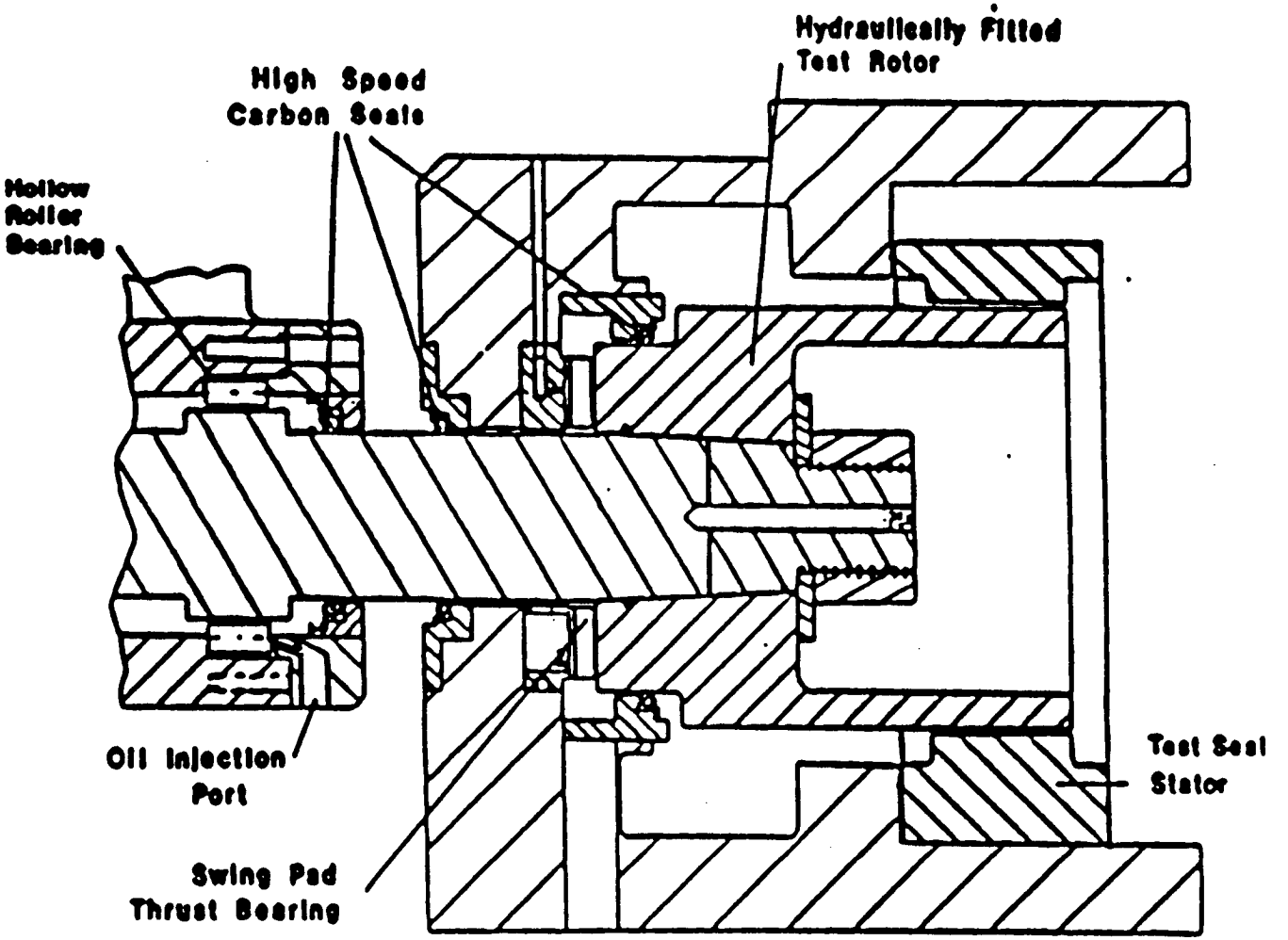

Fig. 26 Cross-sectional view of test section showing rotor-shaft assembly.

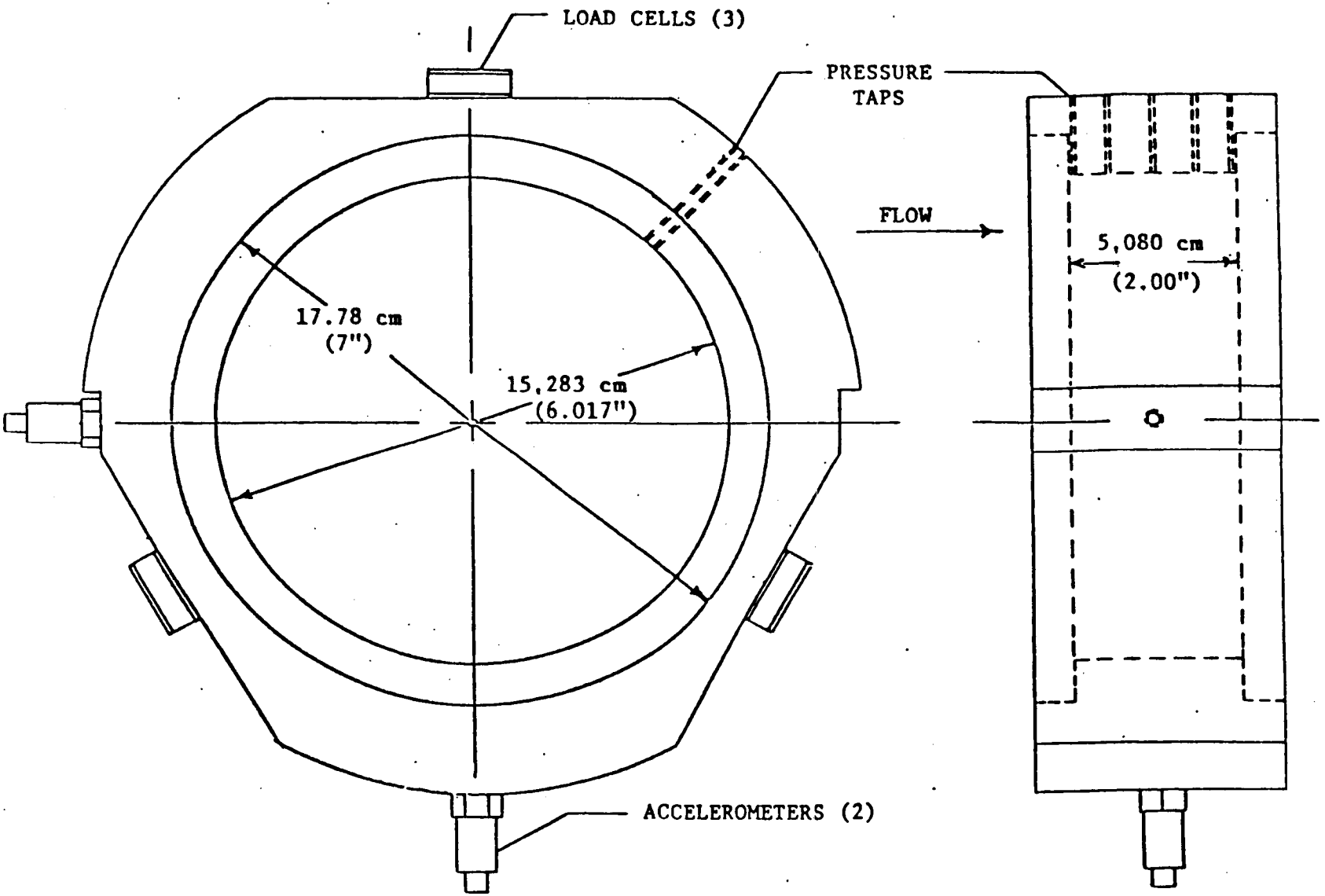

Fig. 27 Detail of smooth stator.

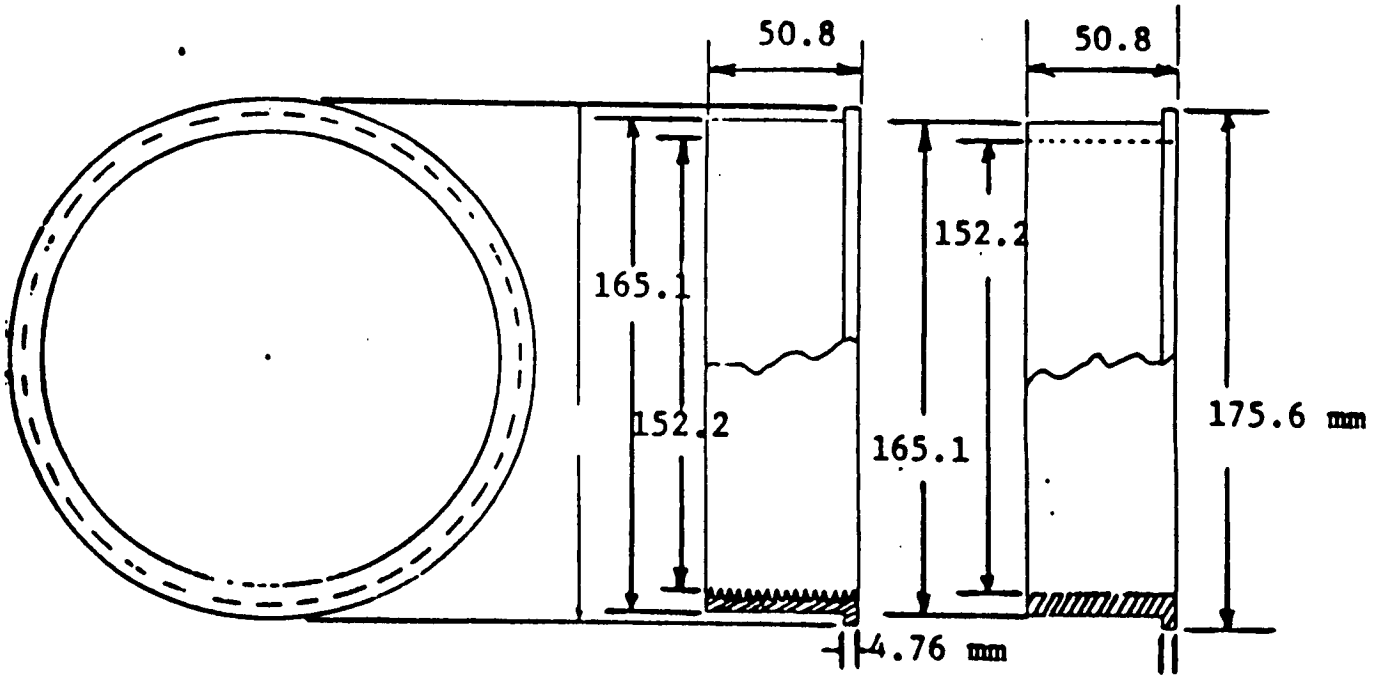

Fig. 28 Smooth and labyrinth stator inserts for 0.4 mm (0.016 in.) radial seal clearance.

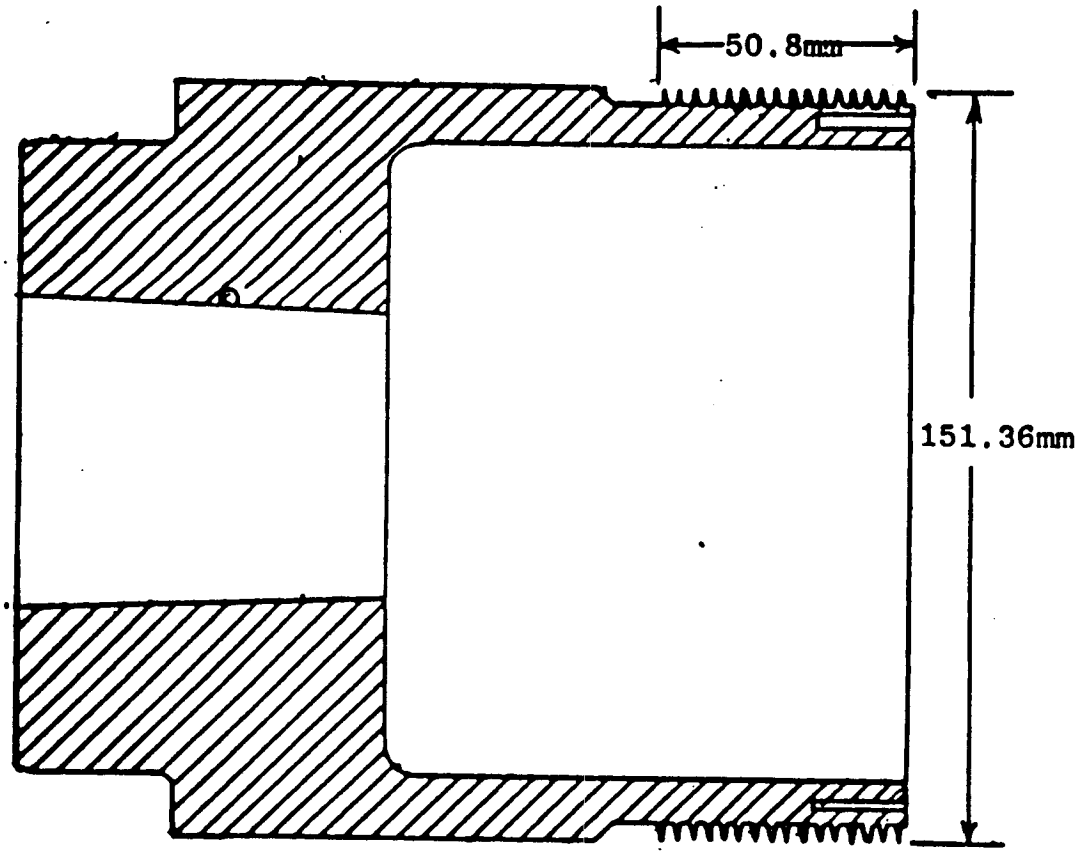

Fig. 29 Detail of labyrinth rotor.

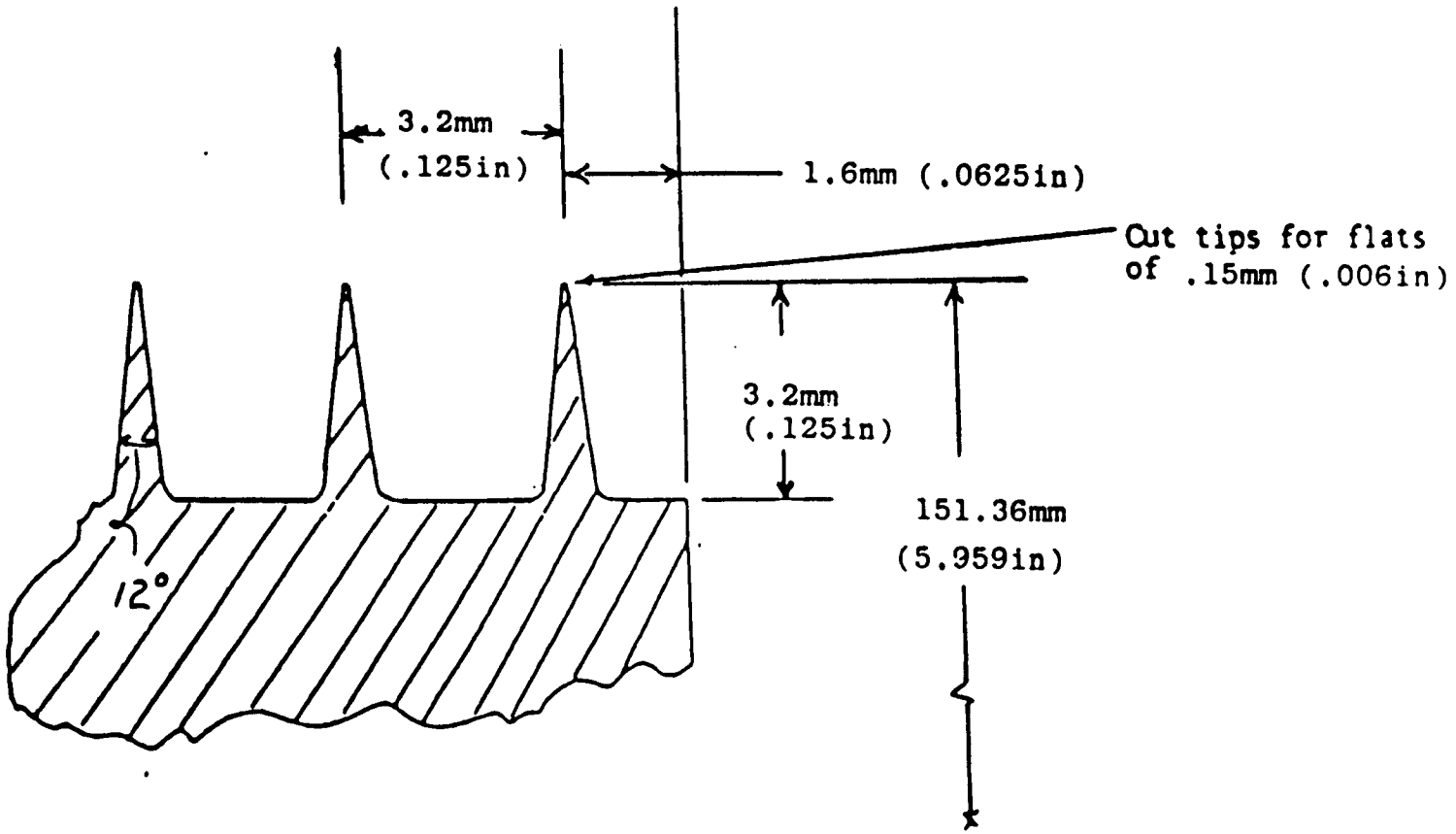

Fig. 30 Detail of labyrinth tooth.

In the past, the seal rotor was press-fitted and secured axially by a bolt circle to the rotor shaft. As the running speed is increased, however, the inertia-induced diametral growth of the rotor exceeds the growth of the shaft. By increasing the interference in stationary rotor-shaft fit, a greater allowance for this growth difference has been provided. Figure 31 shows the present rotor-shaft design, a tapered rotor which is hydraulically expanded during installation. The rotor is inserted over the end of the tapered shaft and a large nut is used to pull the rotor onto the shaft. Fluid is pumped between the shaft and rotor, causing the rotor to expand. This separating force allows the rotor to be pulled onto the shaft until the desired interference fit is achieved.

The problem of high bearing temperatures has been eliminated by replacing a roller-type thrust bearing and modifying the lubricant flow. A Torrington Hydraflex thrust bearing, consisting of eight one-inch rubber-faced pads which are water lubricated, is now in place at the rear of the rotor. In addition, the lubricant for the Torrington hollow-roller bearings which support the shaft has been changed to light turbine oil with a maximum temperature of 270°F. The hollow-roller-bearing caps have been modified to direct the oil flow to the regions of heat buildup. These modifications are shown in figure 31.

The final modification to allow operation of the TAMU gas seal test apparatus at high speeds was the installation of Koppers circumferential seals for the hollow-roller and thrust bearing lubrication systems. At 16,000 rpm, the surface speeds of the shaft and rotor (170 and 350 ft/sec, respectively) exceed the limits of lip

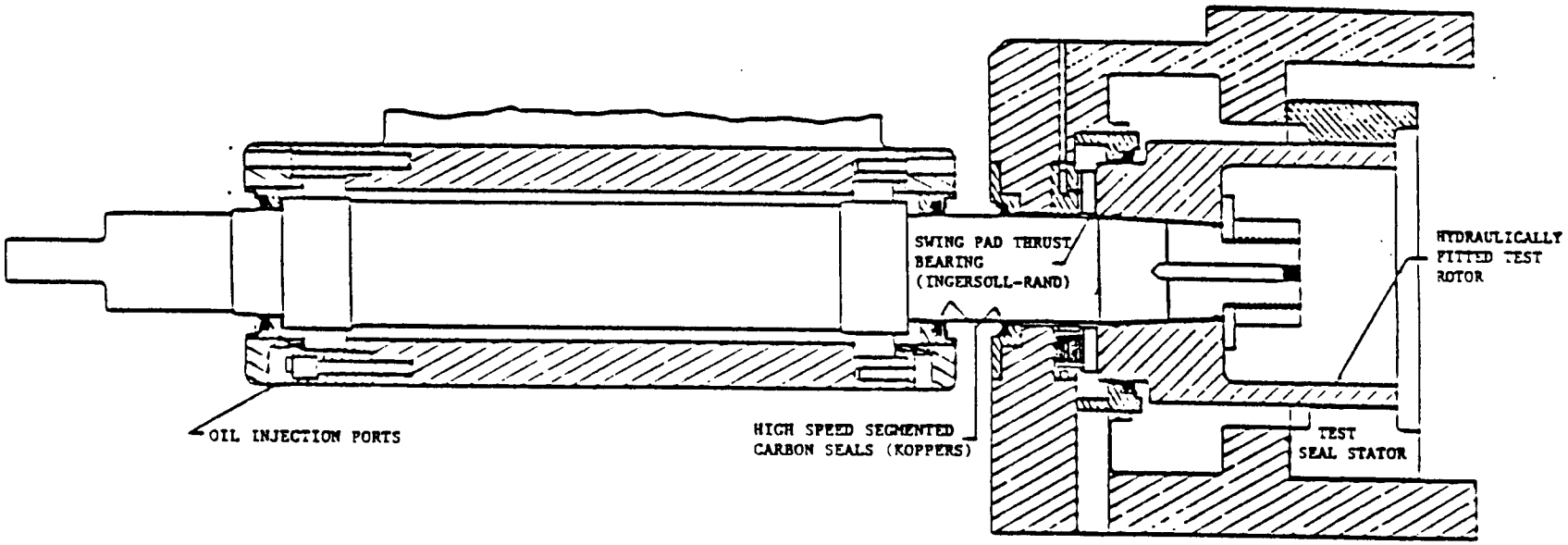

Fig. 31 High speed rotor-shaft assembly.

seals, which had been used on the TAMU apparatus. The Koppers seals in figure 31 were designed for gas applications. The sealing mechanism is a segmented carbon seal ring.

To conclude this discussion of the test hardware, two views of the complete test apparatus are included. Figure 32 shows the assembled rig, while an exploded view is provided in figure 33.

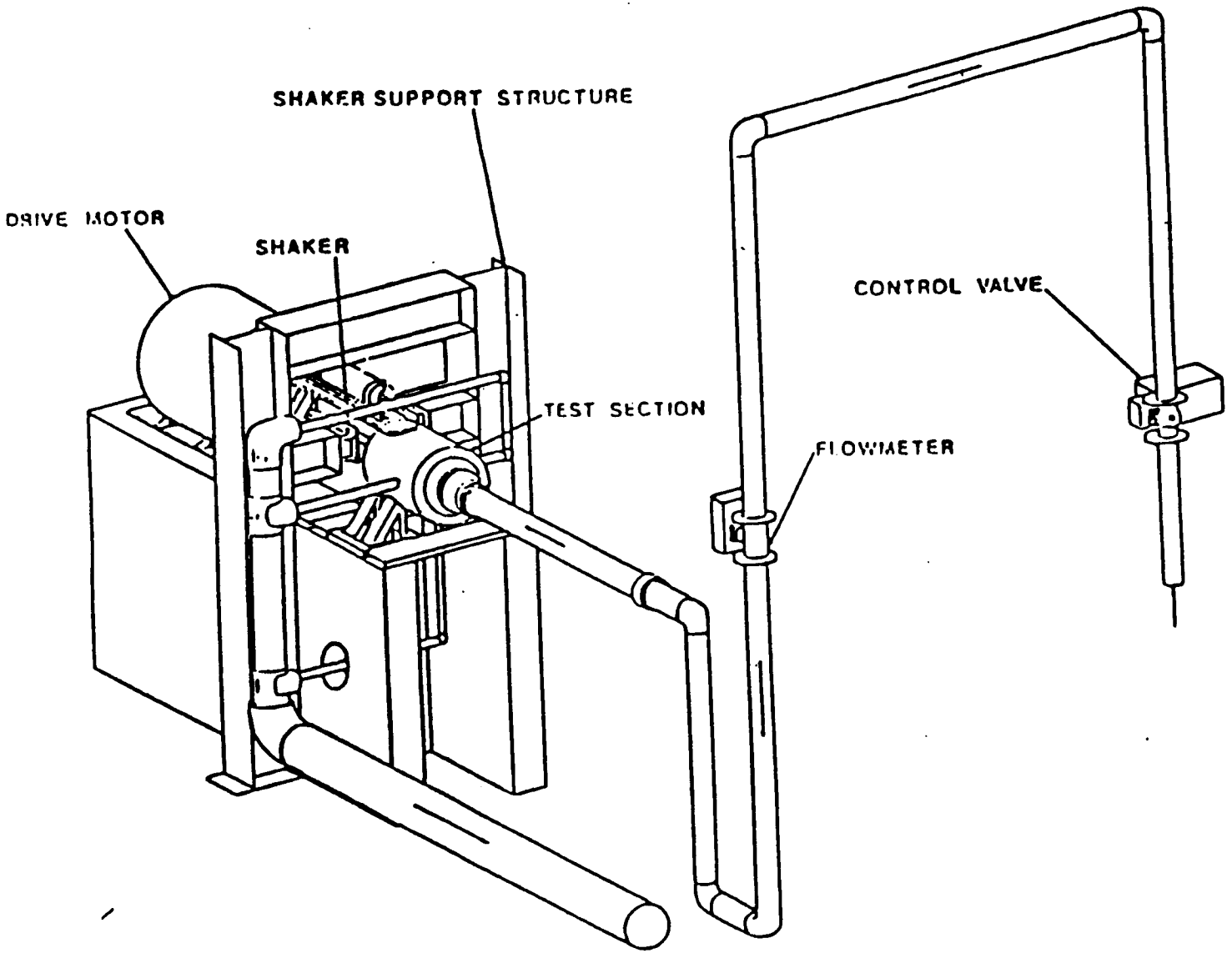

Fig. 32 Test apparatus assembly.

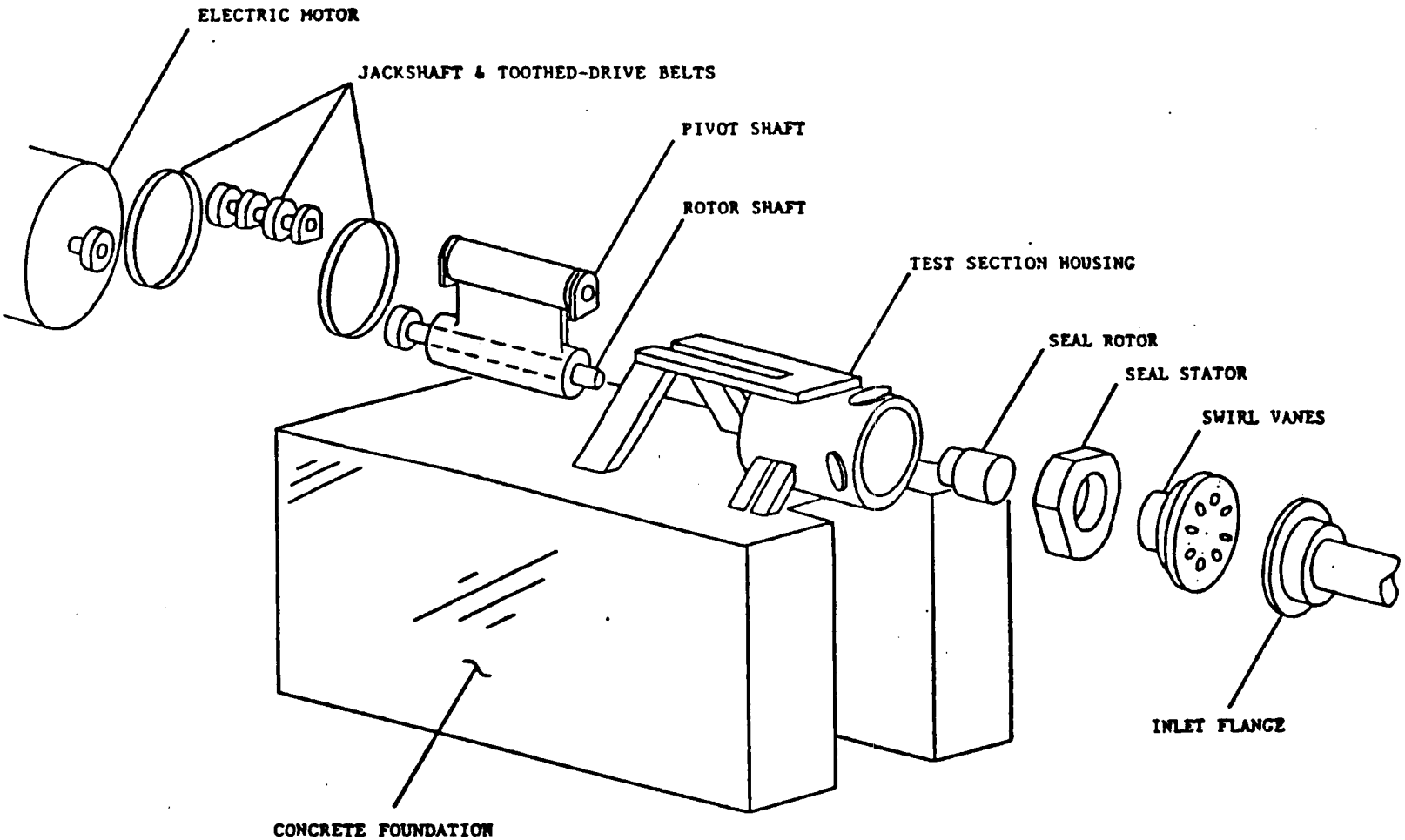

Fig. 33 Exploded view of test apparatus.

INSTRUMENTATION

Having discussed the seal parameters that can be varied, and how the variations are implemented, their measurement will now be described. The types of measurements which are made can be grouped into the following three categories:

1) rotor motion,

2) reaction-force measurements, and

3) fluid flow measurements.

These categories are described individually in the sections that follow.

Rotor Motion Measurements.

The position of the seal rotor within the stator is monitored by four Bently-Nevada eddy-current proximity probes, mounted in the test section housing. These probes are located 90 degrees apart, and correspond to the X and Y- directions. The proximity probes are used to determine the static position and dynamic motion of the rotor, and their resolution is 0.0025 mm (0.1 mil).

Reaction-Force Measurements.

Reaction forces arise due to the motion of the seal rotor within the stator. The reaction forces (F_X, F_Y) exerted on the stator are measured by the three Kistler quartz load cells which support the stator in the test section housing. When the rotor is shaken, vibration is transmitted to the test section housing, both through the thrust bearing and through the housing mounts. The acceleration of the housing and stator generates unwanted inertial "ma" forces which are sensed by the load cells, in addition to those pressure forces

developed by the relative motion of the seal rotor and stator. For this reason, PCB piezoelectric accelerometers with integral amplifiers are mounted in the X and Y-directions on the stator, as shown in figure 27. These accels allow a (stator mass) x (stator acceleration) subtraction to the forces (F_X, F_Y) indicated by the load cells. With this correction, which is described more fully in the next section, only the pressure forces due to relative seal motion are measured.

Force measurement resolution is a function of the stator mass and the resolution of the load cells and accelerometers. Accelerometer resolution is 0.005 g, which must be multiplied by the stator mass in order to obtain an equivalent force resolution. The masses of the stators used in the test program reported here are 11.5 kg(25.3 lb) and 11.0 kg(24.2 lb), corresponding to the smooth and labyrinth stators, respectively. Hence, force resolution for the accelerometers is 0.560 N (0.126 lb) and 0.538 N (0.121 lb), for each stator, respectively. Resolution of the load cells is 0.089 N(0.02 lb). Therefore, the resolution of the force measurement is limited by the accelerometers. With a stator with less mass, and/or accelerometers with greater sensitivity, force resolution could be improved.

Fluid Flow Measurements.

Fluid flow measurements include the leakage (mass flow rate) of air through the seal, the pressure gradient along the seal axis, and the inlet fluid circumferential velocity.

Leakage is measured with a Flow Measurement Systems Inc. turbine flowmeter located in the piping upstream of the test section. Resolution of the flowmeter is 0.0005 acf, and pressures and

temperatures up and downstream of the meter are measured for mass flow rate determination.

For measurement of the axial pressure gradient, the stator has pressure taps drilled along the length of the seal in the axial direction. These pressures, as well as all others, are measured with a 0-1.034 MPa (0-150 psig) Scanivalve differential-type pressure transducer through a 48 port, remotely-controlled Scanivalve model J scanner. Transducer resolution is 0.552 kPa (0.08 psi). Overall accuracy of the pressure measurements is limited by the resolution of the 12 bit A/D converter which can only resolve the pressure signal to $\pm$ 0.62 kPa (0.09 psi). Combined linearity and hysteresis error for the pressure transducer is 0.06%.

In order to determine the circumferential velocity of the air as it enters the seal, the static pressure at the guide vane exit is measured. This pressure, in conjunction with the measured flowrate and inlet air temperature, is used to calculate a guide vane exit Mach number. A compressible flow continuity equation

$$\dot{m} = p_{ex} A_{ex} M_{ex} [(\gamma/RT_t) (1 + (\gamma-1)M_{ex}^2 / 2)]^{1/2} \qquad (93)$$

is rearranged to provide a quadratic equation for Mex

$$M_{ex}^2 = \{-1 + 1 + 4((\gamma-1)/2\gamma) (\dot{m} RT_t / p_{ex} A_{ex})^2\} / (\gamma-1) \qquad (94)$$

where γ is the ratio of specific heats and R is the gas constant for air, T_t is the stagnation temperature of the air, p_{ex} is the static pressure at the vane exit, and A_{ex} is the total exit area of the guide vanes. Since all of the variables in the equation are either known or measured, the vane exit Mach number, and therefore the velocity, can be found.

In order to determine the circumferential component of this inlet velocity, a flow turning angle correction, in accordance with Cohen [46], is employed. The correction has been developed from guide vane cascade tests, and accounts for the fact that the fluid generally is not turned through the full angle provided by the shape of the guide vanes. With this flow deviation angle calculation, the actual flow direction of the air leaving the vanes (and entering the seal) can be determined. Hence, the magnitude and direction of the inlet velocity is known, and the appropriate component is the measured inlet circumferential velocity.

DATA ACQUISITION AND REDUCTION

With the preceding explanations of how the seal parameters are varied, and how these parameters are measured, the discussion of how the raw data is processed and implemented can begin. Data acquisition is directed from a Hewlett-Packard 9816 (16-bit) computer with disk drive and 9.8 megabyte hard disk. The computer controls an H-P 6940B multiprogrammer which has 12-bit A/D and D/A converter boards and transfers control commands to and test data from the instrumentation.

As was previously stated, the major data groups are seal motion/reaction force data and fluid flow data. The motion/reaction force data are used for dynamic coefficient identification. The hardware involved includes the load cells, accelerometers, X-direction motion probe, a Sensotec analog filter unit, a tuneable bandpass filter, and the A/D converter. The operation of these components is illustrated in figure 34, and their outputs are used in a serial sampling scheme which provides the computer with the desired data for

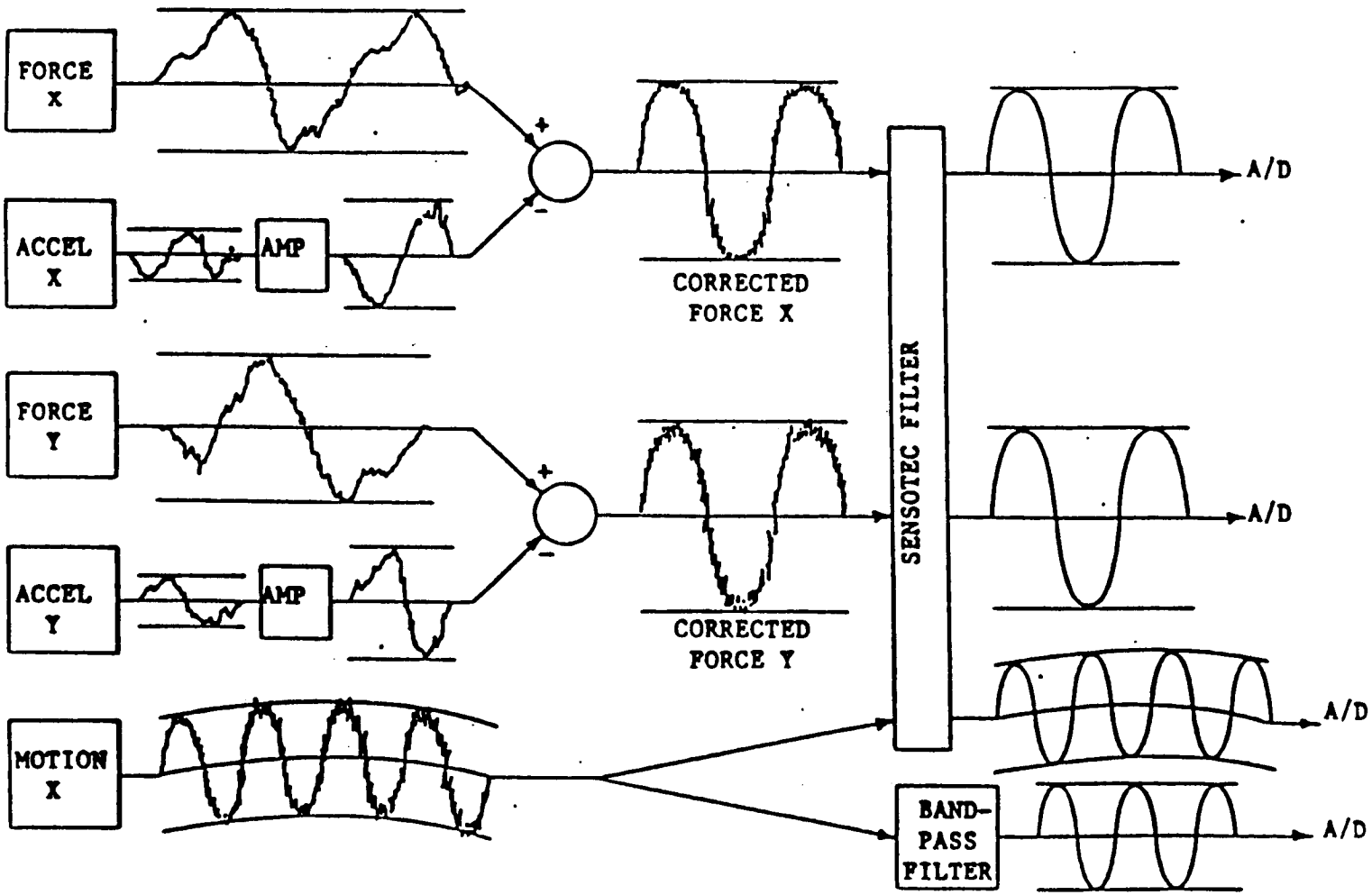

Fig. 34 Signal conditioning schematic for data acquisition.

reduction. Recalling the discussion of the reaction force measurements in the preceding section, a (stator mass) x (stator acceleration) subtraction from the indicated load cell forces is necessitated due to vibration of the stator and test section housing. This subtraction is performed with an analog circuit, and results in corrected F_X and F_Y force components due to relative seal motion. The forced oscillatory shaking motion of the seal rotor is the key to the operation of the serial synchronous sampling (SSS) routine which is employed. The frequency of the rotor oscillation is set by a function generator, and rotor motion is sensed by the X-direction motion probe. The motion signal is filtered by the narrow bandpass filter, and is used as a trigger signal for the SSS routine. Upon the operator's command, the SSS routine is enabled, and the next positive-to- negative crossing of the filtered motion signal triggers a quartz crystal clock/timer. Ten cycles of the corrected $F_X(t)$ signal are sampled, at a rate of 100 samples/cycle. The second positive-to-negative crossing of the filtered motion signal triggers the timer and initiates the sampling of ten cycles of the $F_Y(t)$ signal. Finally, the third positive-to-negative crossing triggers the timer again, and ten cycles of the corrected X(t) signal are sampled. Thus, at every test condition, 1000 data points are obtained for $F_X(t_i)$,$F_Y(t_i)$, and $X(t_i)$, and the data arrays are stored in computer memory.

Some important points need to be stressed concerning this force/motion data acquisition. First, the bandpass filter is used only to provide a steady signal to trigger the timer/clock. Any modulation of the motion signal due to rotor runout is eliminated by this filter,

as long as the rotational frequency and shaking frequency are adequately separated, and the shaking frequencies are selected to provide adequate separation with running speeds. However, the rotor motion and corrected force signals which are sampled and captured for coefficient identification are filtered only by a low-pass filter (500 Hz cutoff), and the effects of runout as well as shaking motion are present in the recorded data. A second point worth noting is that the sample rate is directly dependent on the shaking frequency. As the shaking frequency is increased, the sample rate (samples/second) also increases. In order to get the desired 100 samples/cycle, shaking frequencies must be chosen to correspond to discrete sample rates which are available. Hence, the frequency at which the rotor is shaken is carefully chosen to provide the desired sampling rate and a steady trigger signal. The uncertainty in the shaking frequency is 0.13 Hz for the 74.6 Hz case.

Most of the fluid flow data are used for the input parameters required by the analysis. The upstream (reservoir) pressure and temperature, downstream (sump) pressure, and the inlet circumferential velocity (determined as outlined earlier) are provided directly. The friction-factor values of the rotor and stator are supplied in the form of coefficients, which are obtained from the pressure distribution data for the smooth annular seals, see Nicks [47] and Nelson et al. [48], and are assumed to be the same for the labyrinth surfaces.

PROCEDURE

At the start of each day's testing, the force, pressure, and flowmeter systems are calibrated. The total system, from transducer to

computer, is calibrated for each of these variables. The force system calibration utilizes a system of pulleys and known weights applied in the X and Y-directions. An air-operated dead-weight pressure tester is used for pressure system calibration, and flowmeter system calibration is achieved with an internal precision clock which simulates a known flowrate.

All of the tests performed to date have been made with the rotor executing small motion about a centered position. A typical test begins by centering the seal rotor in the stator with the static capability of the Zonic hydraulic shaker, starting the airflow through the seal, setting the rotational speed of the rotor, and then beginning the shaking motion of the rotor. Data points are taken at rotational speeds of 3000, 6000, 9500, 13000 and 16000 cpm with a tolerance of $\pm$ 10 cpm. At each rotational speed, data points are taken at pressures of 3.08 bar (30 psig), 4.46 bar (50 psig), 5.84 bar (70 psig), 7.22 bar (90 psig), and 8.25 bar (105 psig), as measured upstream of the flowmeter with a tolerance of $\pm$ 0.069 bar (1.0 psig). For each test case (i.e., one particular running speed, shaking frequency, inlet pressure, and prerotation condition), the measured leakage, rotordynamic coefficients, and axial pressure distribution are determined and recorded.

This test sequence is followed for each of two different shaking frequencies, and for five inlet swirl directions. Therefore, twenty-five data points are taken per test with a total of ten tests per seal for shaking about the centered position. Shaking a seal about an eccentric position would require more tests.

CHAPTER IV

TEST RESULTS: INTRODUCTION

The results reported here are from tests of six "see-through" labyrinth seals, three with teeth on the rotor and three with teeth on the stator, each with different radial clearances. Tables 3, 4 and 5 show the pertinant data for each seal configuration. For the remainder of this report, the seals will be referred to as seal 1, seal 2, and seal 3, as given in table 5, in addition to their respective configuration.

The test program had the following objectives:

1) Acquire leakage, stiffness, and damping coefficients as a function of rotor speed, pressure drop, and inlet circumferential velocity for three teeth-on-rotor and three teeth-on-stator labyrinth seals with different radial clearances.

2) Compare the effect of varying the radial seal clearance on the experimentally determined rotordynamic coefficients.

3) Compare test results to the predictions of the new analysis presented in this report.

When shaking about the centered position, the test apparatus can be used to control the rotor speed, reservoir pressure (i.e. supply pressure), circumferential velocity of the inlet air, and the frequency and amplitude of translatory rotor motion. Two shake frequencies, 56.8 and 74.6 Hz, were used during testing with essentially the same results. The results plotted here were obtained

Table 3. Test stator specifications.

	Smooth Stator	Labyrinth Stator
Seal 1		
Diameter:		
upstream	15.197 cm (5.983 in)	15.202 cm (5.985 in)
downstream	15.197 cm (5.983 in)	15.202 cm (5.985 in)
Material:	aluminum	brass
Seal 2		
Diameter:		
upstream	15.217 cm (5.991 in)	15.217 cm (5.991 in)
downstream	15.217 cm (5.991 in)	15.217 cm (5.991 in)
Material:	aluminum	brass
Seal 3		
Diameter:		
upstream	15.245 cm (6.002 in)	15.237 cm (5.999 in)
downstream	15.247 cm (6.003 in)	15.237 cm (5.999 in)
Material:	brass	brass

Table 4. Test rotor specifications.

	Labyrinth Rotor	Smooth Rotor
Seal	1,2,3	1,2,3
Diameter:		
upstream	15.136 cm (5.959 in)	15.136 cm (5.959 in)
downstream	15.136 cm (5.959 in)	15.136 cm (5.959 in)
Material:	304 stainless steel	304 stainless steel

Table 5. Test seal specifications.

	Teeth-On-Rotor	Teeth-On-Stator
Seal 1		
Radial Clearance:		
upstream	0.3048 cm (0.012 in)	0.3302 cm (0.013 in)
downstream	0.3048 cm (0.012 in)	0.3302 cm (0.013 in)
Seal Length:	5.080 cm (2.000 in)	5.080 cm (2.000 in)
Number of teeth:	16	16
Seal 2		
Radial Clearance:		
upstream	0.4064 cm (0.016 in)	0.4064 cm (0.016 in)
downstream	0.4064 cm (0.016 in)	0.4064 cm (0.016 in)
Seal Length:	5.080 cm (2.000 in)	5.080 cm (2.000 in)
Number of teeth:	16	16
Seal 3		
Radial Clearance:		
upstream	0.5461 cm (0.0215 in)	0.5080 cm (0.020 in)
downstream	0.5588 cm (0.022 in)	0.5080 cm (0.020 in)
Seal Length:	5.080 cm (2.000 in)	5.080 cm (2.000 in)
Number of teeth:	16	16

Table 6. Definition of symbols used in figures.

Pressures	Rotor speeds	Inlet circumferential velocities
1 - 3.08 bar	1 - 3000 cpm	1 - High velocity against rotation
2 - 4.46 bar	2 - 6000 cpm	2 - Low velocity against rotation
3 - 5.84 bar	3 - 9500 cpm	3 - Zero circumferential velocity
4 - 7.22 bar	4 - 13000 cpm	4 - Low velocity with rotation
5 - 8.25 bar	5 - 16000 cpm	5 - High velocity with rotation

The pressure for each test is set at the flowmeter of Figure 12.

by shaking at 74.6 Hz at an amplitude between 3 and 4 mils. The actual test points for each of the other three independent variables are shown in Table 6.

Figures 35-37 show the inlet circumferential velocity of the air (U_θ) for the configurations described in table 6 for the seals reported on here. The equation for U_θ is

$$U_\theta = \dot{m} \sin A / \rho A_v$$

where $\dot{m}$ is the fluid mass flow rate, ρ is the fluid density, A_v is the exit area of the fluid turning vanes, and A is the fluid swirl angle at the turning vanes exit as measured from the axial direction. The method used to determine A is described in the TEST APPARATUS AND FACILITY chapter of this report. Negative circumferential velocities represent velocities opposed to the direction of rotor rotation. Positive velocities are in the direction of rotor rotation. Note that curve 3 (representing zero inlet circumferential velocity) lies on the horizontal axis in each figure. The inlet circumferential velocity ratio, the ratio of inlet circumferential velocity to rotor surface velocity, ranged from about -6 to about 6. When reviewing the following figures, table 6 and figures 35-37 should be consulted for the definitions of symbols used.

NORMALIZED PARAMETERS

Before the tests described herein were performed, the TAMU gas seal test apparatus was modified as described in the TEST APPARATUS AND FACILITY chapter to allow operation at running speeds up to 16,000 cpm. As expected, subsequent tests revealed a dependence of the rotor diameter on running speed due to inertia and thermal effects. The

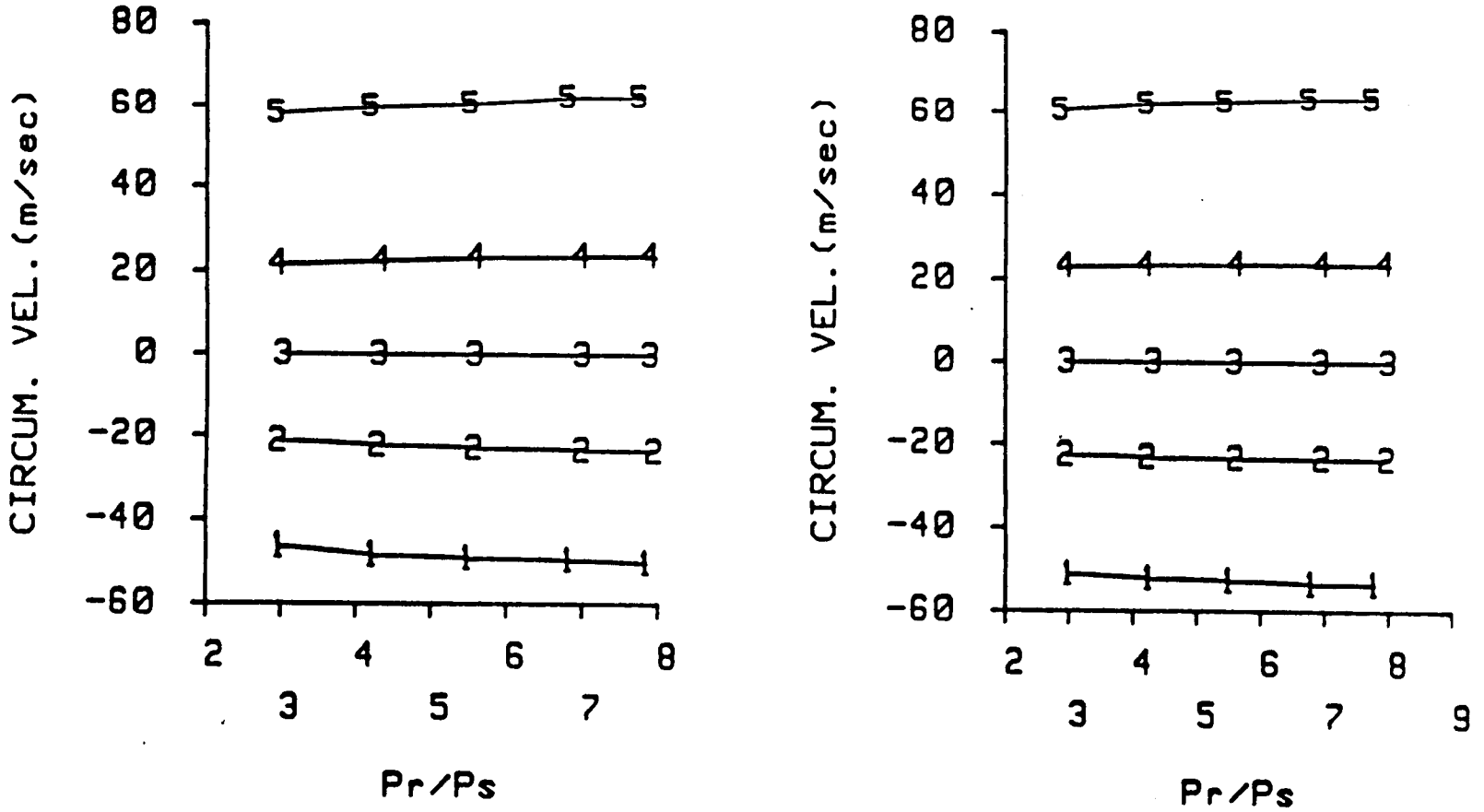

Fig. 35 Inlet circumferential velocities for seal 1. See table 6 for definitions. Teeth-on-rotor (left), teeth-on-stator (right).

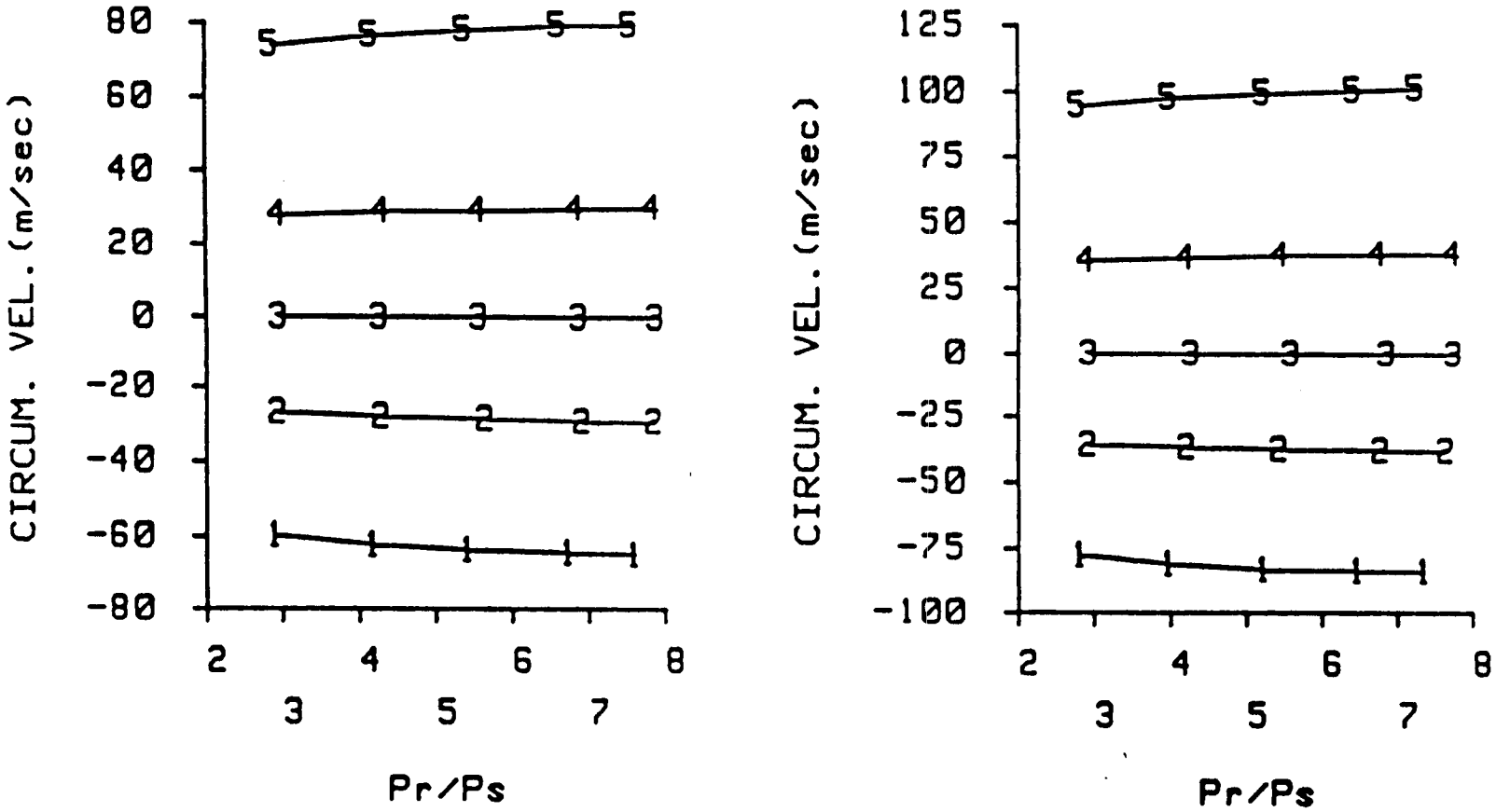

Fig. 36 Inlet circumferential velocities for seal 2. See table 6 for definitions. Teeth-on-rotor (left), teeth-on-stator (right).

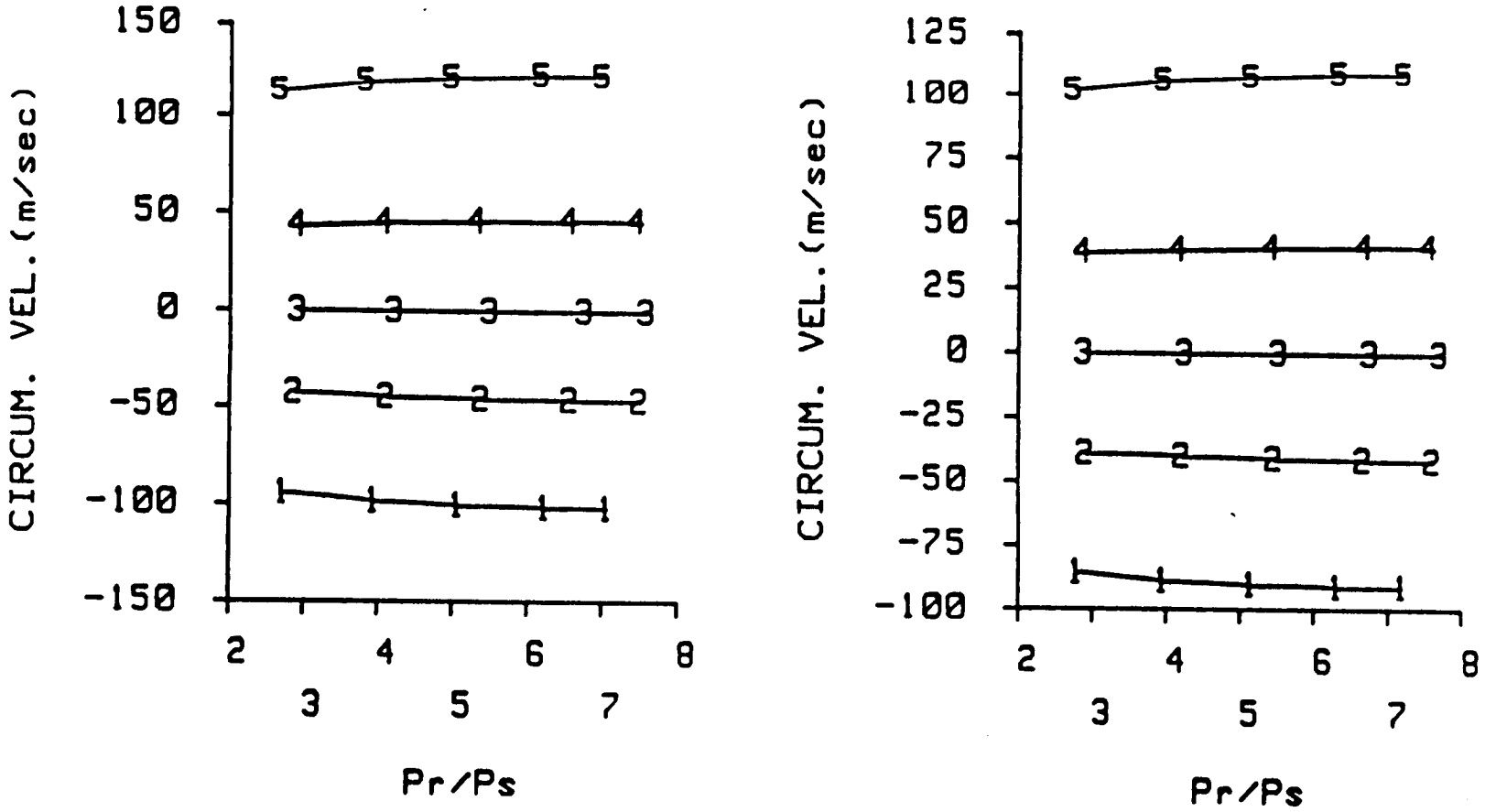

Fig. 37 Inlet circumferential velocities for seal 3. See table 6 for definitions. Teeth-on-rotor (left), teeth-on-stator (right).

Table 7. Growth of rotor with rotational speed.

Rotor speed (rpm)	Diametrical growth (mm)	Diametrical growth (inches x 1000)
3000	0.01	0.4
6000	0.02	0.7
9500	0.03	1.2
13000	0.05	1.9
16000	0.11	4.4

Table 8. Normalized coefficients.

$$\bar{K} = K \frac{H_o}{DL(\Delta P)} \quad \text{(nondim)}$$

$$\bar{C} = C \frac{H_o}{DL(\Delta P)} \quad \text{(sec)}$$

K = stiffness (N/mm)

C = damping (N sec/mm)

H_o = seal exit clearance (mm)

D = seal diameter (m)

L = seal length (m)

ΔP = pressure drop across seal (N/m^2)

rotor growth data, shown in table 7, were obtained from eddy current motion probes positioned at the midspan of the seal. Thus, as the rotor turns faster, the forces in the seal are affected not only by the increased surface speed of the rotor (drag) but also by a change in clearance (friction factor). See table 8 for the definitions of the normalized parameters. Theoretically, normalization would collapse the data and make the presentation simpler and more straight forward. However, this is not the case with the labyrinth seals tested in this study. Figure 38 shows a comparison of dimensional and nondimensional direct stiffness versus rotor speed for the inlet pressure set of table 6. The data did not collapse to a single curve and shows increased irregularity.

Figure 39 shows a comparison of normalized and dimensional direct damping for a teeth-on-stator labyrinth seal versus clearance for the inlet circumferential velocity set of table 6. The normalized results lead one to believe that the direct damping coefficient increases as clearance increases. However, the dimensional results show that the direct damping coefficient decreases as clearances increases. To avoid this type of confusion, the rotordynamic coefficients presented in this study have not been normalized.

RELATIVE UNCERTAINTY

Before the test results are given, a statement about the experimental uncertainty is needed. The method used is that described by Holman [49] for estimating the uncertainty in a calculated result based on the uncertainties in primary measurements. The uncertainty w_R in a result R which is a function of n primary measurements

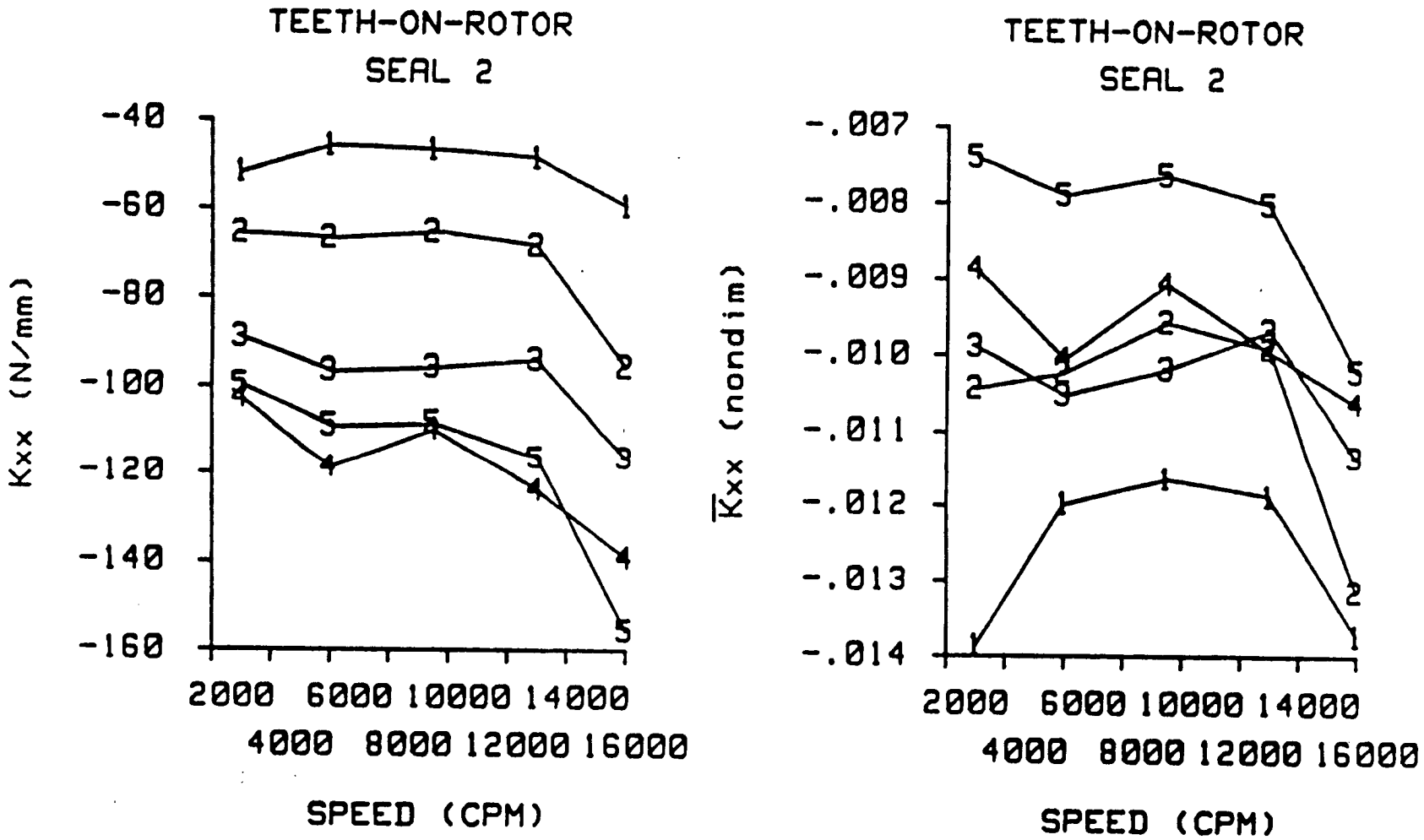

Fig. 38 A comparison of dimensional and nondimensional direct stiffness coefficients. See table 8 for definitions of normalized parameters.

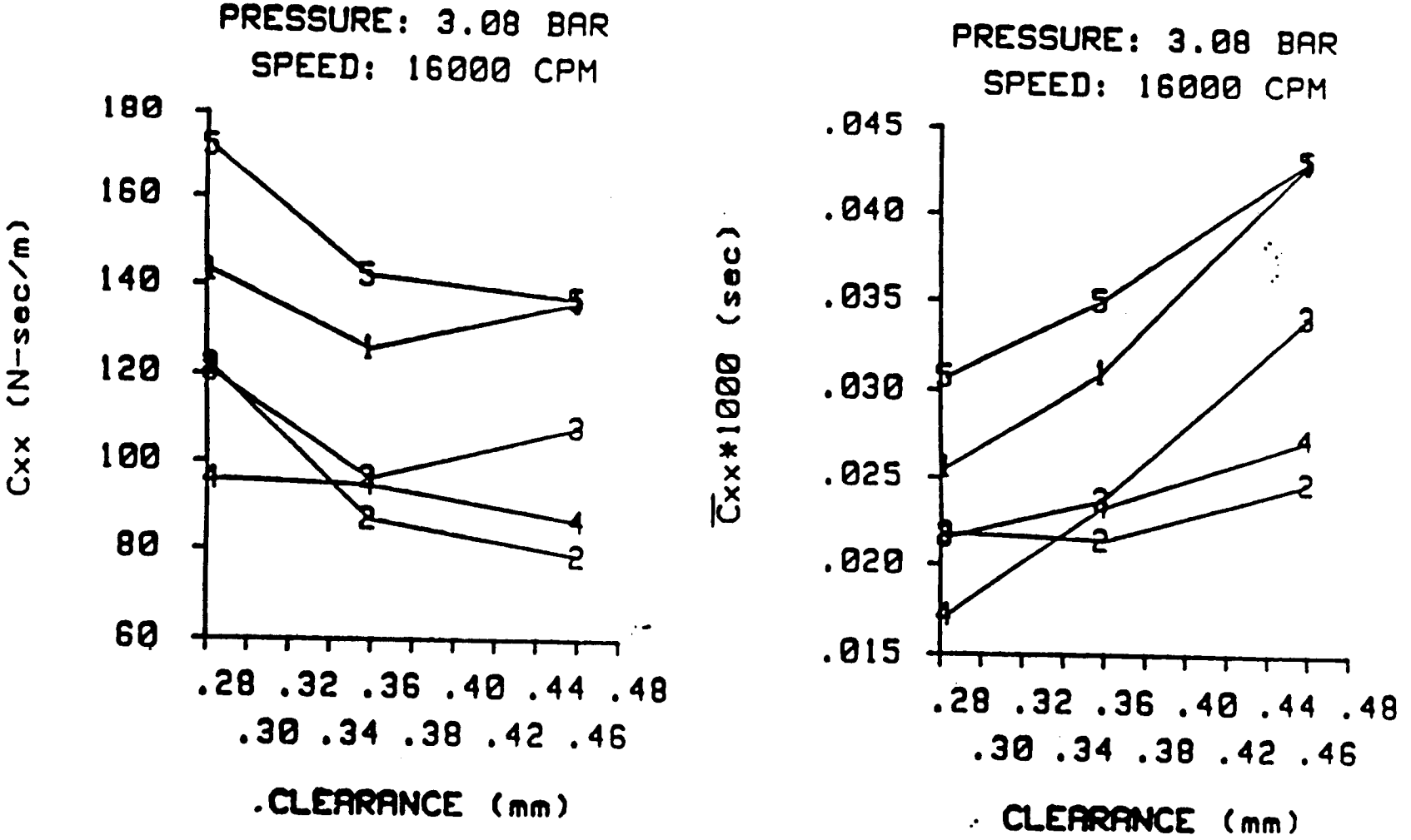

Fig. 39 A comparison of dimensional and normalized direct damping coefficients. See table 8 for definitions of normalized parameters.

$x_1, x_2, x_3, \ldots, x_n$ with uncertainties $w_1, w_2, w_3, \ldots, w_n$ is

$$w_R = \left[\left(\frac{\partial R}{\partial x_1} w_1 \right)^2 + \left(\frac{\partial R}{\partial x_2} w_2 \right)^2 + \ldots + \left(\frac{\partial R}{\partial x_n} w_n \right)^2 \right]^{1/2} \quad (95)$$

In this case, the rotordynamic coefficients are calculated using equation (91). The primary measurements are forces, displacements, and frequency. The uncertainty in these measurements on the TAMU test apparatus are 0.89 N (0.2 lb), 0.0013 mm (0.05 mils), and 0.13 Hz, respectively. For the six seals tested, the estimated uncertainty in the stiffness and damping coefficients were 7 N/mm (40 lb/in) and 0.0875 N-s/mm (0.5 lb-s/in), respectively. The uncertainty in the cross-coupled damping coefficients were of the same order of magnitude as the coefficients themselves. Since the uncertainties in the cross-coupled-damping values were so high, and since the cross-coupled-damping forces are of minor significance compared to the other damping and stiffness forces, comparisons of the cross-coupled-damping coefficients have been omitted from this report.

SELECTION OF REPORT DATA

For each of the six seals tested, there were 125 test points for leakage, direct and cross-coupled stiffness, and direct damping at the 74.6 Hz shake frequency. Generally, a ranking of the three independent variables of the test apparatus in order of the relative effect on the rotordynamic coefficients of a seal is: inlet circumferential velocity, pressure ratio, running speed. The previous report of Scharrer [22] thoroughly catalogued the results for the effects of pressure ratio, rotor speed up to 8000 cpm and inlet circumferential velocity on the rotordynamic coefficients. Since the rotor speed capability of the

test apparatus has been changed, results which show new information concerning rotor speed will be reviewed. Figures in the next two chapters show the dependence of leakage and rotordynamic coefficients on radial seal clearance for inlet swirl conditions of table 6. Figures in Appendix D show additional information on leakage, pressure gradients and rotordynamic coefficients. Generally, solid lines in a figure represent experimental results, and broken lines represent the predictions of the new analysis presented in this report. These figures will be used to compare the effect of radial seal clearance on seal performance, and to evaluate the new analysis presented in this report.

CHAPTER V

TEST RESULTS: RELATIVE PERFORMANCE OF SEALS

This evaluation of the effect on seal performance of varying the radial seal clearance requires frequent use of the information in table 6 and figures 35-37. It might seem obvious, since this report evaluates the effect of radial seal clearance, that the data should be presented as a function of clearance(clearance being on the x-axis). However, since the inlet circumferential velocity is directly dependent on the seal leakage and the seals leak at different rates due to differing cross-sectional areas, inlet circumferential velocity 5 (swirl 5) for seal 1 is less than those for seals 2 and 3. This is a problem because the rotordynamic coefficients are very sensitive to the inlet circumferential velocity. Therefore, the dynamic data will be presented as a function of inlet circumferential velocity at one inlet pressure and one rotor speed. Comparisons of the leakage, direct stiffness, cross-coupled stiffness, direct damping, and stability of the six seals follow.

LEAKAGE

The flow rate of air through each seal was measured with a turbine flowmeter located in the piping upstream of the test section (see figure 32). Figures 40-43 show seal leakage as a function of radial seal clearance for the inlet circumferential velocity set of table 6 for teeth-on-rotor and teeth-on-stator labyrinth seals, respectively. The plot on the left side of the page is for the teeth-on-rotor seal and the one for the teeth-on-stator seal is on

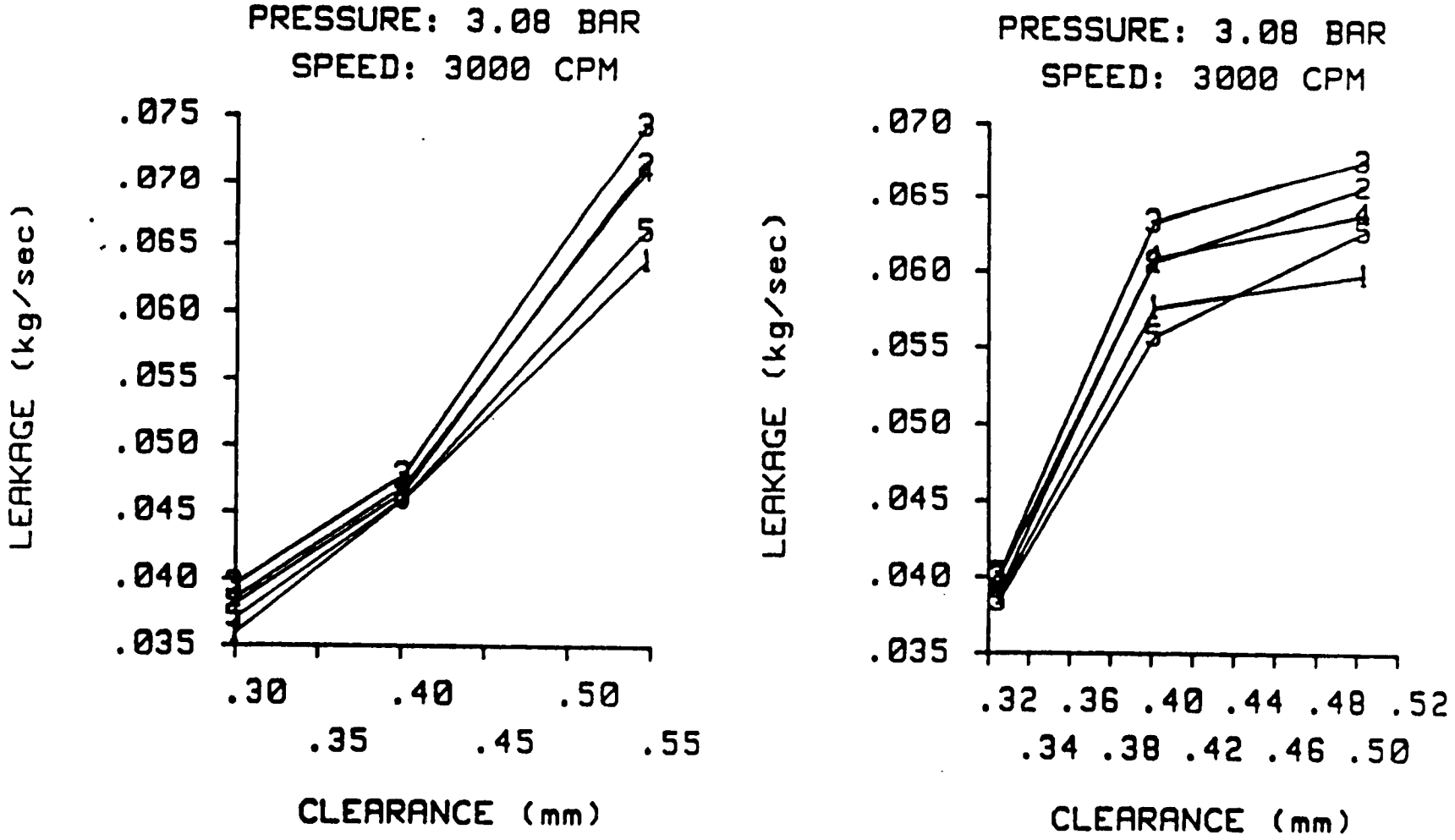

Fig. 40 Leakage versus radial seal clearance at an inlet pressure of 3.08 bar and rotor speed of 3000 cpm. See table 6 for inlet swirl definitions. Teeth-on-rotor (left), teeth-on-stator (right).

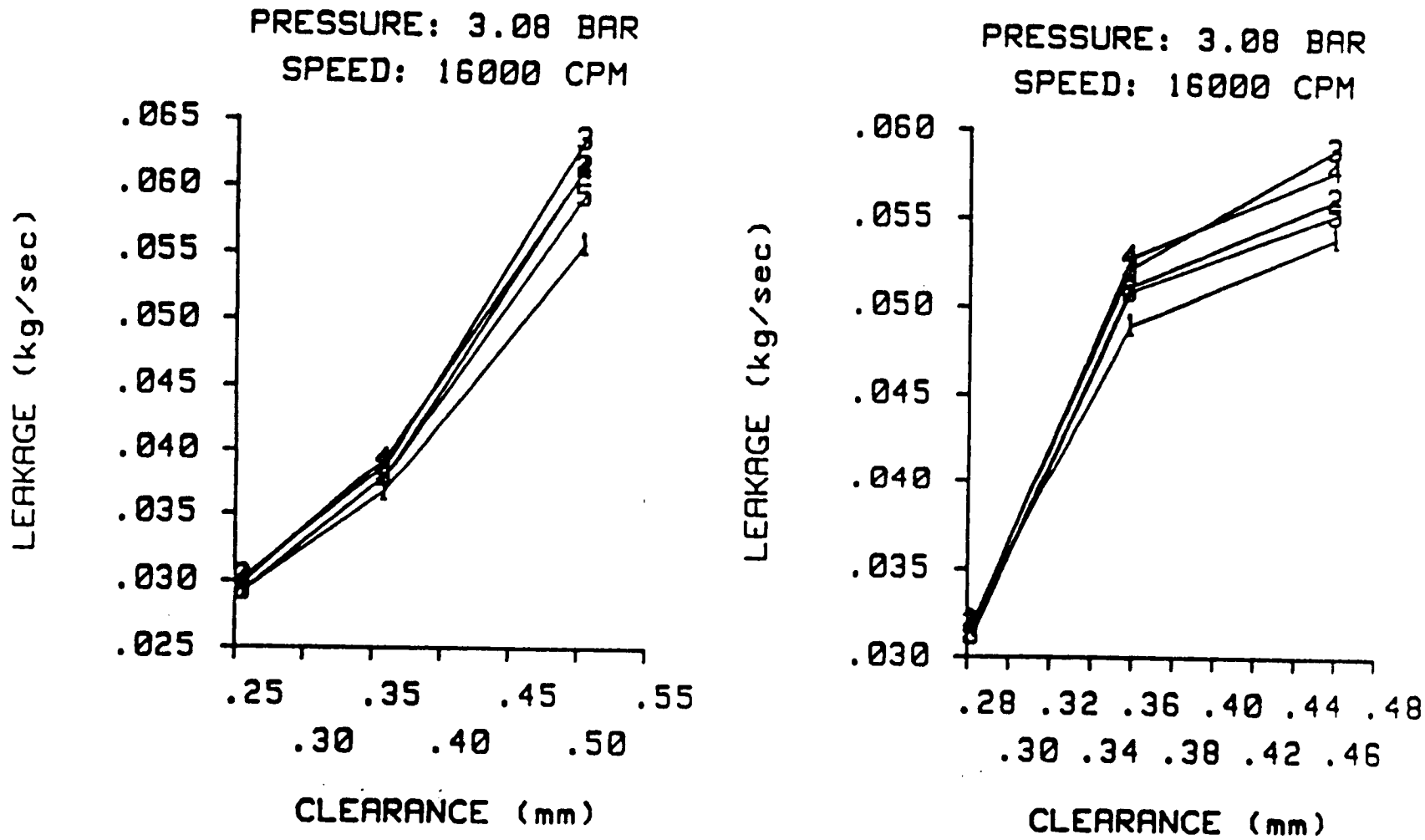

Fig. 41 Leakage versus radial seal clearance at an inlet pressure of 3.08 bar and rotor speed of 16000 cpm. See table 6 for inlet swirl definitions. Teeth-on-rotor (left), teeth-on-stator (right).

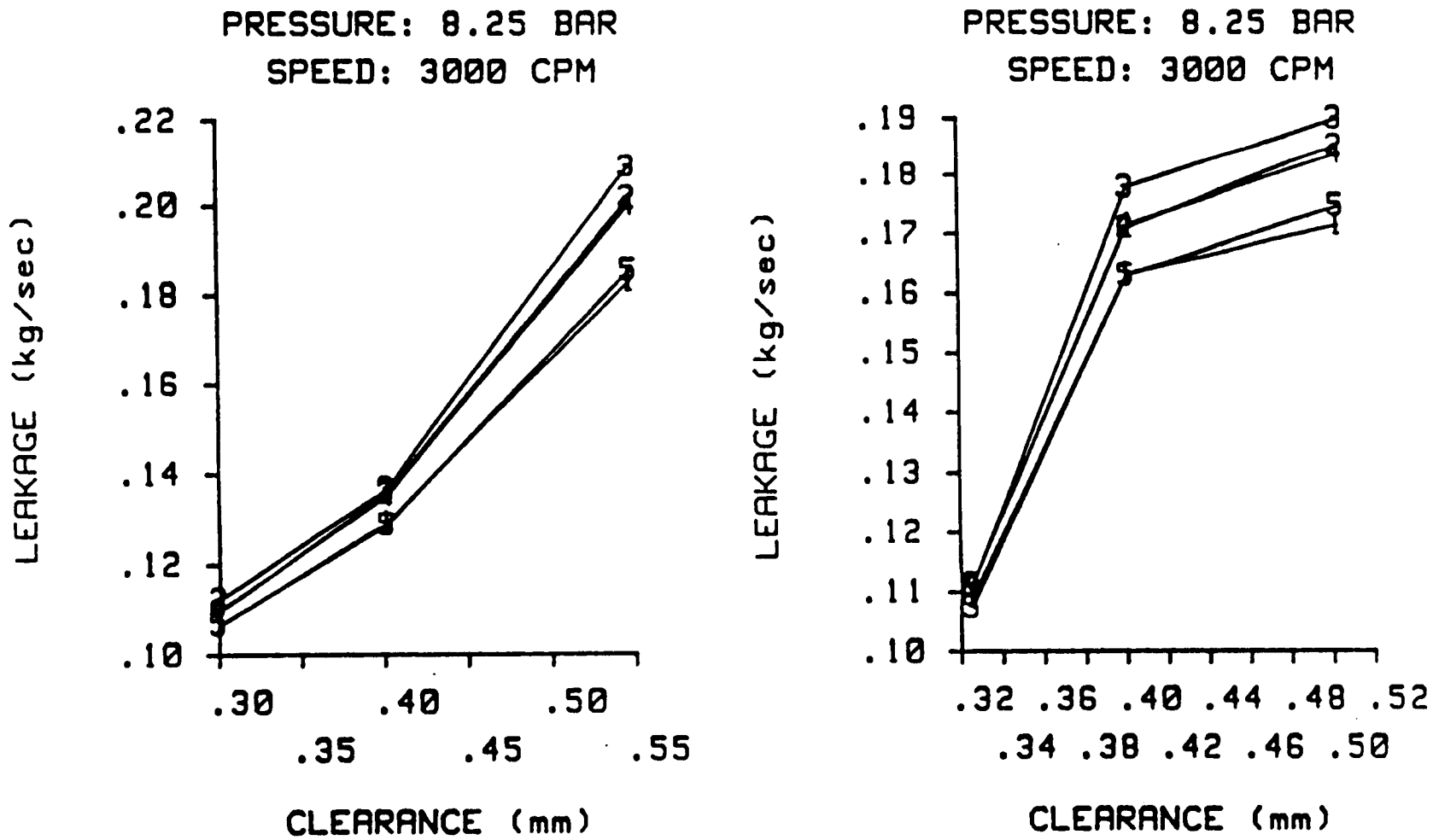

Fig. 42 Leakage versus radial seal clearance at an inlet pressure of 8.25 bar and rotor speed of 3000 cpm. See table 6 for inlet swirl definitions. Teeth-on-rotor (left), teeth-on-stator (right).

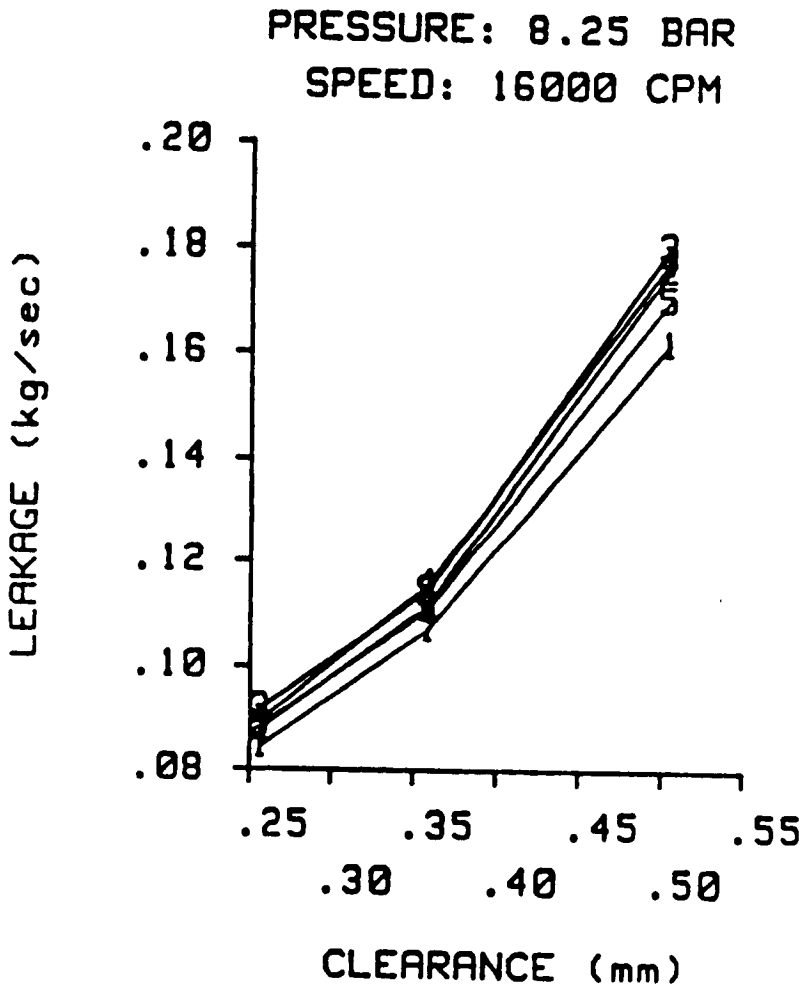

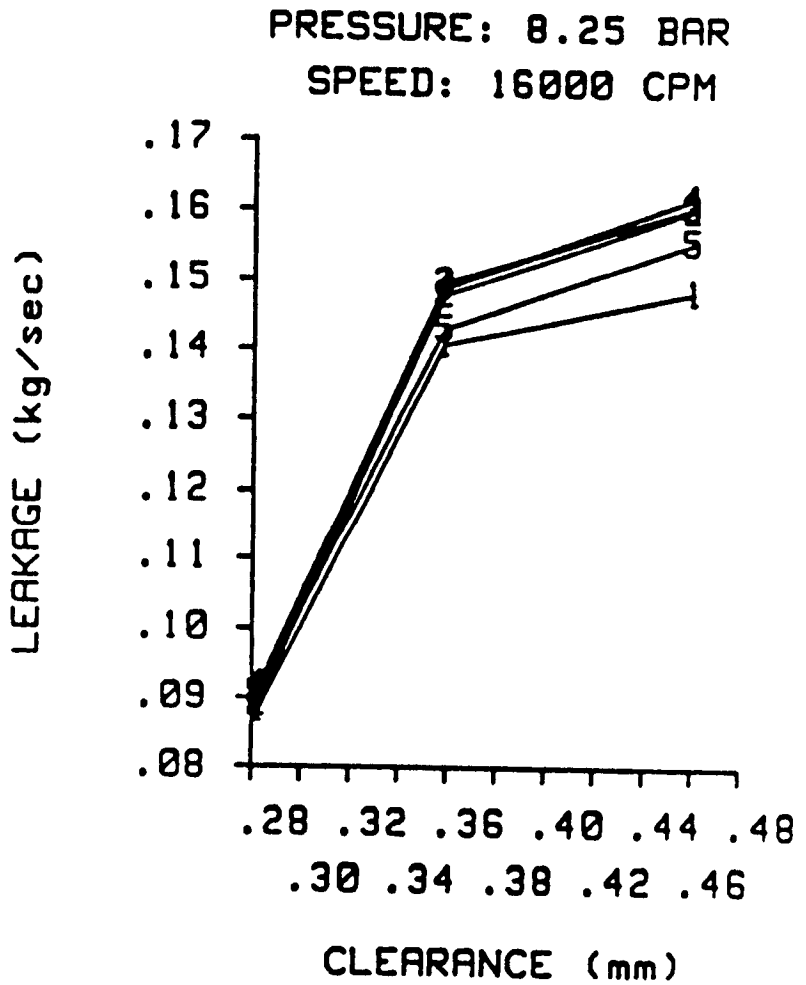

Fig. 43 Leakage versus radial seal clearance at an inlet pressure of 8.25 bar and rotor speed of 16000 cpm. See table 6 for inlet swirl definitions. Teeth-on-rotor (left), teeth-on-stator (right).

the right. This convention will be followed for the remainder of the presentation. A comparison of the leakage of the six seals reveals, as expected, greater leakage occurs for greater radial clearances. The difference in the shapes of the curves, between the two seal types, can be attributed to the difference in the performance characteristics of the two seals.

DIRECT STIFFNESS

Figures 44-47 show the dimensional direct stiffness versus inlet circumferential velocity ratio for the clearances of table 5. These plots show that the direct stiffness decreases in magnitude as clearance increases. One would expect zero direct stiffness values at sufficiently large clearances. Figures 48-50 show the dimensional direct stiffness versus rotor speed for the pressure ratios of table 6 and inlet circumferential velocity 3. The figures show that direct stiffness becomes increasingly negative as rotor speed increases, for the teeth-on-rotor seal, and is unchanged for the teeth-on-stator seal. This effect was not noticeable in the results from the low speed test rig and could be a result of clearance change due to rotor growth. The dimensionless direct stiffness coefficient, defined in table 8, removes the effect of clearance change due to rotor growth from the plot. Figure 51 shows the dimensionless direct stiffness versus rotor speed for seal 1 (minimum clearance seal) at the pressure ratios of table 6 and inlet circumferential velocity 3. The figure shows that the dimensionless direct stiffness increases in magnitude as rotor speed increases, for the teeth-on-rotor seal, and is inconclusive for the teeth-on-stator seal. Associated direct stiffness plots can be found in Appendix D.

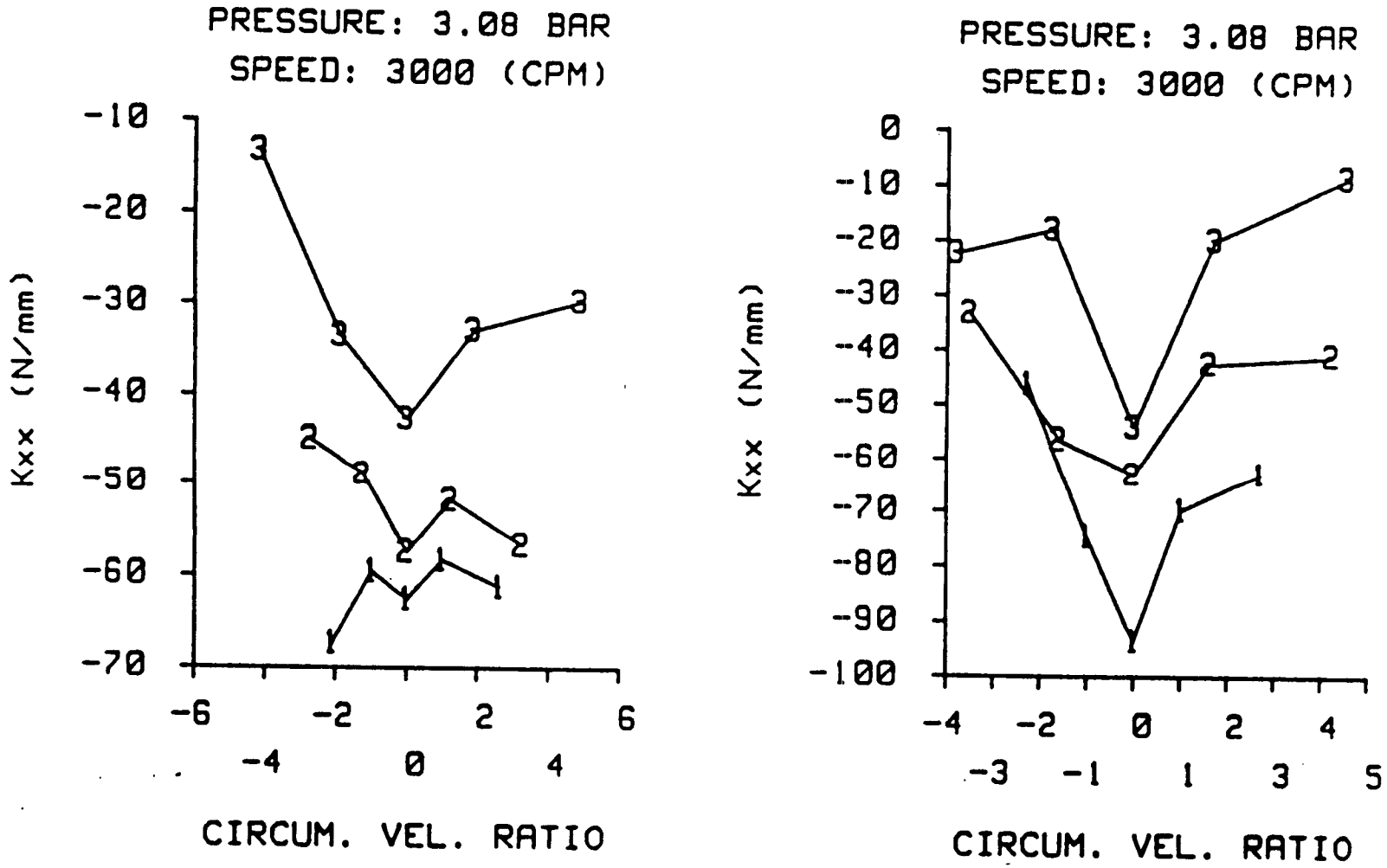

Fig. 44 Direct stiffness versus inlet circumferential velocity ratio at an inlet pressure of 3.08 bar and rotor speed of 3000 cpm. See table 5 for seal clearance definitions. Teeth-on-rotor (left), teeth-on-stator (right).

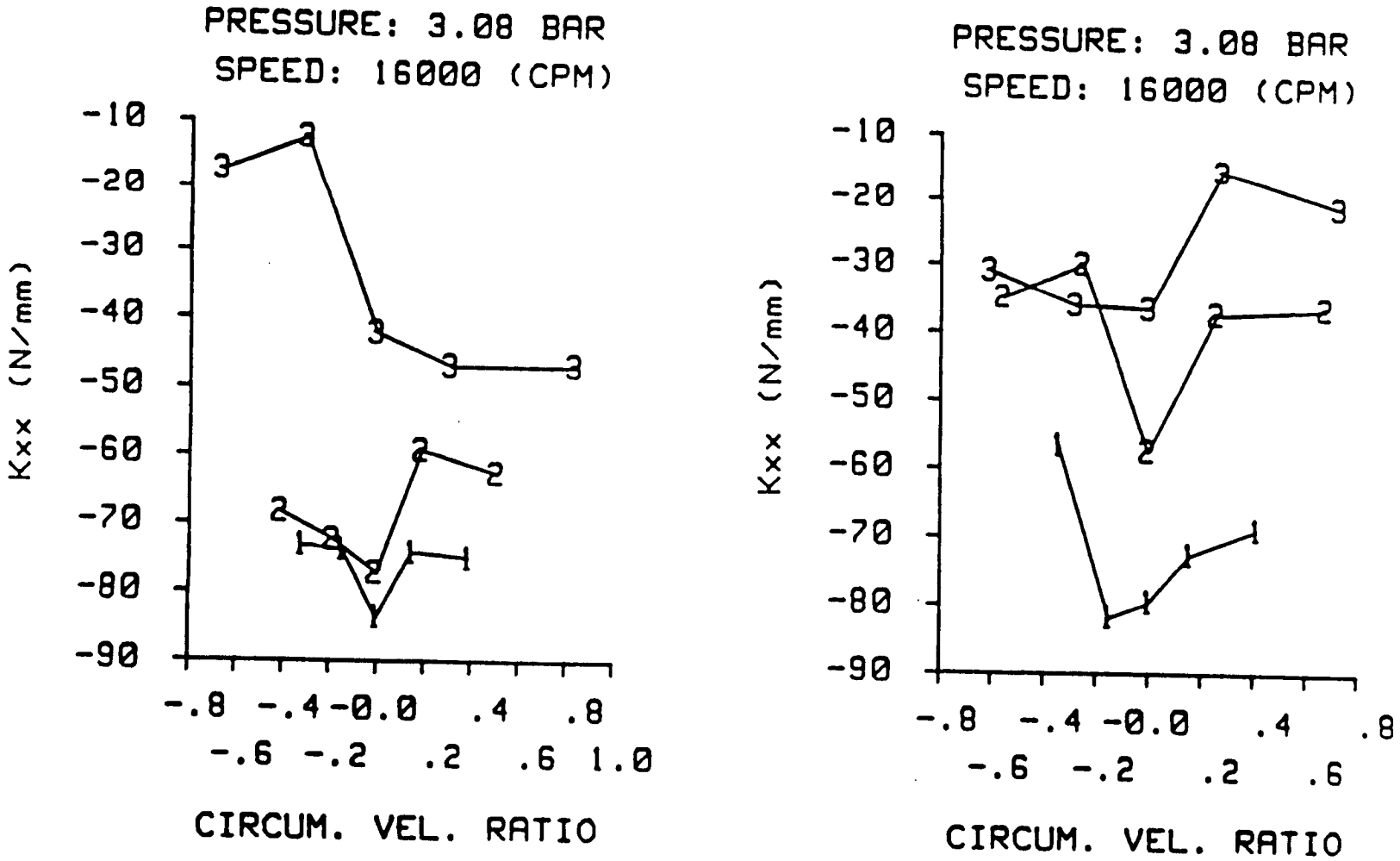

Fig. 45 Direct stiffness versus inlet circumferential velocity ratio at an inlet pressure of 3.08 bar and rotor speed of 16000 cpm. See table 5 for seal clearance definitions. Teeth-on-rotor (left), teeth-on-stator (right).

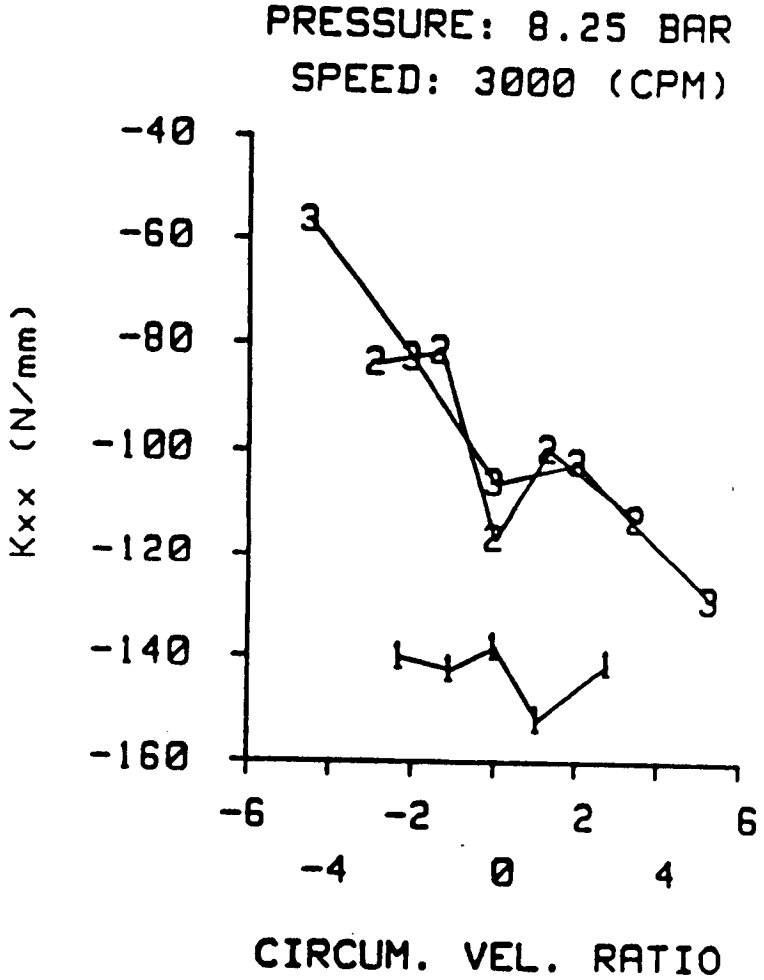

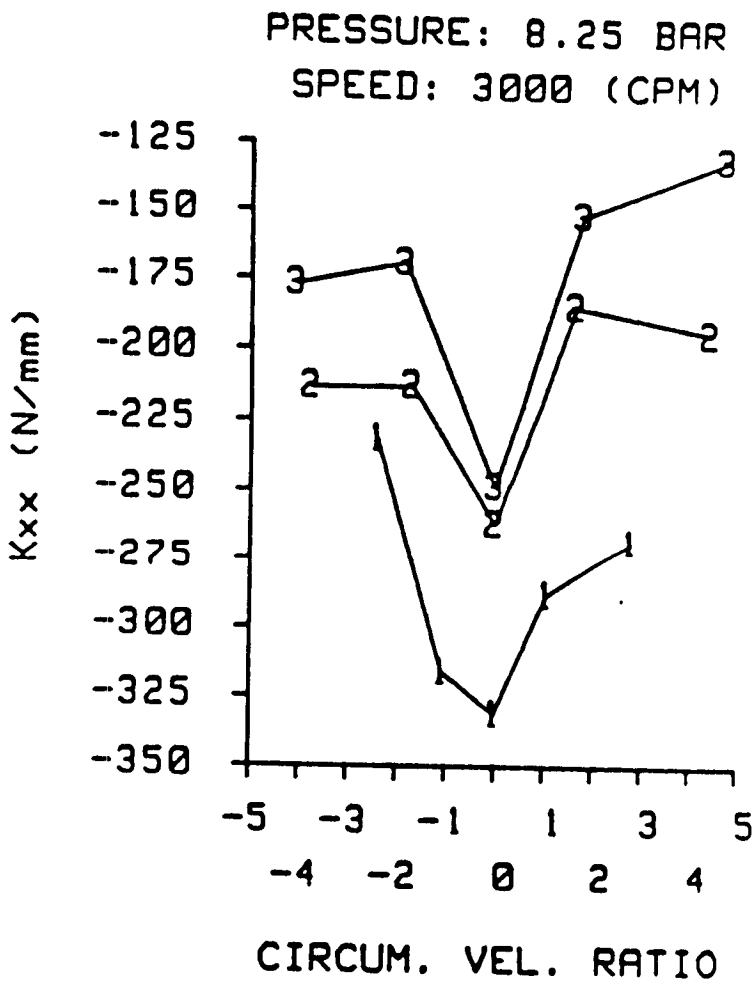

Fig. 46 Direct stiffness versus inlet circumferential velocity ratio at an inlet pressure of 8.25 bar and rotor speed of 3000 cpm. See table 5 for seal clearance definitions. Teeth-on-rotor (left), teeth-on-stator (right).

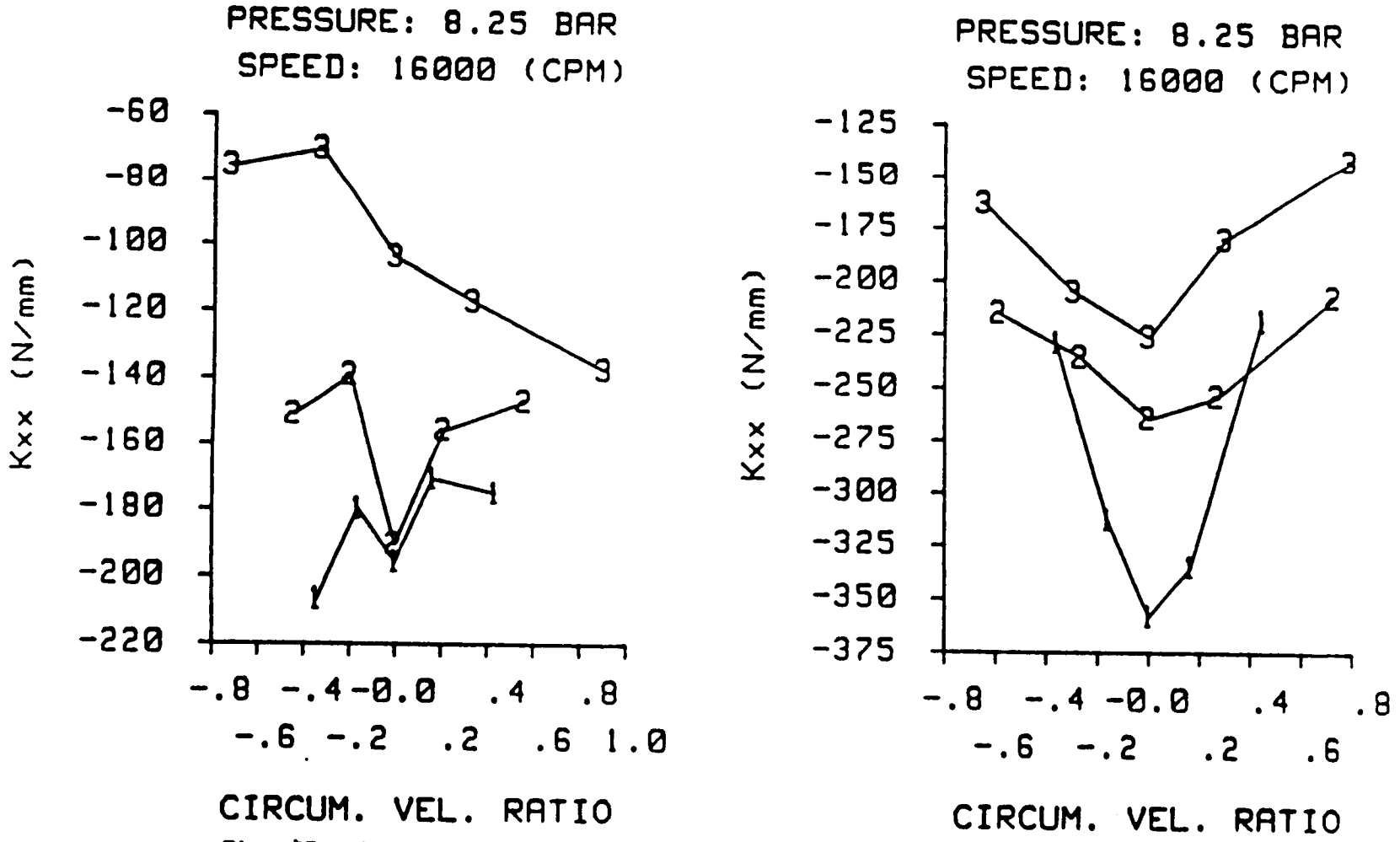

Fig. 47 Direct stiffness versus inlet circumferential velocity ratio at an inlet pressure of 8.25 bar and rotor speed of 16000 cpm. See table 5 for seal clearance definitions. Teeth-on-rotor (left), teeth-on-stator (right).

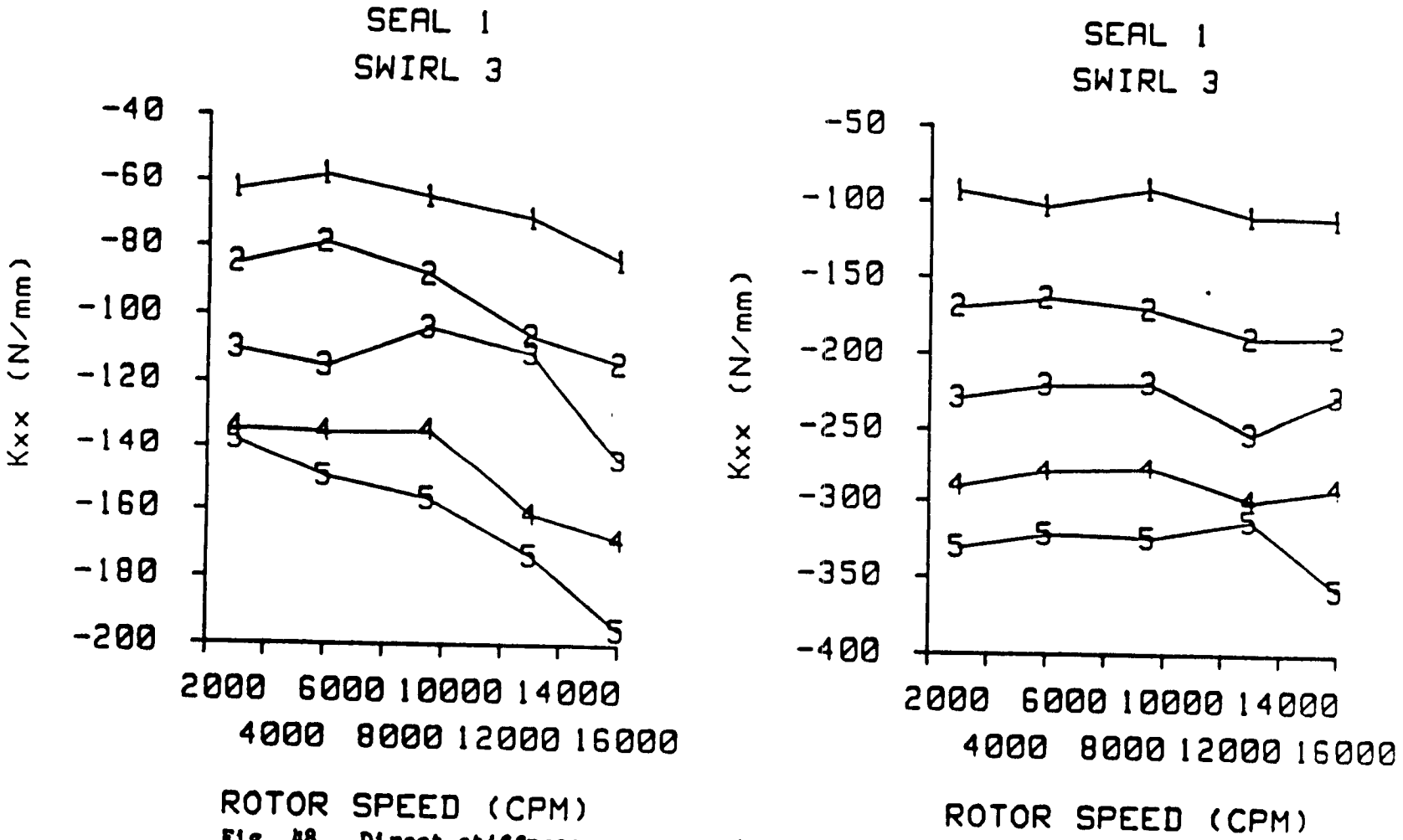

Fig. 48 Direct stiffness versus rotor speed for seal 1 and inlet circumferential velocity 3. See table 6 for pressure ratio definitions. Teeth-on-rotor (left), teeth-on-stator (right).

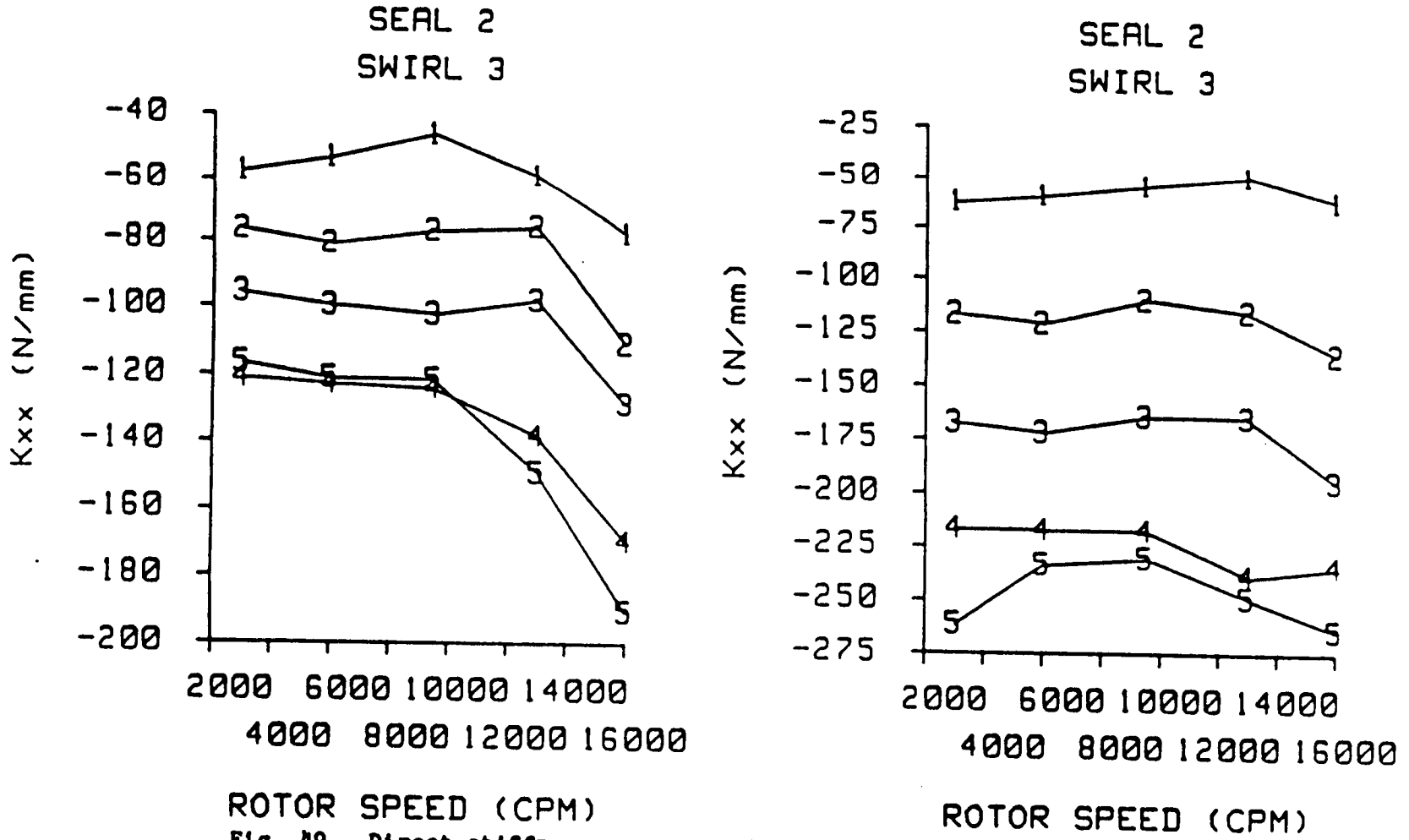

Fig. 49 Direct stiffness versus rotor speed for seal 2 and inlet circumferential velocity 3. See table 6 for pressure ratio definitions. Teeth-on-rotor (left), teeth-on-stator (right).

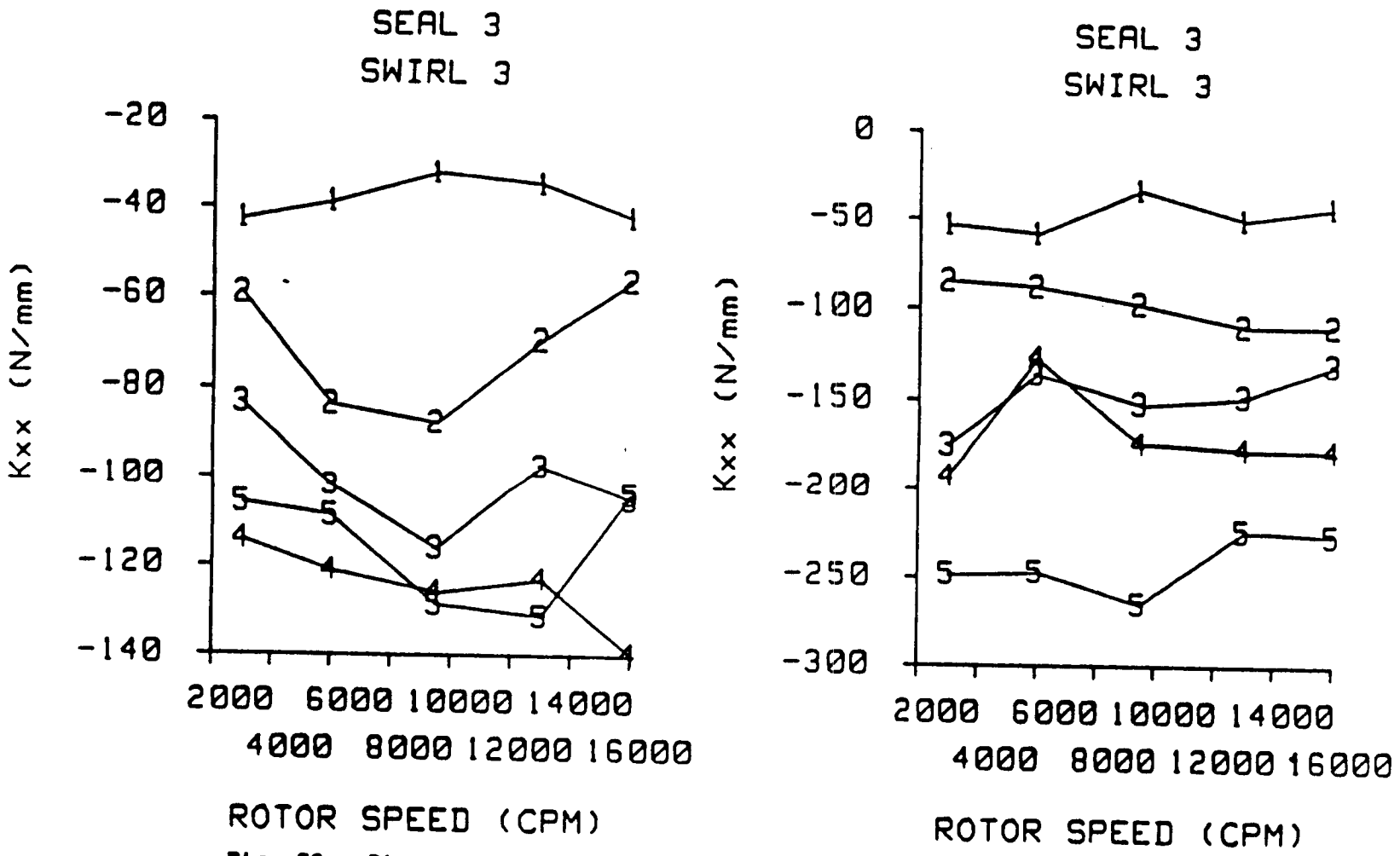

Fig. 50 Direct stiffness versus rotor speed for seal 3 and inlet circumferential velocity 3. See table 6 for pressure ratio definitions. Teeth-on-rotor (left), teeth-on-stator (right).

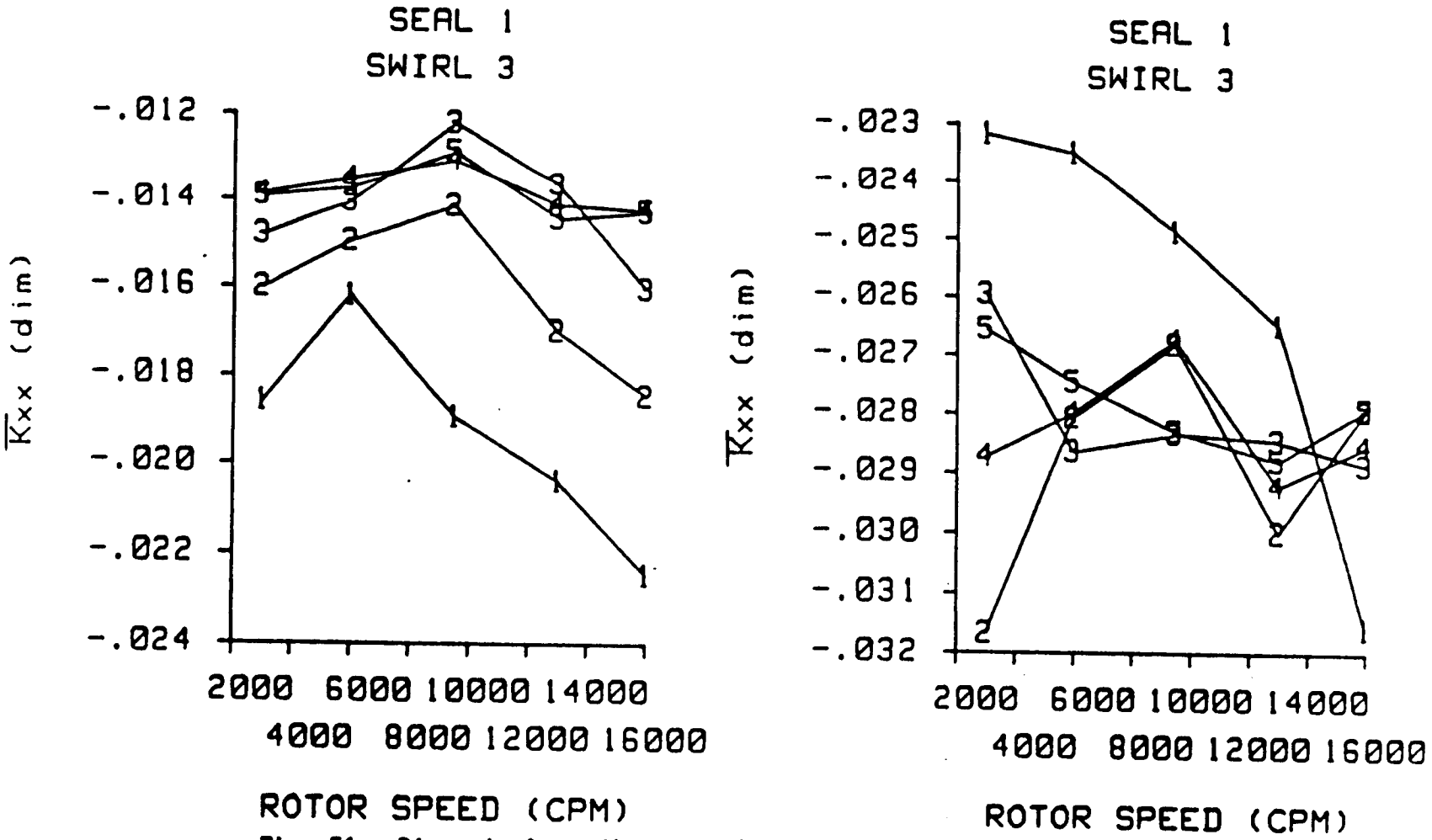

Fig. 51 Dimensionless direct stiffness versus rotor speed for seal 1 and inlet circumferential velocity 3. See table 6 for pressure ratio definitions. Teeth-on-rotor (left), teeth-on-stator (right).

CROSS-COUPLED STIFFNESS

Figures 52-55 show cross-coupled stiffness versus inlet circumferential velocity ratio for the radial clearances of table 5. The plots show, in all cases, that the cross-coupled stiffness is a somewhat linear function of inlet circumferential velocity ratio. The figures do not show any consistent trend with respect to radial seal clearance, for either teeth-on-rotor or teeth-on-stator seals. Figures 56-58 show cross-coupled stiffness versus rotor speed for the pressure ratios of table 6. The figures show that cross-coupled stiffness increases with increasing rotor speed, for the teeth-on-rotor seal, and decreases with increasing rotor speed for the teeth-on-stator seal. This effect was not evident in the results from the low speed test rig. The dimensionless cross-coupled stiffness coefficient, defined in table 8, removes the effect of change of clearance due to rotor growth. Figure 59 shows dimensionless cross-coupled stiffness versus rotor speed for seal 1 for the pressure ratios of table 6 and inlet circumferential velocity 5. The figure shows that cross-coupled stiffness increases for increasing rotor speed, for the teeth-on-rotor seal, and decreases with increasing rotor speed for the teeth-on-stator seal. The decrease in cross-coupled stiffness with rotor speed, for a teeth-on-stator seal, was also evident in tests of an 11 cavity seal for Sulzer [50] and in the steam tests of 1-3 cavity seals by Hisa et al. [8]. Associated cross-coupled stiffness plots can be found in Appendix D.

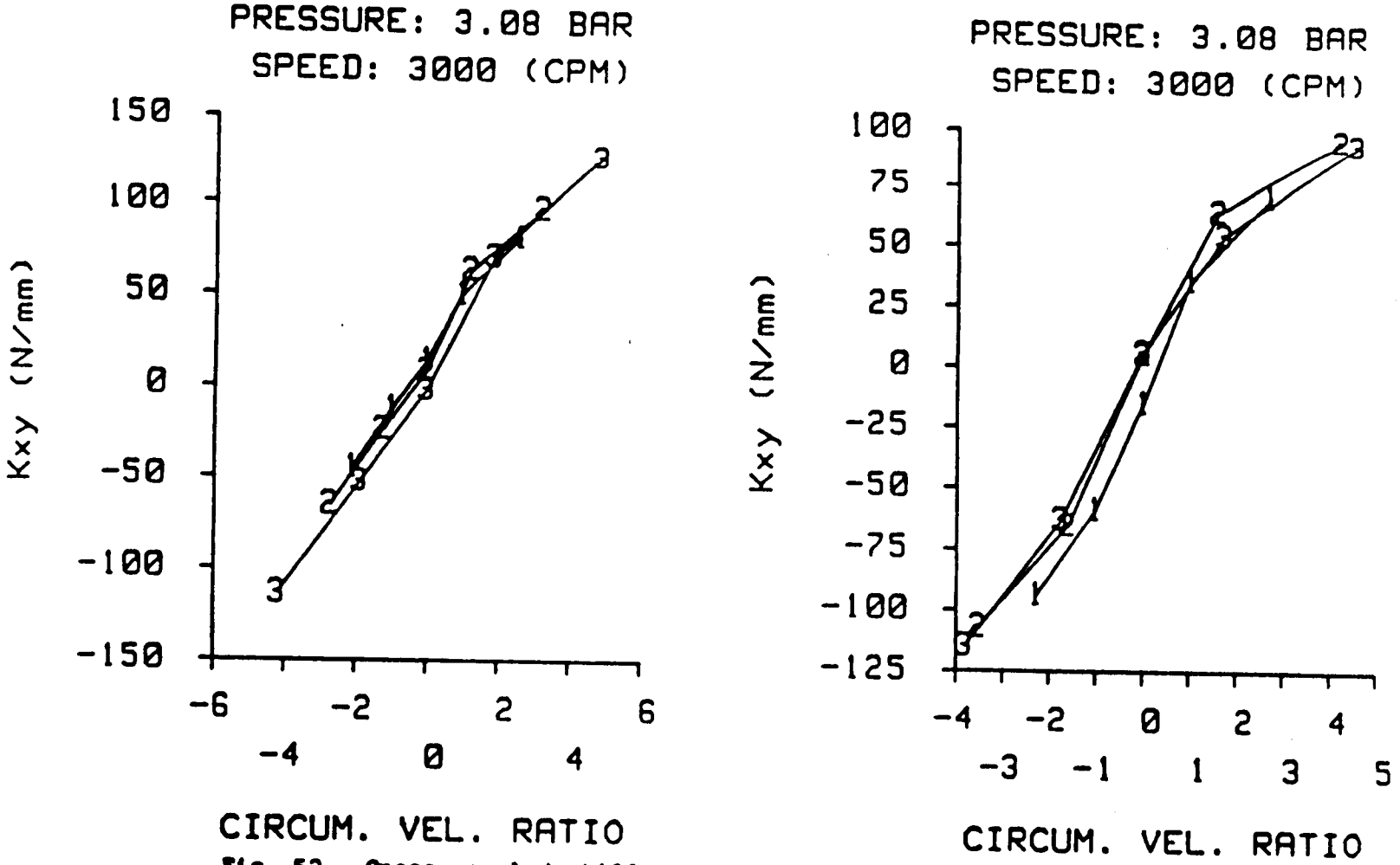

Fig. 52 Cross-coupled stiffness versus inlet circumferential velocity ratio at an inlet pressure of 3.08 bar and rotor speed of 3000 cpm. See table 5 for seal clearance definitions. Teeth-on-rotor (left), teeth-on-stator (right).

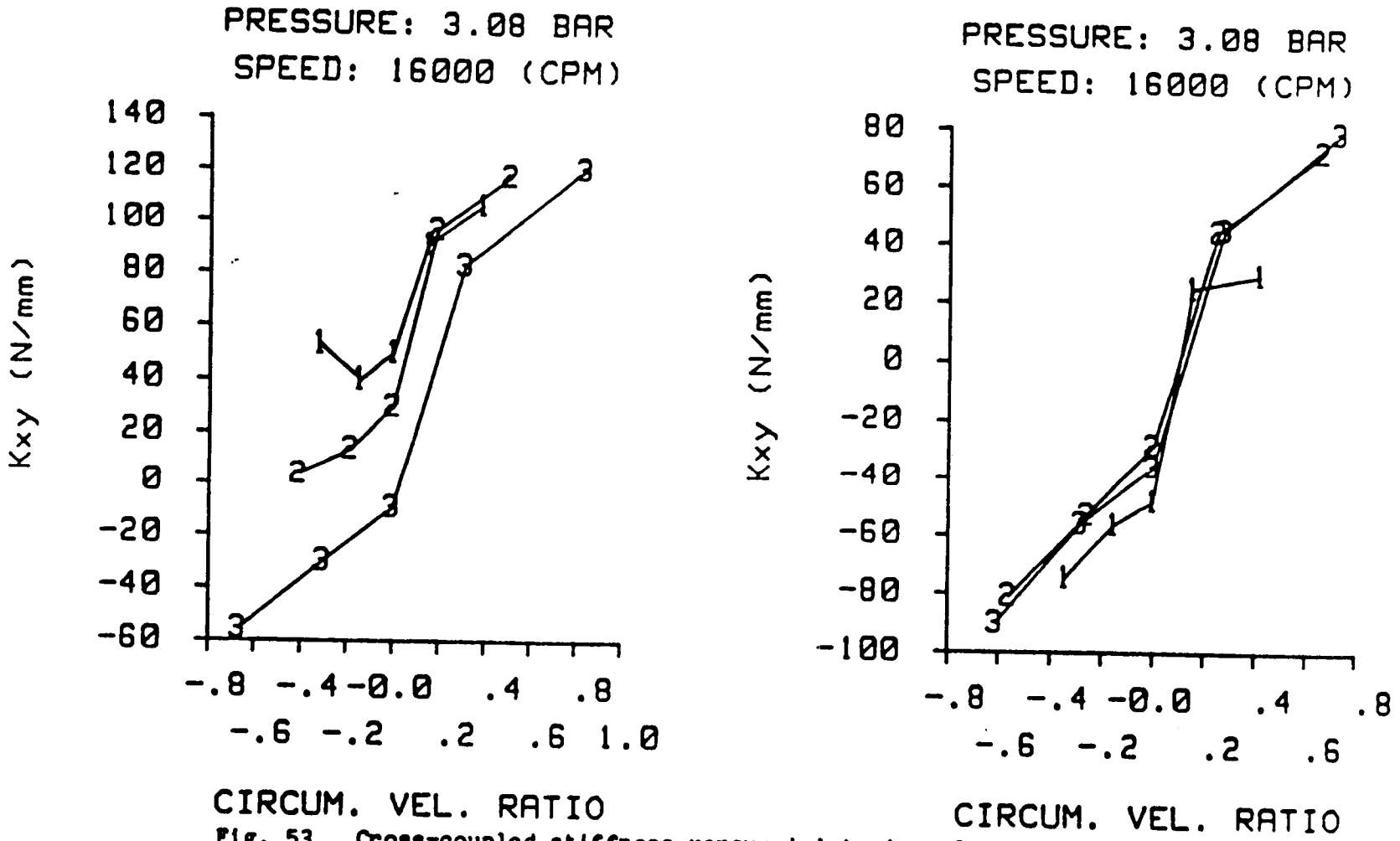

Fig. 53 Cross-coupled stiffness versus inlet circumferential velocity ratio at an inlet pressure of 3.08 bar and rotor speed of 16000 cpm. See table 5 for seal clearance definitions. Teeth-on-rotor (left), teeth-on-stator (right).

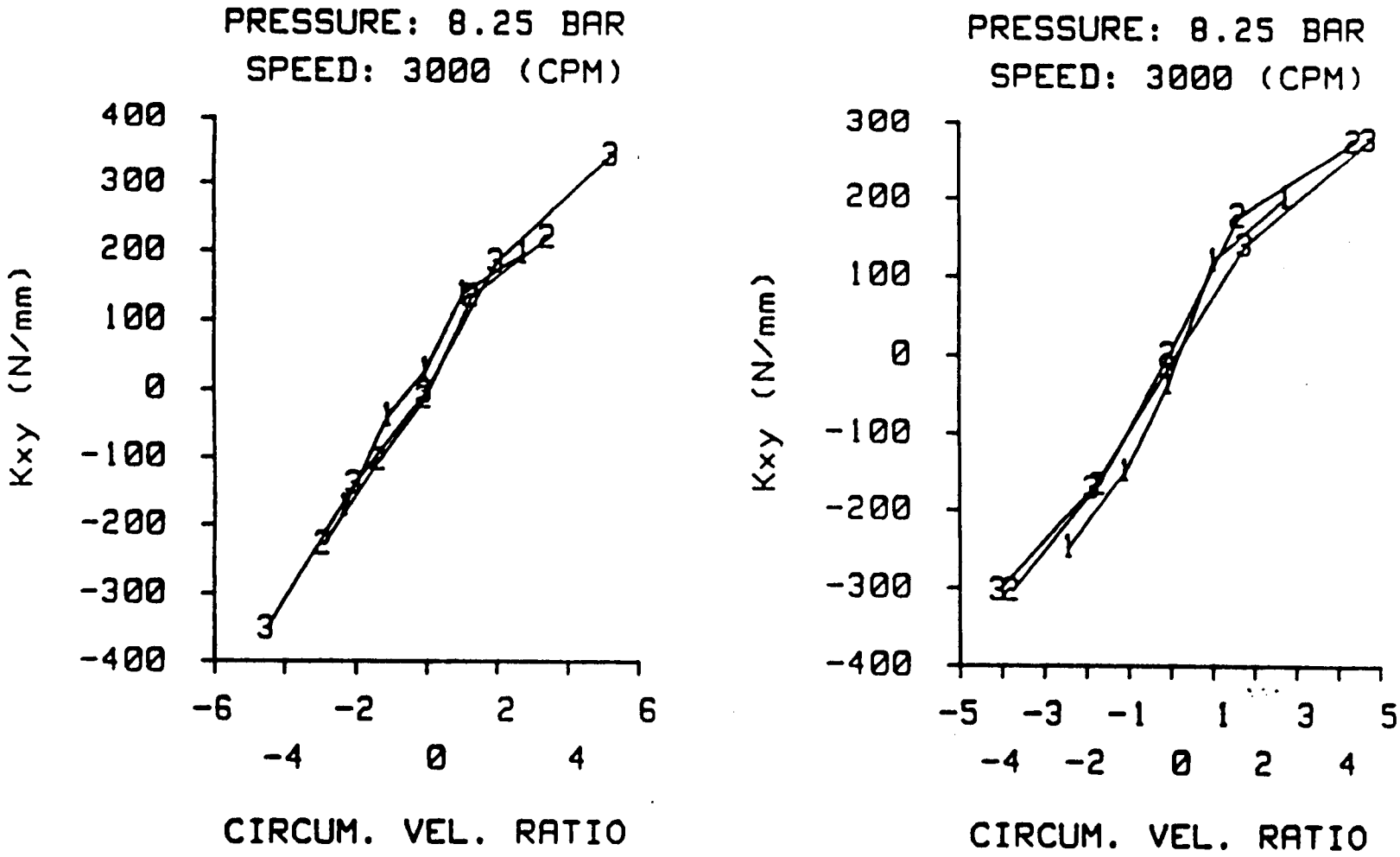

Fig. 54 Cross-coupled stiffness versus inlet circumferential velocity ratio at an inlet pressure of 8.25 bar and rotor speed of 3000 cpm. See table 5 for seal clearance definitions. Teeth-on-rotor (left), teeth-on-stator (right).

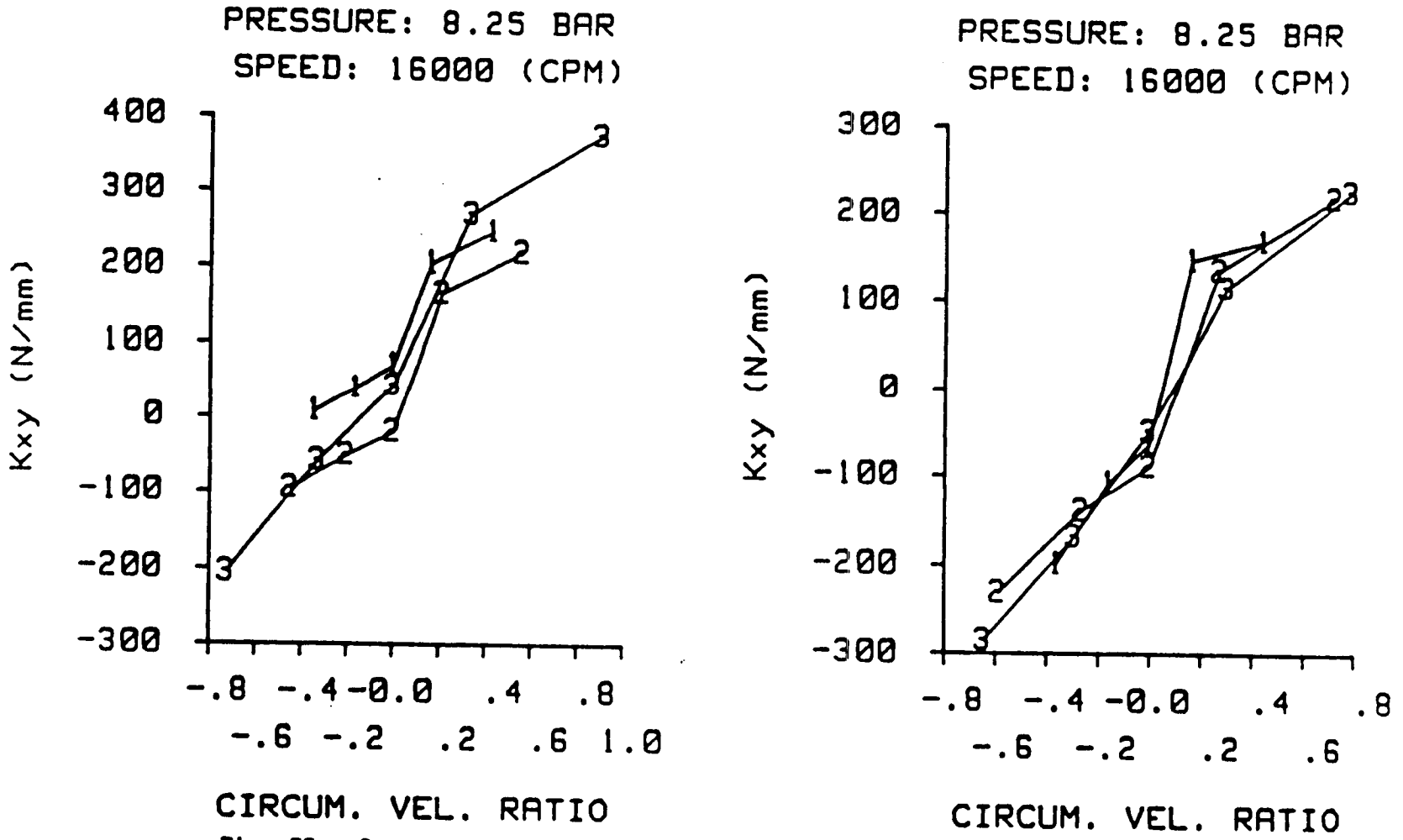

Fig. 55 Cross-coupled stiffness versus inlet circumferential velocity ratio at an inlet pressure of 8.25 bar and rotor speed of 16000 cpm. See table 5 for seal clearance definitions. Teeth-on-rotor (left), teeth-on-stator (right).

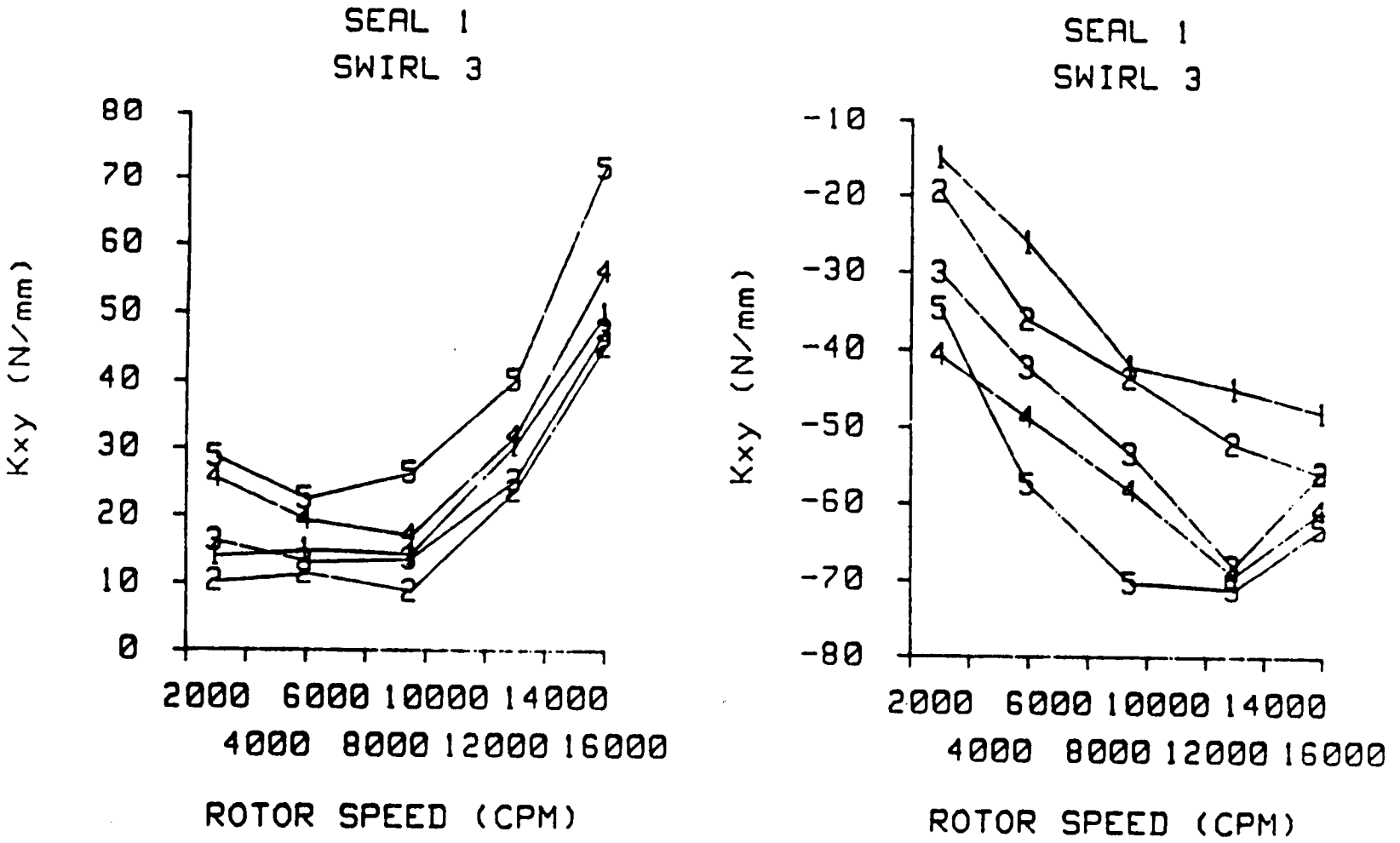

Fig. 56 Cross-coupled stiffness versus rotor speed for seal 1 and inlet circumferential velocity 3. See table 6 for pressure ratio definitions. Teeth-on-rotor (left), teeth-on-stator (right).

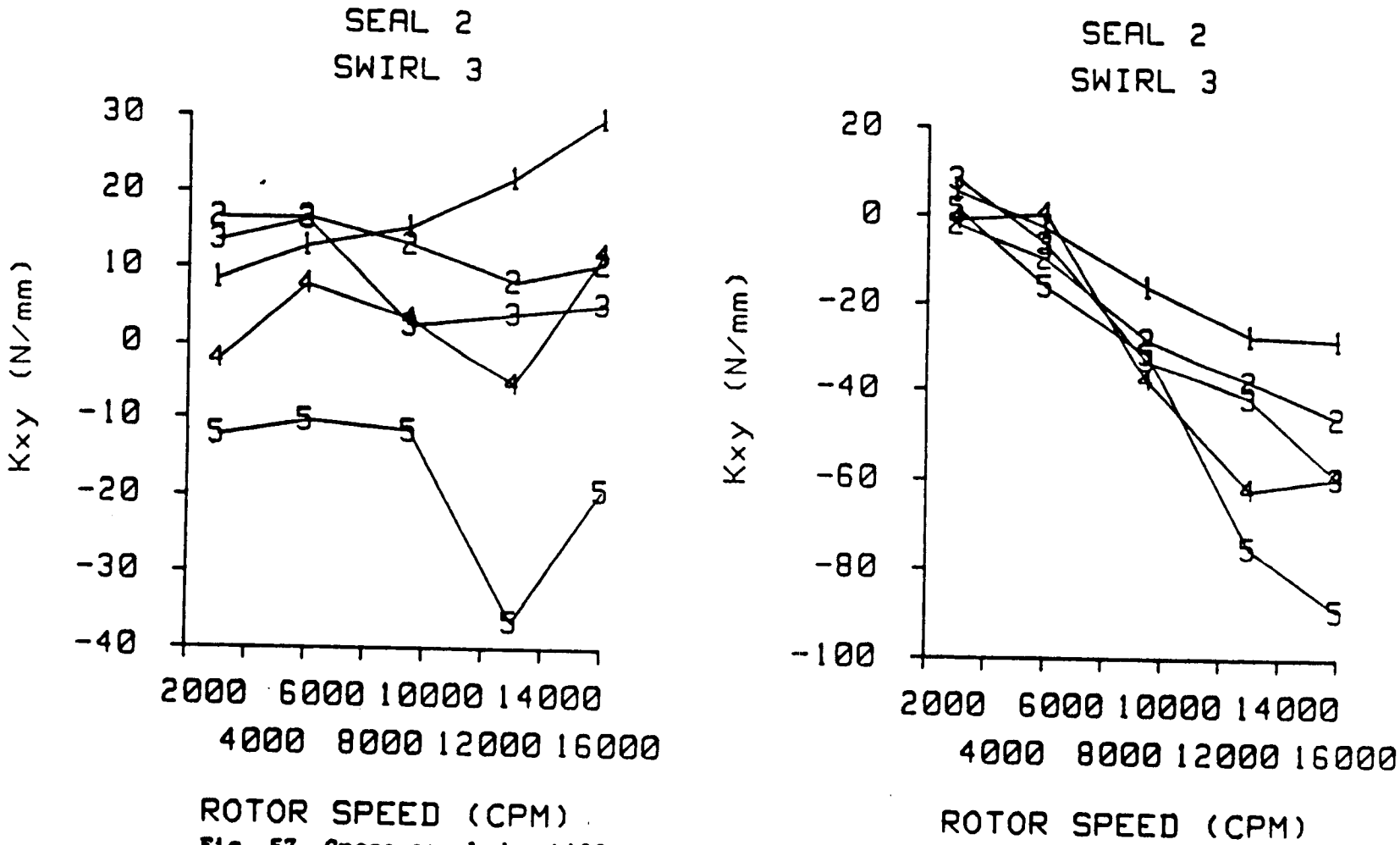

Fig. 57 Cross-coupled stiffness versus rotor speed for seal 2 and inlet circumferential velocity 3. See table 6 for pressure ratio definitions. Teeth-on-rotor (left), teeth-on-stator (right).

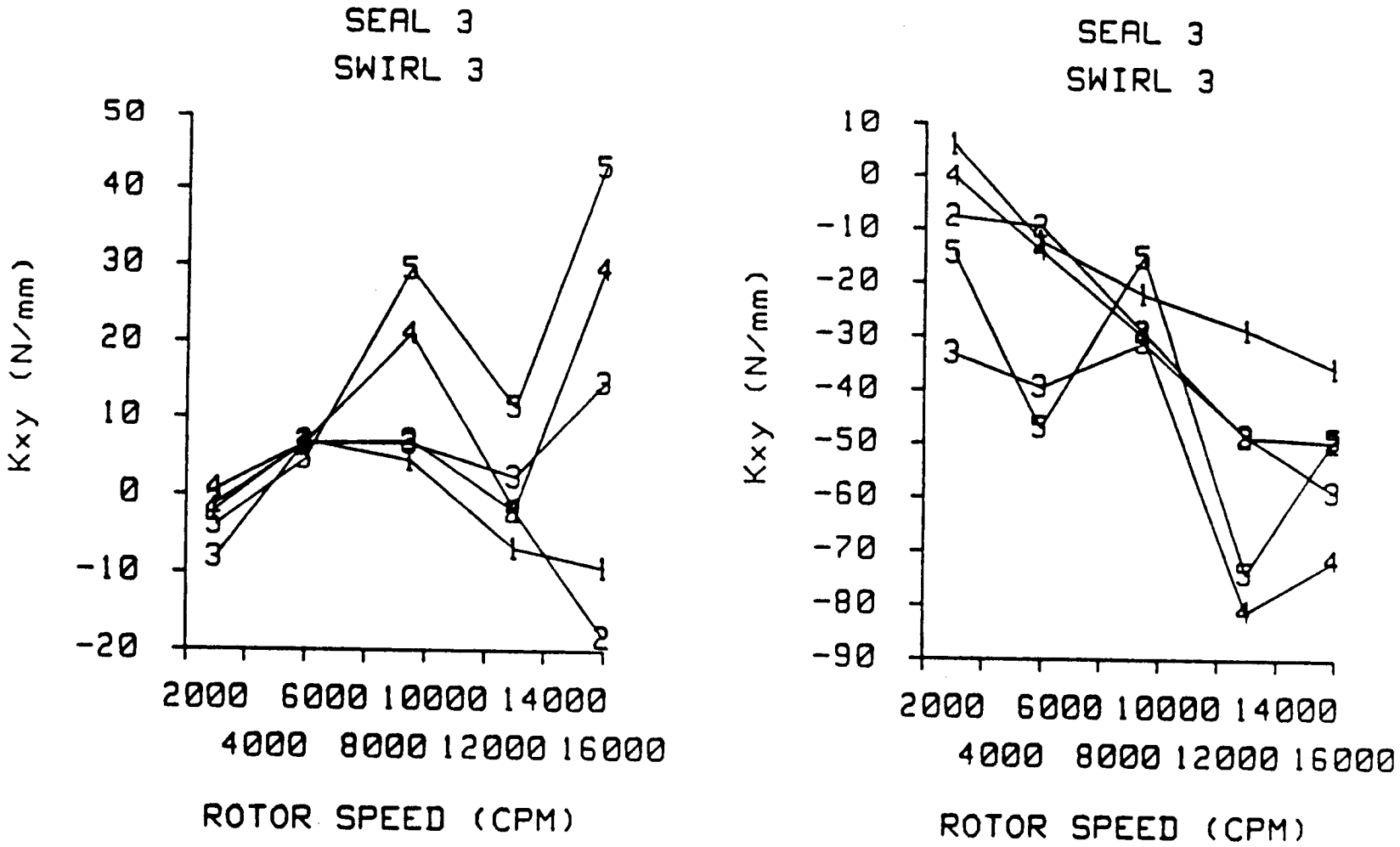

Fig. 58 Cross-coupled stiffness versus rotor speed for seal 3 and inlet circumferential velocity 3. See table 6 for pressure ratio definitions. Teeth-on-rotor (left), teeth-on-stator (right).

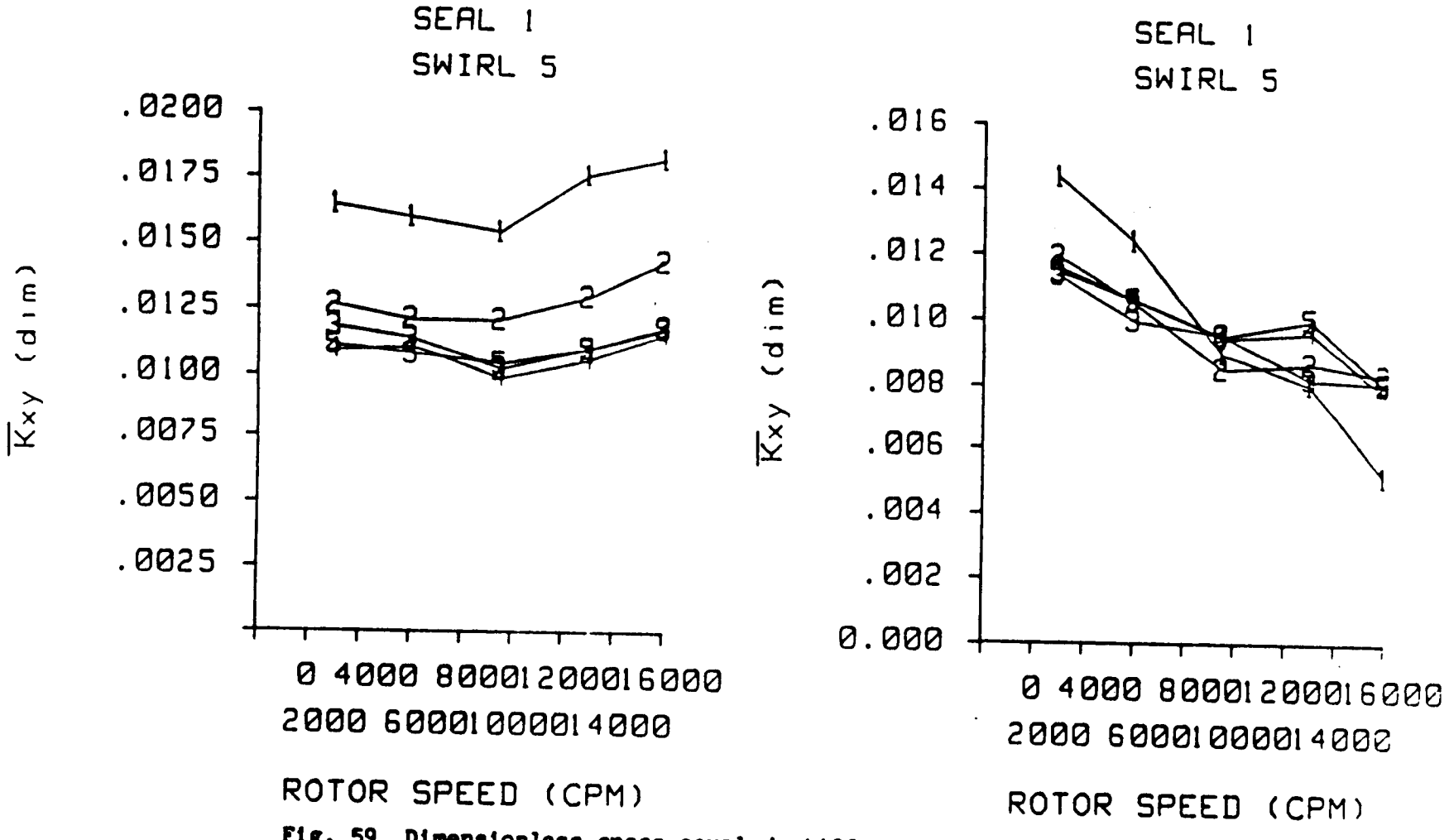

Fig. 59 Dimensionless cross-coupled stiffness versus rotor speed for seal 1 and inlet circumferential velocity 5. See table 6 for pressure ratio definitions. Teeth-on-rotor (left), teeth-on-stator (right).

DIRECT DAMPING

Figures 60-63 show the direct damping versus inlet circumferential velocity ratio for the radial seal clearances of table 4. The data show that the direct damping for a teeth-on-rotor seal increases as clearance is increased while the direct damping for a teeth-on-stator seal decreases as clearance is increased. Figures 64-66 show direct damping versus rotor speed for the pressure ratios of table 6 and inlet circumferential velocity 3. These figures show that the direct damping increases slightly as rotor speed increases, for teeth-on-rotor seals, and decreases slightly as rotor speed increases for teeth-on-stator seals. These results are deceiving, since direct damping is very sensitive to clearance change. The normalized direct damping coefficient, defined in table 8, removes the effects of clearance change due to rotor growth. Figure 67 shows normalized direct damping versus rotor speed for seal 1 for the pressure ratios of table 6 and inlet circumferential velocity 3. This figure shows that direct damping decreases as rotor speed increases for both teeth-on-rotor and teeth-on-stator seals. The result for normalized direct damping versus rotor speed for the teeth-on-rotor seal is inconsistent with the dimensional data. If dimensional direct damping, for a teeth-on-rotor seal, decreases as clearance decreases and increases as rotor speed increases then the normalized value should increase as rotor speed increases because the seal clearance decreases as rotor speed increases. This inconsistency is not readily explainable. Associated direct damping plots can be found in Appendix D.

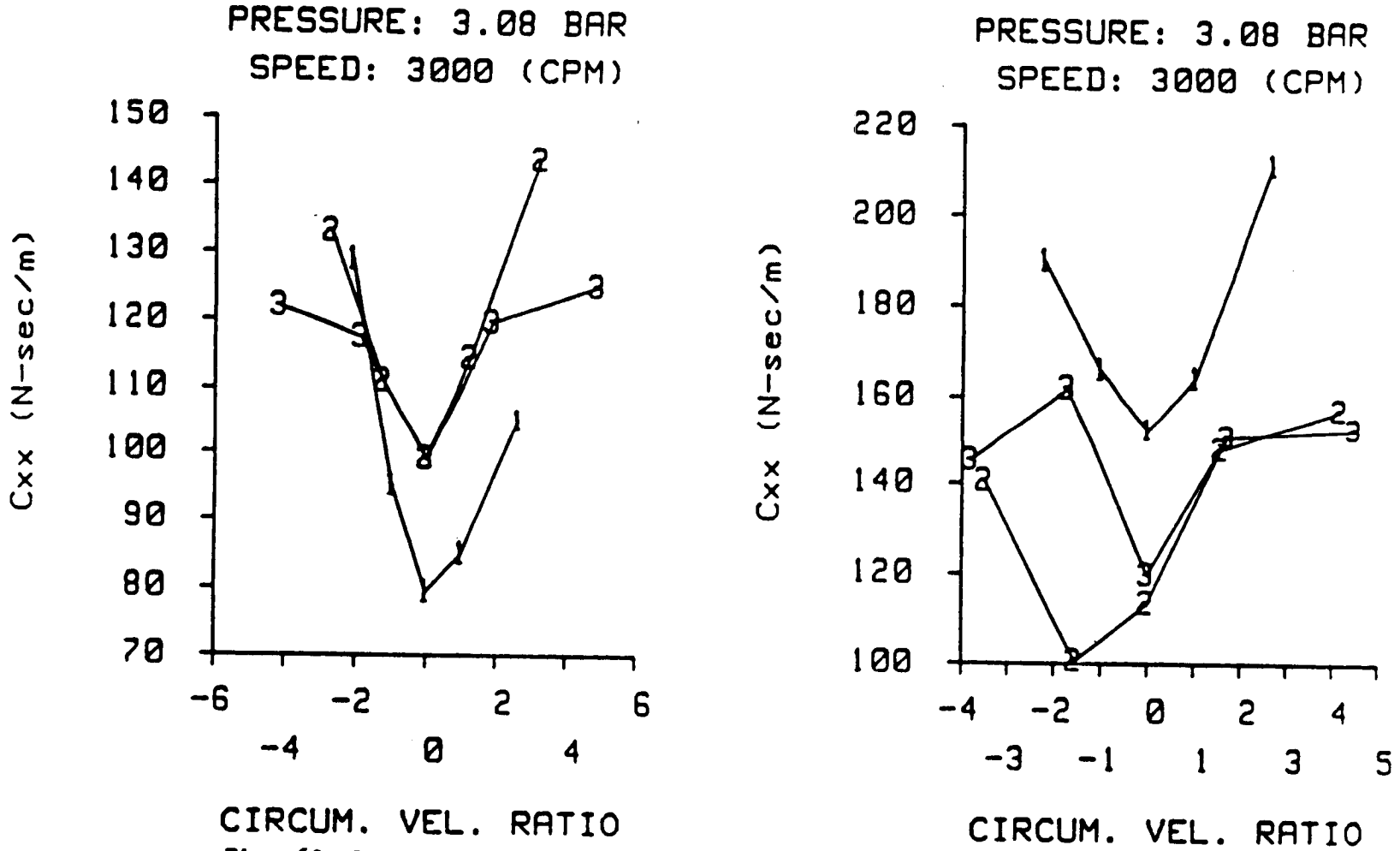

Fig. 60 Direct damping versus inlet circumferential velocity ratio at an inlet pressure of 3.08 bar and rotor speed of 3000 cpm. See table 5 for seal clearance definitions. Teeth-on-rotor (left), teeth-on-stator (right).

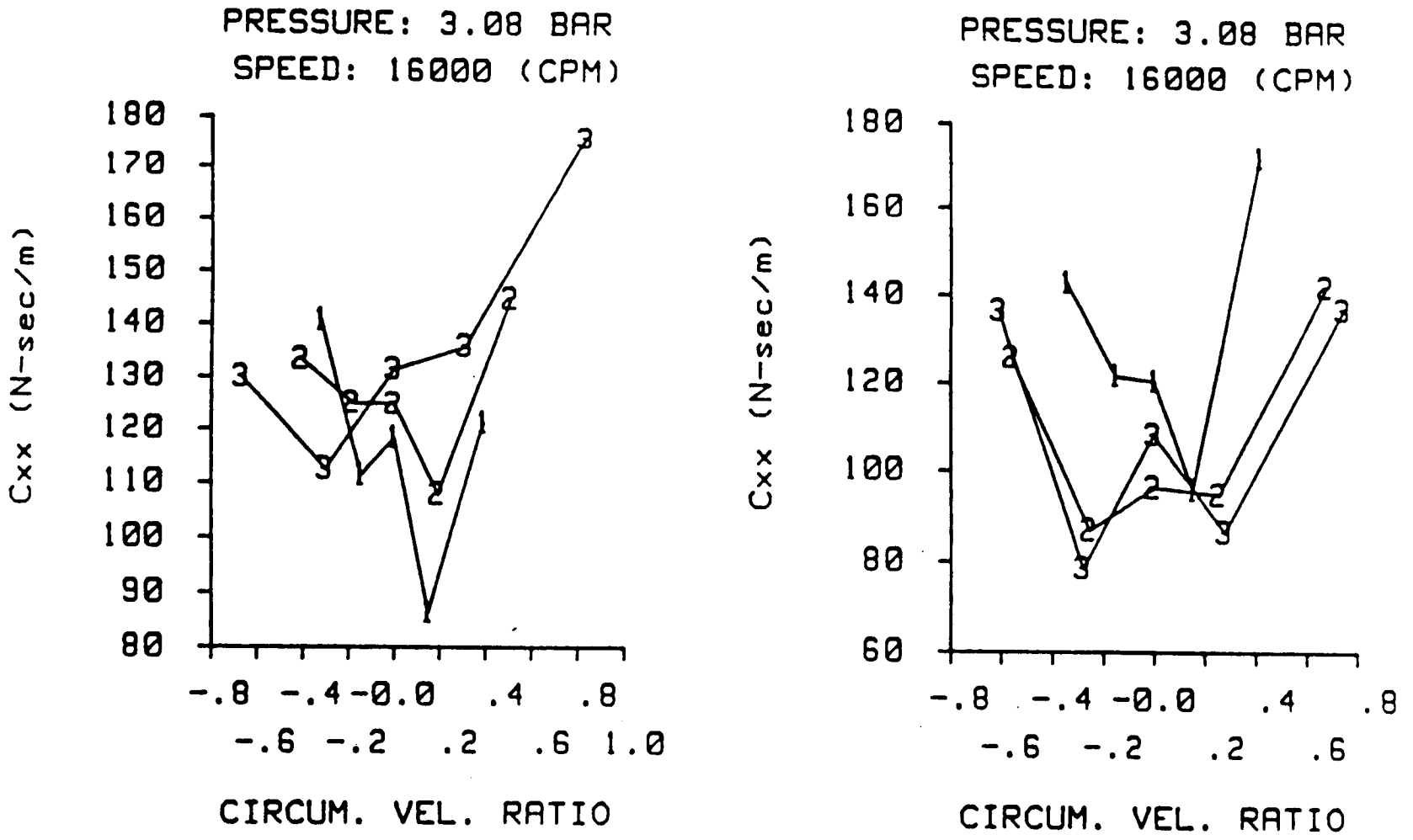

Fig. 61 Direct damping versus inlet circumferential velocity ratio at an inlet pressure of 3.08 bar and rotor speed of 16000 cpm. See table 5 for seal clearance definitions. Teeth-on-rotor (left), teeth-on-stator (right).

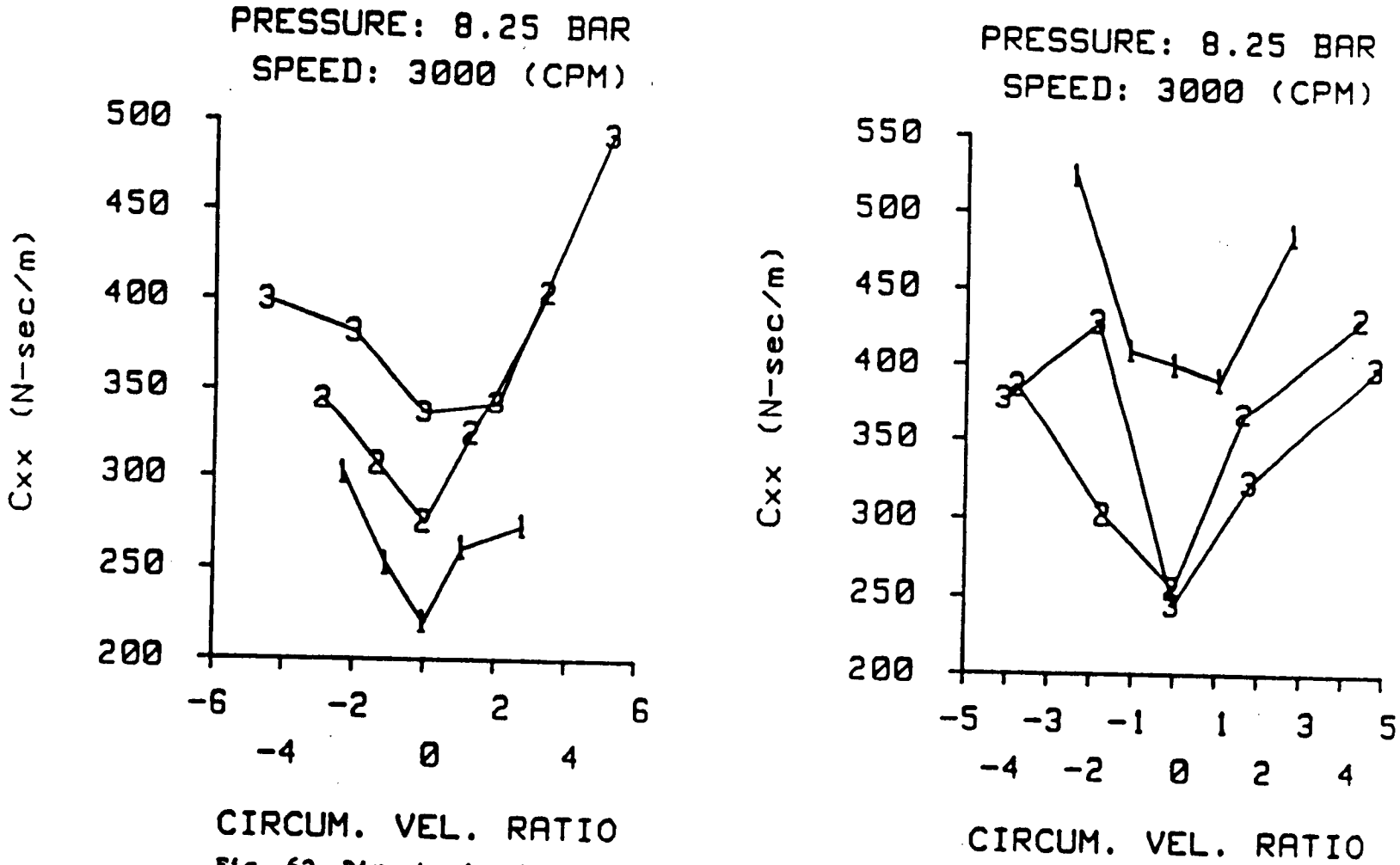

Fig. 62 Direct damping versus inlet circumferential velocity ratio at an inlet pressure of 8.25 bar and rotor speed of 3000 cpm. See table 5 for seal clearance definitions. Teeth-on-rotor (left), teeth-on-stator (right).

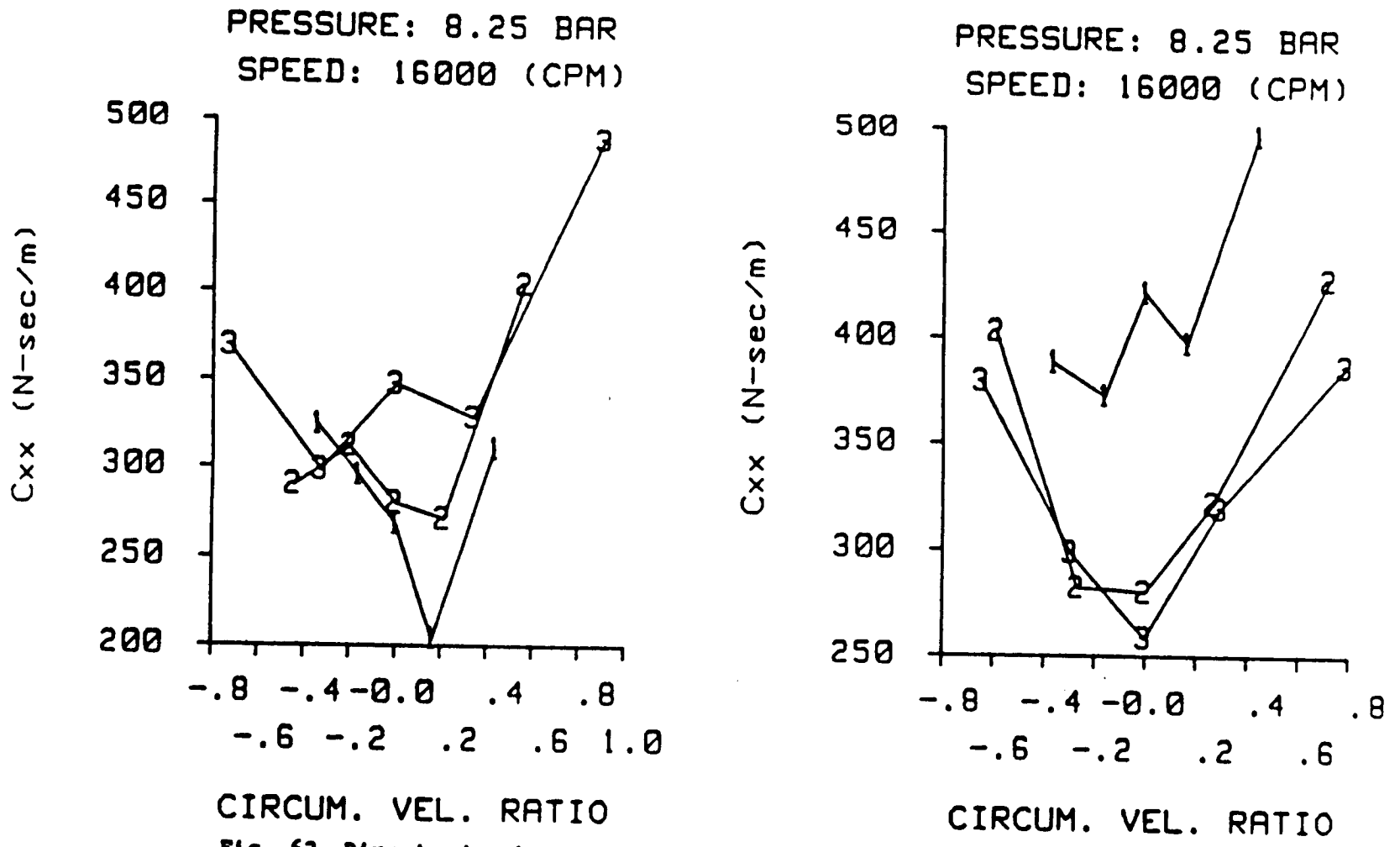

Fig. 63 Direct damping versus inlet circumferential velocity ratio at an inlet pressure of 8.25 bar and rotor speed of 16000 cpm. See table 5 for seal clearance definitions. Teeth-on-rotor (left), teeth-on-stator (right).

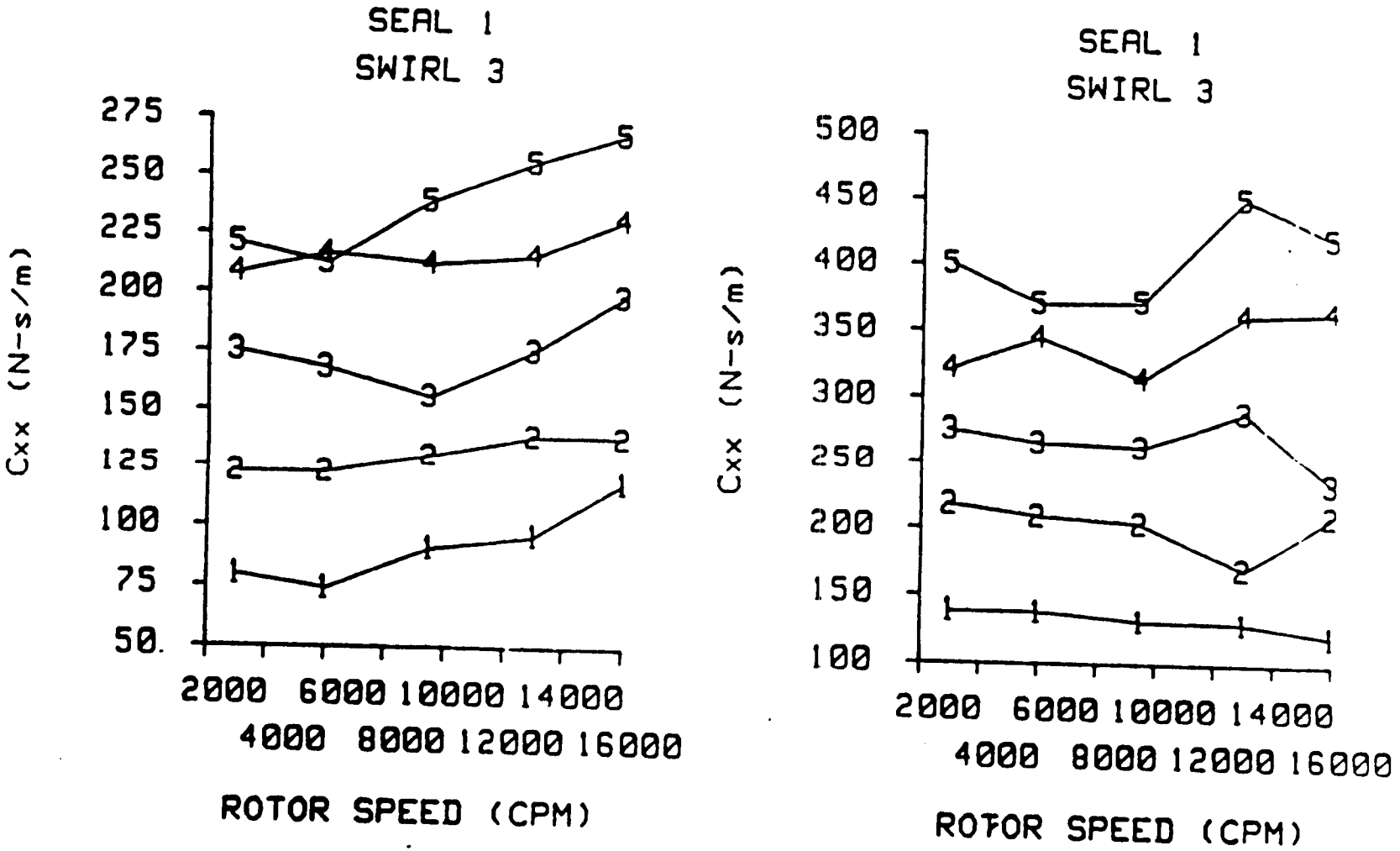

Fig. 64 Direct damping versus rotor speed for seal 1 and inlet circumferential velocity 3. See table 6 for pressure ratio definitions. Teeth-on-rotor (left), teeth-on-stator (right).

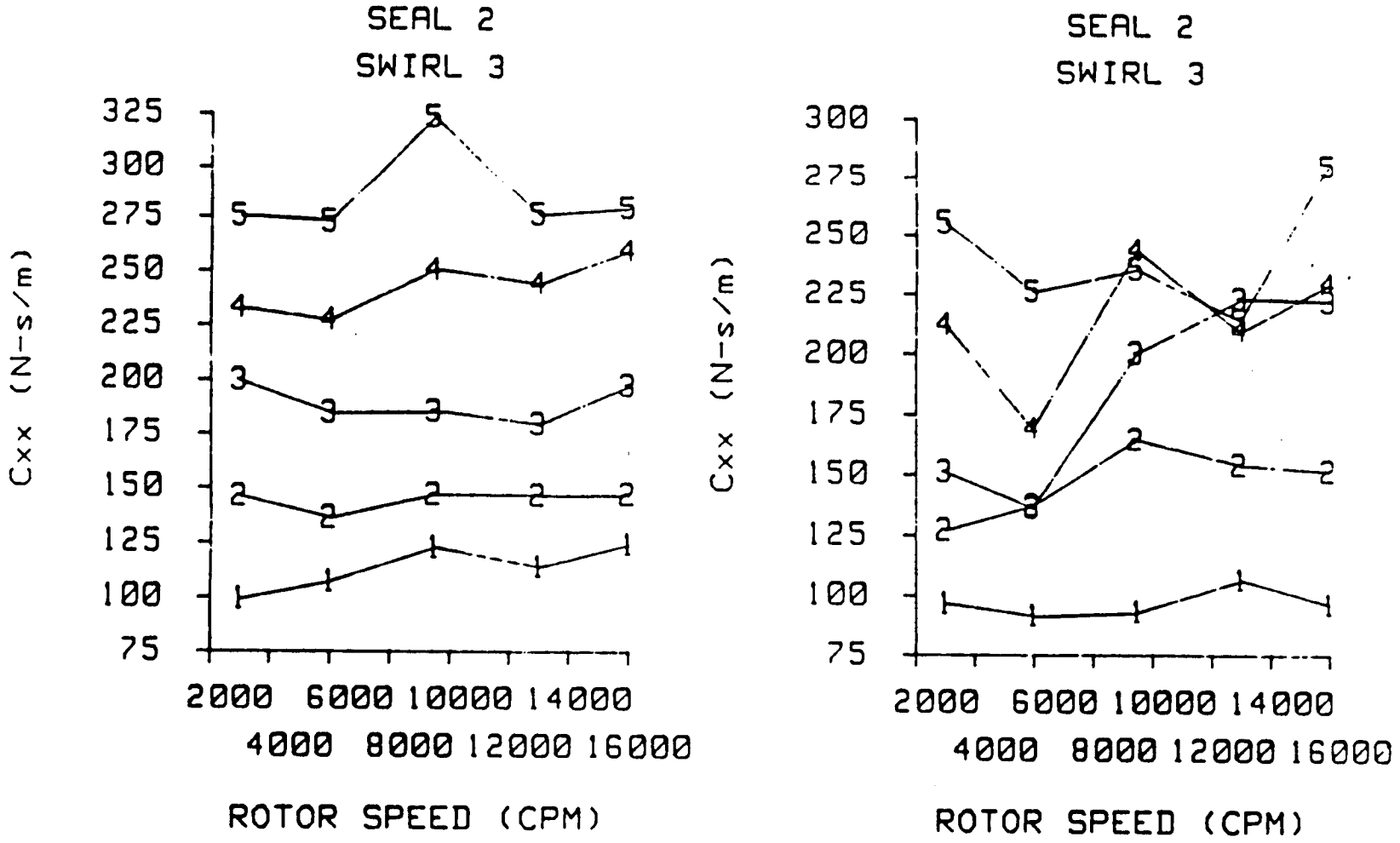

Fig. 65 Direct damping versus rotor speed for seal 2 and inlet circumferential velocity 3. See table 6 for pressure ratio definitions. Teeth-on-rotor (left), teeth-on-stator (right).

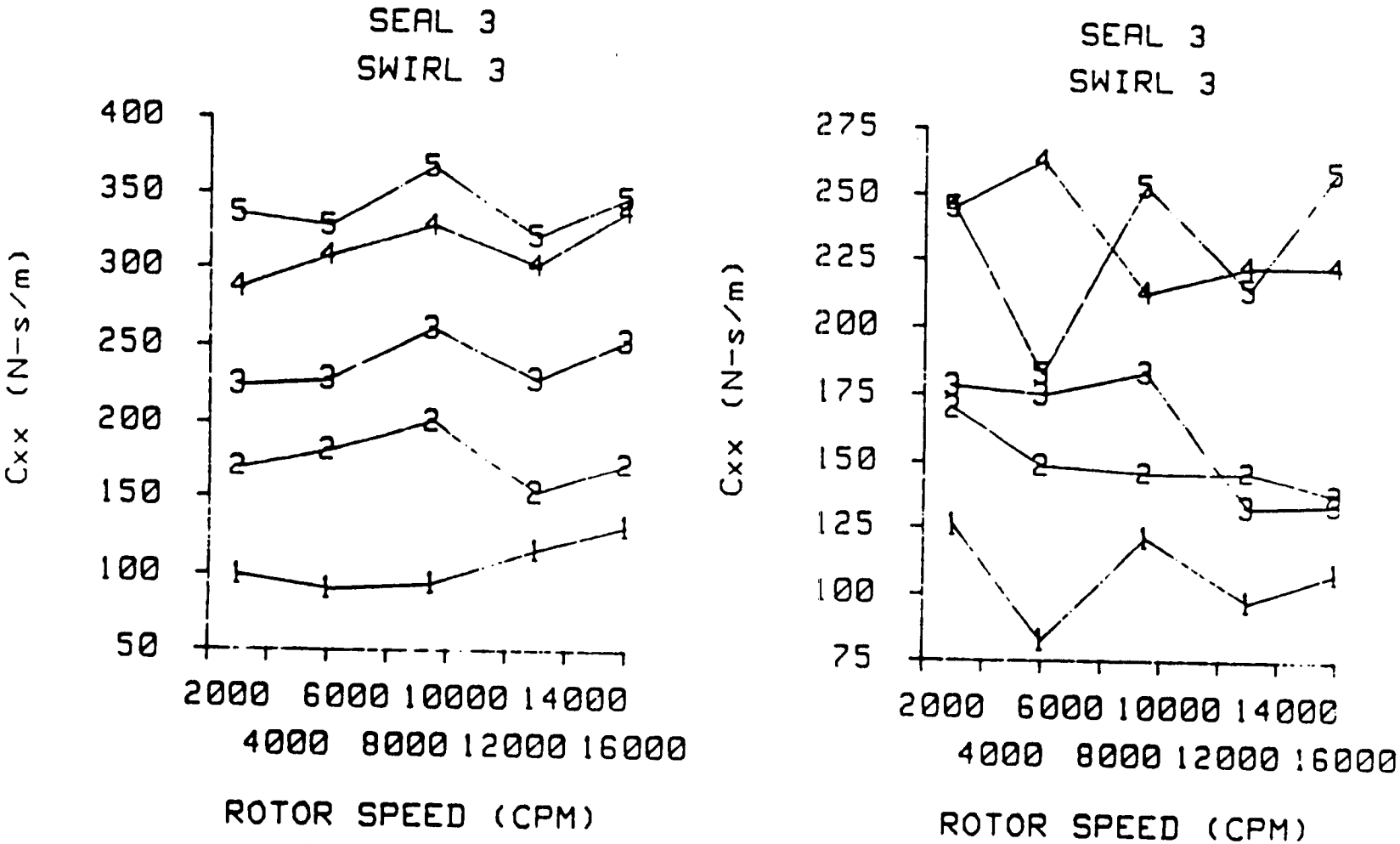

Fig. 66 Direct damping versus rotor speed for seal 3 and inlet circumferential velocity 3. See table 6 for pressure ratio definitions. Teeth-on-rotor (left), teeth-on-stator (right).

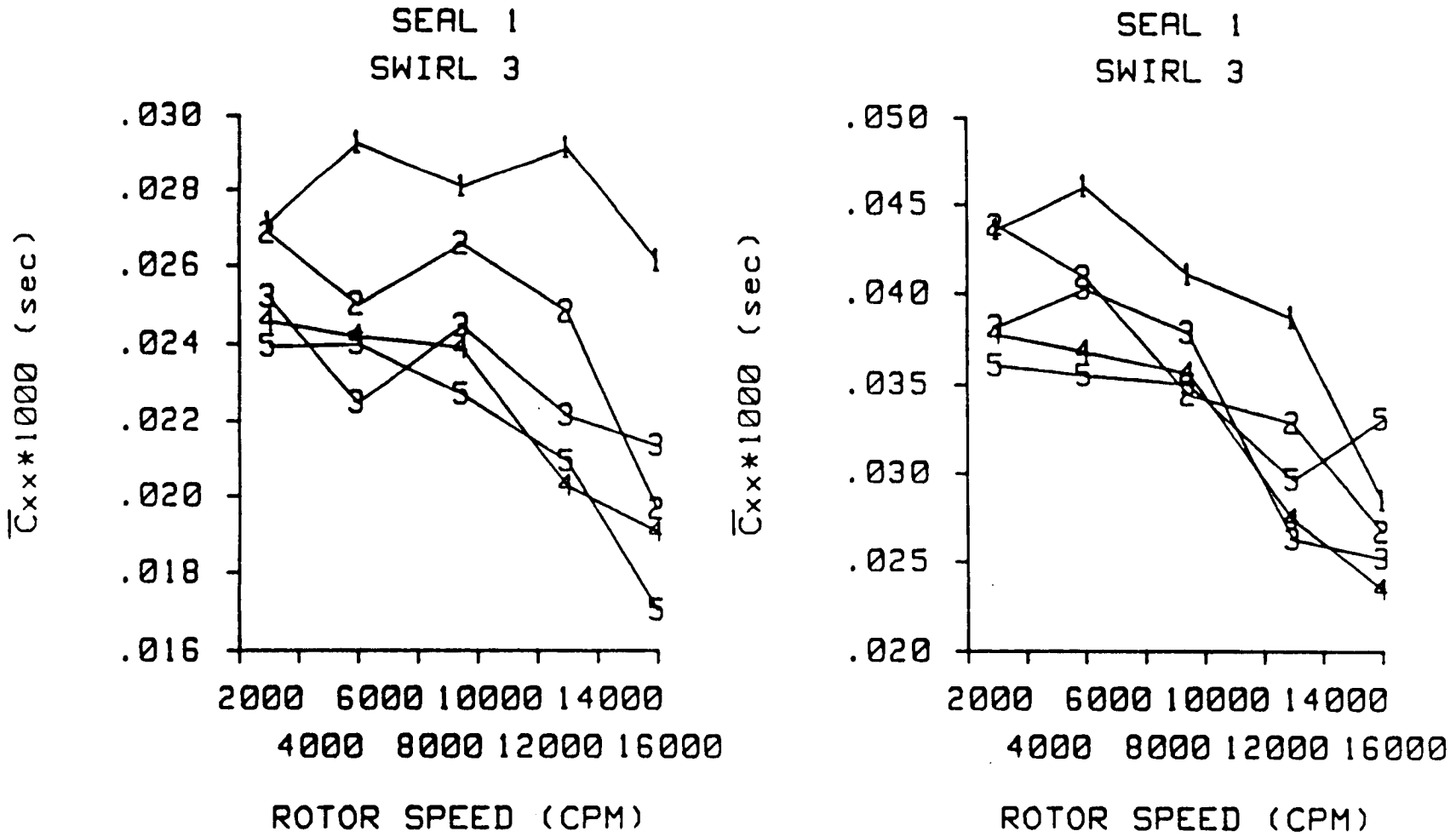

Fig. 67 Normalized direct damping versus rotor speed for seal 1 and inlet circumferential velocity 3. See table 6 for pressure ratio definitions. Teeth-on-rotor (left), teeth-on-stator (right).

STABILITY ANALYSIS

One further parameter of comparison among the test seals is the dimensionless whirl frequency ratio. To understand the value of this parameter, consider a rotor in a circular orbit of amplitude A and frequency ω (Fig. 68). The X and Y components of force in the seal model of equation (79) may be resolved into radial and tangential forces

$$F_r = F_X \cos \omega t + F_Y \sin \omega t$$

$$F_t = -F_X \sin \omega t + F_Y \cos \omega t$$

Expressing the rotor motion as

$$X = A \cos \omega t \qquad \dot{X} = -A\omega \sin \omega t$$

$$Y = A \sin \omega t \qquad \dot{Y} = A\omega \cos \omega t$$

and using equation (79), the resultant radial and tangential forces are illustrated in the figure and are defined by

$$-F_r/A = K + c\omega$$

$$F_t/A = k - C\omega$$

If F_t/A is a positive quantity, the tangential force is destabilizing since it supports the whirling motion of a forward whirling rotor. Conversely, of F_t/A is negative, it opposes the whirling motion of a forward whirling rotor, and is therefore stabilizing. The whirl frequency ratio is defined by

$$\text{Whirl frequency ratio} = k/C\omega \ .$$

From the above discussion, if the whirl ratio is less than one, the tangential force on the rotor is stabilizing. A minimum value of the whirl frequency ratio is optimum for stability.

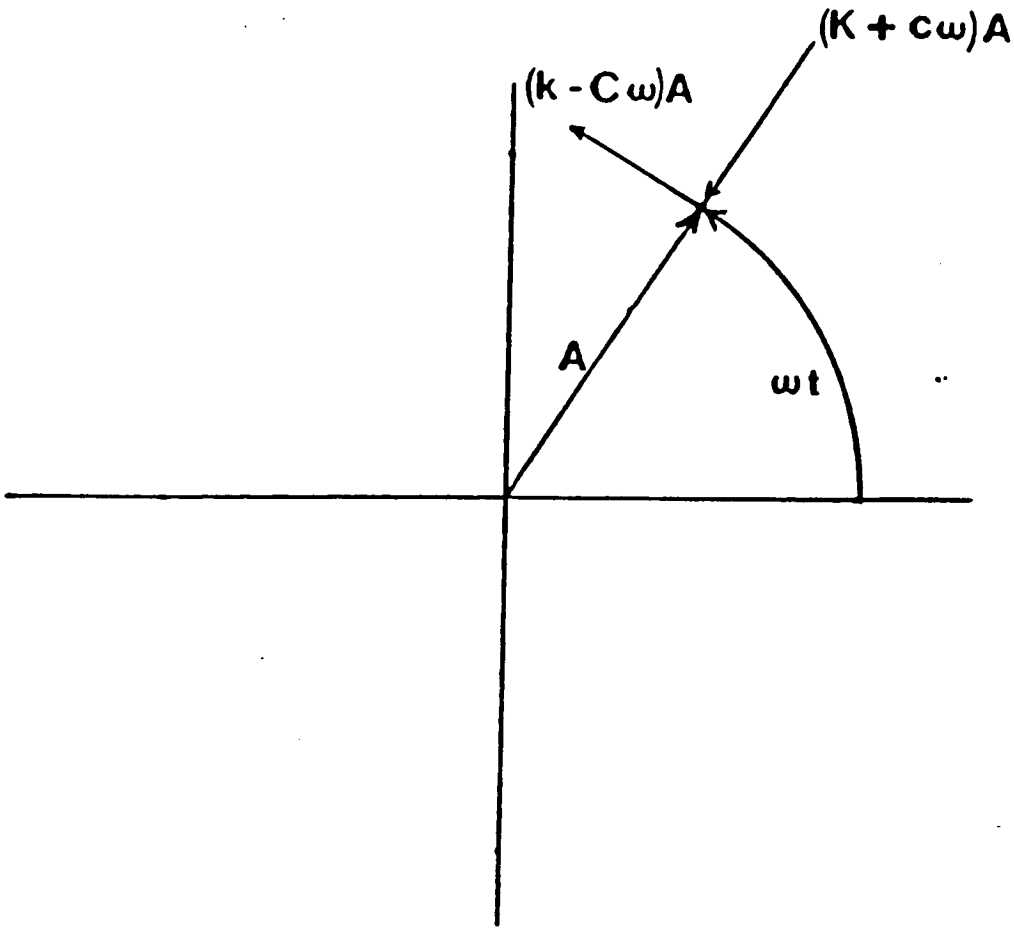

Fig. 68 Forces on a synchronously precessing seal.

Figures 69 and 70 show the whirl frequency ratios at a running speed of 16000 cpm and a shake frequency of 74.6 Hz. For teeth-on-rotor seals, the figures show that as clearance increases the seal becomes more stable. For teeth-on-stator seals the opposite is true; as clearance increases the seal becomes less stable, for the positive inlet circumferential velocity case. The figures also show that the teeth-on-stator seals are more stable than the teeth-on-rotor seals for positive inlet circumferential velocity ratio, as was found previously [6]. Figure 71 shows the whirl frequency ratio versus rotor speed for the seals of table 5. The figure shows that as speed increases, both the teeth-on-rotor and teeth-on-stator seals become more stable.

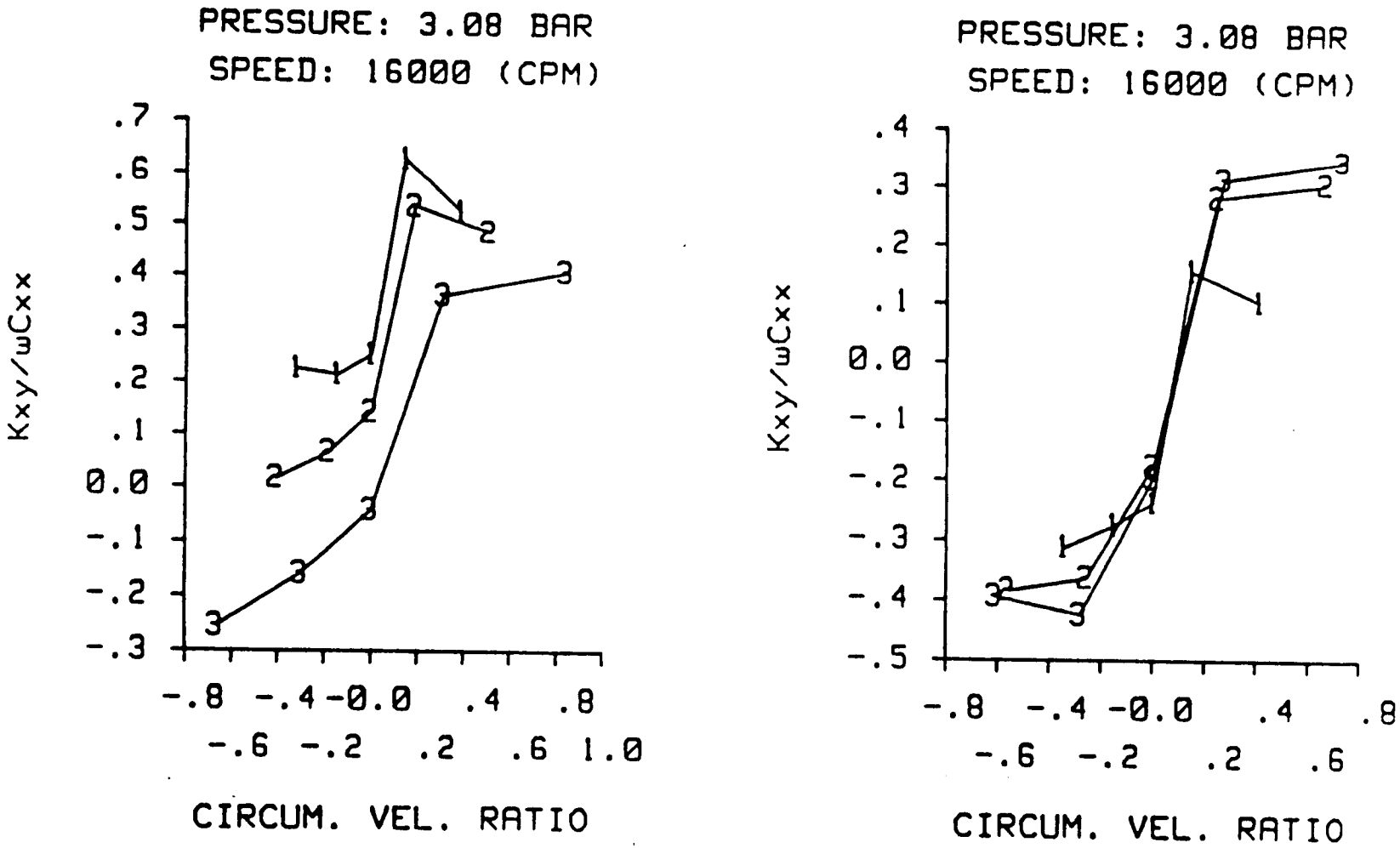

Fig. 69 Whirl frequency ratio versus inlet circumferential velocity ratio at an inlet pressure of 3.08 bar and rotor speed of 16000 cpm. Shake frequency 74.6 Hz. See table 5 for seal clearance definitions. Teeth-on-rotor (left), teeth-on-stator (right).

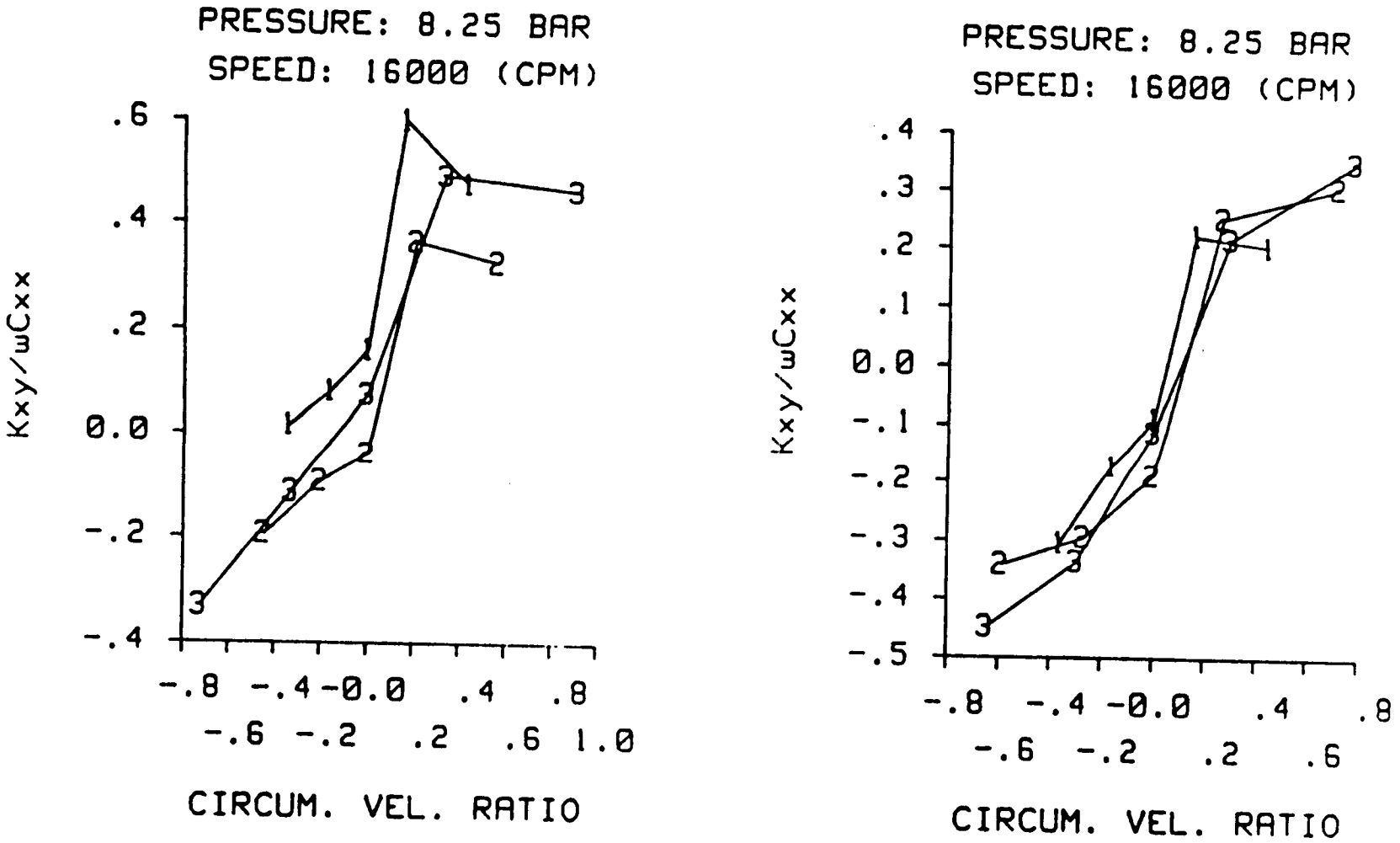

Fig. 70 Whirl frequency ratio versus inlet circumferential velocity ratio at an inlet pressure of 8.25 bar and rotor speed of 16000 cpm. Shake frequency 74.6 Hz. See table 5 for seal clearance definitions. Teeth-on-rotor (left), teeth-on-stator (right).

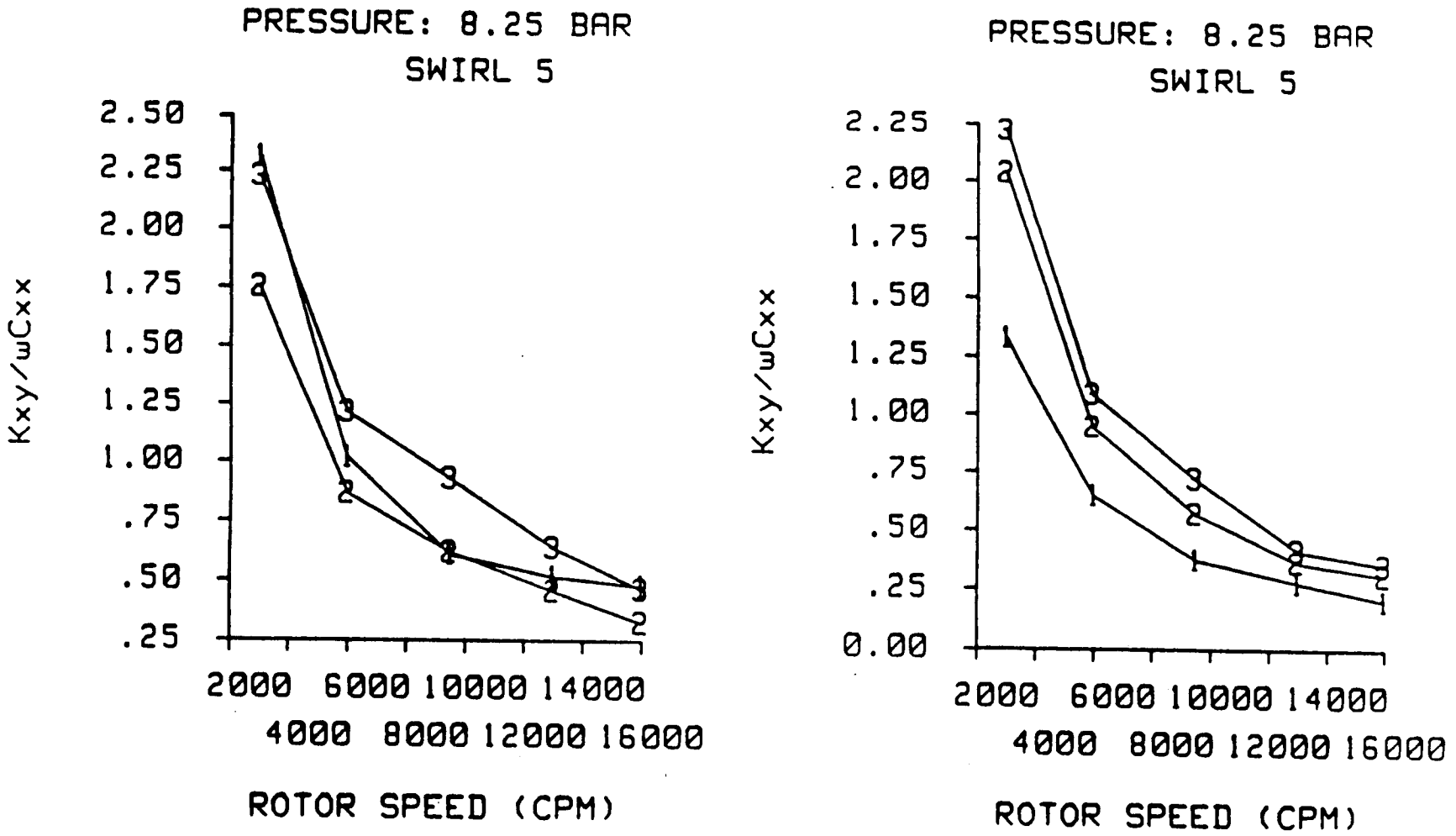

Fig. 71 Whirl frequency ratio versus rotor speed for the seals of table 5 at an inlet pressure of 8.25 bar and inlet circumferential velocity 5.

CHAPTER VI

TEST RESULTS: COMPARISON TO THEORETICAL PREDICTIONS

In this chapter, the experimental results from the tests of three teeth-on-rotor and three teeth-on-stator labyrinth seals are compared to the new analysis presented in the Geometric Boundary Approach section in the THEORETICAL DEVELOPMENT chapter of this report. The seals tested are described in tables 3-5. Tables 5 and 6 and figures 35-37 define the symbols used in the figures. Generally, the solid lines are the experimental points and the broken lines are the predictions.

STATIC RESULTS

Before proceeding with the comparison to the theory, some necessary input parameters to the model must be given. Table 9 shows the variables used as input to the program for the comparisons shown here. The temperature given was fairly constant for all of the tests. The viscosity was calculated for each case using Sutherland's formula [51]. The pressure gradients for the five rotor speeds of table 6 are shown in figure 72 for a single inlet pressure and inlet circumferential velocity. The curves show that the pressure gradient has little or no sensitivity to rotor speed. Any slight differences in the curves are due to variations in the actual points taken. Therefore, only one rotor speed will be used for comparison of the pressure gradients.

Figures 73-75 show a comparison of the experimental and

Table 9. Input parameters for seal program.

Inlet temperature	300K
Ratio of sp. heats	1.4
Gas constant (air)	287.06 J/(kgK)
Compressibility factor	1.0
Rotor friction exp.(mr)	-0.25
Rotor friction const.(nr)	0.079
Stator friction exp.(ms)	-0.25
Stator friction const.(ns)	0.079
Number of teeth	16

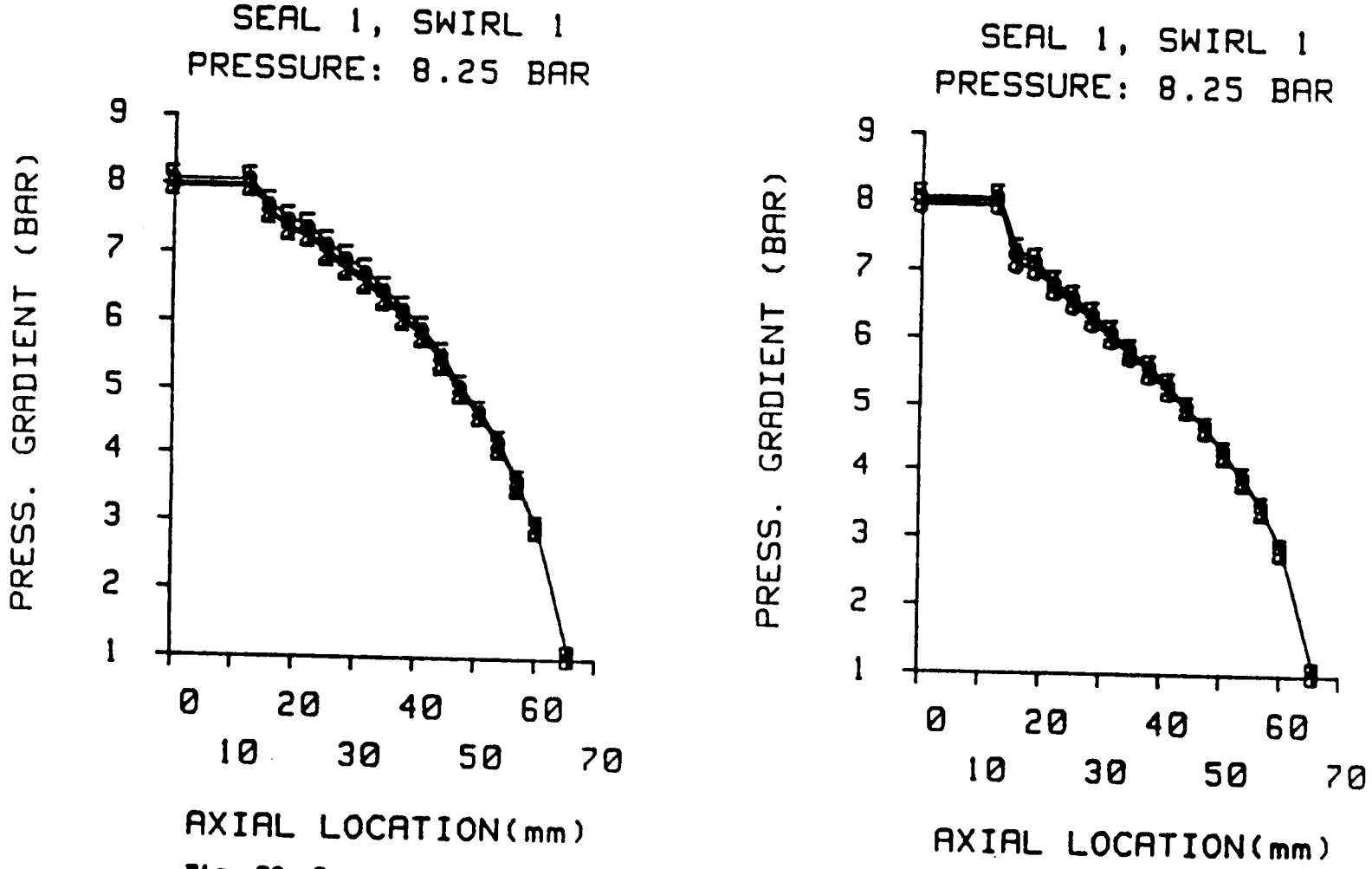

Fig. 72 Pressure gradients of seal 1 for the rotor speeds of table 6 at an inlet pressure of 8.25 bar and inlet circumferential velocity 1. Teeth-on-rotor (left), teeth-on-stator (right).

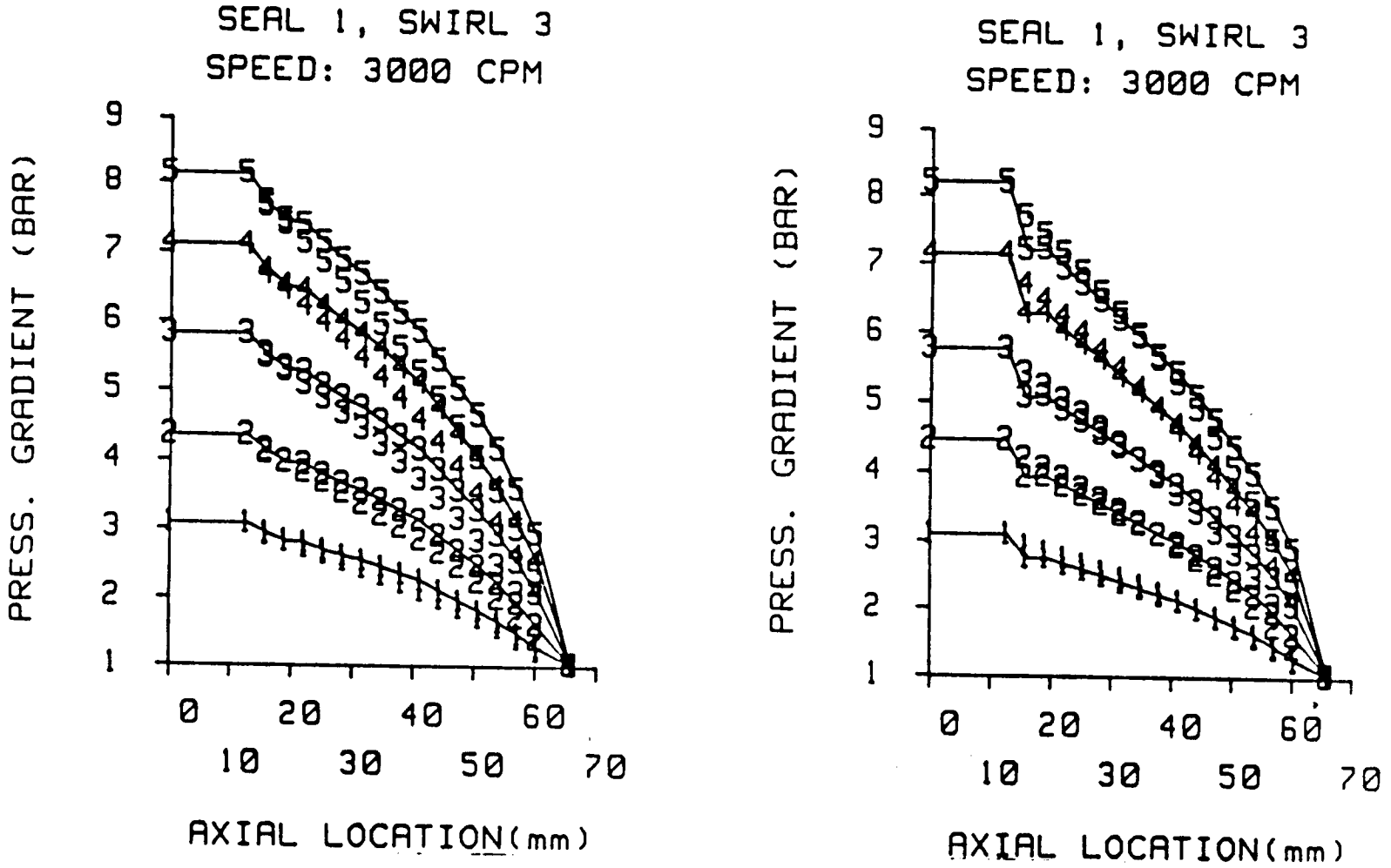

Fig. 73 A comparison of experimental and theoretical pressure gradients of seal 1 for a rotor speed of 3000 cpm and inlet circumferential velocity 3. See table 6 for inlet pressure definitions. Teeth-on-rotor (left), teeth-on-stator (right).

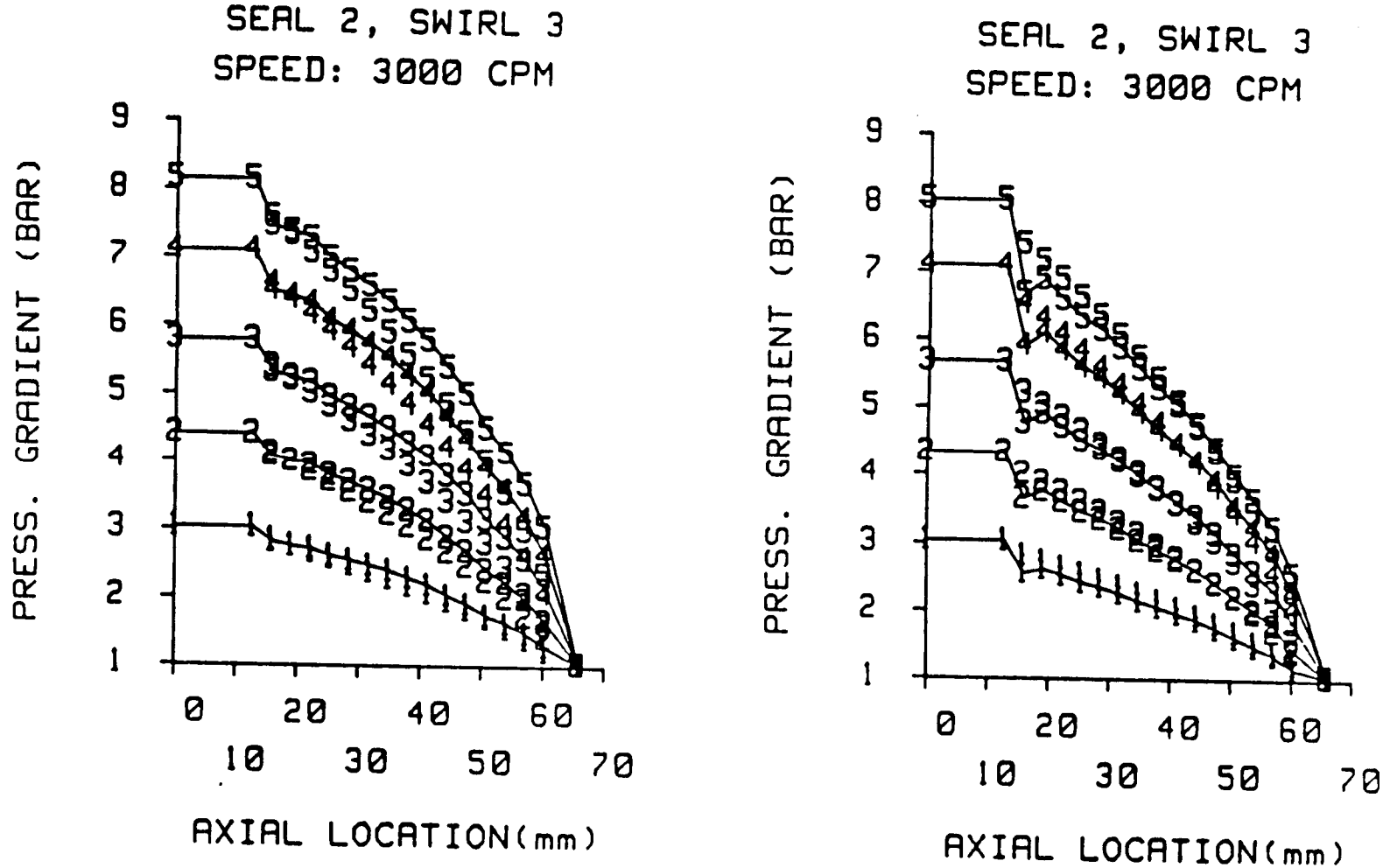

Fig. 74 A comparison of experimental and theoretical pressure gradients of seal 2 for a rotor speed of 3000 cpm and inlet circumferential velocity 3. See table 6 for inlet pressure definitions. Teeth-on-rotor (left), teeth-on-stator (right).

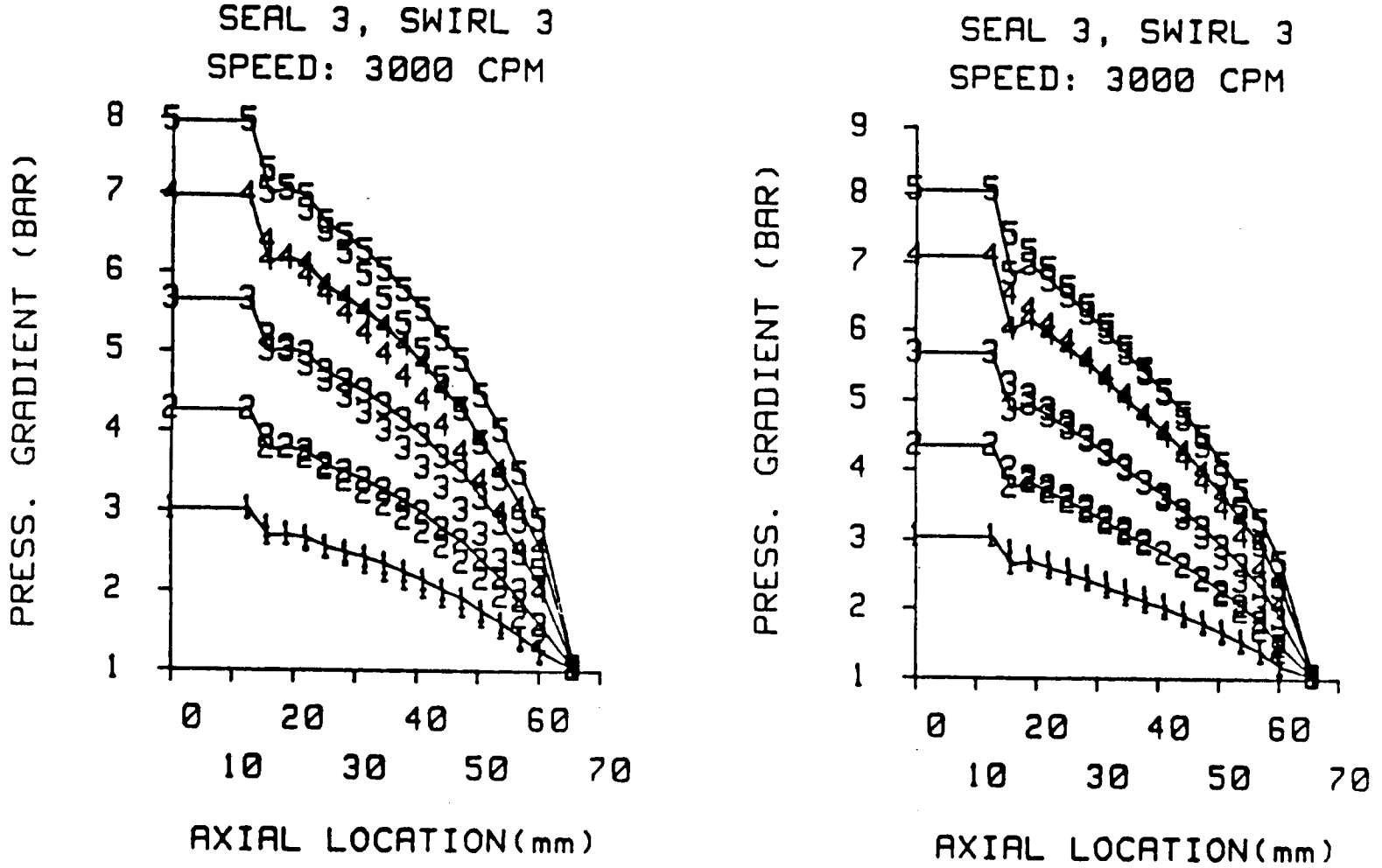

Fig. 75 A comparison of experimental and theoretical pressure gradients of seal 3 for a rotor speed of 3000 cpm and inlet circumferential velocity 3. See table 6 for inlet pressure definitions. Teeth-on-rotor (left), teeth-on-stator (right).

theoretical pressure gradients for the no-inlet-circumferential-velocity case. The figures show that the theory underpredicts the cavity pressures for the teeth-on-rotor case and overpredicts the cavity pressures for the teeth-on-stator case. This difference is due to the difference in the inlet losses for the two seal types. The theory accurately predicts the inlet loss for the teeth-on-rotor case. However, the teeth-on-stator seal has a much larger inlet loss followed by a pressure recovery. This positive pressure recovery cannot be modelled by a simple leakage equation. The remainder of the pressure gradient comparison plots can be found in Appendix D.

Figures 76-78 show a comparison of experimental and theoretical leakage versus inlet circumferential velocity ratio for the inlet pressure set of table 6. The plots show that the theory underpredicts the leakage for both seal types by about 25%. This is much worse than the 5% error for the theory of Childs and Scharrer [18]. This difference is due to the change in the equation for the kinetic energy carryover coefficient, μ_2. The change in the coefficient was made in order to obtain a local equation which would yield a clearance perturbation. The former coefficient was a global equation and could not be perturbed. The contribution of this coefficient to the first-order equations and the subsequent solution is very substantial. In effect, the leakage calculation was sacrificed in order to improve the calculation of the dynamic coefficients.

DYNAMIC RESULTS

The experimental and theoretical results to be compared include the direct and cross-coupled stiffness and direct damping coefficients.

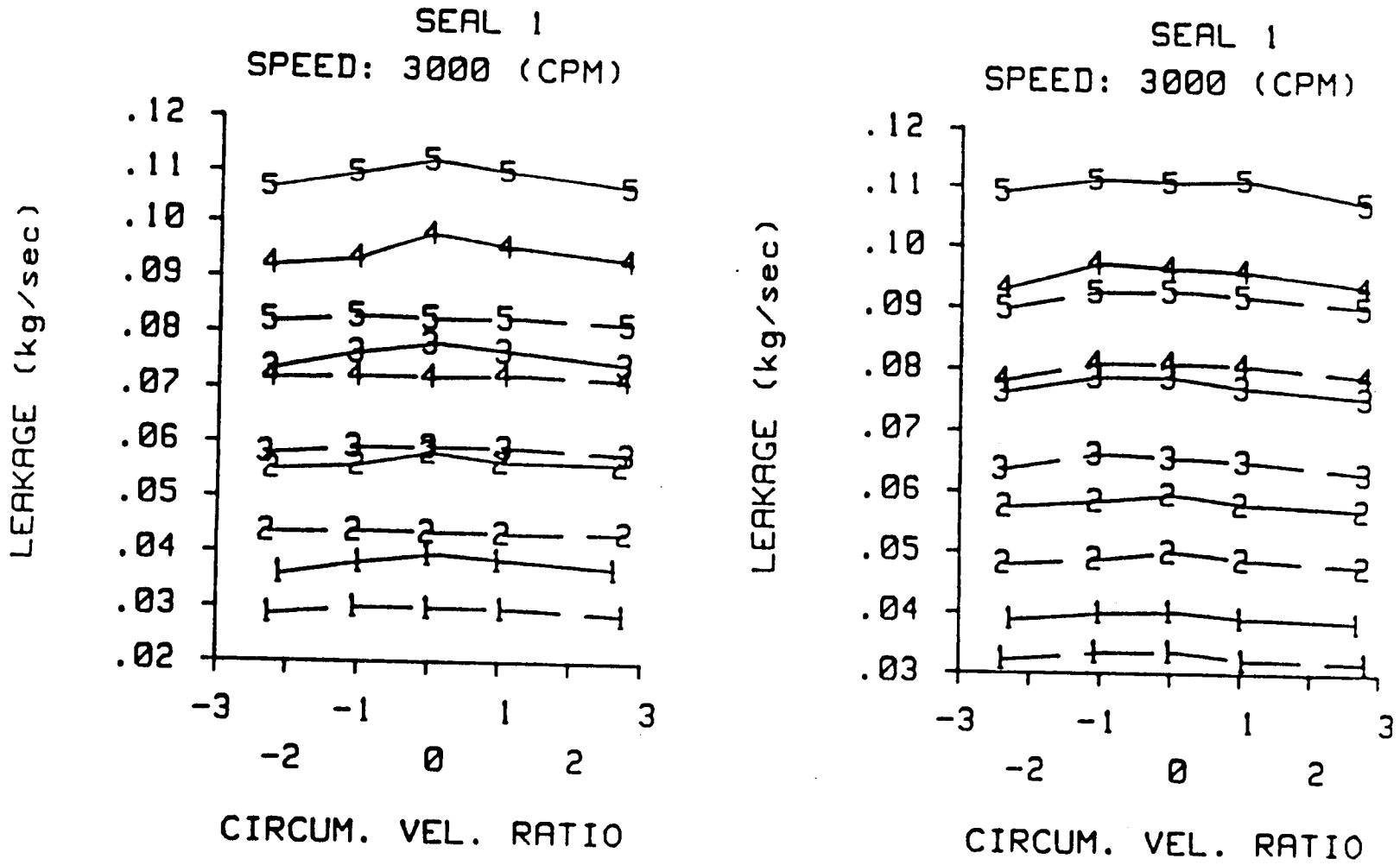

Fig. 76 A comparison of experimental and theoretical leakage versus inlet circumferential velocity ratio for seal 1 at a rotor speed of 3000 cpm. See table 6 for inlet pressure definitions. Teeth-on-rotor (left), teeth-on-stator (right).

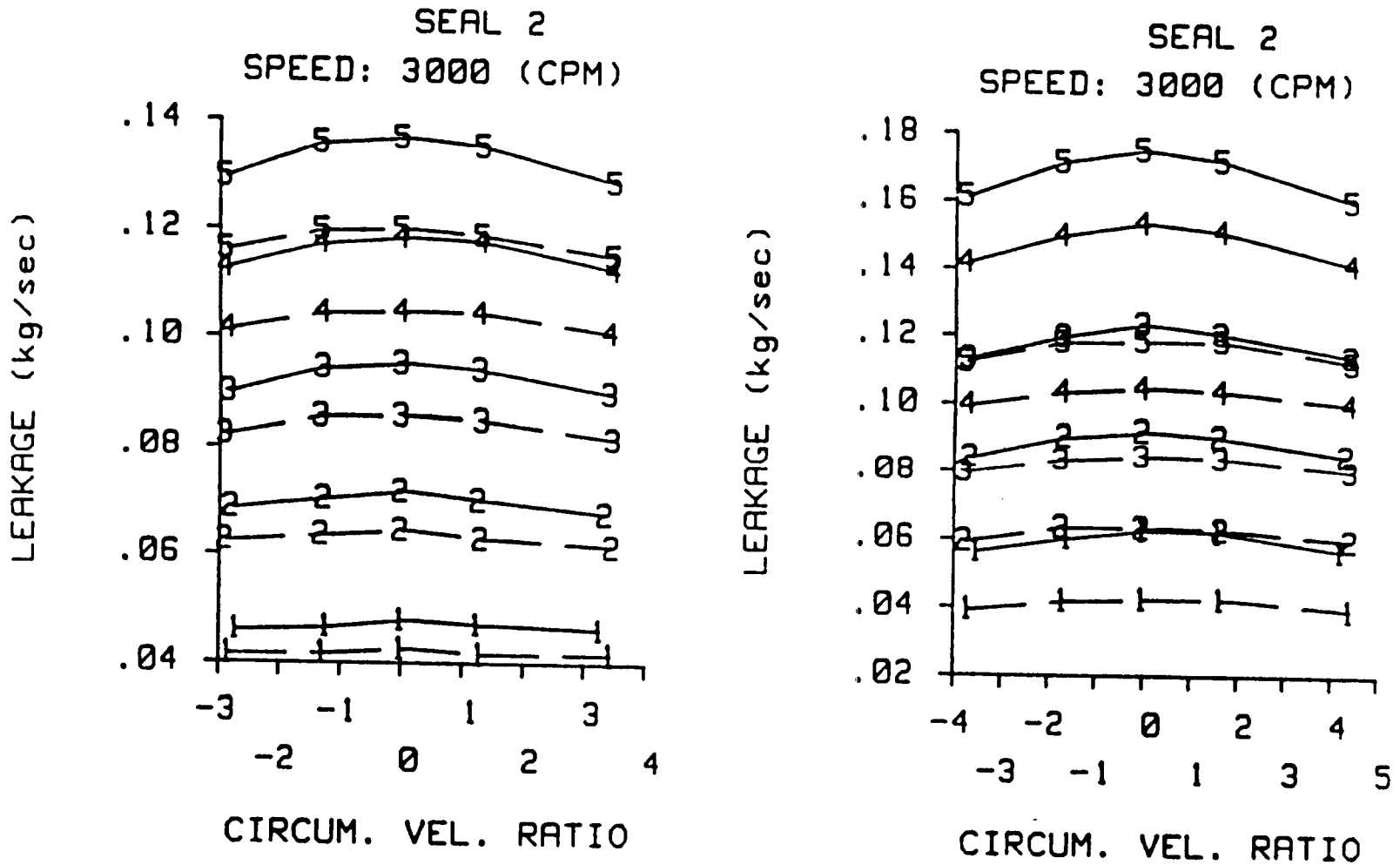

Fig. 77 A comparison of experimental and theoretical leakage versus inlet circumferential velocity ratio for seal 2 at a rotor speed of 3000 cpm. See table 6 for inlet pressure definitions. Teeth-on-rotor (left), teeth-on-stator (right).

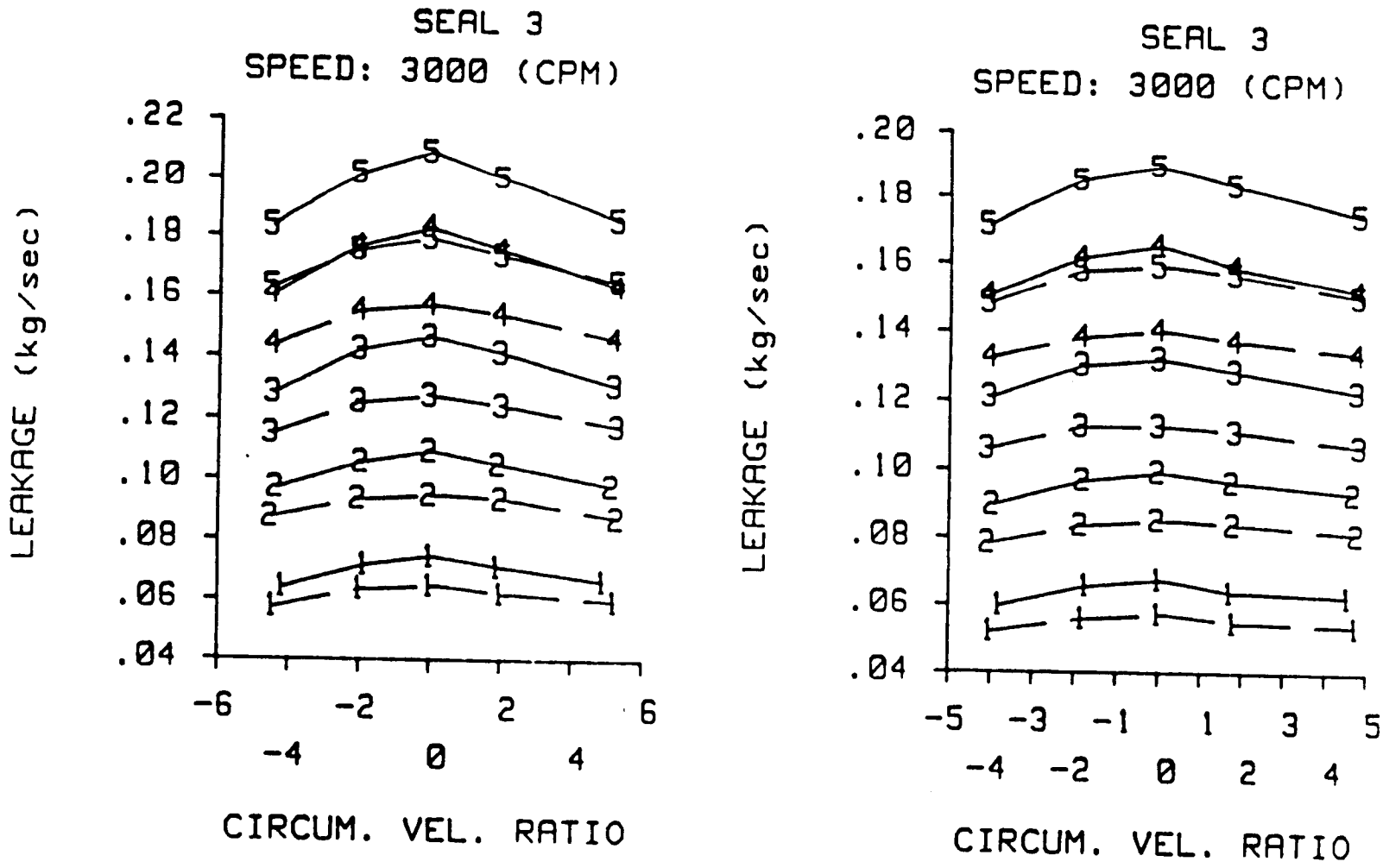

Fig. 78 A comparison of experimental and theoretical leakage versus inlet circumferential velocity ratio for seal 3 at a rotor speed of 3000 cpm. See table 6 for inlet pressure definitions. Teeth-on-rotor (left), teeth-on-stator (right).

A cross-coupled damping comparison has been omitted because of the uncertainty present in the experimental values (see the Relative Uncertainty section). Of the remaining three coefficients, the direct stiffness comparison will be presented first, and the direct damping comparison will be last.

Direct stiffness

Figures 79-82 show a comparison of experimental and theoretical direct stiffness versus inlet circumferential velocity ratio for the seals defined in table 5. The figures show that the theory correctly predicts a decrease in direct stiffness as clearance increases, for both seal types. The figures also show that for both inlet pressures, the theory overpredicts the direct stiffness at low rotor speeds and underpredicts the direct stiffness at high rotor speeds. This trend is made clearer by figures 83-85. Figures 83-85 show a comparison of experimental and theoretical direct stiffness versus rotor speed for the inlet pressure set of table 6 and inlet circumferential velocity 5. The figures show that the theory is oversensitive to rotor speed. Some of the test data did show an decrease in direct stiffness with rotor speed, but not with the sensitivity predicted by the theory. This is an improvement over the previous theory of Childs and Scharrer [18] which consistently underpredicts direct stiffness.

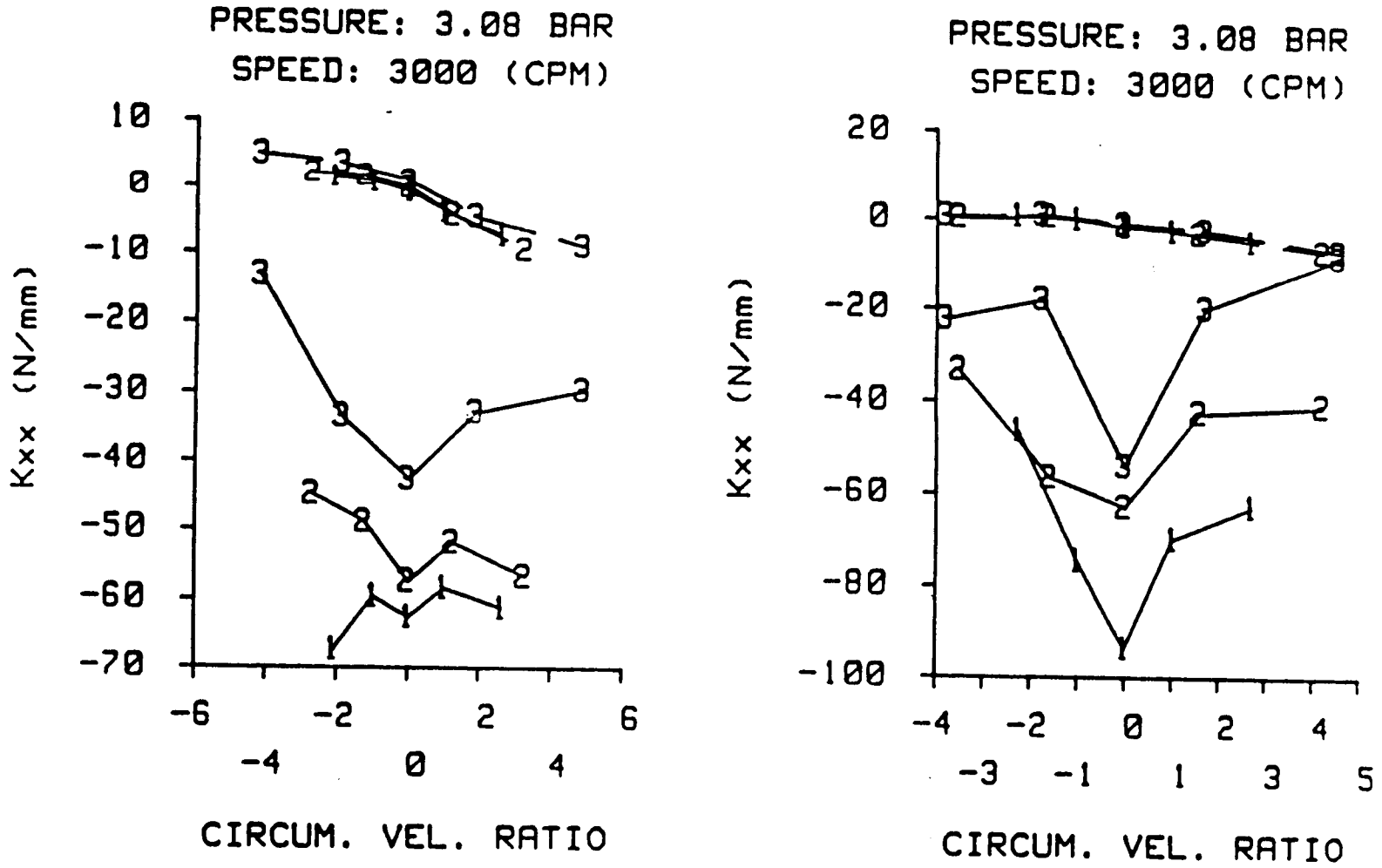

Fig. 79 A comparison of experimental and theoretical direct stiffness versus inlet circumferential velocity ratio at an inlet pressure of 3.08 bar and rotor speed of 3000 cpm. See table 5 for seal definitions. Teeth-on-rotor (left), teeth-on-stator (right).

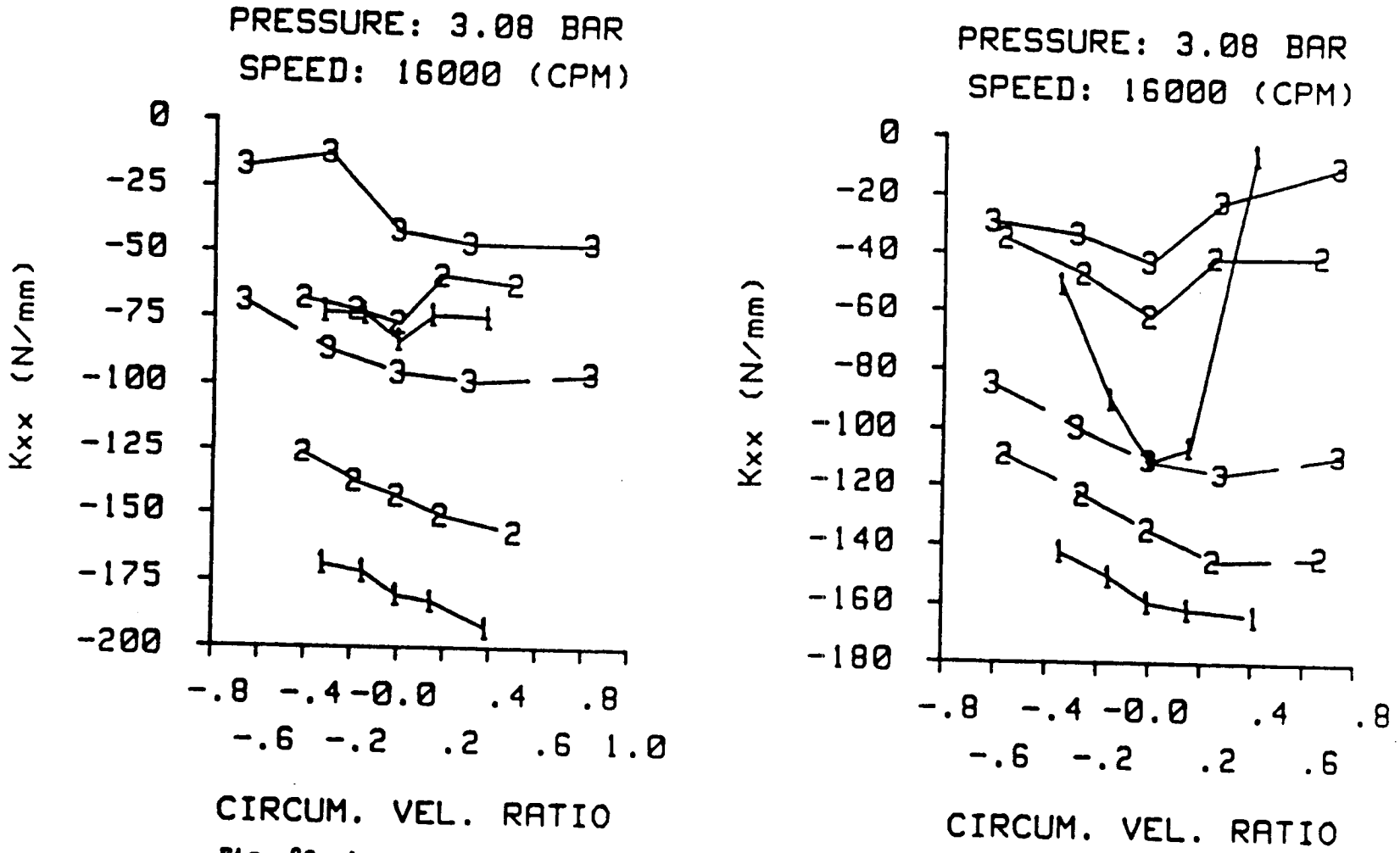

Fig. 80 A comparison of experimental and theoretical direct stiffness versus inlet circumferential velocity ratio at an inlet pressure of 3.08 bar and rotor speed of 16000 cpm. See table 5 for seal definitions. Teeth-on-rotor (left), teeth-on-stator (right).

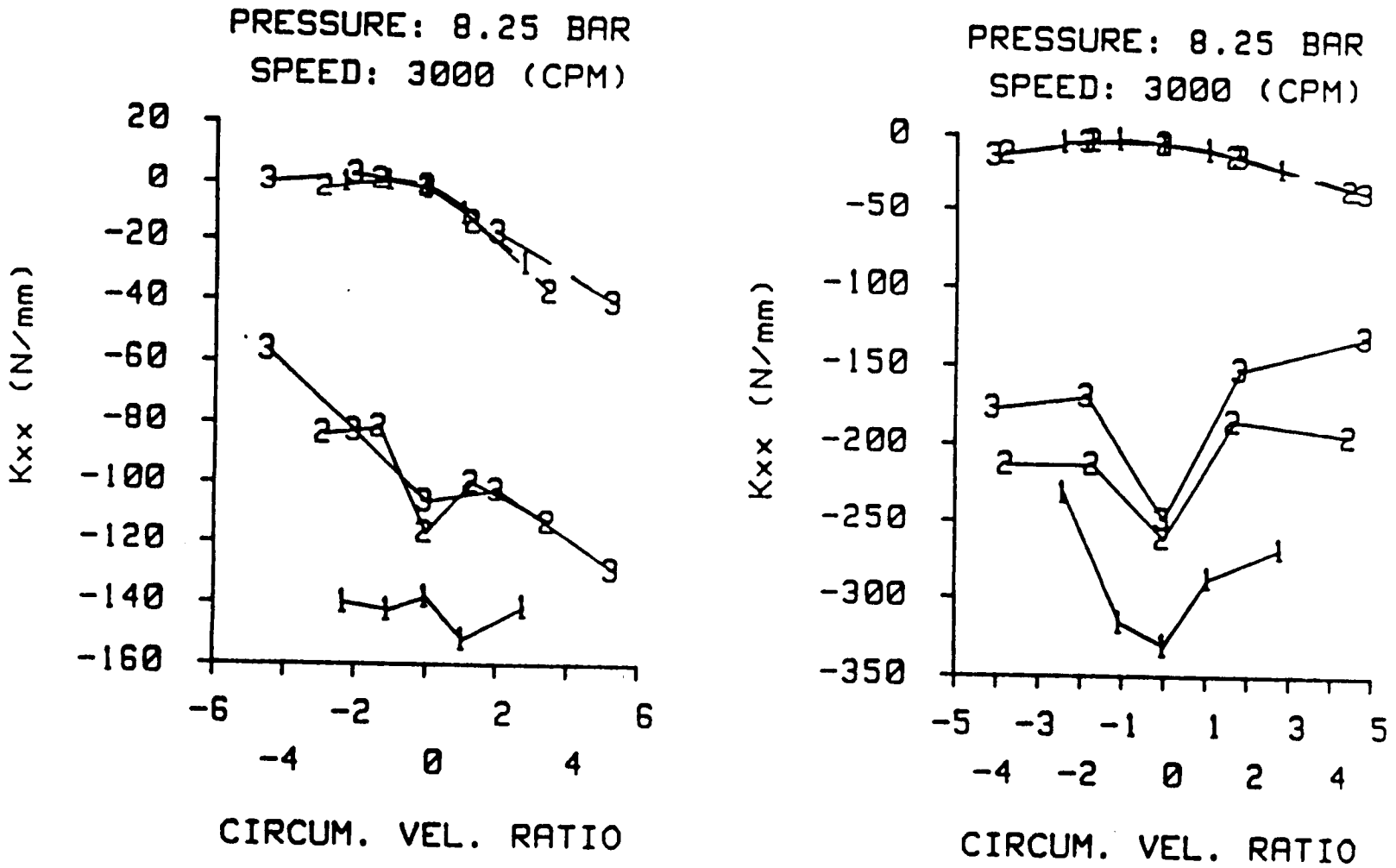

Fig. 81 A comparison of experimental and theoretical direct stiffness versus inlet circumferential velocity ratio at an inlet pressure of 8.25 bar and rotor speed of 3000 cpm. See table 5 for seal definitions. Teeth-on-rotor (left), teeth-on-stator (right).

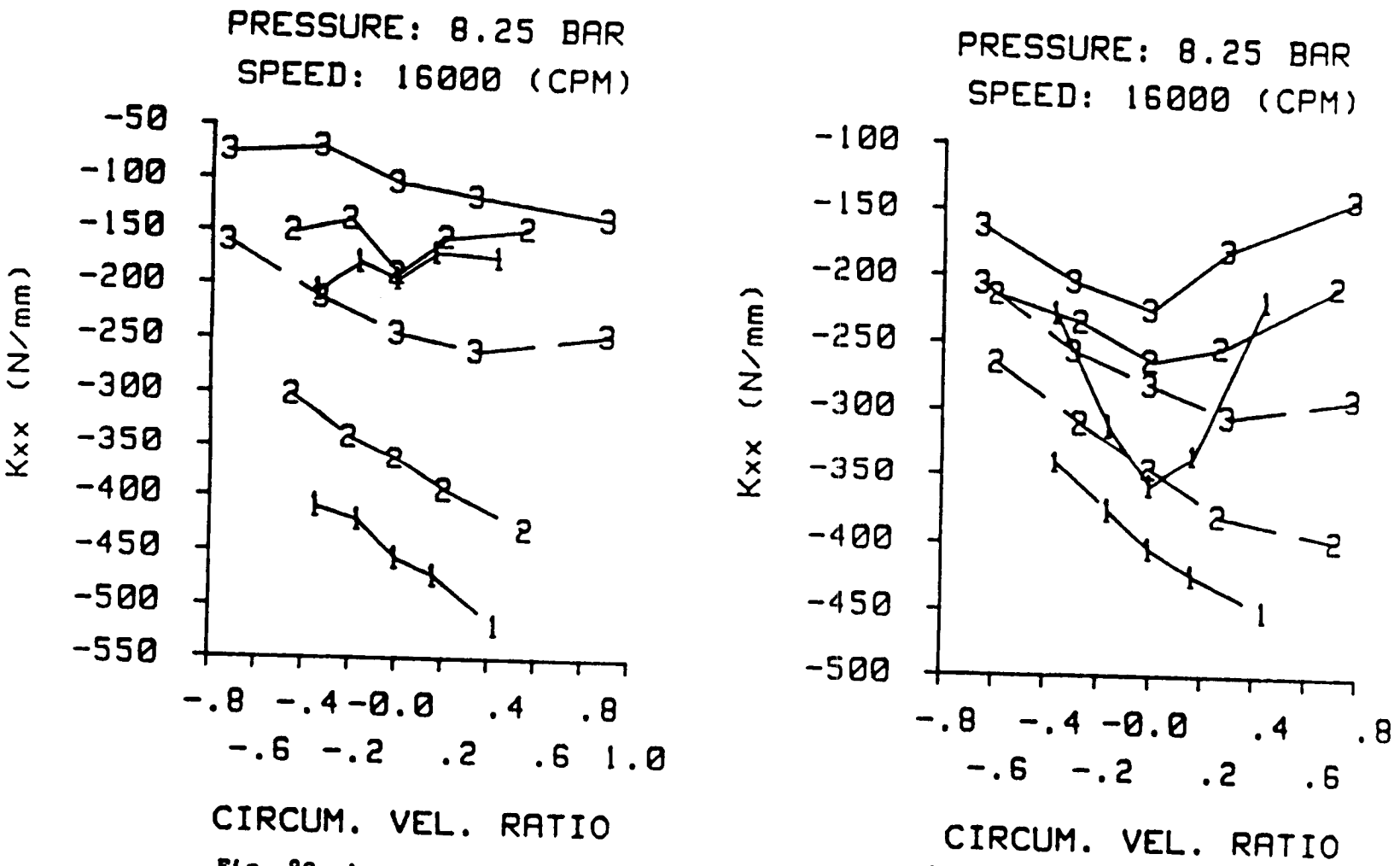

Fig. 82 A comparison of experimental and theoretical direct stiffness versus inlet circumferential velocity ratio at an inlet pressure of 8.25 bar and rotor speed of 16000 cpm. See table 5 for seal definitions. Teeth-on-rotor (left), teeth-on-stator (right).

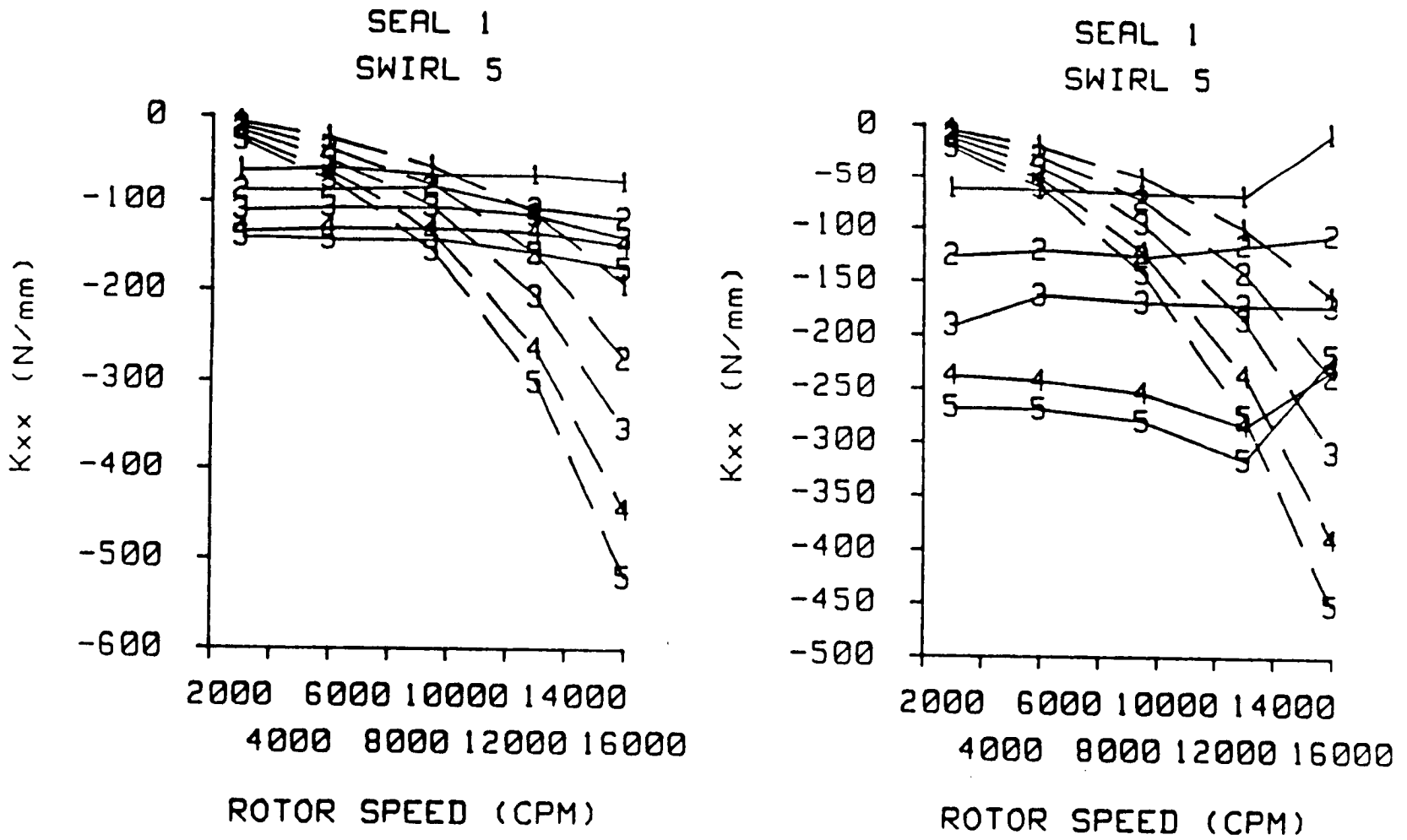

Fig. 83 A comparison of experimental and theoretical direct stiffness versus rotor speed for seal 1 and inlet circumferential velocity 5. See table 6 for definitions. Teeth-on-rotor (left), teeth-on-stator (right).

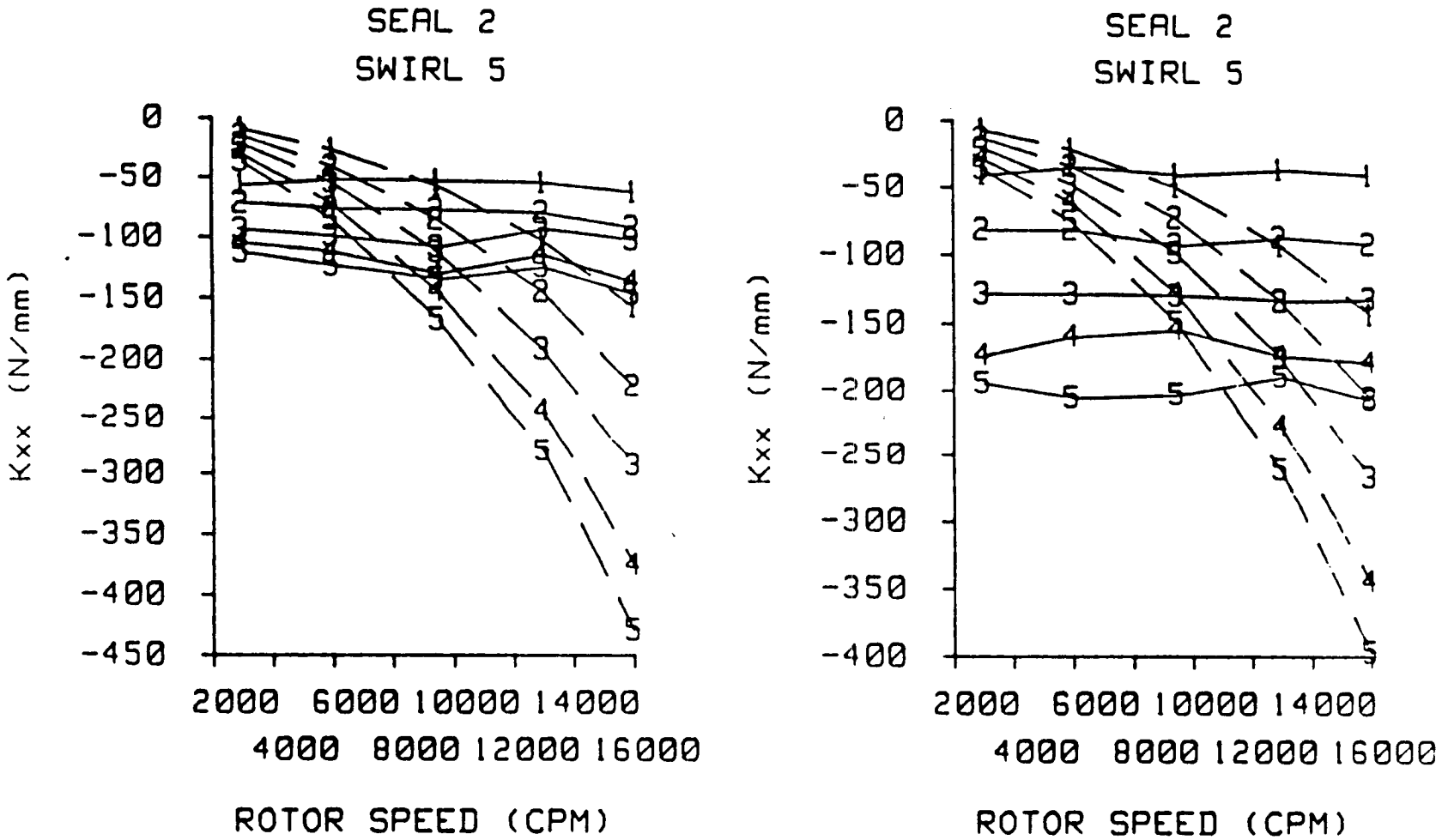

Fig. 84 A comparison of experimental and theoretical direct stiffness versus rotor speed for seal 2 and inlet circumferential velocity 5. See table 6 for definitions. Teeth-on-rotor (left), teeth-on-stator (right).

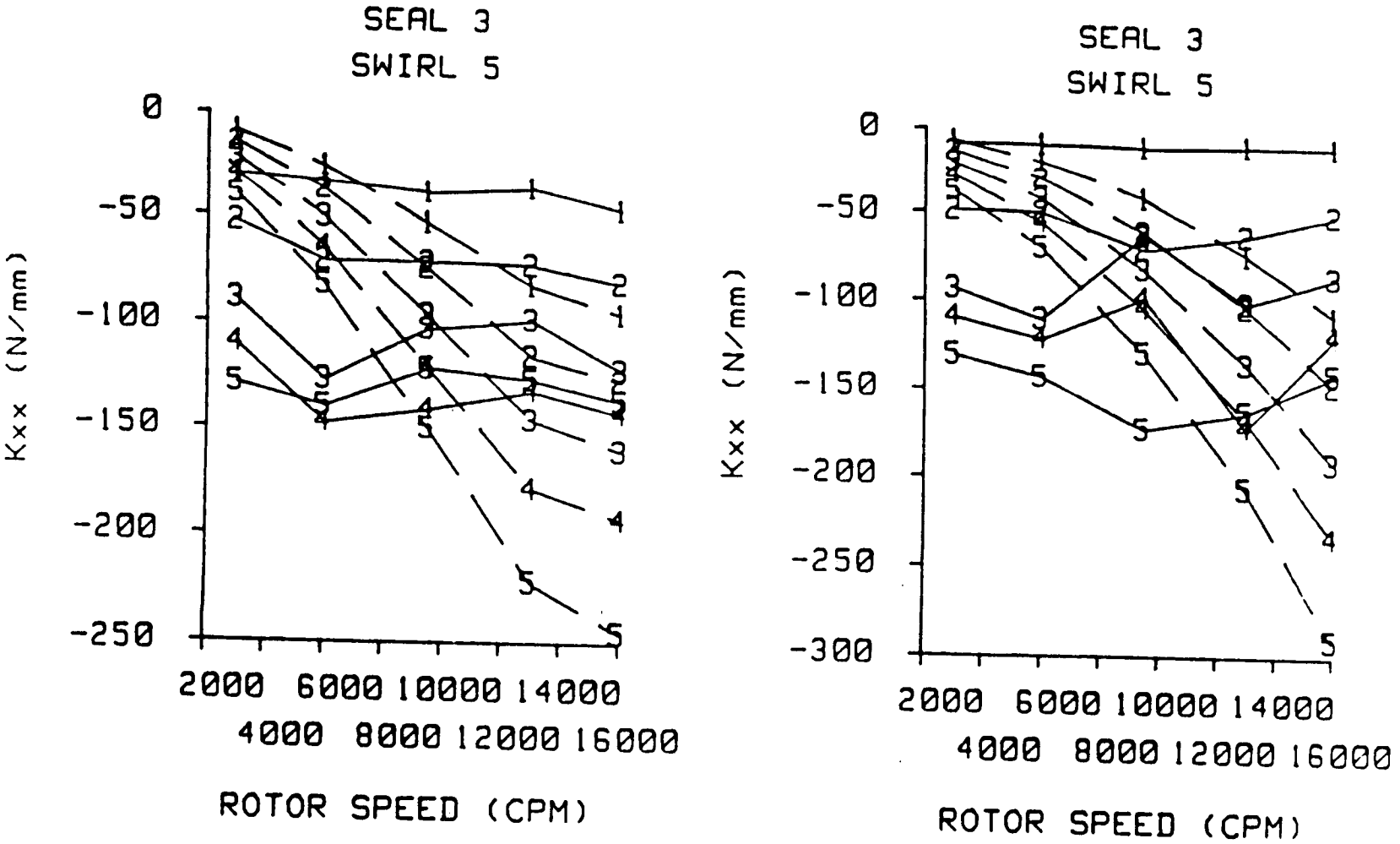

Fig. 85 A comparison of experimental and theoretical direct stiffness versus rotor speed for seal 3 and inlet circumferential velocity 5. See table 6 for definitions. Teeth-on-rotor (left), teeth-on-stator (right).

Cross-coupled stiffness

Figures 86-89 show a comparison of experimental and theoretical cross-coupled stiffness versus inlet circumferential velocity ratio for the seals defined in table 5. The figures show that, like the test results, there is no consistent trend with clearance. The figures also show that the theory does an excellent job of predicting the cross-coupled stiffness for the low rotor speed results and a reasonable job for the high rotor speed results. Rotor speed effects are much clearer in figures 90-92. Figures 90-92 show a comparison of experimental and theoretical cross-coupled stiffness versus rotor speed for the inlet pressure set of table 6 and inlet circumferential velocity 5. These figures show that the theory predicts reasonably well until higher speeds are reached. The theory then predicts a sharp upswing in the cross-coupled stiffness at high speeds. This effect is shown by the experimental data in figure 90. The larger clearance seals do not show this effect at the speeds tested. Perhaps at higher speeds, larger clearance seals will show this effect.

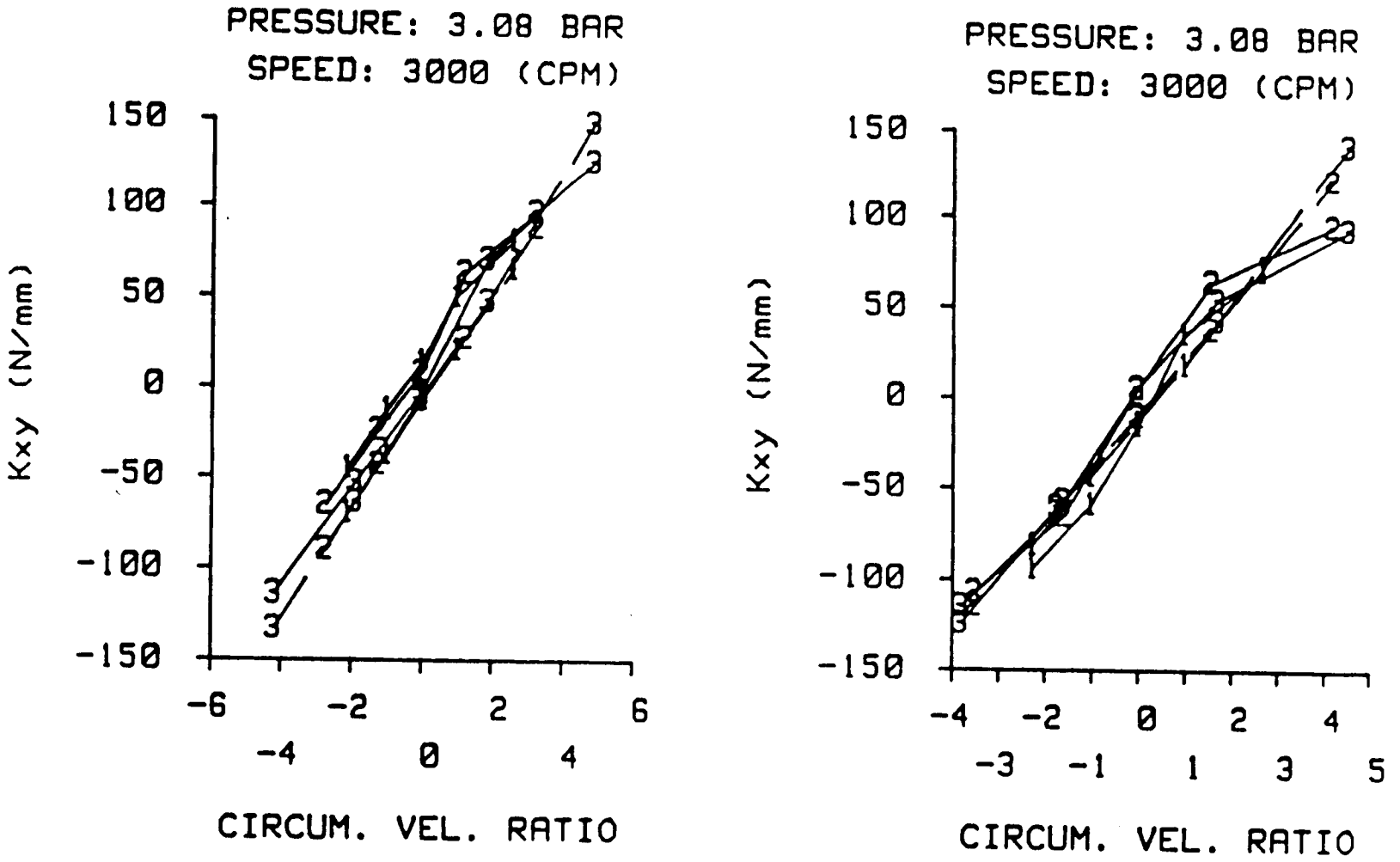

Fig. 86 A comparison of experimental and theoretical cross-coupled stiffness versus inlet circumferential velocity ratio at an inlet pressure of 3.08 bar and rotor speed of 3000 cpm. See table 5 for seal definitions. Teeth-on-rotor (left), teeth-on-stator (right).

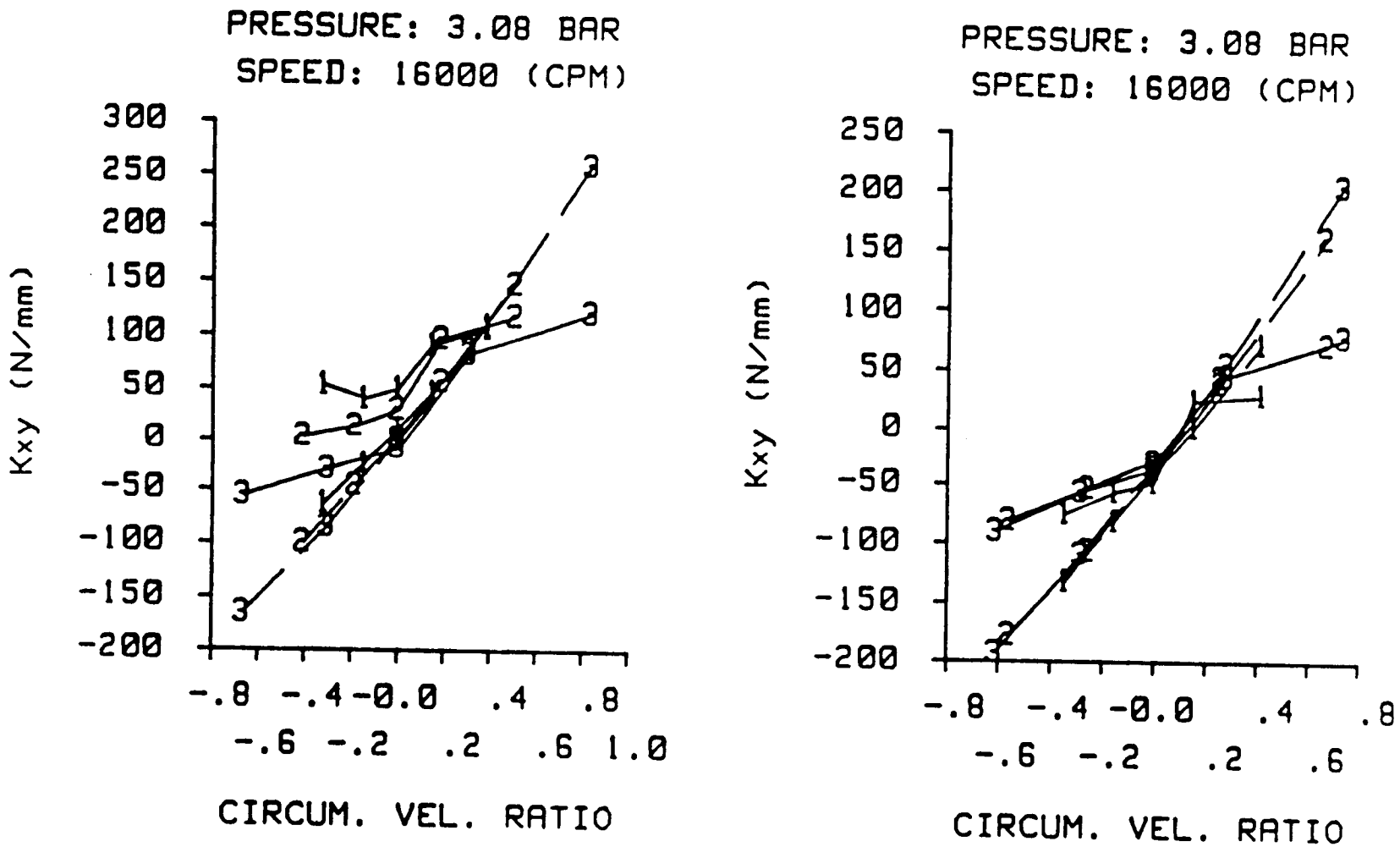

Fig. 87 A comparison of experimental and theoretical cross-coupled stiffness versus inlet circumferential velocity ratio at an inlet pressure of 3.08 bar and rotor speed of 16000 cpm. See table 5 for seal definitions. Teeth-on-rotor (left), teeth-on-stator (right).

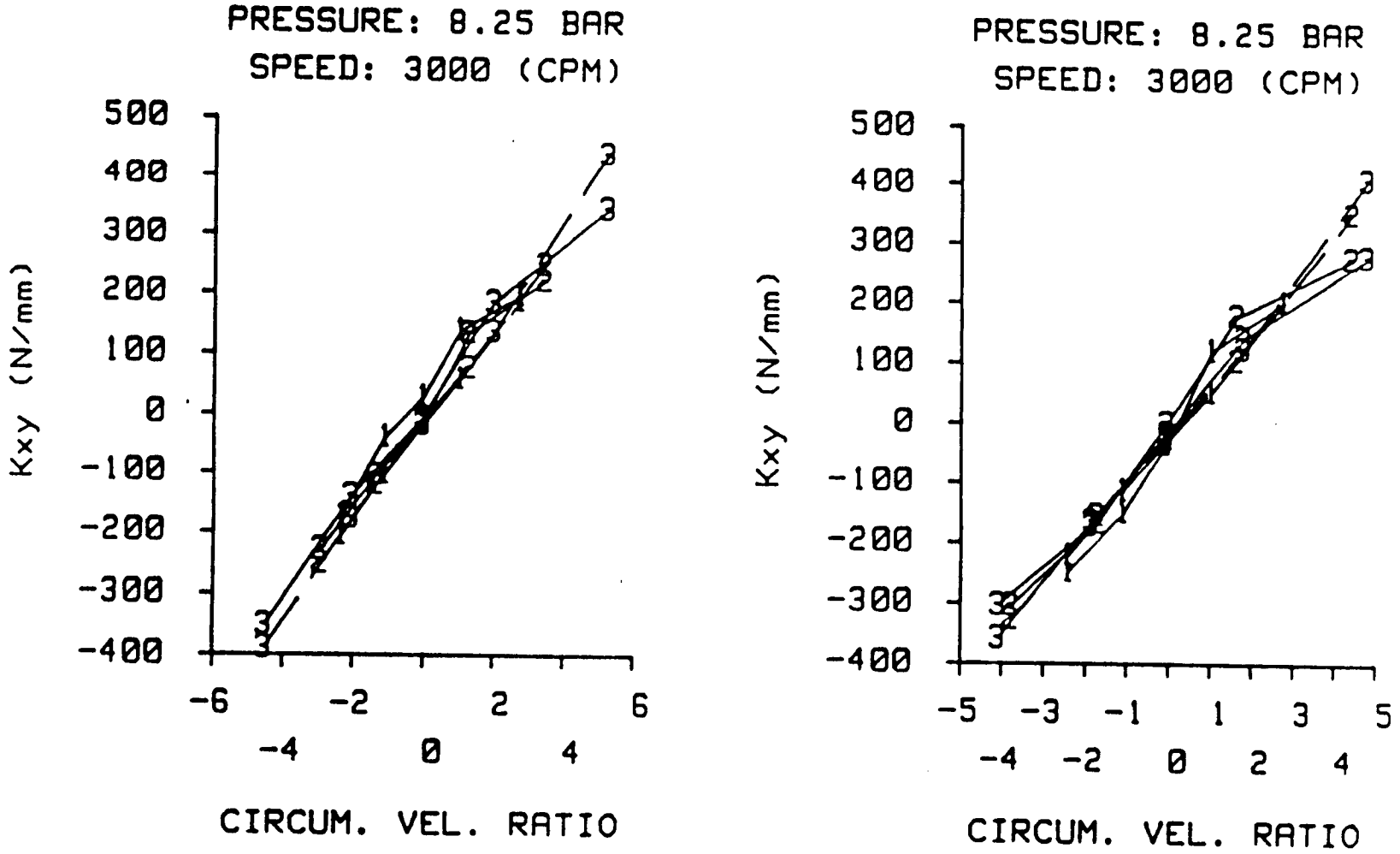

Fig. 88 A comparison of experimental and theoretical cross-coupled stiffness versus inlet circumferential velocity ratio at an inlet pressure of 8.25 bar and rotor speed of 3000 cpm. See table 5 for seal definitions. Teeth-on-rotor (left), teeth-on-stator (right).

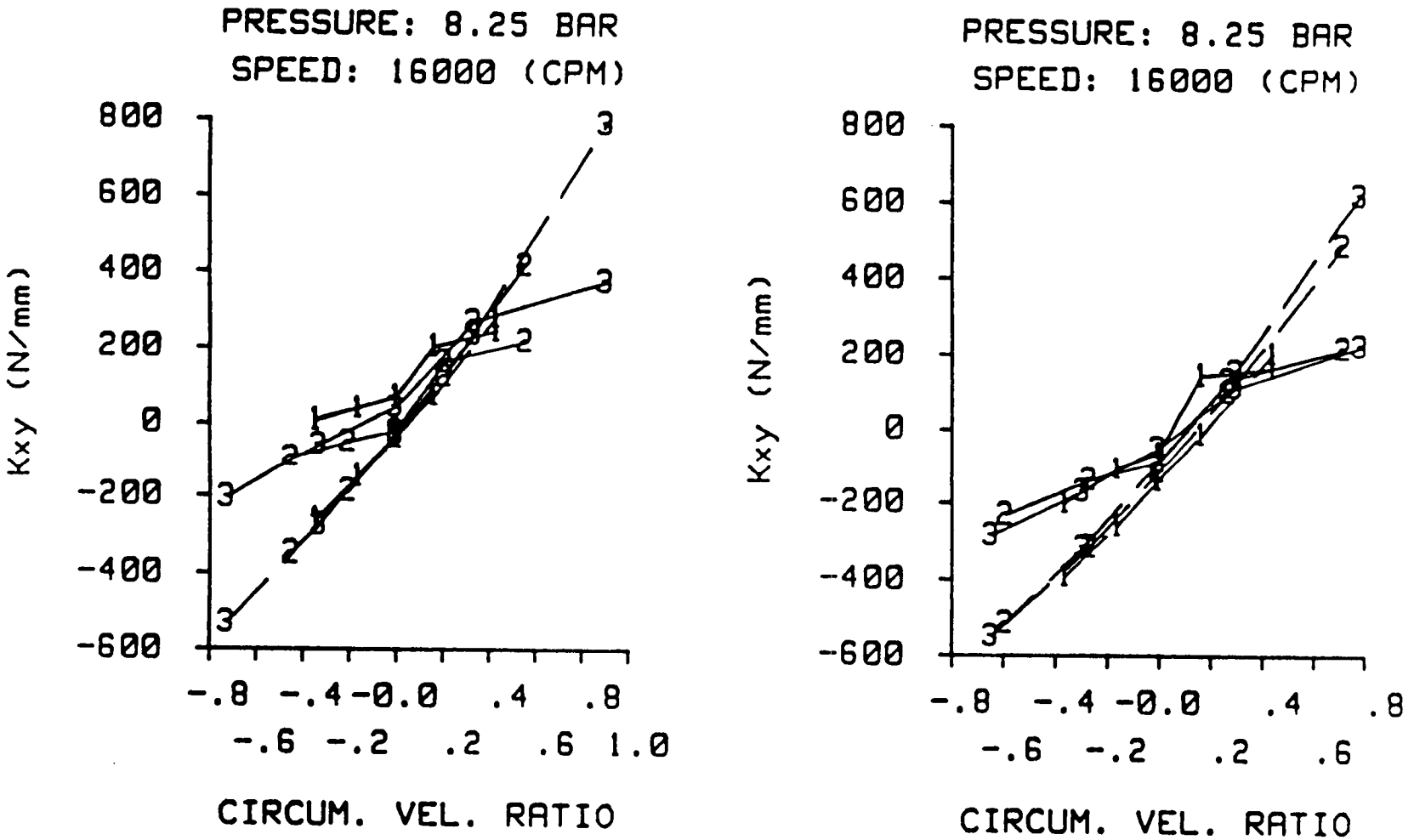

Fig. 89 A comparison of experimental and theoretical cross-coupled stiffness versus inlet circumferential velocity ratio at an inlet pressure of 8.25 bar and rotor speed of 16000 cpm. See table 5 for seal definitions. Teeth-on-rotor (left), teeth-on-stator (right).

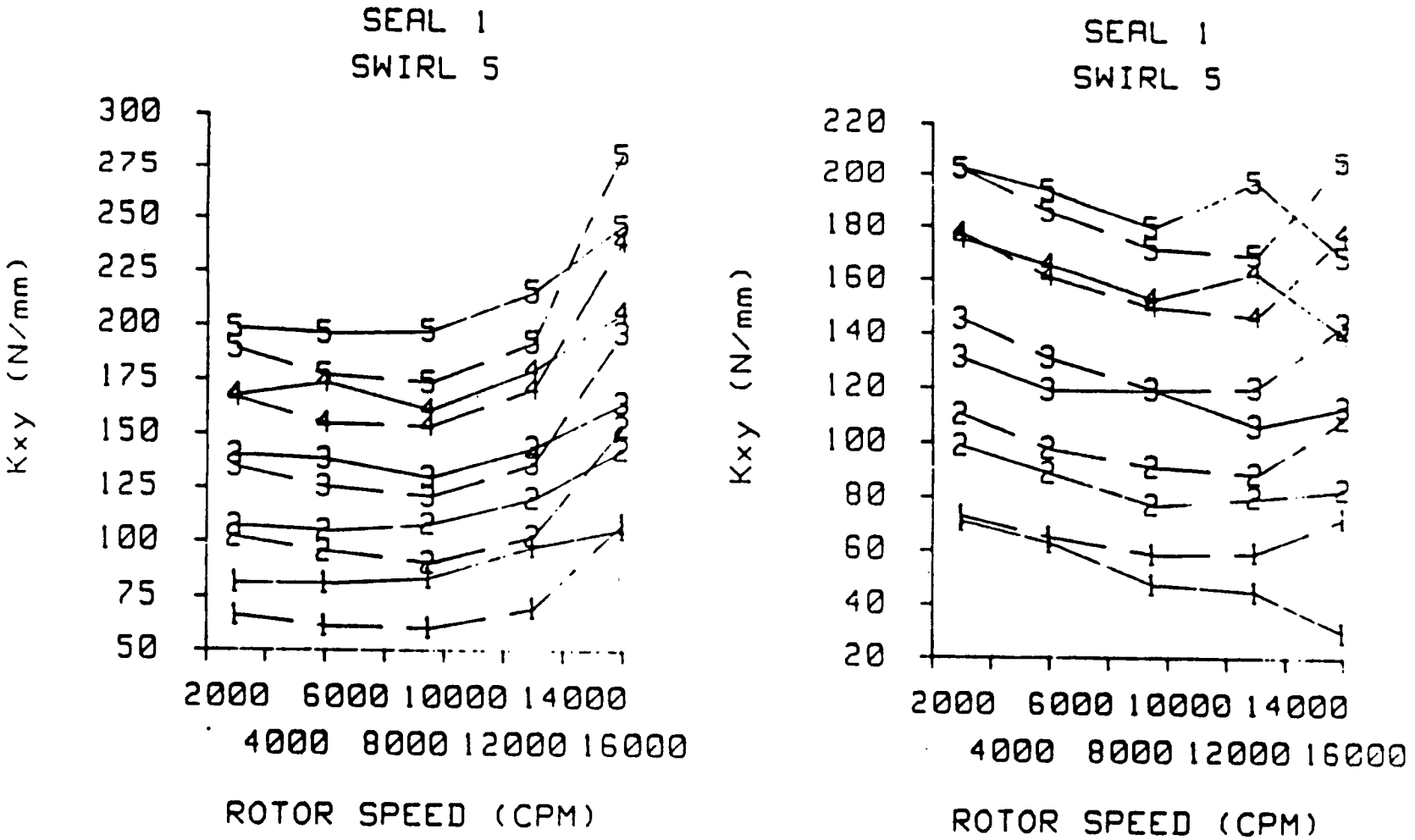

Fig. 90 A comparison of experimental and theoretical cross-coupled stiffness versus rotor speed for seal 1 and inlet circumferential velocity 5. See table 6 for definitions. Teeth-on-rotor (left), teeth-on-stator (right).

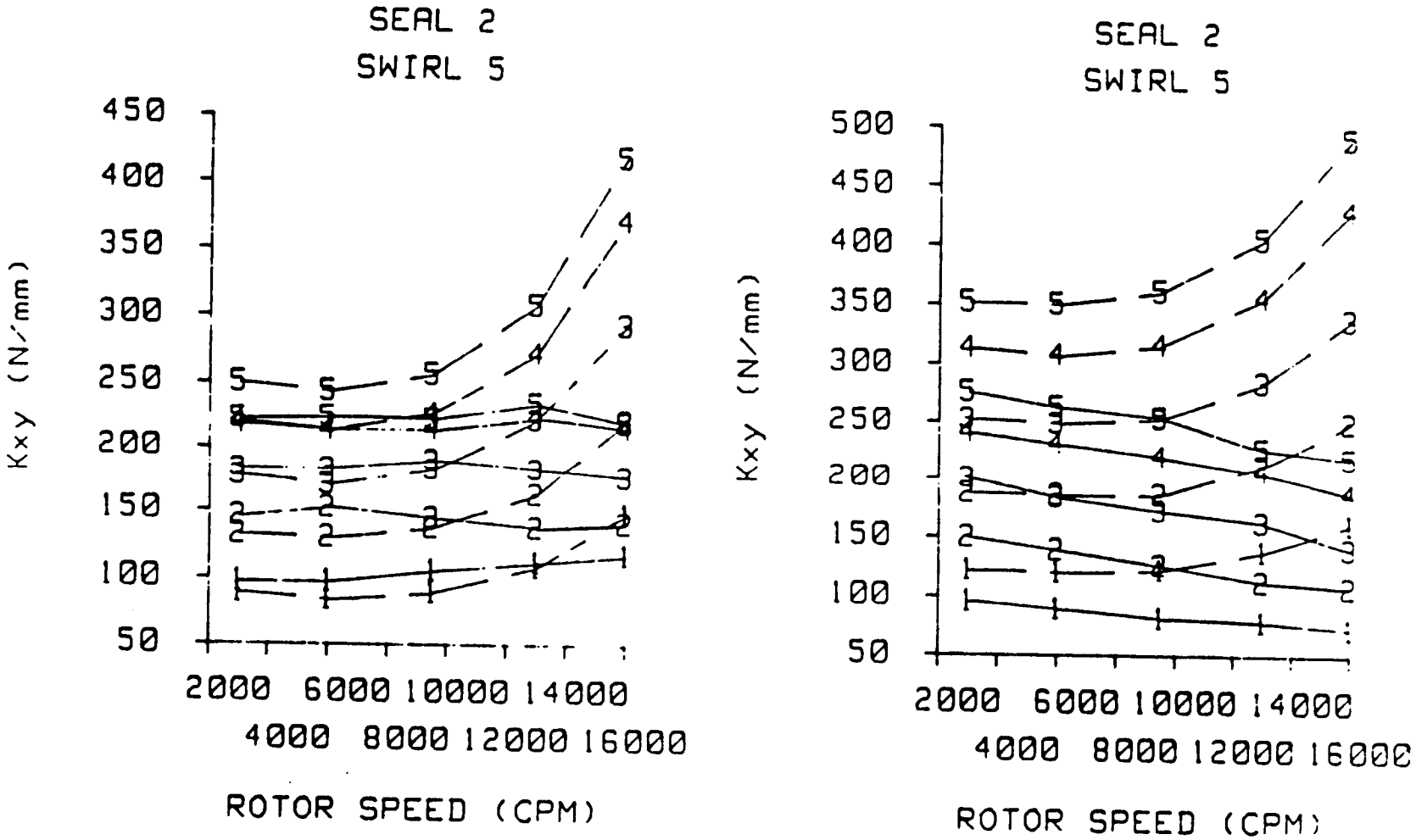

Fig. 91 A comparison of experimental and theoretical cross-coupled stiffness versus rotor speed for seal 2 and inlet circumferential velocity 5. See table 6 for definitions. Teeth-on-rotor (left), teeth-on-stator (right).

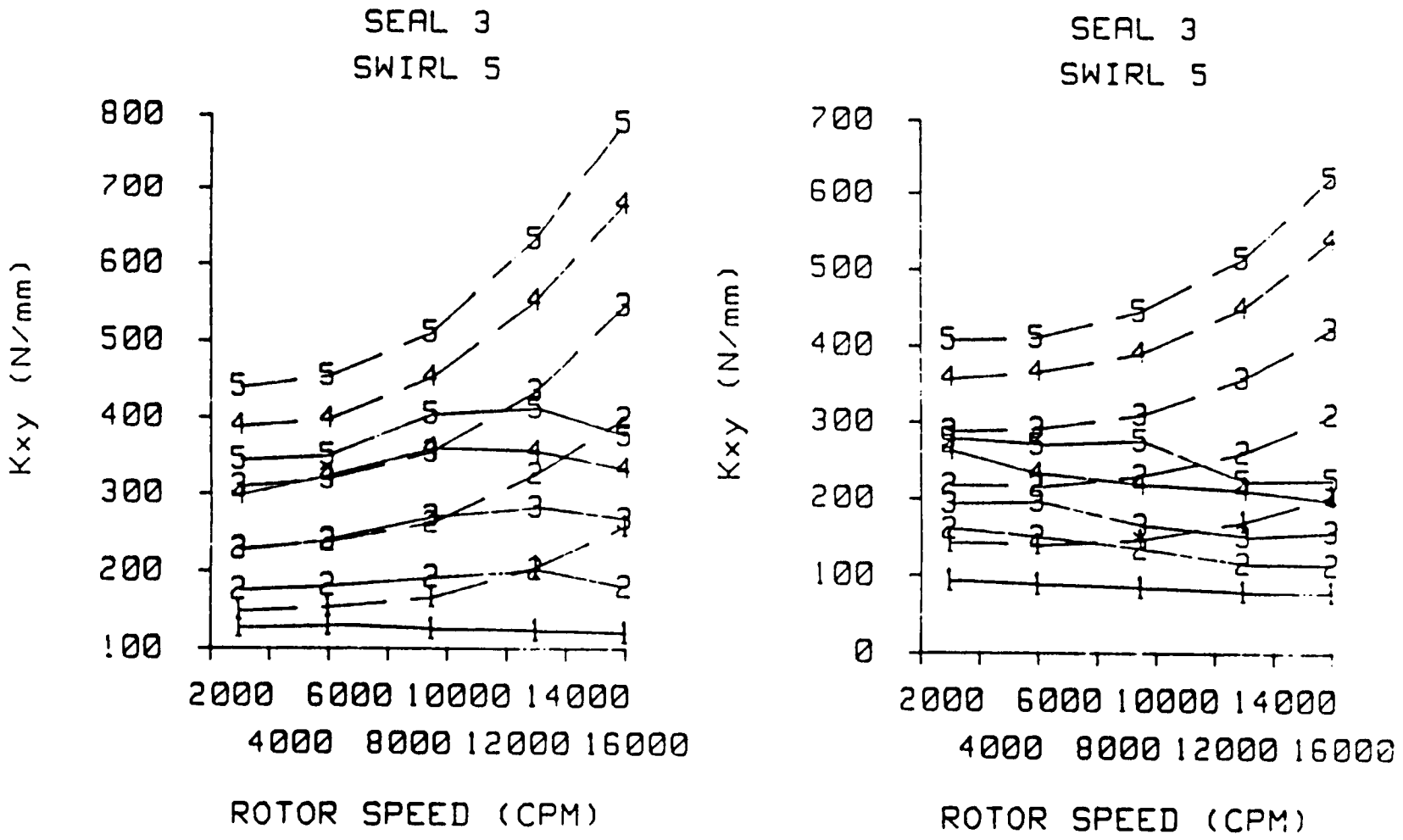

Fig. 92 A comparison of experimental and theoretical cross-coupled stiffness versus rotor speed for seal 3 and inlet circumferential velocity 5. See table 6 for definitions. Teeth-on-rotor (left), teeth-on-stator (right).

Direct damping

Figures 93-96 show a comparison of experimental and theoretical direct damping versus inlet circumferential velocity ratio for the seals defined in table 5. The figures show that the theory correctly predicts an increase in direct damping for an increase in clearance for the teeth-on-rotor seal. However, the theory incorrectly predicts the same trend for teeth-on-stator seals. This error renders the theory suspect when used for teeth-on-stator seals whose geometry differs significantly from those tested in this study. However, the theory averages an error of 40% for the teeth-on-rotor seals, which is a great improvement over the 75% error of the previous theory of Childs and Scharrer [18]. Figures 97-99 show a comparison of experimental and theoretical direct damping versus rotor speed for the inlet pressure set of table 6 and inlet circumferential velocity 5. These figures show that the theory predicts more speed sensitivity than is shown by the experimental data. Perhaps at higher speeds, the test data will show the same trends.

Comparison to theory of [18]

Figures 100 and 101 provide a brief comparison of the present theory to the theory of Childs and Scharrer [18]. Figure 100 shows cross-coupled stiffness versus pressure ratio for a teeth-on-rotor labyrinth seal at 16000 cpm. The figure shows that the present theory follows the experimental data closely while the former theory deviates as pressure ratio is increased. Figure 101 shows direct damping versus pressure ratio for a teeth-on-rotor seal at 16000 cpm. The figure shows that the present theory follows the experimental data more closely than the former theory.

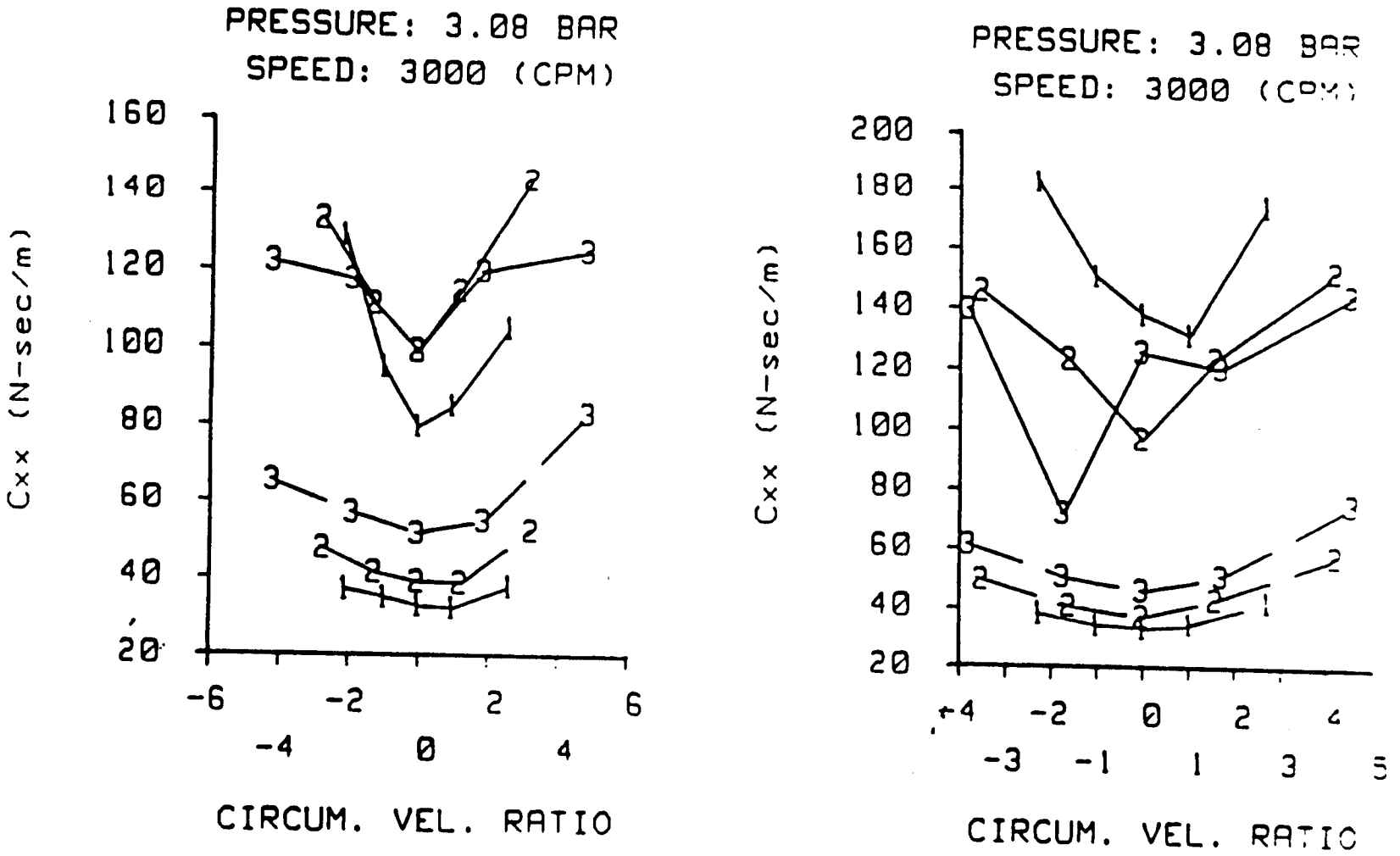

Fig. 93 A comparison of experimental and theoretical direct damping versus inlet circumferential velocity ratio at an inlet pressure of 3.08 bar and rotor speed of 3000 cpm. See table 5 for seal definitions. Teeth-on-rotor (left), teeth-on-stator (right).

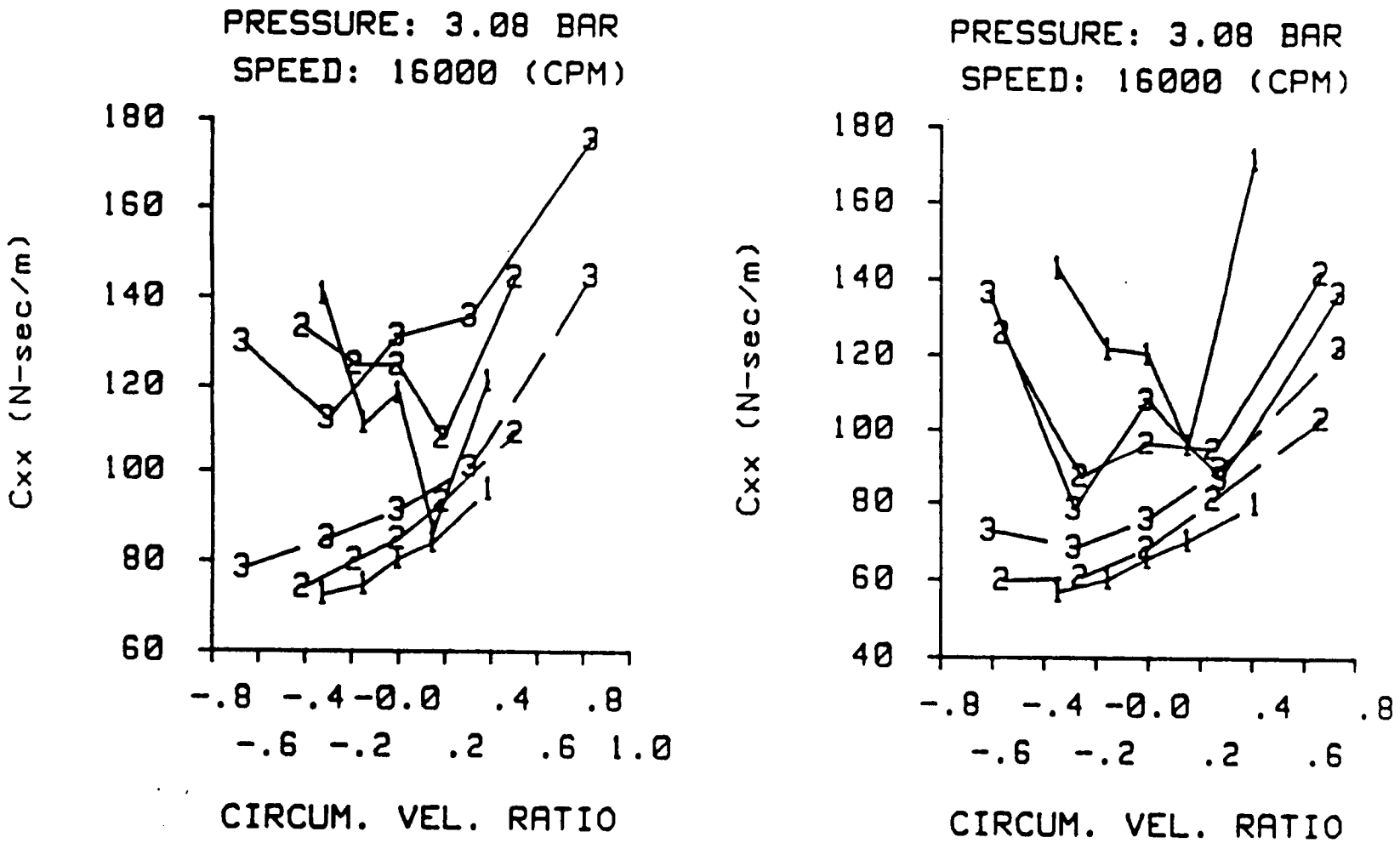

Fig. 94 A comparison of experimental and theoretical direct damping versus inlet circumferential velocity ratio at an inlet pressure of 3.08 bar and rotor speed of 16000 cpm. See table 5 for seal definitions. Teeth-on-rotor (left), teeth-on-stator (right).

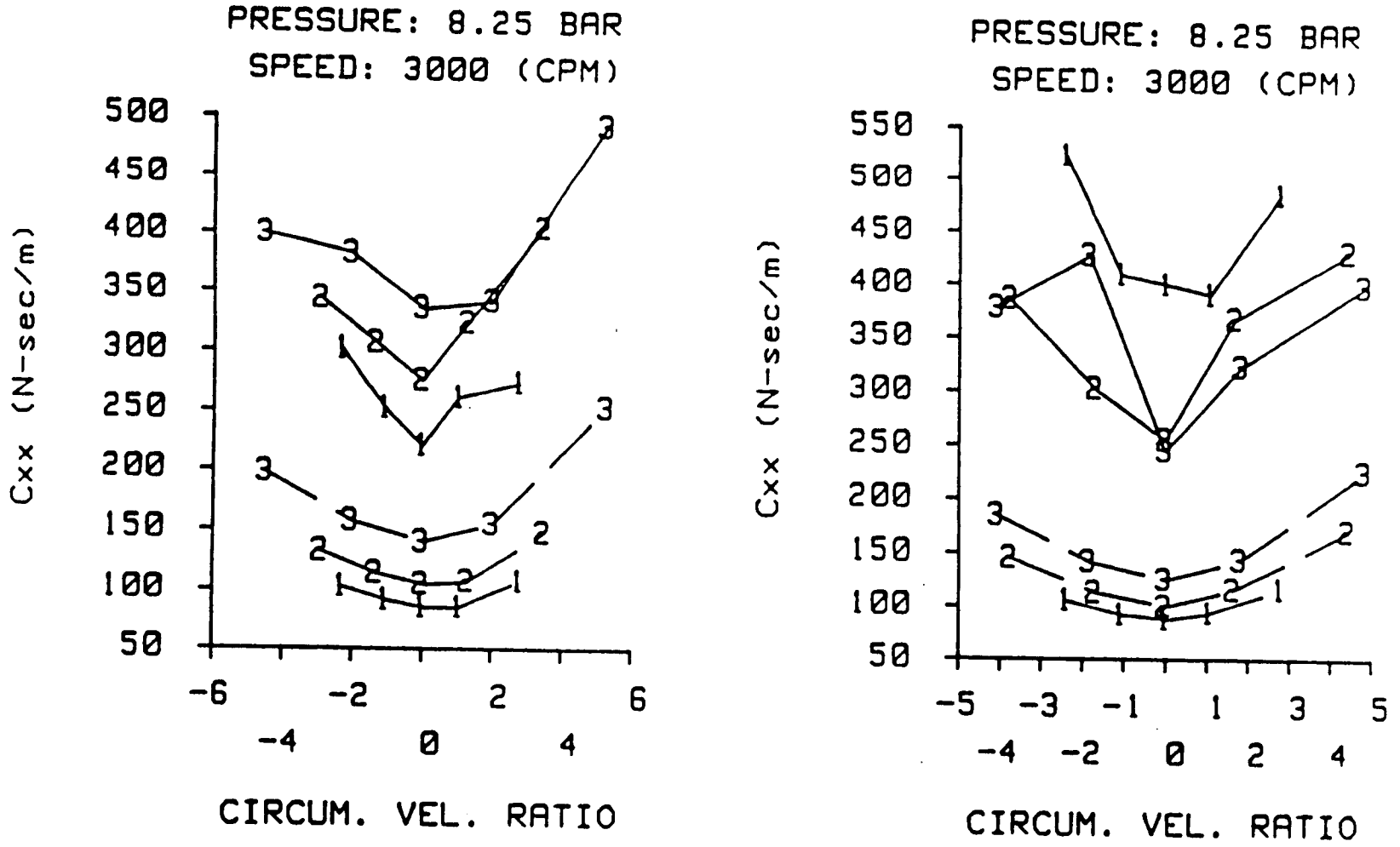

Fig. 95 A comparison of experimental and theoretical direct damping versus inlet circumferential velocity ratio at an inlet pressure of 8.25 bar and rotor speed of 3000 cpm. See table 5 for seal definitions. Teeth-on-rotor (left), teeth-on-stator (right).

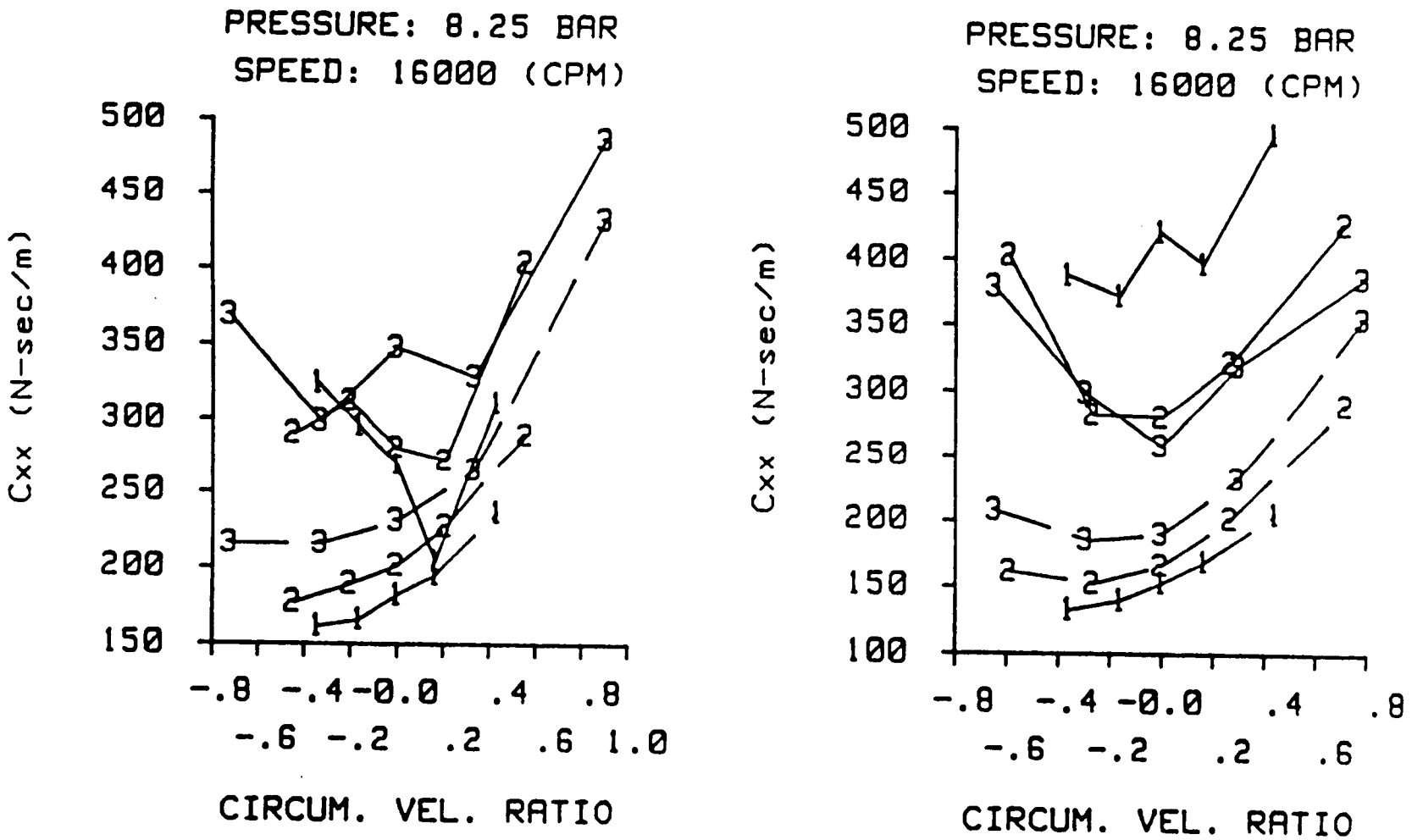

Fig. 96 A comparison of experimental and theoretical direct damping versus inlet circumferential velocity ratio at an inlet pressure of 8.25 bar and rotor speed of 16000 cpm. See table 5 for seal definitions. Teeth-on-rotor (left), teeth-on-stator (right).

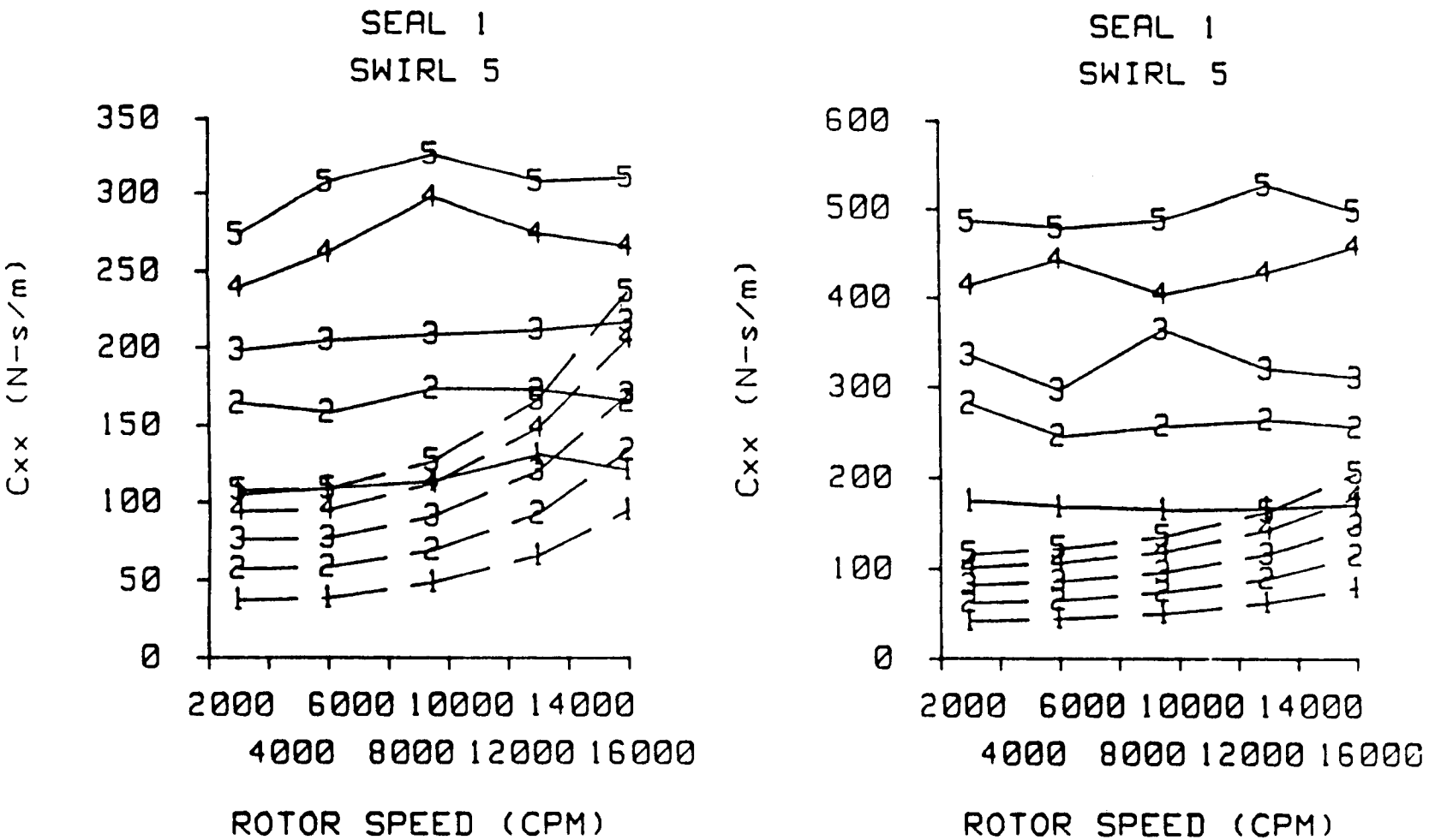

Fig. 97 A comparison of experimental and theoretical direct damping versus rotor speed for seal 1 and inlet circumferential velocity 5. See table 6 for definitions. Teeth-on-rotor (left), teeth-on-stator (right).

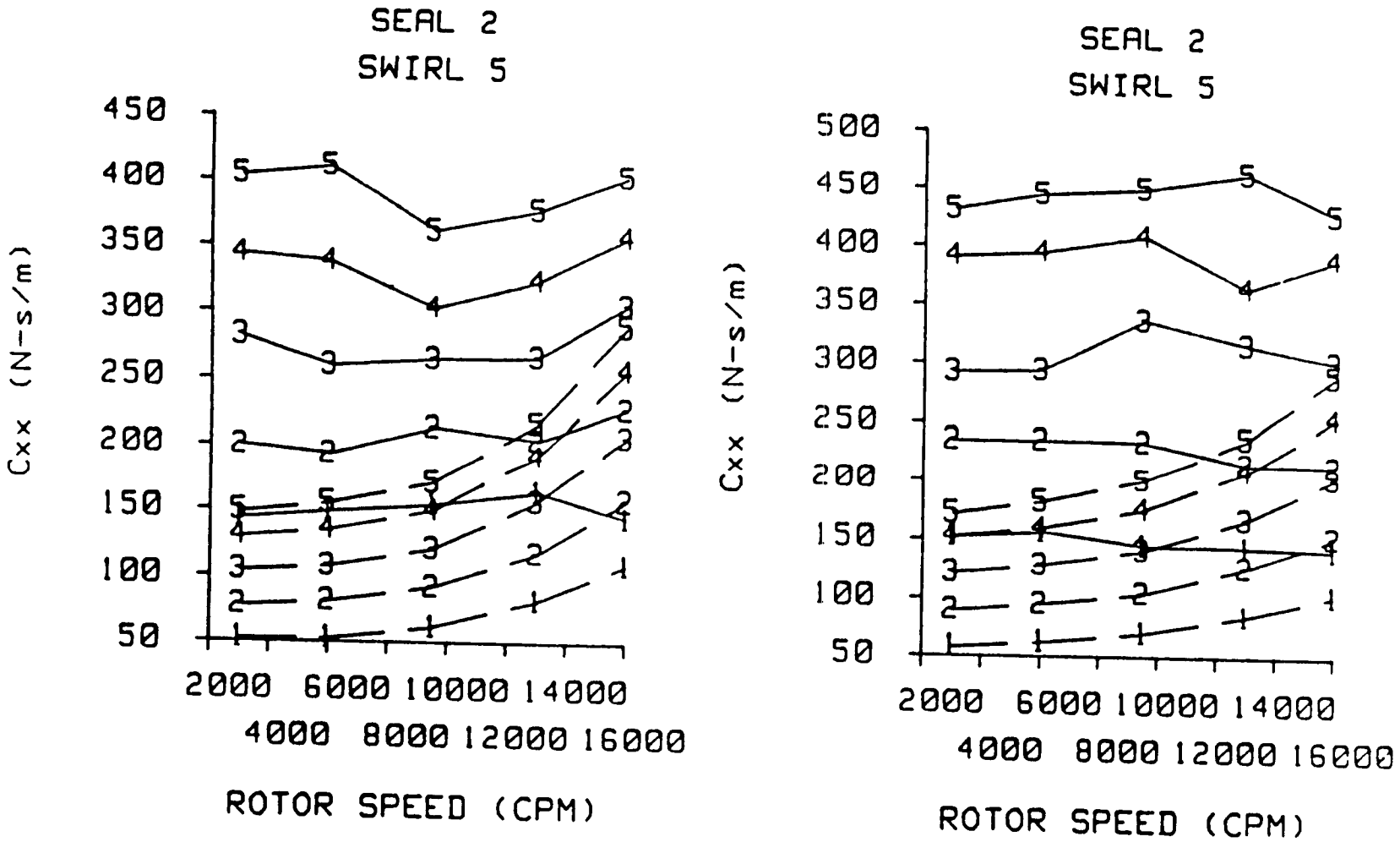

Fig. 98 A comparison of experimental and theoretical direct damping versus rotor speed for seal 2 and inlet circumferential velocity 5. See table 6 for definitions. Teeth-on-rotor (left), teeth-on-stator (right).

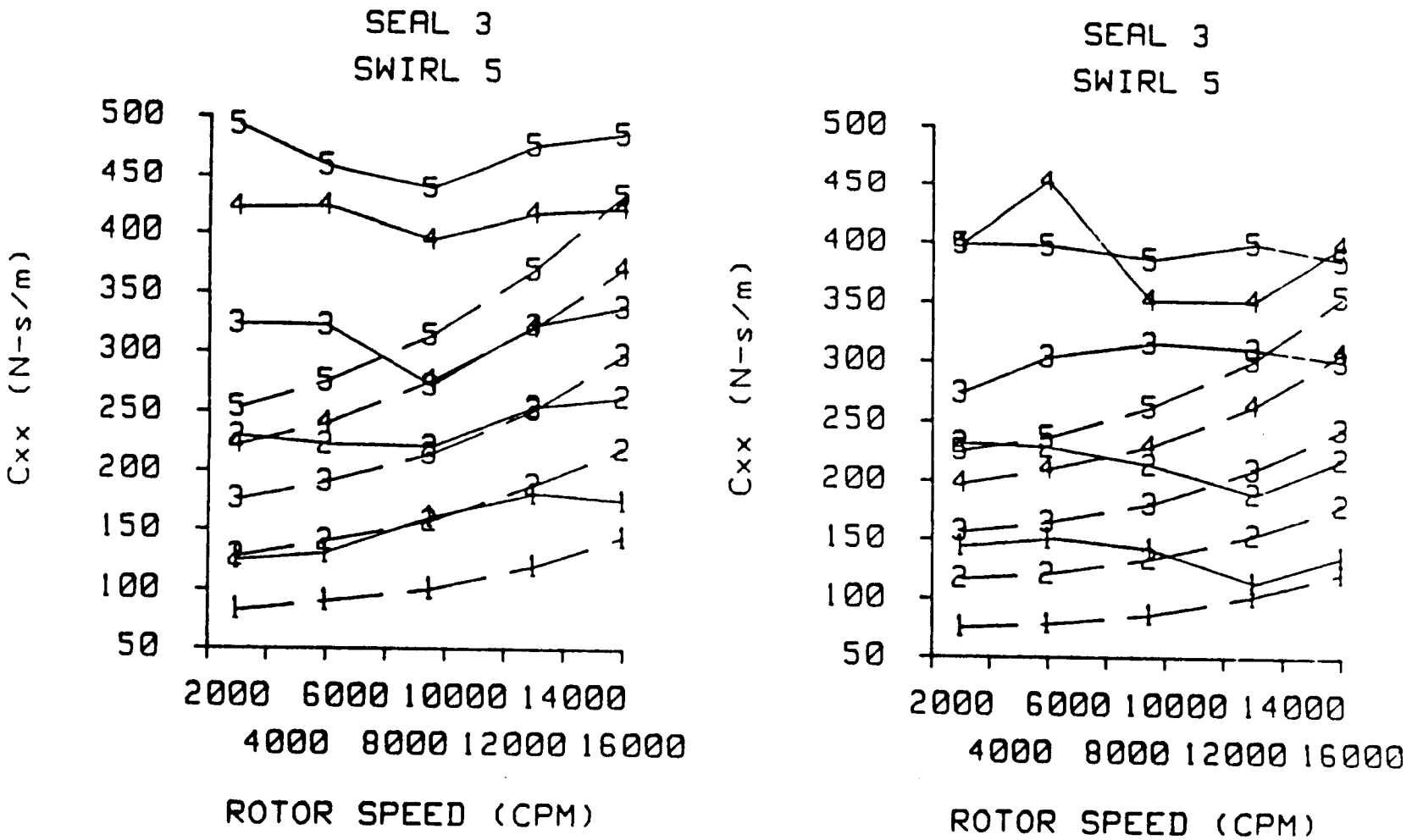

Fig. 99 A comparison of experimental and theoretical direct damping versus rotor speed for seal 3 and inlet circumferential velocity 5. See table 6 for definitions. Teeth-on-rotor (left), teeth-on-stator (right).

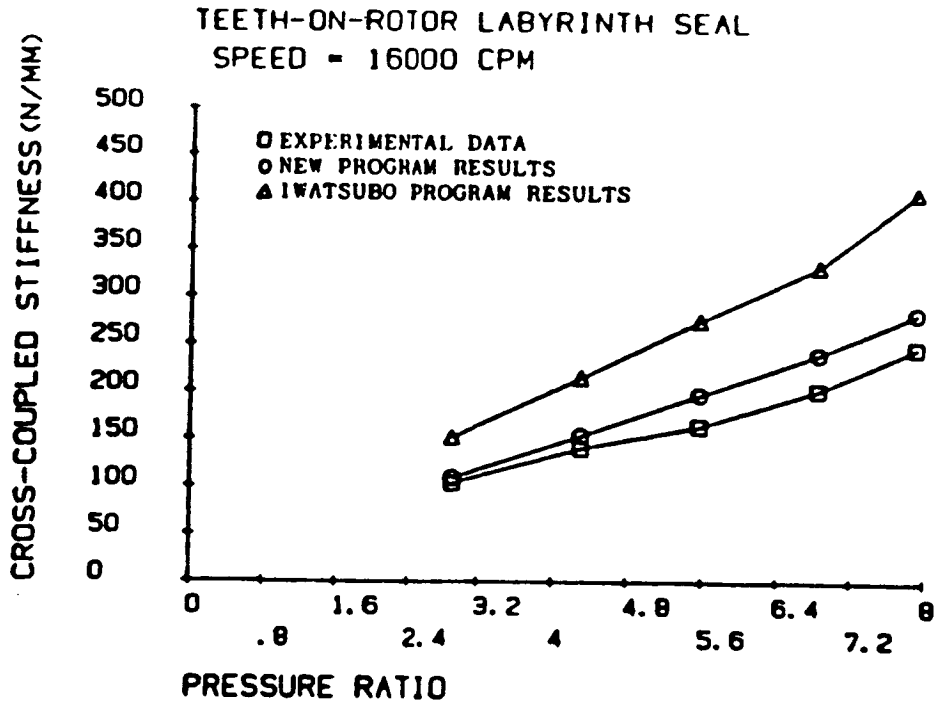

Fig. 100 A comparison of experimental and theoretical results of this report with those of [18] for cross-coupled stiffness.

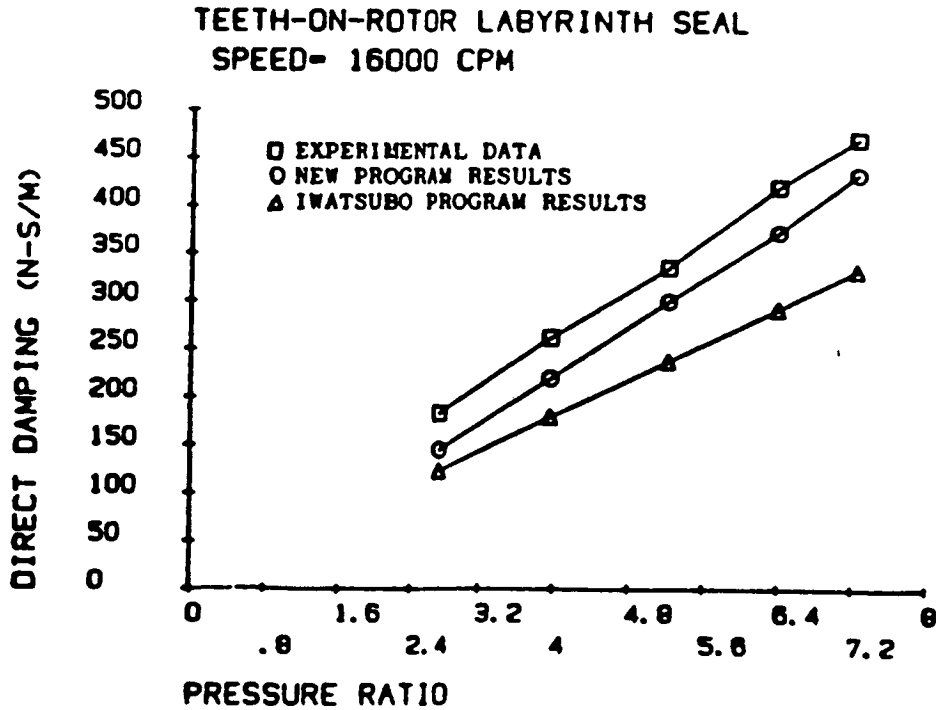

Fig. 101 A comparison of experimental and theoretical results of this report with those of [18] for direct damping.

CHAPTER VII

CONCLUSIONS

A new analysis utilizing a two control volume model which incorporates a solution for the recirculating velocity in the cavity and information from a 2-D CFD calculation, has been presented for the problem of calculating rotordynamic coefficients for labyrinth seals. This analysis was developed to provide both an improved prediction for the rotordynamic coefficients and a more detailed model for the flow in a labyrinth seal. A seal-test facility has been developed and modified for high speed testing for the study of various types of gas seals. A method for determining rotordynamic coefficients from experimental data has been established, and consistent, repeatable results have been obtained.

A comparison between the CFD results of Rhode and the results of new analysis presented in this report support the following conclusions:

(1) The new two-control-volume model accurately predicts the stator wall shear stress for a teeth-on-rotor labyrinth seal cavity.

(2) The analysis predicts the cavity wall shear stress of a teeth-on-rotor seal within 25% of the average of the CFD result.

(3) The 2-D jet flow theory used in this analysis accurately predicts magnitude of the recirculation velocity along the dividing streamline.

(4) The CFD results show that the mixing length parameter, ℓ, used in the equation for the free shear stress is relatively constant,

for teeth-on-rotor seals, and need not be considered a function of seal geometry, as was assumed by Jenny et al. [21].

The experimental results of the previous section support the following conclusions:

(1) For teeth-on-rotor seals the direct damping increases as clearance increases; for teeth-on-stator seals, the direct damping decreases as clearance increases.

(2) Direct stiffness and direct damping show little or no sensitivity to rotor speed up to 16000 cpm. Cross-coupled stiffness shows a sharp upswing at higher rotor speeds, for a teeth-on-rotor seal. Cross-coupled stiffness decreases as rotor speed increases, for a teeth-on-stator seal.

(3) Direct stiffness is negative and increases as clearance increases, for both seal configurations. Cross-coupled stiffness showed no consistent trend with respect to clearance changes.

(4) As clearance decreases, teeth-on-rotor seals become less stable and teeth-on-stator seals become more stable.

The theoretical results of the previous section support the following conclusions:

(1) Theoretical results for leakage underpredict the test results presented in this report by about 25%. Leakage increases as clearance increases for both seal types.

(2) Theoretical results for pressure gradient are underestimated for teeth-on-rotor seals and overestimated for teeth-on-stator seals.

(3) The theory correctly predicts that direct stiffness is negative and increases as clearance increases, for both seal

configurations. The theory incorrectly predicts an approximately quadratic increase in the direct stiffness magnitude (becoming more negative) as speed increases. Test results show scant sensitivity.

(4) The theory accurately predicts an increase in cross-coupled stiffness at high speeds, for a teeth-on-rotor seal.

(5) For teeth-on-rotor seals, the theory correctly predicts an increase in direct damping for an increase in clearance. However, the theory incorrectly predicts the same trend for a teeth-on-stator seal.

(6) The theory incorrectly predicts an approximately quadratic increase in direct damping with running speed. Test results show no systematic change in direct damping with running speed.

(7) A comparison with test results for a teeth-on-rotor seal shows that the theory presented in this report does a better job of predicting direct damping and cross-coupled stiffness than does the theory of Childs and Scharrer [18]. A comparison with the theory of Jenny et al. [21] was not possible, as discussed in the THEORETICAL DEVELOPMENT chapter of this report.

In summary, the analysis presented here is considered useful for predicting cross-coupled stiffness for both teeth-on-rotor and teeth-on-stator labyrinth seals directly. These results were reasonable and consistent for the various geometries and operating conditions presented. However, the results for the direct damping coefficient for teeth-on-stator labyrinth seals were not consistent with test results for clearance change effects. This discrepancy renders the analysis suspect for predicting these coefficients for teeth-on-stator seals whose geometry differs significantly from the seals tested in this

study. Predictions for the remaining coefficients can be modified using the appropriate correction factor from the comparison plots presented in this study.

In the future, if any advances are to be made in the prediction of rotordynamic coefficients for labyrinth gas seals, they will probably involve the perturbation of a finite difference solution. The "bulk flow" model presented in this report is too crude to model the complex flowfield present in a labyrinth cavity.

REFERENCES

1. Wachter, J., and Benckert, H., "Querkrafte aus Spaltdichtungen-Eine mogliche Ursache fur die Laufunruhe von Turbomaschinen," Atomkernenergie Bd. 32, 1978, Lfg. 4, pp. 239-246.

2. Wachter, J., and Benckert, H., "Flow Induced Spring Coefficients of Labyrinth Seals for Applications in Rotordynamic," NASA CP 2133 Proceedings of a workshop held at Texas A&M University 12-14 May 1980, Entitled Rotordynamic Instability Problems of High Performance Turbomachinery, pp. 189-212.

3. Benckert, H., "Stromungsbedinte Federkennwerte in Labyrinthdichtungen," Doctoral dissertation at University of Stuttgart, 1980.

4. Wright, D.V., "Labyrinth Seal Forces on a Whirling Rotor," Rotor Dynamical Instability. Proceedings of the ASME Applied Mechanics, Bioengineering, and Fluids Engineering Conference, June 20-22, 1983, Houston, Texas. pp. 19-31.

5. Brown, R.D, and Leong, Y.M.M.S, " Experimental Investigation of Lateral Forces Induced by Flow Through Model Labyrinth Glands," NASA CP 2338, Rotordynamic Instability Problems in High Performance Turbomachinery, proceedings of a workshop held at Texas A&M University 28-30 May, 1984. pp. 187-210.

6. Childs, D.W. and Scharrer, J.K., "Experimental Rotordynamic Coefficient Results for Teeth-On-Rotor and Teeth-On-Stator Labyrinth Gas Seals," ASME Paper No. 86-GT-12.

7. Kanemitsu, Y. and Ohsawa, M., "Experimental Study on Flow Induced Force of Labyrinth Seal," Proceedings of the Post IFToMM Conference on Flow Induced Force in Rotating Machinery, September 18-19, 1986, Kobe University, Kobe, Japan, pp. 106-112.

8. Hisa, S., Sakakida, H., Asatu, S. and Sakamoto, T., "Steam Excited Vibration in Rotor-Bearing System," Proceedings of the International Conference on Rotordynamics, September 14-17, 1986, Tokoyo, Japan, pp. 635-641.

9. Alford, J. S., "Protecting Turbomachinery from Self-Excited Rotor Whirl," Transactions ASME J. of Engineering for Power, October 1965, pp. 333-344.

10. Spürk, J. H., and Keiper, R., "Selbsterregte Schwingungen bei Turbomaschinen infolge der Labyrinthstromung," Ingerieur-Archive 43, 1974, pp. 127-135.

11. Vance, J. M., and Murphy, B. T., "Labyrinth Seal Effects on Rotor Whirl Stability," Inst. of Mechanical Engineer, 1980, pp. 369-373.

12. Kostyuk, A. G., "A Theoretical Analysis of the Aerodynamic Forces in the Labyrinth Glands of Turbomachines," Teploenergetica, 19 (11)0, 1972, pp. 39-44.

13. Iwatsubo, T., "Evaluation of Instability Forces of Labyrinth Seals in Turbines or Compressors," NASA CP 2133 Proceedings of a workshop at Texas A&M University 12-14 May 1980, Entitled Rotordynamic Instability Problems in High Performance Turbomachinery, pp. 139-167.

14. Iwatsubo, T., Matooka, N., and Kawai, R., "Flow Induced Force and Flow Pattern of Labyrinth Seal," NASA CP 2250 Proceedings of a workshop at Texas A&M University 10-12 May 1982, Entitled Rotordynamic Instability Problems in High Performance Turbomachinery, pp. 205-222.

15. Kurohashi, M., Inoue, Y., Abe, T., and Fujikawa, T., "Spring and Damping Coefficients of the Labyrinth Seal," Paper No. C283/80 delivered at the Second International Conference on Vibrations in Rotating Machinery, The Inst. of Mech. Engineering.

16. Gans, B.E, "Prediction of the Aero-Elastic Force in a Labyrinth Type Seal and its Impact on Turbomachinery Stability," M.S. Thesis M.I.T., 1983.

17. Martinez-Sanchez, M., Lee, O.W.K., Czajkowski, E., "The Prediction of Force Coefficients for Labyrinth Seals," NASA CP 2338, Rotordynamic Instability Problems in High Performance Turbomachinery, proceedings of a workshop held at Texas A&M University 28-30 may, 1984. pp. 235-256.

18. Childs, D.W., and Scharrer, J.K., "An Iwatsubo Based Solution for Labyrinth Seals: A Comparison to Experimental Results," ASME Trans. Journal of Engineering for Gas Turbines and Power, April 1986, Vol. 108, pp. 325-331

19. Hauck, L., "Exciting Forces due to Swirl-Type Flow in Labyrinth Seals," Proceedings IFTOMM Conference on Rotordynamic Problems in Power Plants, 28 September-1 October 1981.

20. Fujikawa, T., Kameoka, T., Abe, T., "A Theoretical Approach to Labyrinth Seal Forces," NASA CP 2338, Rotordynamic Instability Problems in High Performance Turbomachinery, proceedings of workshop held at Texas A&M University 28-30 May, 1984. pp.173-186.

21. Jenny, R.J., Wyssmann, H.P., Pham, T.C., "Prediction of Stiffness and Damping Coefficients for Centrifugal Compressor Labyrinth Seals," ASME 84-GT-86. Presented at the 29th International Gas Turbine Conference and Exhibit, Amsterdam, The Netherlands, June 4-7, 1984.

22. Scharrer, J.K., "A Comparison of Experimental and Theoretical Results for Rotordynamic Coefficients for Labyrinth Gas Seals," TRC Report SEAL-2-85, Texas A&M University, May 1985.

23. Rhode, D., Private correspondence, Texas A&M University, 1985.

24. Rhode, D., "Simulation of Subsonic Flow Through a Generic Labyrinth Seal Cavity," ASME Paper No. 85-GT-76.

25. Stoff, H., "Incompressible Flow in a Labyrinth Seal," Journal of Fluid Mechanics, Vol. 100, part 4, pp. 817-829, 1980.

26. Korst, H.H., Page, R.H., and Childs, M.E., Univ. of Illinois Eng. Exp. Report ME TN 392-1, Urbana, Illinois, April 1954.

27. Liepman, H.W. and Laufer, J., NACA TN1257, 1947.

28. Korst, H.H. and Tripp, W., "The Pressure on a Blunt Trailing Edge Separating Two Supersonic Two-Dimensional Airstreams of Different Mach Number and Stagnation Pressure But Identical Stagnation Temperature," Proceedings of the 5th Midwestern Conference on Fluid Mechanics, University of Michigan Press, Ann Arbor, Michigan pp. 187-200, 1957.

29. Goertler, H., Z. Angew Math. Mech., 22, pp. 244-254, 1942.

30. Glauert, M.B., "The Wall Jet," Journal of Fluid Mechanics, 1, pp. 625, 1956.

31. Schlichting, H., Boundary Layer Theory, McGraw-Hill, New York, NY, pp.621, 1979.

32. Nelson, C.C. and Nguyen, D.T., "Comparison of Hirs' Equation with Moody's Equation for Determining Rotordynamic Coefficients of Annular Pressure Seals," ASME Paper No. 86-TRIB-19, also accepted for the ASME Journal of Tribology.

33. Blasius, H., "Forschungoarb", Ing.-Wes., No 131, 1913.

34. Yamada, Y., Trans. Japan Soc. Mechanical Engineers, Vol. 27, No. 180, 1961, pp. 1267.

35. Abramovich, G.N., The Theory of Turbulent Jets, MIT Press, Cambridge, Massachusetts, 1963.

36. Schlichting, H., Boundary Layer Theory, McGraw-Hill, New York, NY, pp. 579, 1979.

37. Jerie, J., "Flow Through Straight-Through Labyrinth Seals," Proceedings of the 7th International Congress on Applied Mechanics, Vol.2, pp. 70-82, 1948.

38. Komotori, K. and Mori, H., "Leakage Characteristics of Labyrinth Seals," Fifth International Conference on Fluid Sealing, 1971, Paper E4, pp. 45-63.

39. Wyssmann, H.R., "Theory and Measurements of Labyrinth Seal Coefficients for Rotor Stability of Turbocompressors," Proceedings of a workshop at Texas A&M University 2-4 June 1986, Entitled Rotordynamic Instability Problems in High Performance Turbomachinery (in press).

40. Vermes, G., "A Fluid Mechanics Approach to the Labyrinth Seal Leakage Problem," ASME Journal of Engineering for Power, Vol. 83, No. 2, April 1961, pp. 161-169.

41. Gurevich, M.I., The Theory Of Jets In An Ideal Fluid, Pergamon Press, London, England, 1966, pp. 319-323.

42. Egli, A.: The Leakage of Steam Through Labyrinth Glands, Trans. ASME, Vol. 57, 1935, pp. 115-122.

43. John, J.E.A, Gas Dynamics, Wylie, New York, NY, 1979.

44. Iino, T., and Kaneko, H., "Hydraulic Forces Caused by Annular Pressure Seals in Centrifugal Pumps," NASA CP 2133, Rotordynamic Instability Problems in High Performance Turbomachinery, proceedings of a workshop held at Texas A&M Univ., 12-14 May 1980.

45. Bowen, W.L., and Bhateje, R., "The Hollow Roller Bearing," ASME Paper No. 79-LUB-15, ASME-ASLE Lubrication Conference, Dayton, Ohio, 16-18 October 1979.

46. Cohen, H., Rogers, G.F.C., and Saravanamuttoo, H.I.H., Gas Turbine Theory, Longman Group Limited, London, England, 1972.

47. Nicks, C.O.,"A Comparison of Experimental and Theoretical Results for Leakage, Pressure Distribution, and Rotordynamic Coefficients for Annular Gas Seals," M.S. Thesis, Texas A&M University, 1984.

48. Nelson, C.,Childs, D.W., Nicks, C.O., Elrod, D.," Theory Versus Experiment for the Rotordynamic Coefficients of Annular Gas Seals: Part 2. Constant-Clearance and Convergent-Tapered Geometry," ASME Journal of Tribology, Vol. 108, pp. 433-438, July 1986.

49. Holman, J.P., Experimental Methods for Engineers, McGraw-Hill, New York, NY, 1978, pp. 45.

50. Childs, D.W., Scharrer, J.K., and Hale, R.K., "Rotordynamic Coefficients for Sulzer Teeth-On-Stator Labyrinth Gas Seal," Texas A&M Univ. Turbomachinery Lab. Report TRC-SEAL-3-86, 1986.

51. Schlichting, H., Boundary Layer Theory, McGraw-Hill, New York, NY, pp. 328, 1979.

C.3

APPENDIX A

GOVERNING EQUATIONS FOR TEETH-ON-STATOR SEAL

Reduced Equations

The main difference between the teeth-on-stator equations and the teeth-on-rotor equations occurs in the momentum equations. The shear stresses acting on control volume I are now the rotor shear stress, τ_r, and the free shear stress, τ_j. Similarly, the shear stresses acting on control volume II are now the stator shear stress, τ_s, and the free shear stress, τ_j. These difference are evident in the reduce form of the continuity and momentum equations given below:

Continuity I

$$\frac{\partial \rho A_1}{\partial t} + \frac{\partial \rho W_1 A_1}{Rs_1 \partial \theta} + \dot{m}_{i+1} - \dot{m}_i + \frac{\partial \rho A_2}{\partial t} + \frac{\partial \rho W_2 A_2}{Rs_2 \partial \theta} = 0 \qquad (A1)$$

Momentum I

$$\rho A_1 \frac{\partial W_1}{\partial t} + \frac{\rho W_1 A_1}{Rs_1} \frac{\partial W_1}{\partial \theta} + \left[\frac{\partial \rho A_2}{\partial t} + \frac{\partial W_2 A_2 \rho}{Rs_2 \partial \theta}\right](W_{oi}-W_{1i}) \qquad (A2)$$

$$+ \dot{m}_i(W_{1i}-W_{1i-1}) = -\frac{A_1}{Rs_1}\frac{\partial P_i}{\partial \theta} + \tau_{ji} L_i + \tau_{ri} ar_i L_i$$

Momentum II

$$\rho A_2 \frac{\partial W_2}{\partial t} + \frac{\rho W_2 A_2}{Rs_2} \frac{\partial W_2}{\partial \theta} + \left[\frac{\partial \rho A_2}{\partial t} + \frac{\partial \rho W_2 A_2}{Rs_2 \partial \theta}\right](W_{2i}-W_{oi}) \qquad (A3)$$

$$= -\frac{A_2}{Rs_2}\frac{\partial P_i}{\partial \theta} - \tau_{ji} L_i - \tau_{si} as_i L_i$$

where as_i and ar_i are defined as

$$as_i = (2B+L)/L \quad ; \quad ar_i = 1.0$$

The rotor shear stress in the circumferential direction is now defined using the smaller hydraulic diameter and the velocity components of control volume I.

$$\tau_r = \frac{1}{2}\rho\sqrt{(Rs_1\omega-W_1)^2+U_1^2}\,(Rs_1\omega-W_1)\,nr\left(\frac{\sqrt{(Rs_1\omega-W_1)^2+U_1^2}\,Dh_{1i}}{\nu}\right)^{mr} \quad (A4)$$

where Dh_{1i} is the hydraulic diameter of C.V. I, defined by

$$Dh_{1i} = 2Cr_iL/(Cr_i+L) \quad (A5)$$

Similarly, the stator shear stress in the circumferential direction is now defined using the larger hydraulic diameter and the velocity components of control volume II.

$$\tau_s = \frac{1}{2}\rho\sqrt{W_2^2+U_2^2}\,W_2\;\; ns\left(\frac{\sqrt{W_2^2+U_2^2}\,Dh_{2i}}{\nu}\right)^{ms} \quad (A6)$$

where Dh_{2i} is the hydraulic diameter of C.V. II, defined by

$$Dh_{2i} = 2BL/(B+L) \quad (A7)$$

The definition of the free shear stress remains the same. However, since CFD results were only available for the teeth-on-rotor configuration, the sensitive mixing length ratio ℓ/b may change for a teeth-on-stator seal.

Zeroth-Order Equations

Continuity: $$\dot{m}_{oi+1} = \dot{m}_{oi} \quad (A8)$$

Momentum I: $$\dot{m}_{oi}(W_{1oi}-W_{1oi-1}) = (\tau_{jio}+\tau_{rioari})L_i \quad (A9)$$

Momentum II: $$\tau_{jio}L_i = -\tau_{sioasi}L_i \quad (A10)$$

First-Order Equations

The first-order equations remain exactly the same as before. Since changes were made in the locations and definitions of the rotor and stator shear stress terms, the following changes in the coefficients of the first-order equations are necessary:

$$X_4 = -\frac{\dot{m}_o(W_{1i}-W_{1i-1})P_{oi}}{P_{oi-1}^2 - P_{oi}^2} + \frac{\dot{m}_o(W_{1i}-W_{1i-1})}{\pi P_{oi}}\mu_{1i}(4S_{1i}-5)\left(\frac{\gamma-1}{\gamma}\right)(S_{1i}+1) - \frac{\tau_{jiL_i}}{P_{oi}}$$

$$- \left[\frac{\tau_{ri}(1+mr)U_{1i}L_i a r_i}{(Rs\omega - W_{1i})^2 + U_{1i}^2} + \frac{\tau_{ji}(U_{2i}-U_{1i})L_i(\phi-1)}{(W_{2i}-W_{1i})^2+(U_{2i}-U_{1i})^2}\right]$$

$$x\left[\frac{-U_{1i}}{P_{oi}} - \frac{U_{1i}\,P_{oi}}{P_{oi-1}^2 - P_{oi}^2} + \frac{\mu_{1i}U_{1i}(4S_{1i}-5)}{\pi P_{oi}}\left(\frac{\gamma-1}{\gamma}\right)(S_{1i}+1)\right] - \frac{\tau_{ri}(1+mr)L_i}{P_{oi}}$$

$$X_5 = \frac{\dot{m}_o(W_{1i}-W_{1i-1})P_{oi-1}}{P_{oi-1}^2 - P_{oi}^2} - \frac{\dot{m}_o(W_{1i}-W_{1i-1})}{\pi P_{oi}}\mu_{1i}(4S_{1i}-5)\left(\frac{\gamma-1}{\gamma}\right)\left(\frac{P_{oi-1}}{P_{oi}}\right)^{\frac{-1}{\gamma}}$$

$$- \left[\frac{\tau_{ri}(1+mr)U_{1i}L_i a r_i}{(Rs\omega - W_{1i})^2 + U_{1i}^2} + \frac{\tau_{ji}(U_{2i}-U_{1i})L_i(\phi-1)}{(W_{2i}-W_{1i})^2+(U_{2i}-U_{1i})^2}\right]$$

$$x\left[\frac{U_{1i}\,P_{oi-1}}{P_{oi-1}^2 - P_{oi}^2} - \frac{\mu_{1i}U_{1i}(4S_{1i}-5)}{\pi P_{oi}}\left(\frac{\gamma-1}{\gamma}\right)\left(\frac{P_{oi-1}}{P_{oi}}\right)^{\frac{-1}{\gamma}}\right]$$

$$X_6 = \dot{m}_o + \frac{\tau_{ri}L_i a r_i}{Rs\omega - W_{1i}} + \frac{\tau_{ri}(1+mr)(Rs\omega - W_{1i})L_i a r_i}{(Rs\omega - W_{1i})^2 + U_{1i}^2} + \frac{\tau_{ji}L_i}{W_{2i}-W_{1i}}$$

$$+ \frac{\tau_{ji}(W_{2i}-W_{1i})L_i}{(W_{2i}-W_{1i})^2+(U_{2i}-U_{1i})^2}$$

$$X_8 = \frac{\dot{m}_o(W_{1i}-W_{1i-1})}{Cr_i}\left[1 + \frac{(L_i - Tp_i)}{17.04Cr_i}\left(\frac{\mu_{2i-1}^2}{\mu_{2i}}\right)^2\right] - \frac{\tau_{ri}a r_i L_i mr Dh_{1i}}{2Cr_i^2}$$

$$Y_4 = \left[\frac{-U_{1i}}{P_{oi}} - \frac{U_{1i}\,P_{oi}}{P_{oi-1}^2 - P_{oi}^2} + \frac{\mu_{1i}U_{1i}(4S_{1i}-5)}{\pi P_{oi}}\left(\frac{\gamma-1}{\gamma}\right)(S_{1i}+1)\right]$$

$$X\left[\frac{\tau_{ji}(U_{2i}-U_{1i})L_i(\phi-1)}{(W_{2i}-W_{1i})^2+(U_{2i}-U_{1i})^2} + \frac{\tau_{si}(1+ms)\phi U_{2i}a s_i L_i}{W_{2i}^2 + U_{2i}^2}\right] + \frac{\tau_{ji}L_i}{P_{oi}} - \frac{\tau_{si}(1+ms)a s_i L_i}{P_{oi}}$$

$$Y_5 = \frac{\tau_{si}a s_i L_i}{W_{2i}} + \frac{\tau_{si}(1+ms)W_{2i}a s_i L_i}{W_{2i}^2 + U_{2i}^2} + \frac{\tau_{ji}L_i}{W_{2i}-W_{1i}} + \frac{\tau_{ji}L_i(W_{2i}-W_{1i})}{(W_{2i}-W_{1i})^2+(U_{2i}-U_{1i})^2}$$

$$Y_6 = \left[\frac{U_{1i}\,P_{oi-1}}{P_{oi-1}^2 - P_{oi}^2} - \frac{\mu_{1i}U_{1i}(4S_{1i}-5)}{\pi\, P_{oi}}\left(\frac{\gamma-1}{\gamma}\right)\left(\frac{P_{oi-1}}{P_{oi}}\right)^{\frac{-1}{\gamma}}\right]$$

$$x\left[\frac{\tau_{ji}(U_{2i}-U_{1i})L_i(\phi-1)}{(W_{2i}-W_{1i})^2+(U_{2i}-U_{1i})^2} + \frac{\tau_{si}(1+ms)\phi U_{2i}a s_i L_i}{W_{2i}^2 + U_{2i}^2}\right]$$

APPENDIX B

DEFINITION OF THE FIRST ORDER CONTINUITY AND MOMENTUM EQUATION COEFFICIENTS

$$G_1 = \frac{L_i(Cr_i+B_i)}{RT}; \quad G_2 = \frac{Cr_iW_{1i}L_i}{RTRs_1} + \frac{B_iL_iW_{2i}}{RTRs_2}; \quad G_3 = \frac{Po_iL_iCr_i}{RTRs_1}; \quad G_4 = \frac{Po_iB_iL_i}{RTRs_2}$$

$$G_5 = \frac{\dot{m}_o\, Po_i}{Po_{i-1}^2 - Po_i^2} + \frac{\dot{m}_o\, \mu_{1i+1}}{\pi}(5 - 4S_{1i+1})\left(\frac{\gamma-1}{\gamma Po_{i+1}}\right)\left(\frac{Po_i}{Po_{i+1}}\right)^{\frac{-1}{\gamma}}$$

$$+ \frac{\dot{m}_o\, \mu_{1i}}{\pi}(5 - 4S_{1i})\left(\frac{\gamma-1}{\gamma Po_i}\right)\left(\frac{Po_{i-1}}{Po_i}\right)^{\frac{\gamma-1}{\gamma}} + \frac{\dot{m}_o\, Po_i}{Po_i^2 - Po_{i+1}^2}$$

$$G_6 = \frac{-\dot{m}_o\, Po_{i-1}}{Po_{i-1}^2 - Po_i^2} - \frac{\dot{m}_o\, \mu_{1i}}{\pi}(5 - 4S_{1i})\left(\frac{\gamma-1}{\gamma Po_i}\right)\left(\frac{Po_{i-1}}{Po_i}\right)^{\frac{-1}{\gamma}}$$

$$G_7 = \frac{-\dot{m}_o\, Po_{i+1}}{Po_i^2 - Po_{i+1}^2} - \frac{\dot{m}_o\, \mu_{1i+1}}{\pi}(5 - 4S_{1i+1})\left(\frac{\gamma-1}{\gamma Po_{i+1}}\right)\left(\frac{Po_i}{Po_{i+1}}\right)^{\frac{\gamma-1}{\gamma}}$$

$$G_8 = \frac{\dot{m}_o(Cr_i - Cr_{i+1})}{Cr_iCr_{i+1}} - \frac{\dot{m}_o(L_i - Tp_i)}{17.04Cr_i^2}\left(\frac{\mu_{2i}^2-1}{\mu_{2i}}\right)^2 + \frac{\dot{m}_o(L_{i+1} - Tp_{i+1})}{17.04Cr_{i+1}}\left(\frac{\mu_{2i+1}^2-1}{\mu_{2i+1}}\right)^2$$

$$G_9 = \frac{Po_iL_i}{RT}; \quad G_{10} = \frac{Po_iW_{1i}L_i}{RTRs_1};$$

$$X_1 = \frac{Po_iCr_iL_i}{RT}; \quad X_2 = \frac{Cr_iL_i}{Rs_1}; \quad X_3 = \frac{B_iL_i}{RT}(W_{oi} - W_{1i})$$

$$X_4 = \frac{-\dot{m}_o(W_{1i} - W_{1i-1})Po_i}{Po_{i-1}^2 - Po_i^2} + \frac{\dot{m}_o(W_{1i} - W_{1i-1})}{\pi Po_i}\mu_{1i}(4S_{1i}-5)\left(\frac{\gamma-1}{\gamma}\right)(S_{1i}+1) - \frac{\tau_{ji}L_i}{Po_i}$$

$$+ \left[\frac{\tau_{si}(1+ms)U_{1i}L_ia_{si}}{W_{1i}^2 + U_{1i}^2} - \frac{\tau_{ji}(U_{2i} - U_{1i})L_i(\phi-1)}{(W_{2i} - W_{1i}) + (U_{2i} - U_{1i})^2}\right]$$

$$x\left[\frac{-U_{1i}}{Po_i} - \frac{U_{1i}\, Po_i}{Po_{i-1}^2 - Po_i^2} + \frac{\mu_{1i}U_{1i}(4S_{1i}-5)}{\pi Po_i}\left(\frac{\gamma-1}{\gamma}\right)(S_{1i}+1)\right] + \frac{\tau_{si}(1+ms)L_i}{Po_i}$$

$$X_5 = \frac{\dot{m}_o(W_{1i} - W_{1i-1})Po_{i-1}}{Po_{i-1}^2 - Po_i^2} - \frac{\dot{m}_o(W_{1i} - W_{1i-1})}{\pi Po_i}\mu_{1i}(4S_{1i}-5)\left(\frac{\gamma-1}{\gamma}\right)\left(\frac{Po_{i-1}}{Po_i}\right)^{\frac{-1}{\gamma}}$$

$$+\left[\frac{\tau_{si}(1+ms)U_{1i}L_i as_i}{W_{1i}^2+U_{1i}^2}-\frac{\tau_{ji}(U_{2i}-U_{1i})L_i(\phi-1)}{(W_{2i}-W_{1i})^2+(U_{2i}-U_{1i})^2}\right]$$

$$\times\left[\frac{U_{1i}}{P_{oi-1}}\frac{P_{oi-1}}{P_{oi}}-\frac{\mu_{1i}U_{1i}(4S_{1i}-5)}{\pi P_{oi}}\frac{\gamma-1}{\gamma}\left(\frac{P_{oi-1}}{P_{oi}}\right)^{\frac{-1}{\gamma}}\right]$$

$$X_6=\dot{m}_o+\frac{\tau_{si}L_i as_i}{W_{1i}}+\frac{\tau_{si}(1+ms)W_{1i}L_i as_i}{W_{1i}^2+U_{1i}^2}+\frac{\tau_{ji}L_i}{W_{2i}-W_{1i}}+\frac{\tau_{ji}(W_{2i}-W_{1i})L_i}{(W_{2i}-W_{1i})^2+(U_{2i}-U_{1i})^2}$$

$$X_7=\frac{-\tau_{ji}L_i}{W_{2i}-W_{1i}}-\frac{\tau_{ji}L_i(W_{2i}-W_{1i})}{(W_{2i}-W_{1i})^2+(U_{2i}-U_{1i})^2};$$

$$X_8=\frac{\dot{m}_o(W_{1i}-W_{1i-1})}{Cr_i}\left[1+\frac{(L_i-Tp_i)}{17.04Cr_i}\frac{\mu_{2i}^2-1^2}{\mu_{2i}}\right]-\frac{\tau_{si}as_iL_imsDh_{1i}}{2Cr_i}$$

$$Y_1=\frac{P_{oi}L_iB_i}{RT};\quad Y_2=\frac{B_iL_i(W_{2i}-W_{oi})}{RT};\quad Y_3=\frac{B_iL_i}{Rs_2}$$

$$Y_4=\left[\frac{U_{1i}}{P_{oi}}+\frac{U_{1i}}{P_{oi-1}}\frac{P_{oi}}{P_{oi}}-\frac{\mu_{1i}U_{1i}(4S_{1i}-5)}{\pi P_{oi}}\frac{\gamma-1}{\gamma}(S_{1i}+1)\right]$$

$$\times\left[\frac{\tau_{ji}(U_{2i}-U_{1i})L_i(\phi-1)}{(W_{2i}-W_{1i})^2+(U_{2i}-U_{1i})^2}-\frac{\tau_{ri}(1+mr)\phi U_{2i}arL_i}{(Rs_2\omega-W_{2i})^2+U_{2i}^2}\right]+\frac{\tau_{ji}L_i}{P_{oi}}-\frac{\tau_{ri}(1+mr)ar_iL_i}{P_{oi}}$$

$$Y_5=\frac{\tau_{ri}ar_iL_i}{Rs_2\omega-W_{2i}}+\frac{\tau_{ri}(1+mr)(Rs_2\omega-W_{2i})ar_iL_i}{(Rs_2\omega-W_{2i})^2+U_{2i}^2}+\frac{\tau_{ji}L_i}{W_{2i}-W_{1i}}$$

$$+\frac{\tau_{ji}L_i(W_{2i}-W_{1i})}{(W_{2i}-W_{1i})^2+(U_{2i}-U_{1i})^2}$$

$$Y_6=\left[\frac{U_{1i}}{P_{oi-1}}\frac{P_{oi-1}}{P_{oi}}-\frac{\mu_{1i}U_{1i}(4S_{1i}-5)}{\pi P_{oi}}\frac{\gamma-1}{\gamma}\left(\frac{P_{oi-1}}{P_{oi}}\right)^{\frac{-1}{\gamma}}\right]$$

$$\times\left[\frac{\tau_{ji}(U_{2i}-U_{1i})L_i(\phi-1)}{(W_{2i}-W_{1i})^2+(U_{2i}-U_{1i})^2}-\frac{\tau_{ri}(1+mr)\phi U_{2i}arL_i}{(Rs_2\omega-W_{2i})^2+U_{2i}^2}\right]$$

$$Y_7=\frac{-\tau_{ji}L_i}{(W_{2i}-W_{1i})}-\frac{\tau_{ji}L_i(W_{2i}-W_{1i})}{(W_{2i}-W_{1i})^2+(U_{2i}-U_{1i})^2};\quad Y_8=0.0$$

APPENDIX C

SEPARATION OF THE CONTINUITY AND MOMENTUM EQUATIONS AND DEFINITION OF THE SYSTEM MATRIX ELEMENTS

CONTINUITY:

$$\cos(\theta+\omega t): (G_1\omega + G_2)P^+_{s1} + G_3 W^+_{1s1} + G_4 W^+_{2s1} + G_5 P^+_{c1} + G_6 P^+_{c1-1} + G_7 P^+_{c1+1} = G_8 (a-b)/2$$

$$\sin(\theta+\omega t): -(G_1\omega + G_2)P^+_{c1} - G_3 W^+_{1c1} - G_4 W^+_{2c1} + G_5 P^+_{s1} + G_6 P^+_{s1-1} + G_7 P^+_{s1+1} = \left[\frac{G_9}{\omega 2} + G_{10}\right](b-a)$$

$$\cos(\theta-\omega t): (-G_1\omega + G_2)P^-_{s1} + G_3 W^-_{1s1} + G_4 W^-_{2s1} + G_5 P^-_{c1} + G_6 P^-_{c1-1} + G_7 P^-_{c1+1} = G_8 (a+b)/2$$

$$\sin(\theta-\omega t): (G_1\omega - G_2)P^-_{c1} - G_3 W^-_{1c1} - G_4 W^-_{2c1} + G_5 P^-_{s1} + G_6 P^-_{s1-1} + G_7 P^-_{s1+1} = \left[\frac{G_9}{\omega 2} - G_{10}\right](a+b)$$

MOMENTUM I:

$$\cos(\theta+\omega t): X_1 W^+_{1s1}\left[\frac{W_{1i}}{Rs_1} + \omega\right] + \left[\frac{X_3 W_{2i}}{Rs_2} + X_2 + X_3\omega\right]P^+_{s1} + \frac{X_3 P_{oi}}{Rs_2} W^+_{2s1} + X_4 P^+_{c1} + X_5 P^+_{c1+1} + X_6 W^+_{1c1} + X_7 W^+_{2c1} - \dot{m}_o W^+_{1c1-1} = X_8(b-a)/2$$

$$\sin(\theta+\omega t): -X_1 W^+_{1c1}\left[\frac{W_{1i}}{Rs_1} + \omega\right] - \left[\frac{X_3 W_{2i}}{Rs_2} + X_2 + X_3\omega\right]P^+_{c1} - \frac{X_3 P_{oi}}{Rs_2} W^+_{2c1} + X_4 P^+_{s1} + X_5 P^+_{s1+1} + X_6 W^+_{1s1} + X_7 W^+_{2s1} - \dot{m}_o W^+_{1s1-1} = 0$$

$$\cos(\theta-\omega t): X_1 W^-_{1s1}\left[\frac{W_{1i}}{Rs_1} - \omega\right] + \left[\frac{X_3 W_{2i}}{Rs_2} + X_2 - X_3\omega\right]P^-_{s1} + \frac{X_3 P_{oi}}{Rs_2} W^-_{2s1} + X_4 P^-_{c1} + X_5 P^-_{c1+1} + X_6 W^-_{1c1} + X_7 W^-_{2c1} - \dot{m}_o W^-_{1c1-1} = -X_8(a+b)/2$$

$$\sin(\theta-\omega t): -X_1 W^-_{1c1}\left[\frac{W_{1i}}{Rs_1} - \omega\right] - \left[\frac{X_3 W_{2i}}{Rs_2} + X_2 - X_3\omega\right]P^-_{c1} - \frac{X_3 P_{oi}}{Rs_2} W^-_{2c1} + X_4 P^-_{s1} + X_5 P^-_{s1+1} + X_6 W^-_{1s1} + X_7 W^-_{2s1} - \dot{m}_o W^-_{1s1-1} = 0$$

MOMENTUM II:

$$\cos(\theta+\omega t): \; Y_1\omega\, W^{+}_{2s1} + \left[\frac{Y_1 W_{21}}{Rs_2} + \frac{Y_2 P_{01}}{Rs_2}\right] W^{+}_{2s1} + \left[Y_2\omega + Y_3 + \frac{Y_2 W_{21}}{Rs_2}\right] P^{+}_{s1}$$
$$+ Y_4\, P^{+}_{c1} + Y_5\, W^{+}_{2c1} + Y_6\, P^{+}_{c1-1} + Y_7\, W^{+}_{1c1} = Y_8(b-a)/2$$

$$\sin(\theta+\omega t): \; -Y_1\omega\, W^{+}_{2c1} - \left[\frac{Y_2 W_{21}}{Rs_2} + Y_3 + Y_2\omega\right] P^{+}_{c1} - \left[\frac{Y_2 P_{01}}{Rs_2} + \frac{Y_1 W_{21}}{Rs_2}\right] W^{+}_{2c1}$$
$$+ Y_4\, P^{+}_{s1} + Y_5\, W^{+}_{2s1} + Y_6\, P^{+}_{s1-1} + Y_7\, W^{+}_{1s1} = 0$$

$$\cos(\theta-\omega t): \; -Y_1\omega\, W^{-}_{2s1} + \left[\frac{Y_2 W_{21}}{Rs_2} + Y_3 - Y_2\omega\right] P^{-}_{s1} + \left[\frac{Y_2 P_{01}}{Rs_2} + \frac{Y_1 W_{21}}{Rs_2}\right] W^{-}_{2s1}$$
$$+ Y_4\, P^{-}_{c1} + Y_5\, W^{-}_{2c1} + Y_6\, P^{-}_{c1-1} + Y_7\, W^{-}_{1c1} = -Y_8(a+b)/2$$

$$\sin(\theta-\omega t): \; Y_1\omega\, W^{-}_{2c1} - \left[\frac{Y_2 W_{21}}{Rs_2} + Y_3 - Y_2\omega\right] P^{-}_{c1} - \left[\frac{Y_2 P_{01}}{Rs_2} + \frac{Y_1 P_{01}}{Rs_2}\right] W^{-}_{2c1}$$
$$+ Y_4\, P^{-}_{s1} + Y_5\, W^{-}_{2s1} + Y_6\, P^{-}_{s1-1} + Y_7\, W^{-}_{1s1} = 0$$

A_{i-1} MATRIX

$$A_{1,2} = A_{2,1} = A_{3,4} = A_{4,3} = G_6$$

$$A_{5,2} = A_{6,1} = A_{7,4} = A_{8,3} = X_5$$

$$A_{5,6} = A_{6,5} = A_{7,8} = A_{8,7} = -\dot{m}_0$$

$$A_{9,2} = A_{10,1} = A_{11,4} = A_{12,3} = Y_6$$

The remaining elements are zero.

A_i MATRIX

$$A_{1,1} = -A_{2,2} = G_1\,\omega + G_2$$

$$A_{3,3} = -A_{4,4} = G_1\,\omega + G_2$$

$$A_{1,2} = A_{2,1} = A_{3,4} = A_{4,3} = G_5$$

$$A_{5,2} = A_{6,1} = A_{7,4} = A_{8,3} = X_4$$

$$A_{5,1} = -A_{6,2} = X_5\,\omega + X_2 + X_5 W_{21}/Rs_2$$

$$A_{7,3} = -A_{8,4} = -X_5\,\omega + X_2 + X_5 W_{21}/Rs_2$$

$$A_{9,2} = A_{10,1} = A_{11,4} = A_{12,3} = Y_4$$

$$A_{9,1} = -A_{10,2} = Y_2\,\omega + Y_3 + Y_2 W_{21}/Rs_2$$

$$A_{11,3} = -A_{12,4} = -Y_2\,\omega + Y_3 + Y_2 W_{21}/Rs_2$$

$$A_{1,5} = -A_{2,6} = A_{3,7} = -A_{4,8} = G_3$$

$$A_{5,5} = -A_{6,6} = X_1\left[\omega + \frac{W_{11}}{Rs_1}\right]$$

$$A_{7,7} = -A_{8,8} = X_1\left[\frac{W_{11}}{Rs_1} - \omega\right]$$

$$A_{5,6} = A_{6,5} = A_{7,8} = A_{8,7} = X_6$$

$$A_{9,6} = A_{10,5} = A_{11,8} = A_{12,7} = Y_7$$

$$A_{1,9} = A_{3,11} = -A_{2,10} = -A_{4,12} = G_4$$

$$A_{5,9} = -A_{6,10} = A_{7,11} = -A_{8,12} = X_3\,P_{01}/Rs_2$$

$$A_{5,10} = A_{6,9} = A_{7,12} = A_{8,11} = X_7$$

$$A_{9,9} = -A_{10,10} = Y_1\,\omega + Y_1\,W_{21}/Rs_2 + Y_2 P_{01}/Rs_2$$

$$A_{11,11} = -A_{12,12} = -Y_1\,\omega + Y_1\,W_{21}/Rs_2 + Y_2 P_{01}/Rs_2$$

$$A_{9,10} = A_{10,9} = A_{11,12} = A_{12,11} = Y_8$$

The remaining elements are zero.

A_{i+1} MATRIX

$$A_{1,2} = A_{2,1} = A_{3,4} = A_{4,3} = G_7$$

The remaining elements are zero.

B AND C COLUMN VECTORS

$$B = \begin{bmatrix} \frac{G_0}{2} \\ -\frac{G_0}{2}\omega - \frac{G_{10}}{2} \\ \frac{G_0}{2} \\ \frac{G_0}{2}\omega - \frac{G_{10}}{2} \\ -\frac{X_0}{2} \\ 0 \\ -\frac{X_0}{2} \\ 0 \\ -\frac{Y_0}{2} \\ 0 \\ -\frac{Y_0}{2} \\ 0 \end{bmatrix} \qquad C = \begin{bmatrix} -\frac{G_0}{2} \\ \frac{G_0}{2}\omega + \frac{G_{10}}{2} \\ \frac{G_0}{2} \\ \frac{G_0}{2}\omega - \frac{G_{10}}{2} \\ \frac{X_0}{2} \\ 0 \\ -\frac{X_0}{2} \\ 0 \\ \frac{Y_0}{2} \\ 0 \\ -\frac{Y_0}{2} \\ 0 \end{bmatrix}$$

APPENDIX D

THEORY VS. EXPERIMENT

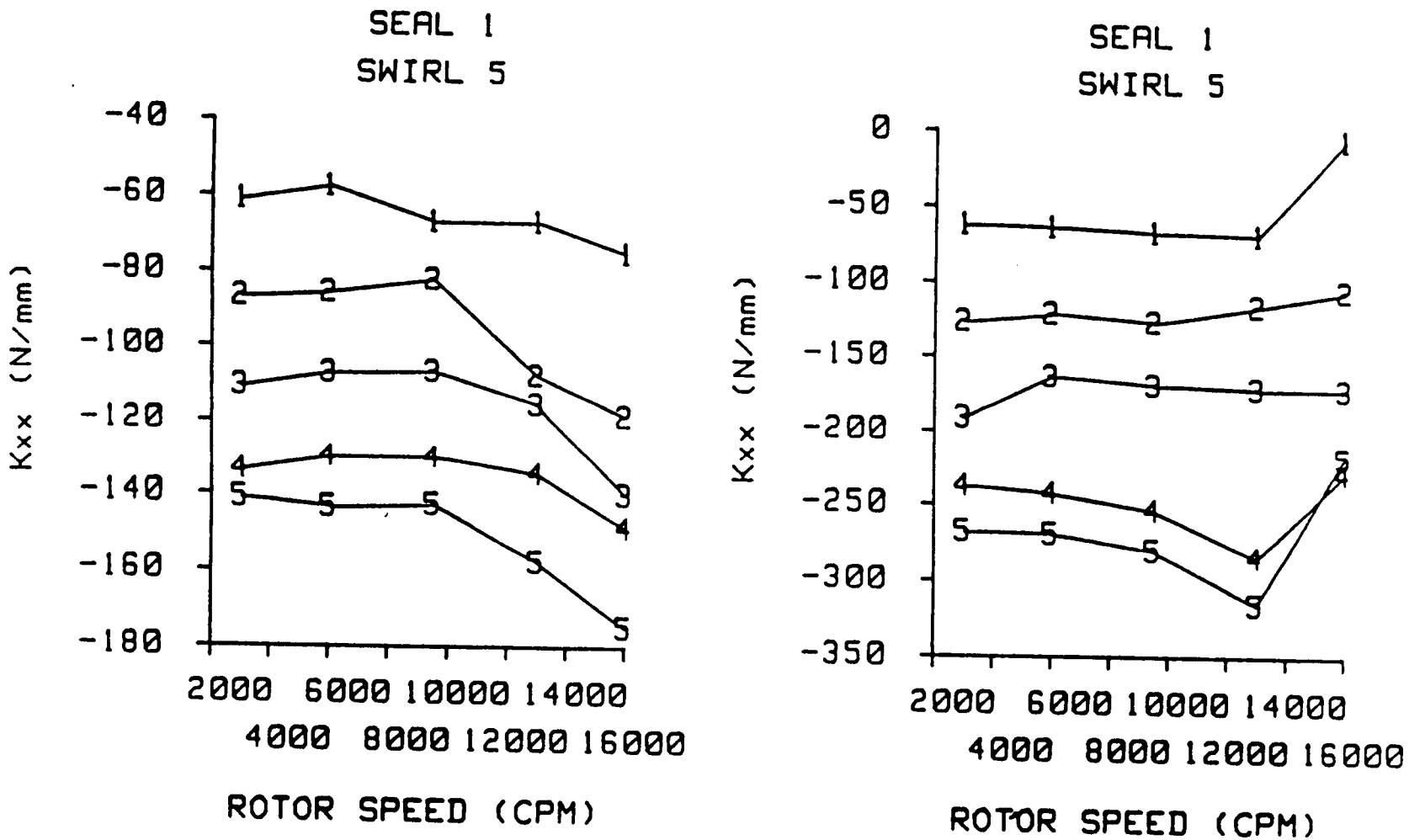

Fig. D1 Direct stiffness versus rotor speed for seal 1 and inlet circumferential velocity 5. See table 6 for pressure ratio definitions. Teeth-on-rotor (left), teeth-on-stator (right).

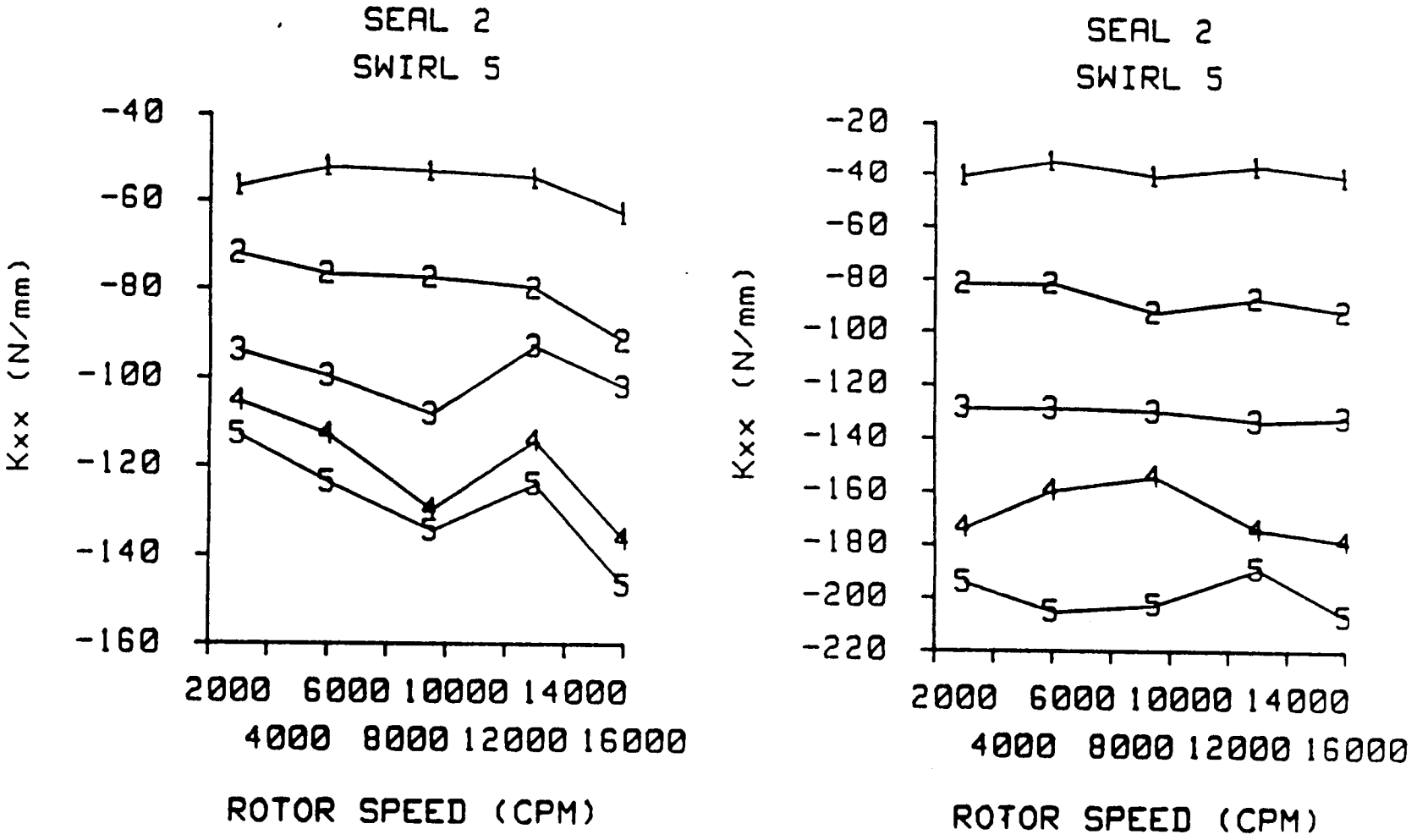

Fig. D2 Direct stiffness versus rotor speed for seal 2 and inlet circumferential velocity 5. See table 6 for pressure ratio definitions. Teeth-on-rotor (left), teeth-on-stator (right).

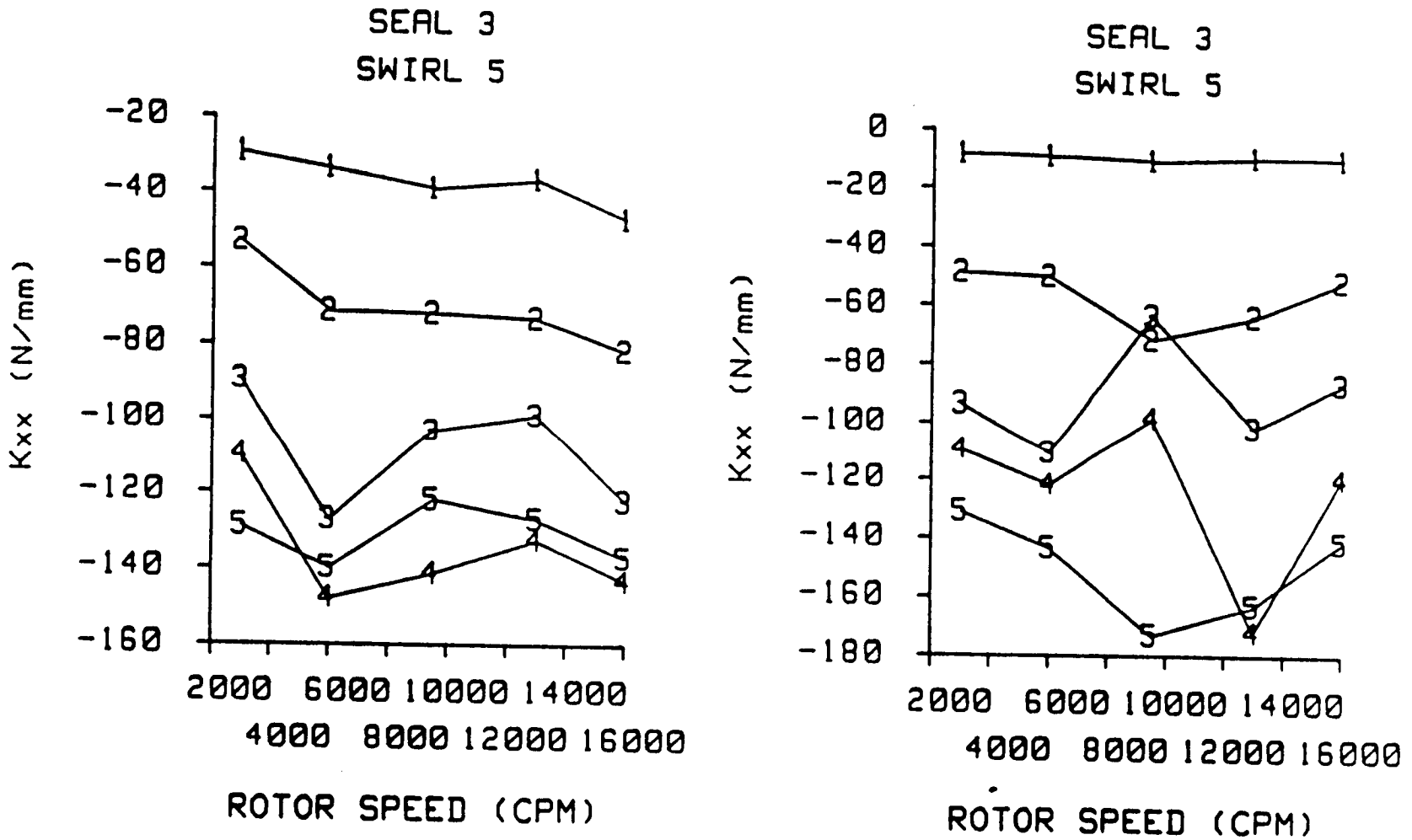

Fig. D3 Direct stiffness versus rotor speed for seal 3 and inlet circumferential velocity 5. See table 6 for pressure ratio definitions. Teeth-on-rotor (left), teeth-on-stator (right).

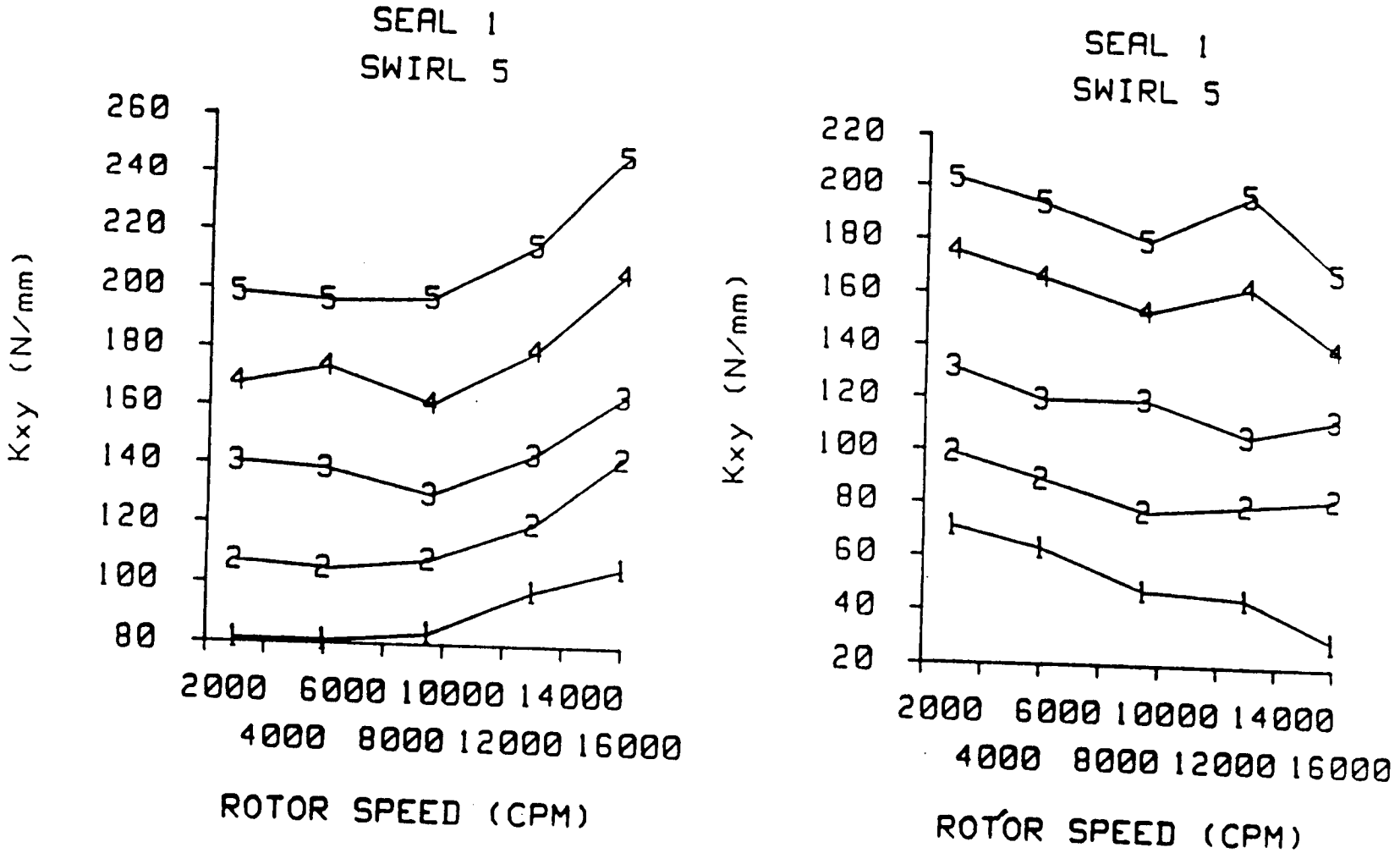

Fig. D4 Cross-coupled stiffness versus rotor speed for seal 1 and inlet circumferential velocity 5. See table 6 for pressure ratio definitions. Teeth-on-rotor (left), teeth-on-stator (right).

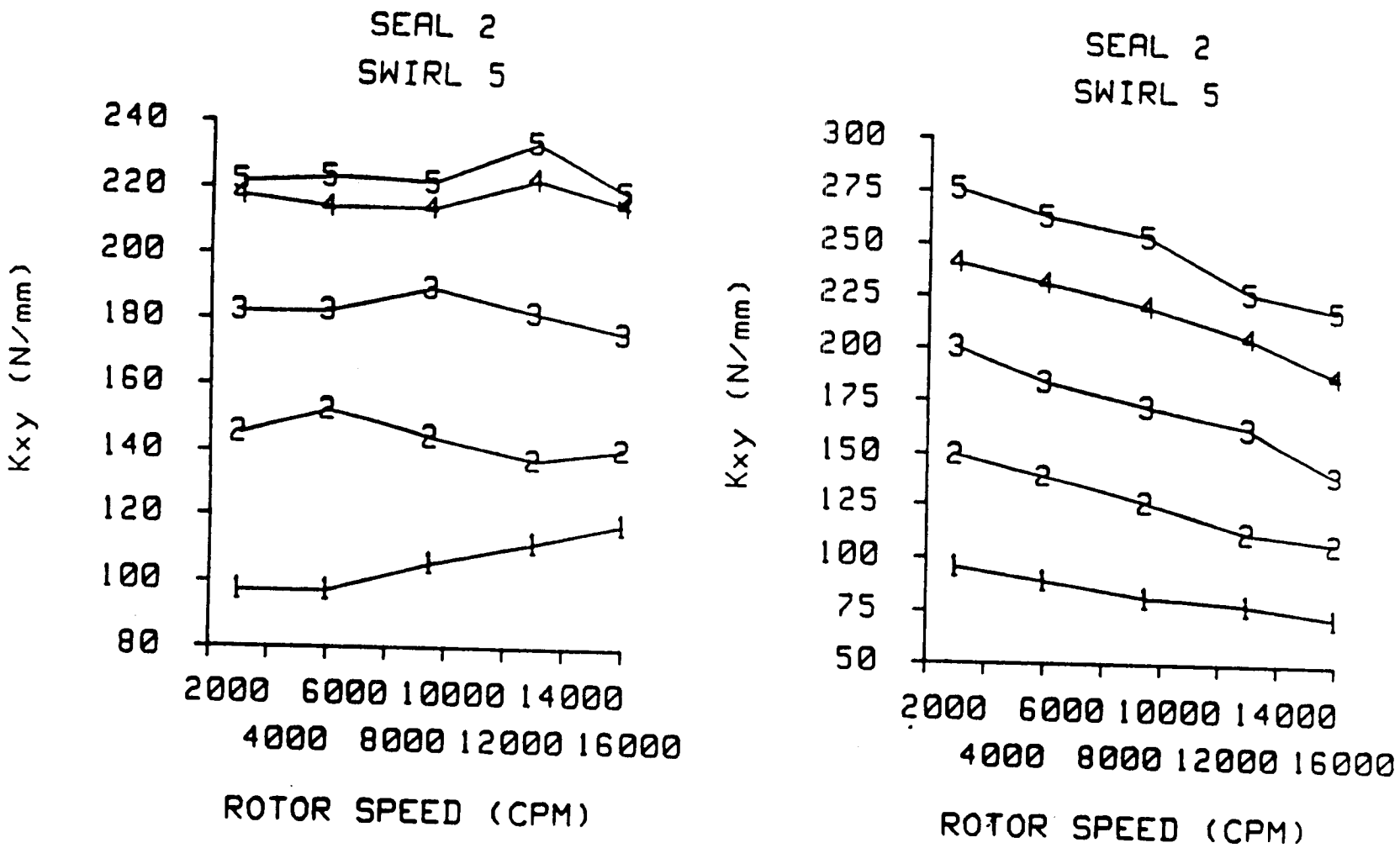

Fig. D5 Cross-coupled stiffness versus rotor speed for seal 2 and inlet circumferential velocity 5. See table 6 for pressure ratio definitions. Teeth-on-rotor (left), teeth-on-stator (right).

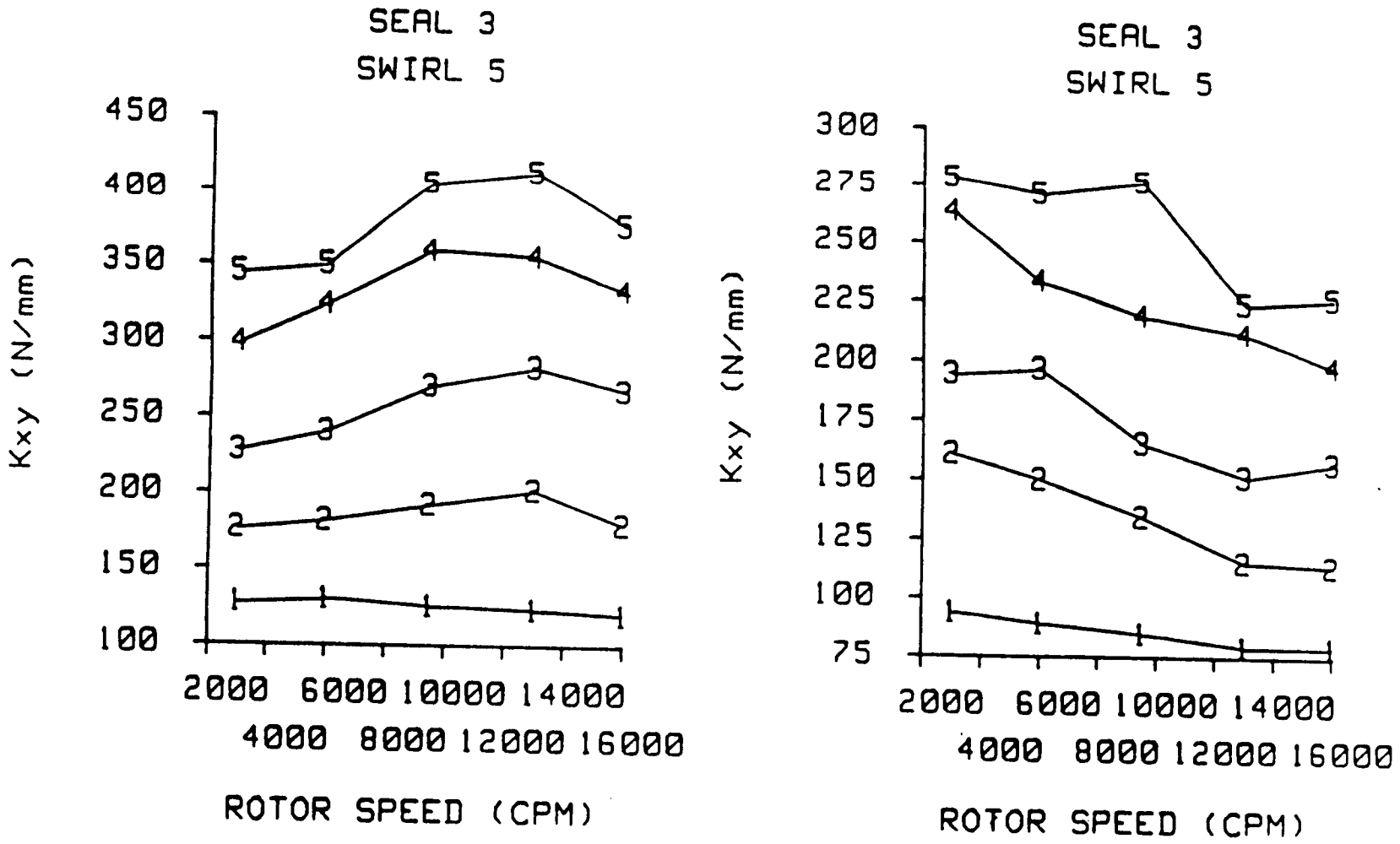

Fig. D6 Cross-coupled stiffness versus rotor speed for seal 3 and inlet circumferential velocity 5. See table 6 for pressure ratio definitions. Teeth-on-rotor (left), teeth-on-stator (right).

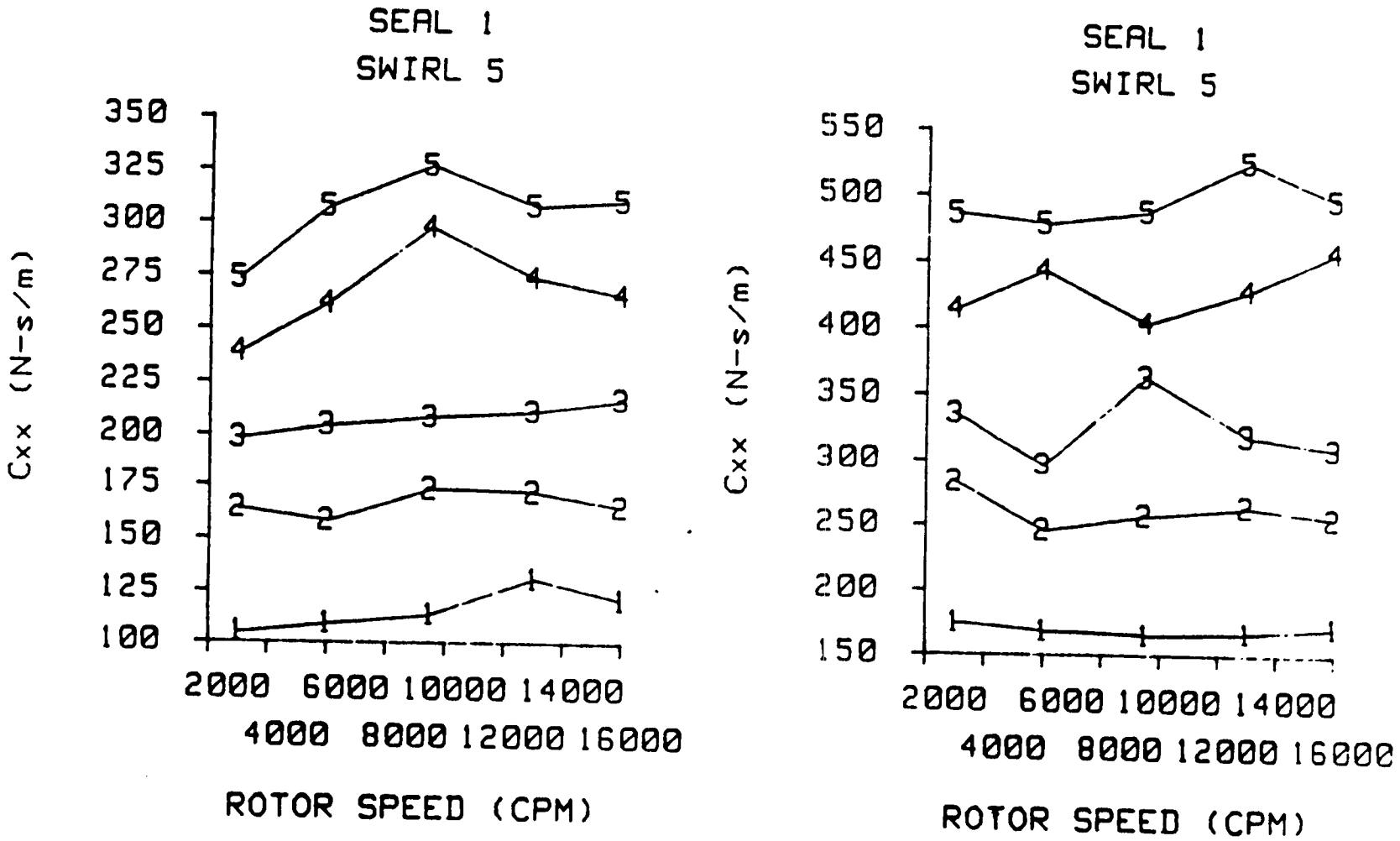

Fig. D7 Direct damping versus rotor speed for seal 1 and inlet circumferential velocity 5. See table 6 for pressure ratio definitions. Teeth-on-rotor (left), teeth-on-stator (right).

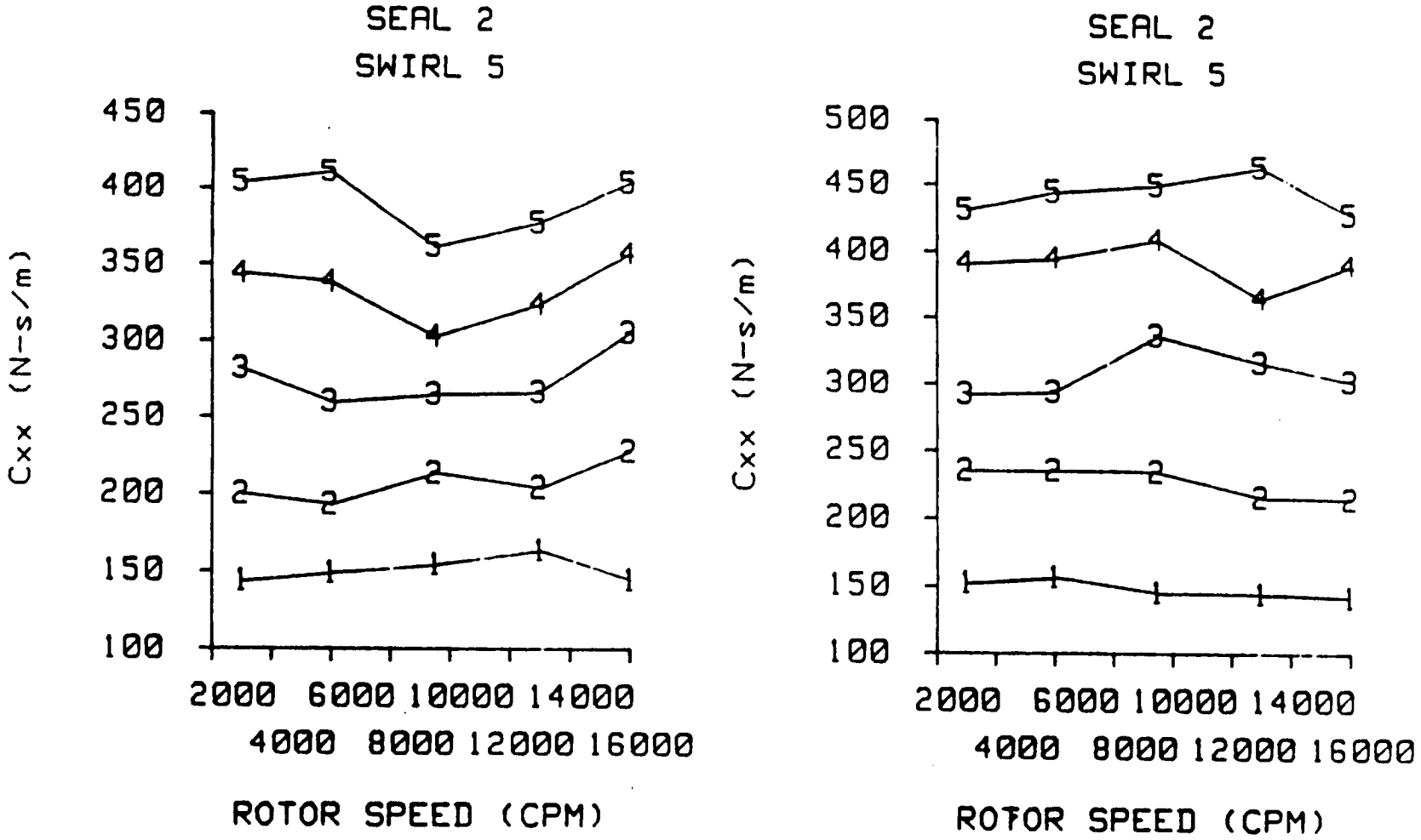

Fig. D8 Direct damping versus rotor speed for seal 2 and inlet circumferential velocity 5. See table 6 for pressure ratio definitions. Teeth-on-rotor (left), teeth-on-stator (right).

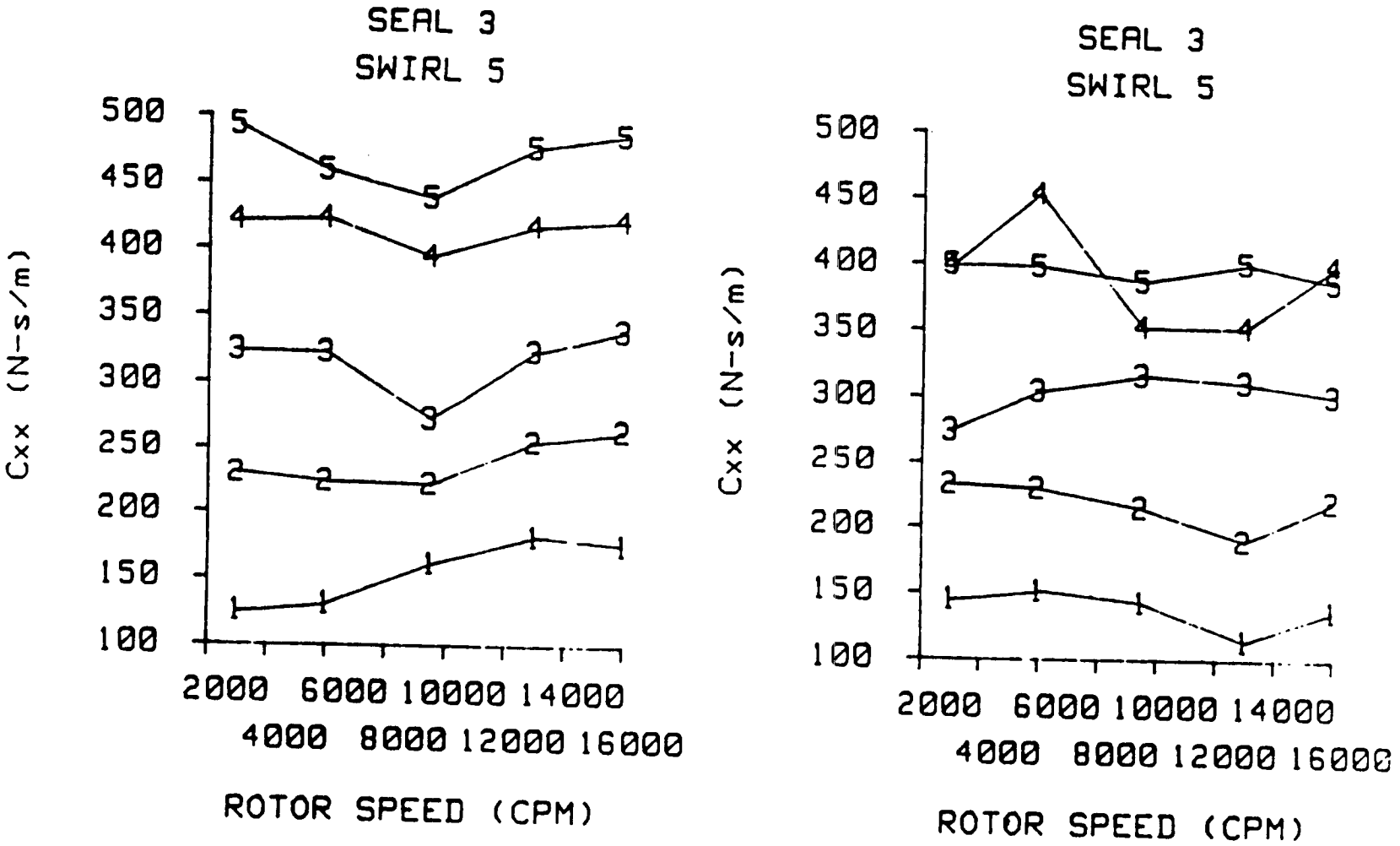

Fig. D9 Direct damping versus rotor speed for seal 3 and inlet circumferential velocity 5. See table 6 for pressure ratio definitions. Teeth-on-rotor (left), teeth-on-stator (right).

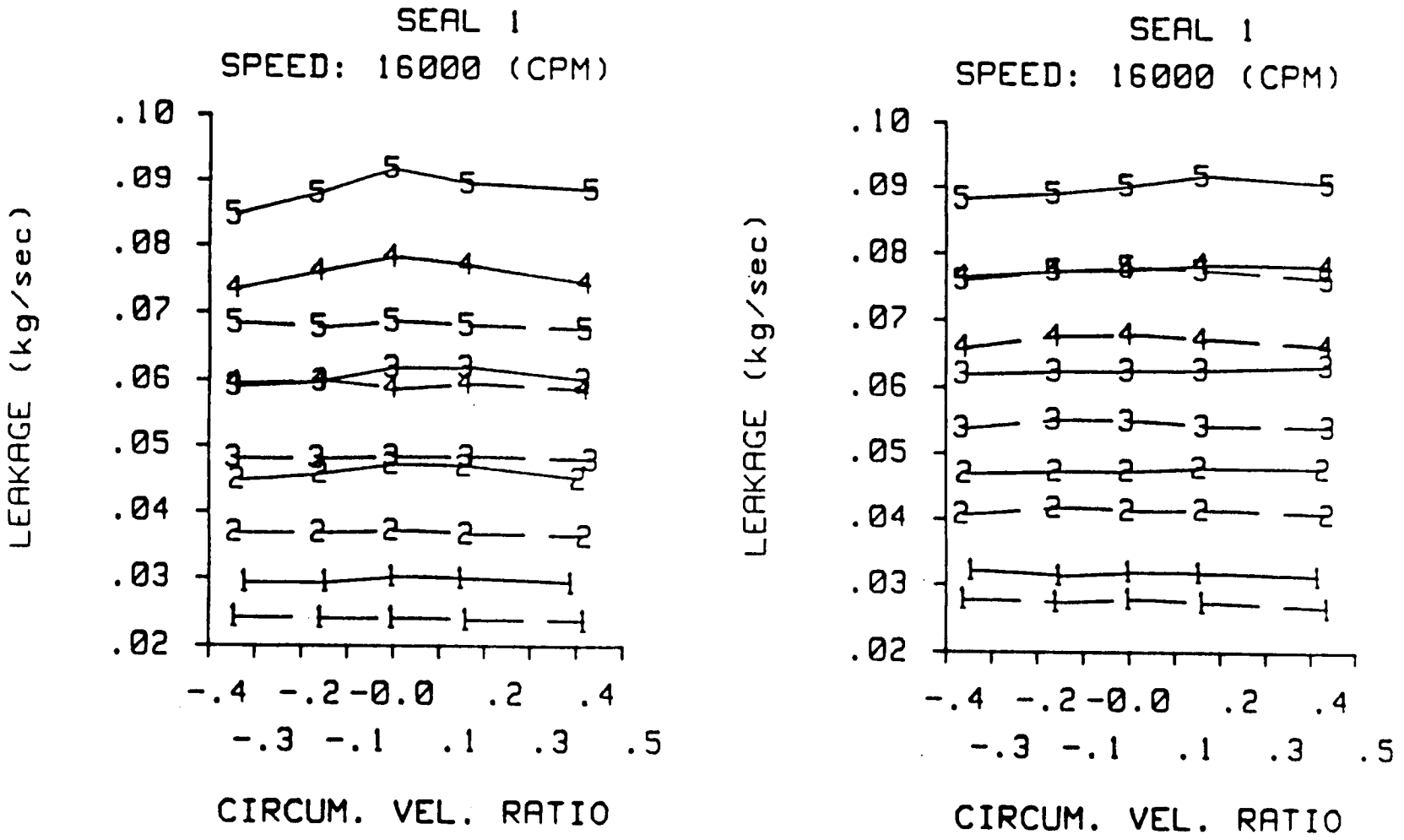

Fig. D10 A comparison of experimental and theoretical leakage versus inlet circumferential velocity ratio for seal 1 at a rotor speed of 16000 cpm. See table 6 for pressure definitions. Teeth-on-rotor (left), teeth-on-stator (right).

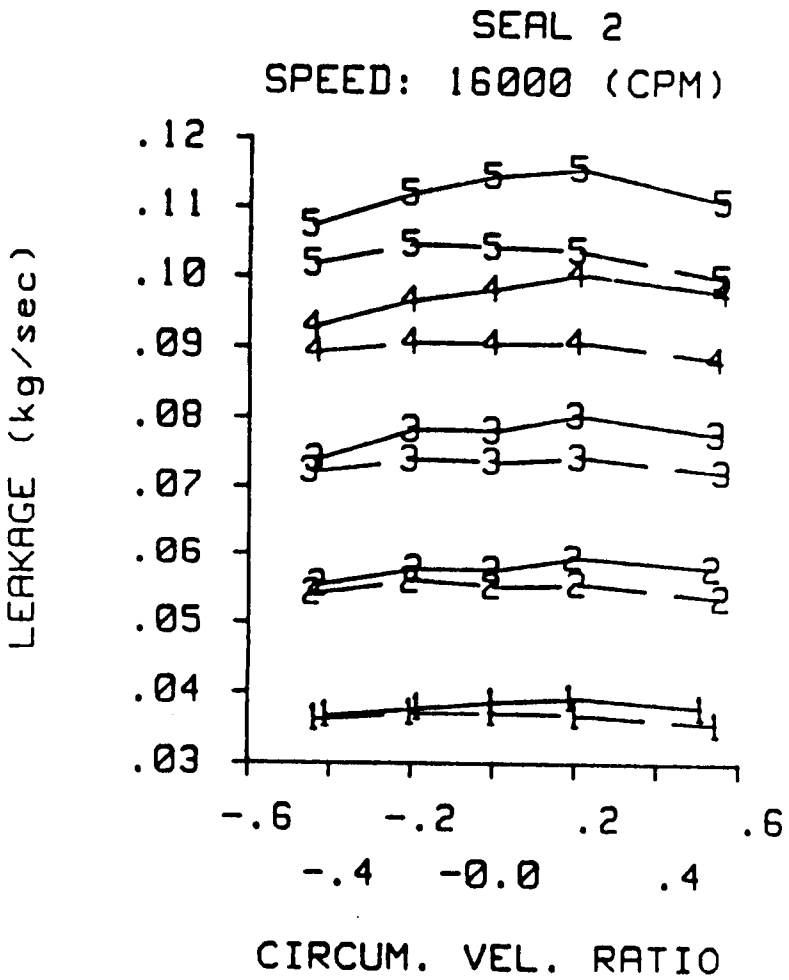

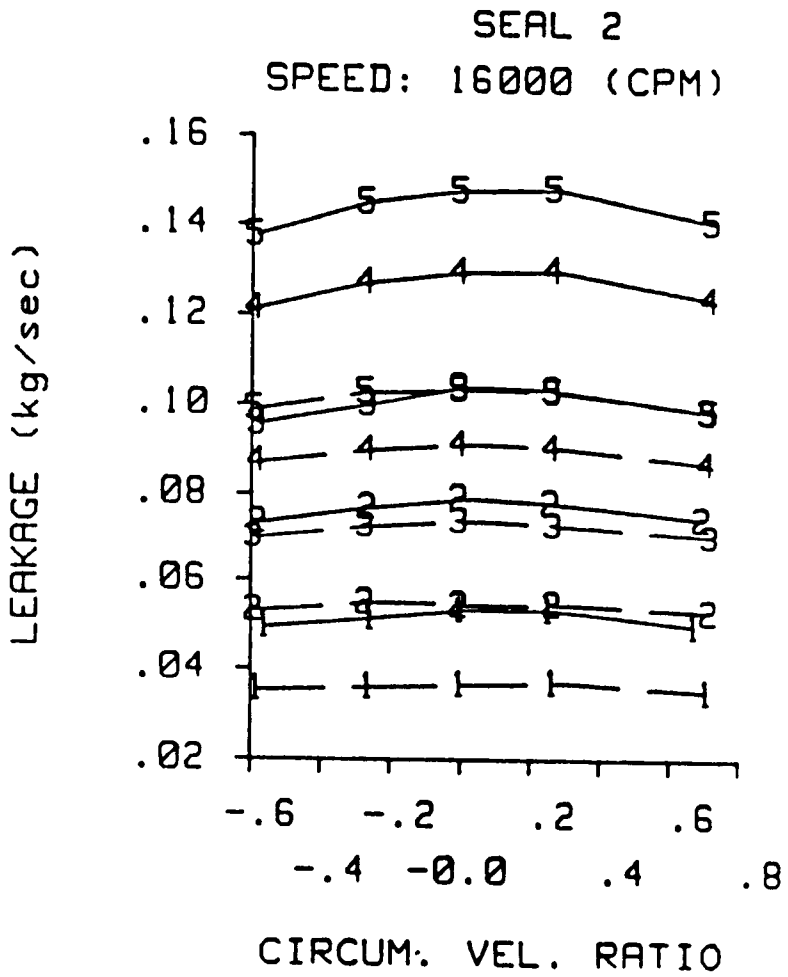

Fig. D11 A comparison of experimental and theoretical leakage versus inlet circumferential velocity ratio for seal 2 at a rotor speed of 16000 cpm. See table 6 for pressure definitions. Teeth-on-rotor (left), teeth-on-stator (right).

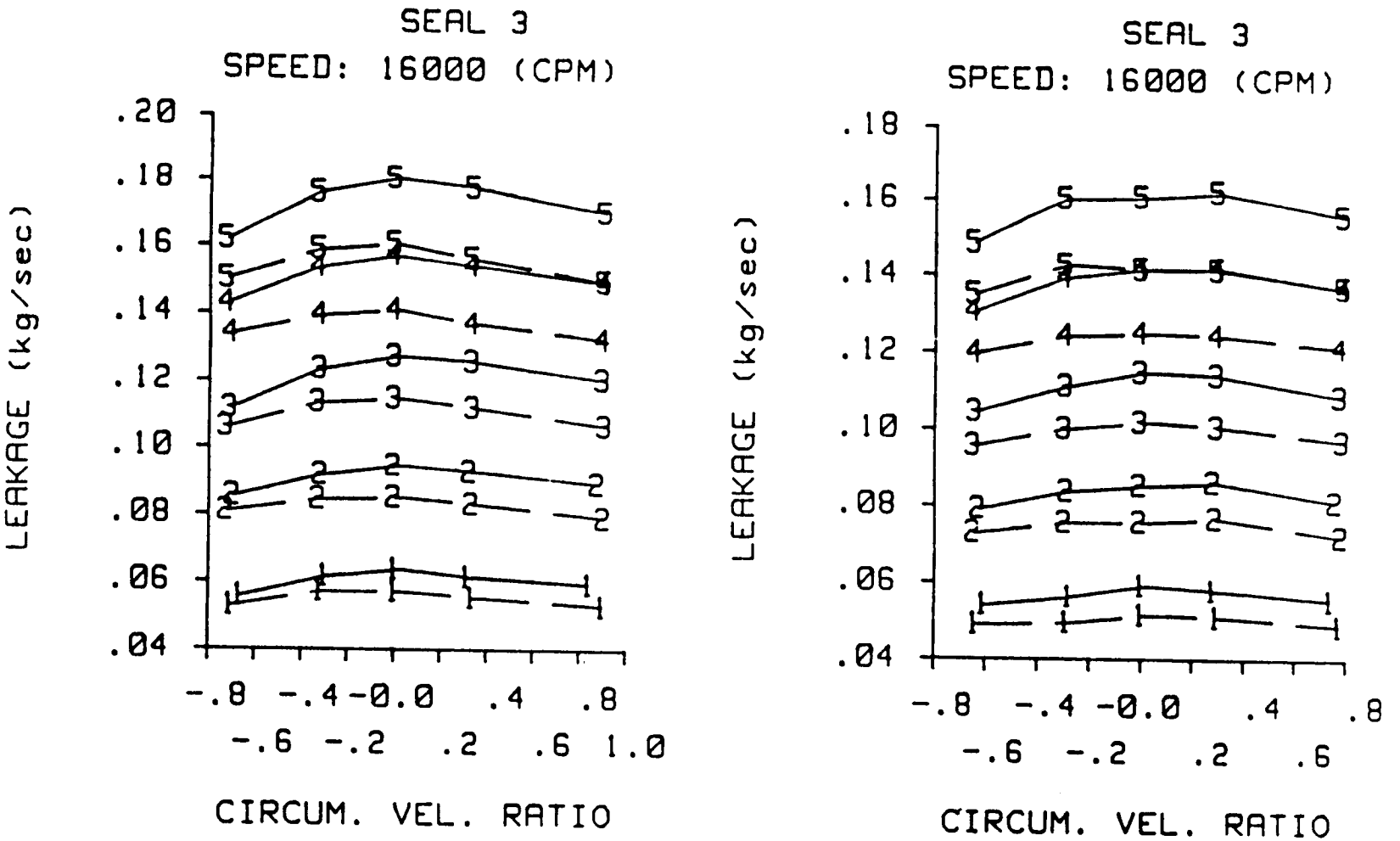

Fig. D12 A comparison of experimental and theoretical leakage versus inlet circumferential velocity ratio for seal 3 at a rotor speed of 16000 cpm. See table 6 for pressure definitions. Teeth-on-rotor (left), teeth-on-stator (right).

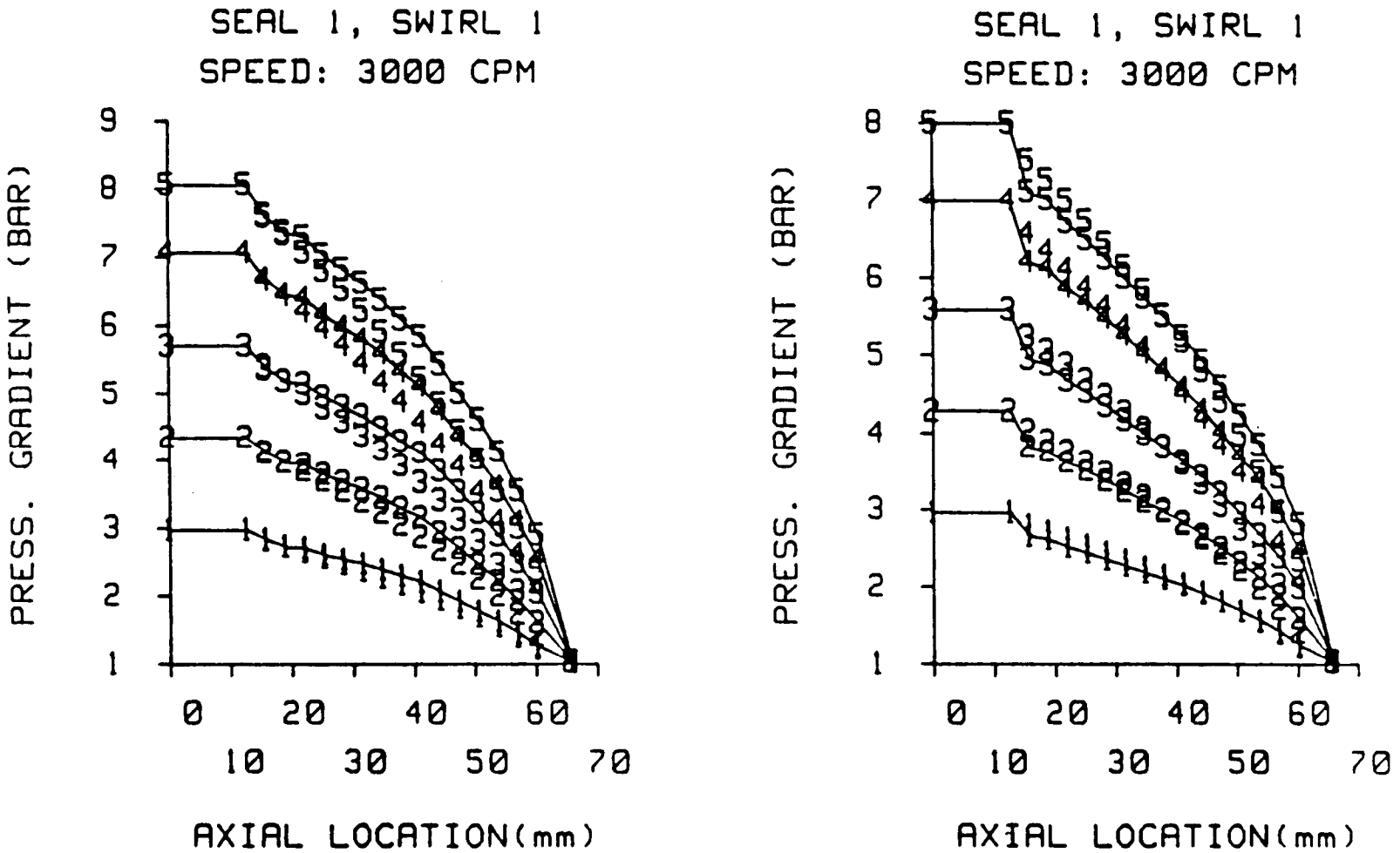

Fig. D13 A comparison of experimental and theoretical pressure gradients of seal 1 for a rotor speed of 3000 cpm and inlet circumferential velocity 1. See table 6 for pressure definitions. Teeth-on-rotor (left), teeth-on-stator (right).

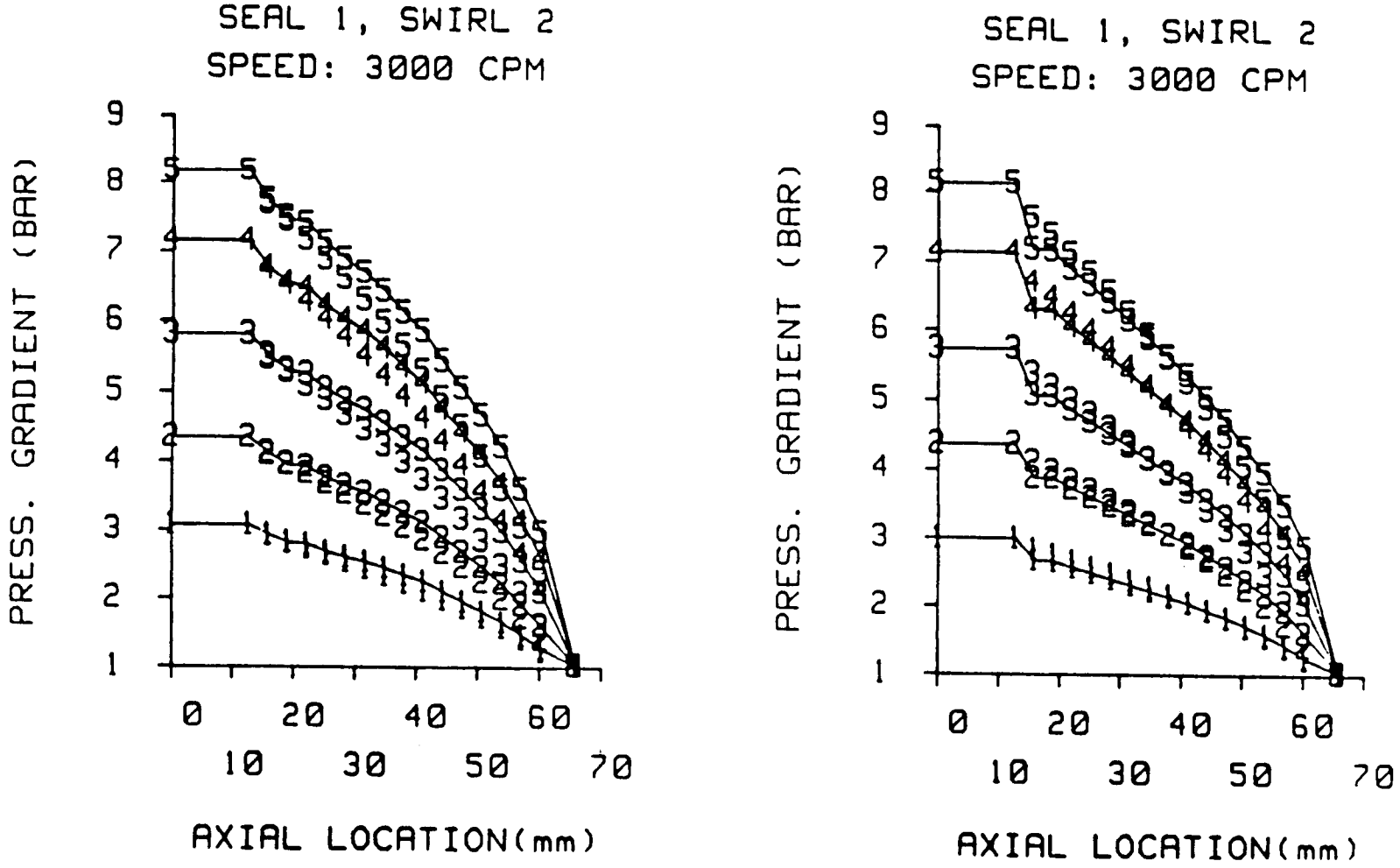

Fig. D14 A comparison of experimental and theoretical pressure gradients of seal 1 for a rotor speed of 3000 cpm and inlet circumferential velocity 2. See table 6 for pressure definitions. Teeth-on-rotor (left), teeth-on-stator (right).

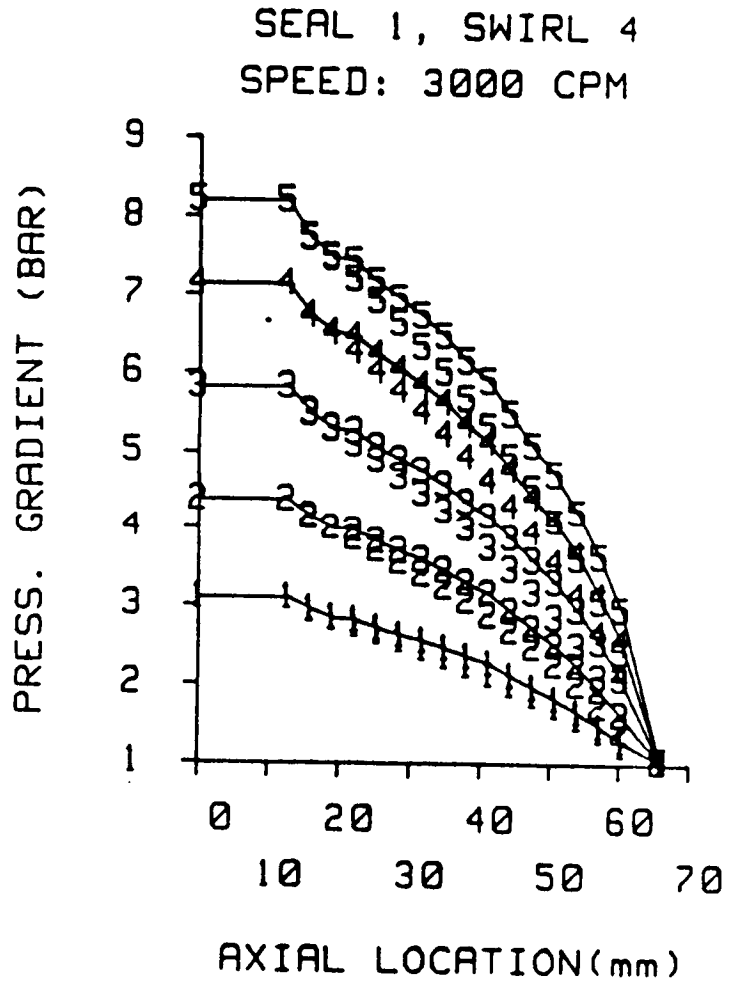

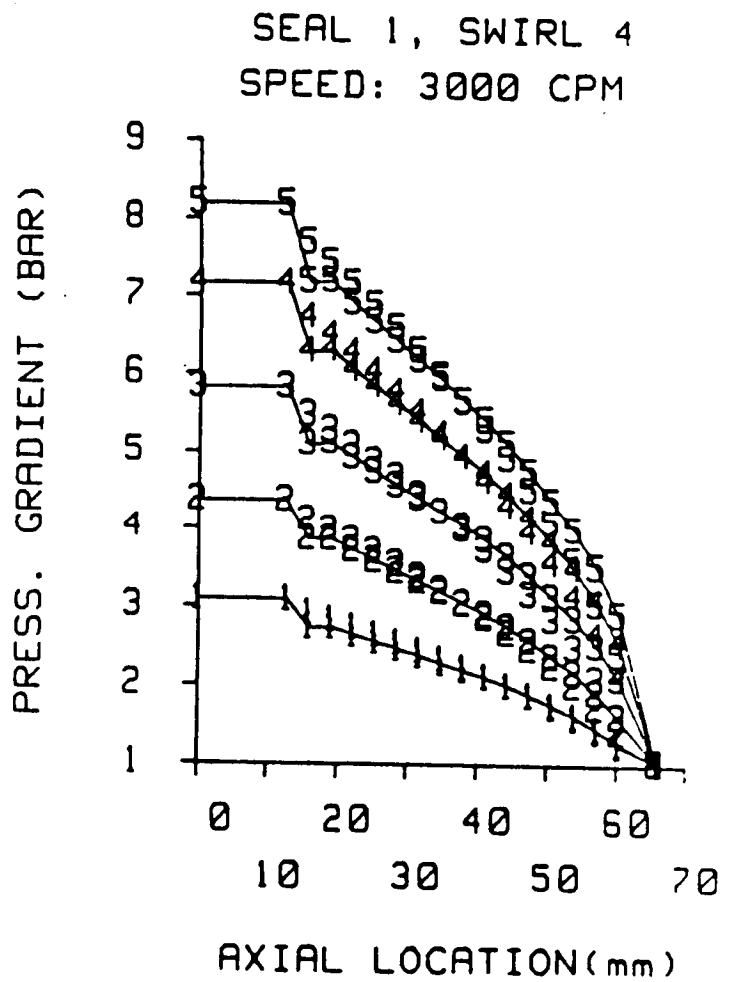

Fig. D15 A comparison of experimental and theoretical pressure gradients of seal 1 for a rotor speed of 3000 cpm and inlet circumferential velocity 4. See table 6 for pressure definitions. Teeth-on-rotor (left), teeth-on-stator (right).

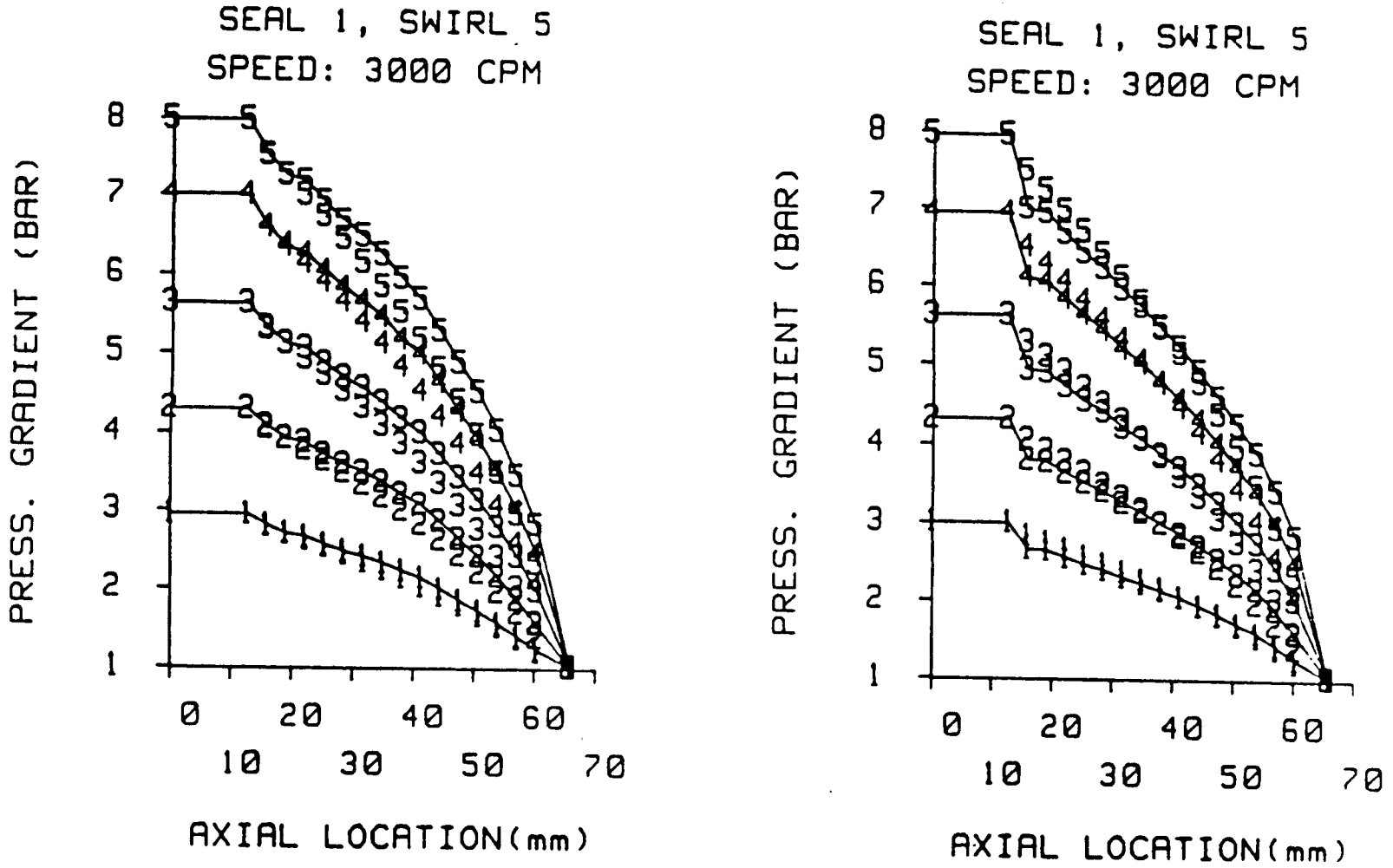

Fig. D16 A comparison of experimental and theoretical pressure gradients of seal 1 for a rotor speed of 3000 cpm and inlet circumferential velocity 5. See table 6 for pressure definitions. Teeth-on-rotor (left), teeth-on-stator (right).

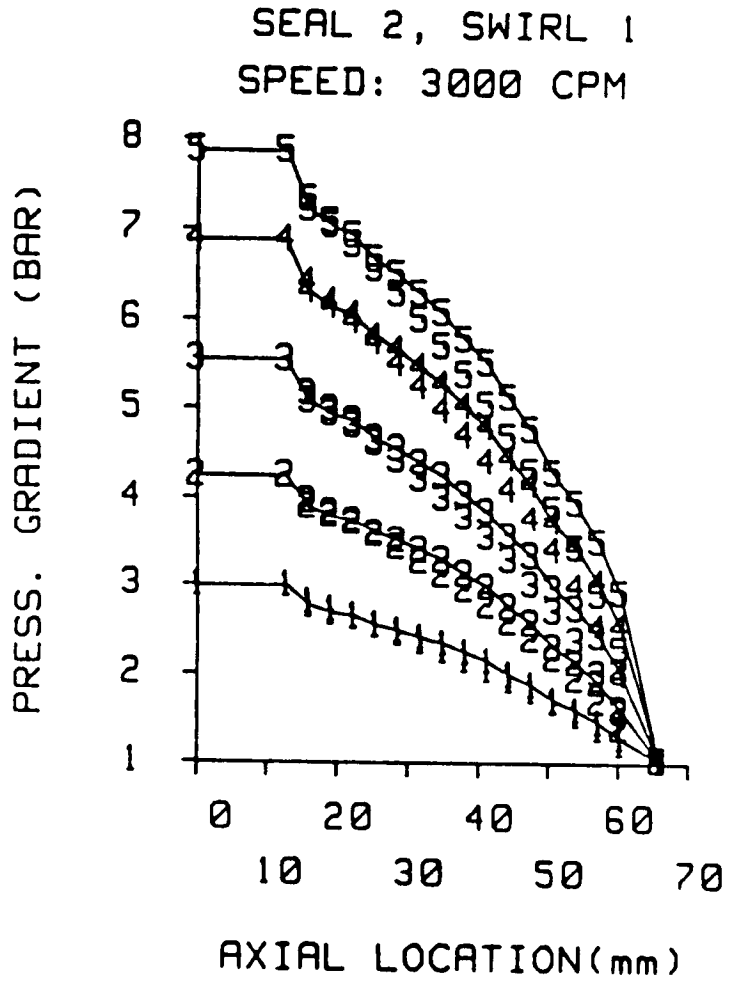

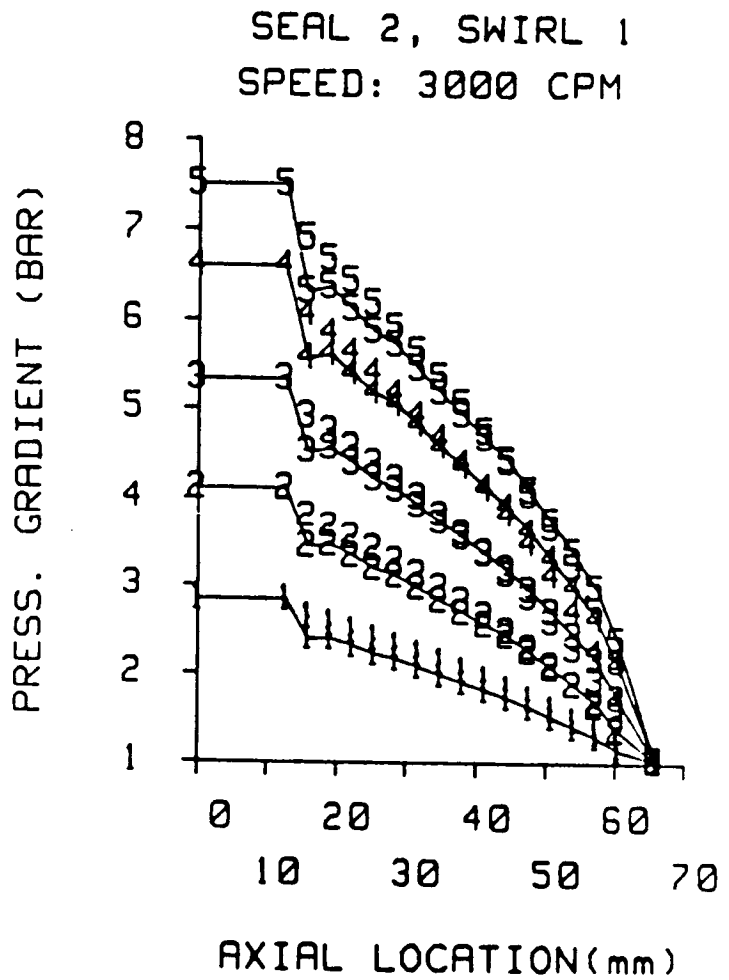

Fig. D17 A comparison of experimental and theoretical pressure gradients of seal 2 for a rotor speed of 3000 cpm and inlet circumferential velocity 1. See table 6 for pressure definitions. Teeth-on-rotor (left), teeth-on-stator (right).

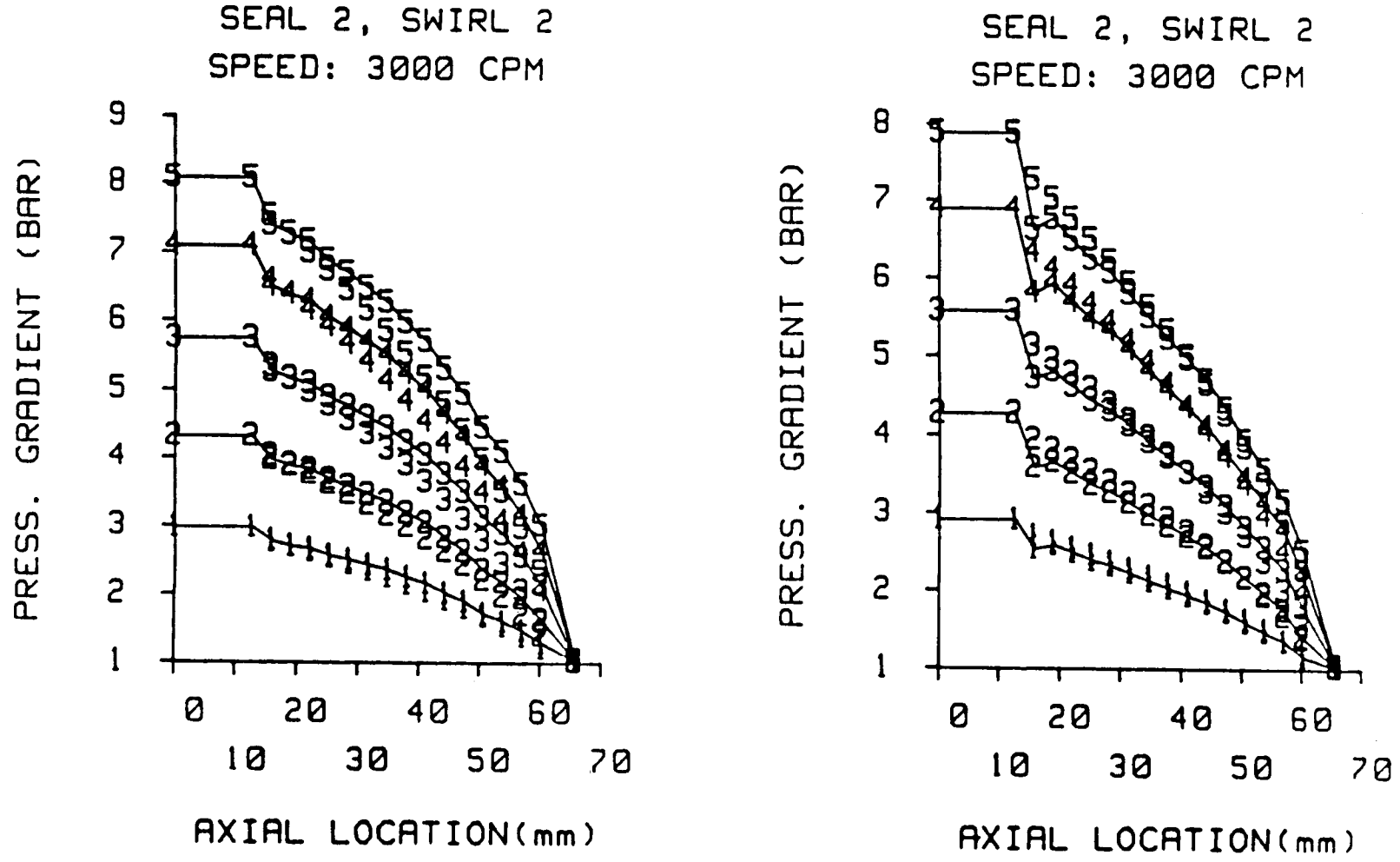

Fig. D18 A comparison of experimental and theoretical pressure gradients of seal 2 for a rotor speed of 3000 cpm and inlet circumferential velocity 2. See table 6 for pressure definitions. Teeth-on-rotor (left), teeth-on-stator (right).

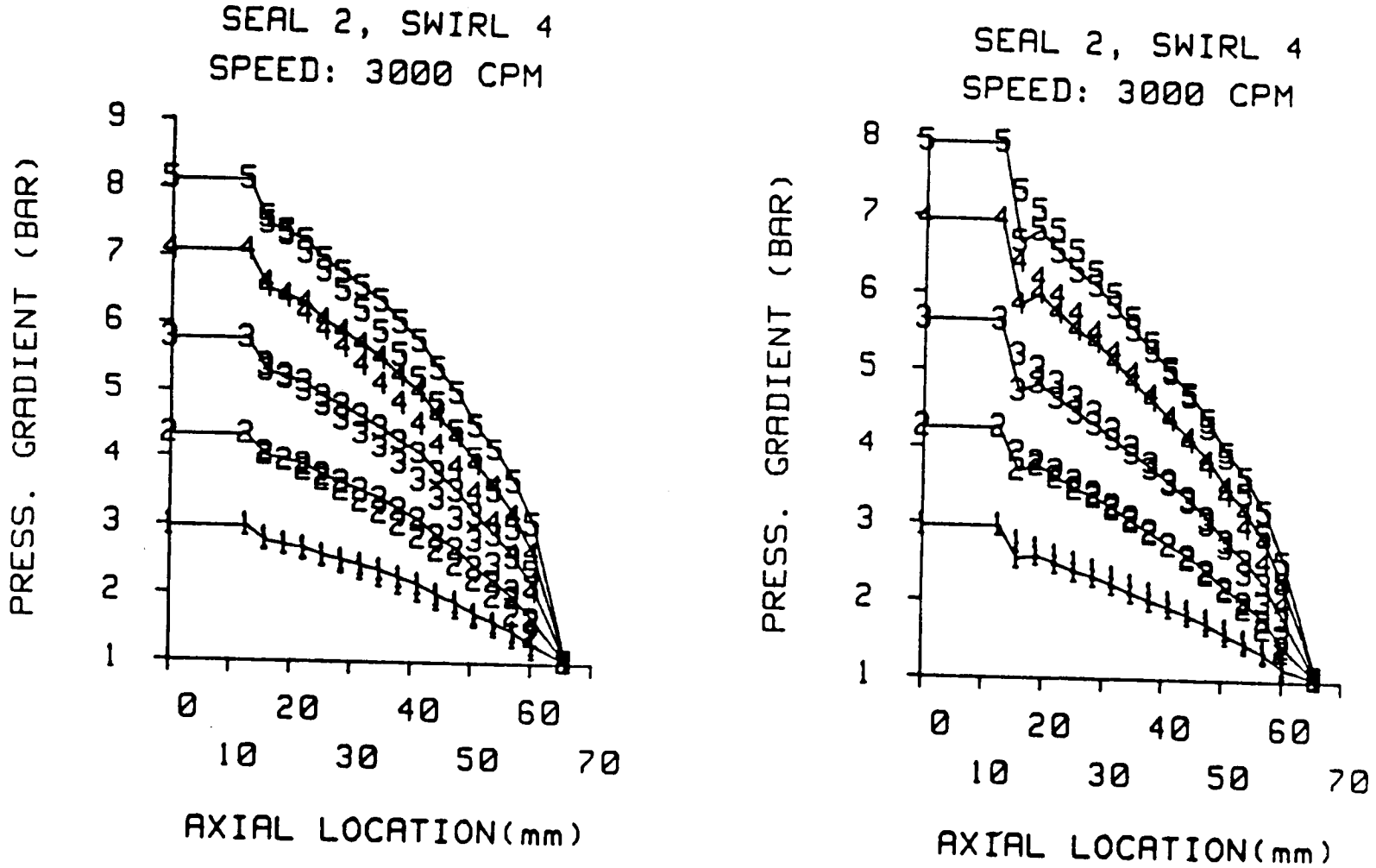

Fig. D19 A comparison of experimental and theoretical pressure gradients of seal 2 for a rotor speed of 3000 cpm and inlet circumferential velocity 4. See table 6 for pressure definitions. Teeth-on-rotor (left), teeth-on-stator (right).

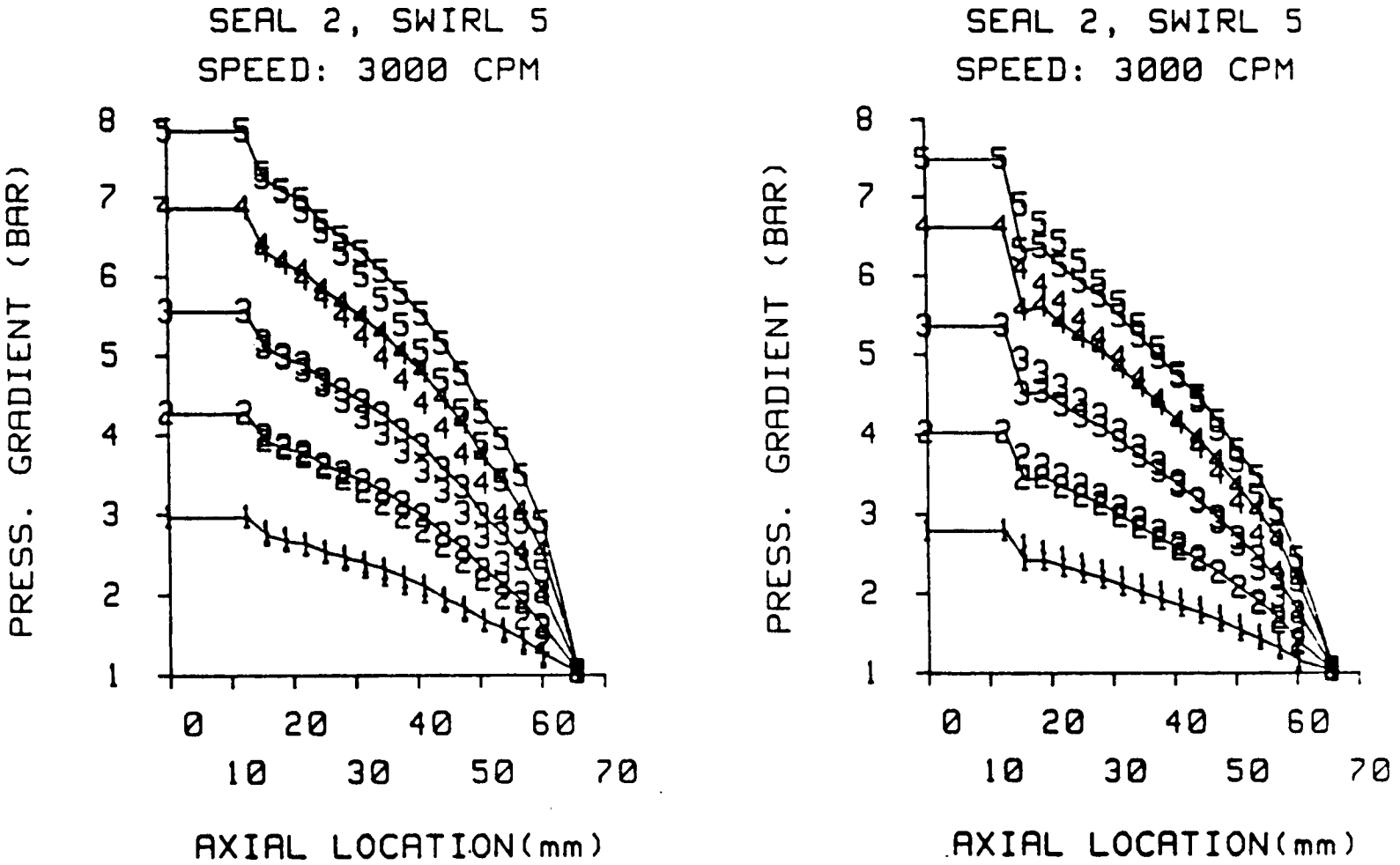

Fig. D20 A comparison of experimental and theoretical pressure gradients of seal 2 for a rotor speed of 3000 cpm and inlet circumferential velocity 5. See table 6 for pressure definitions. Teeth-on-rotor (left), teeth-on-stator (right).

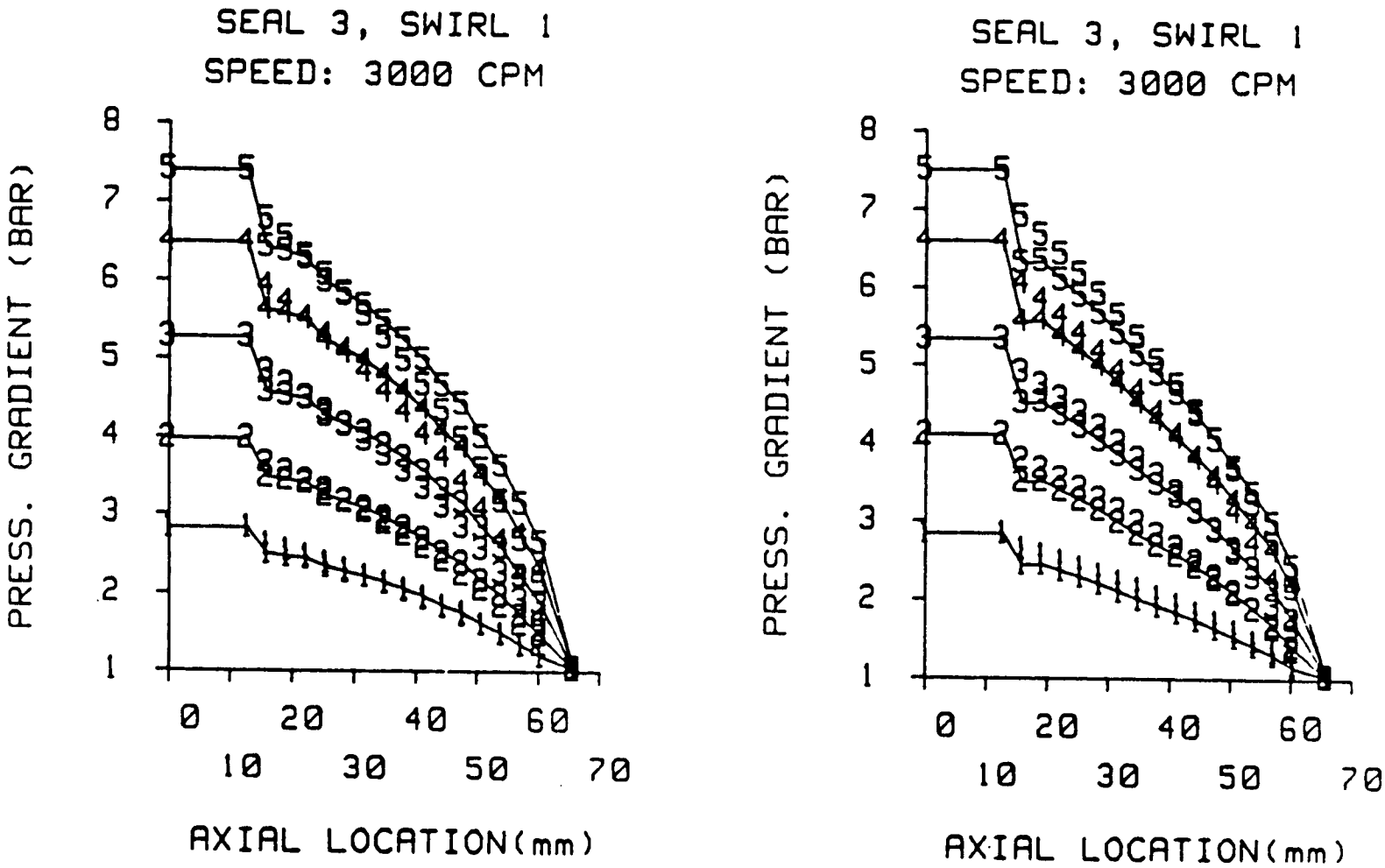

Fig. D21 A comparison of experimental and theoretical pressure gradients of seal 3 for a rotor speed of 3000 cpm and inlet circumferential velocity 1. See table 6 for pressure definitions. Teeth-on-rotor (left), teeth-on-stator (right).

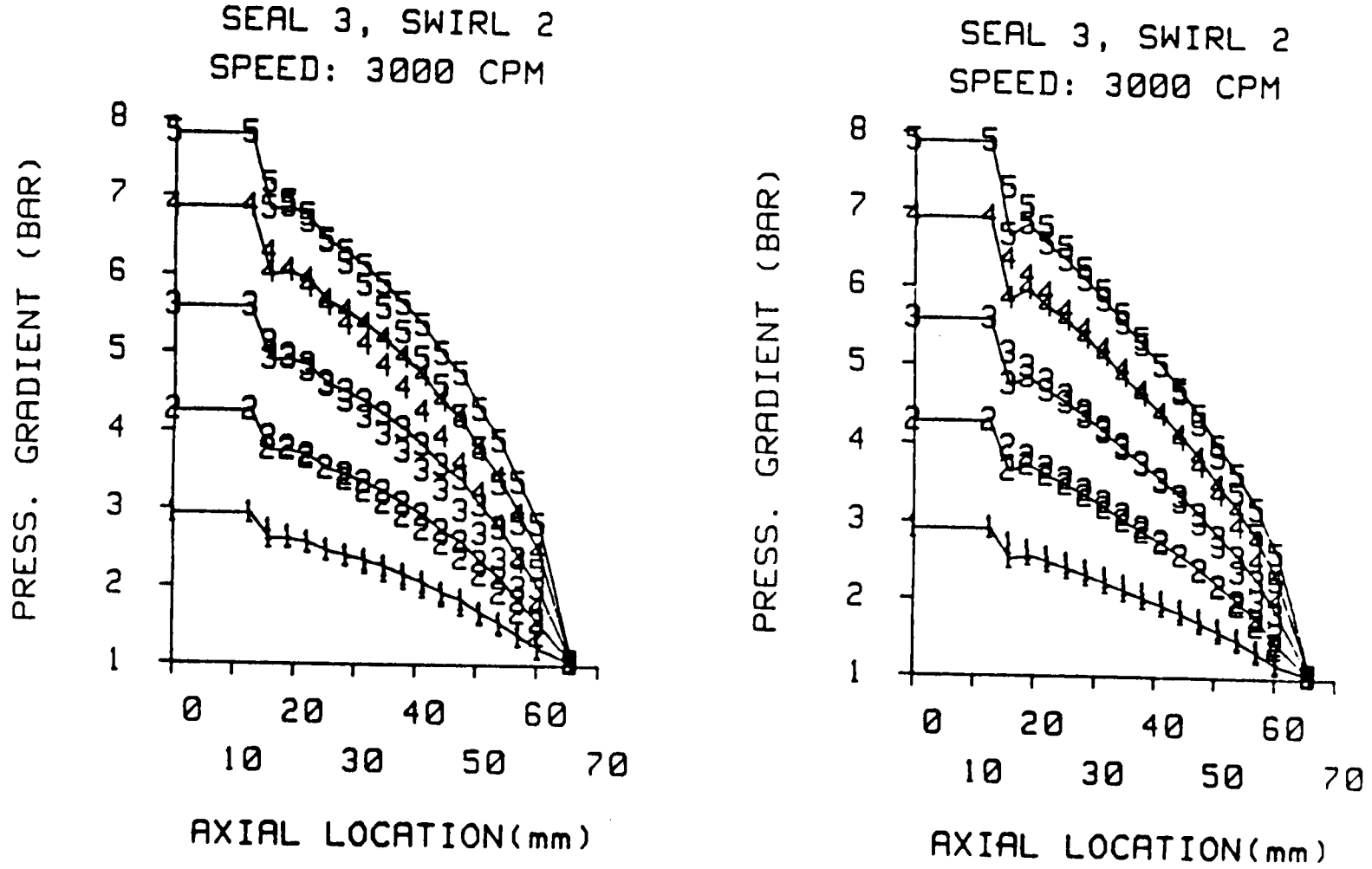

Fig. D22 A comparison of experimental and theoretical pressure gradients of seal 3 for a rotor speed of 3000 cpm and inlet circumferential velocity 2. See table 6 for pressure definitions. Teeth-on-rotor (left), teeth-on-stator (right).

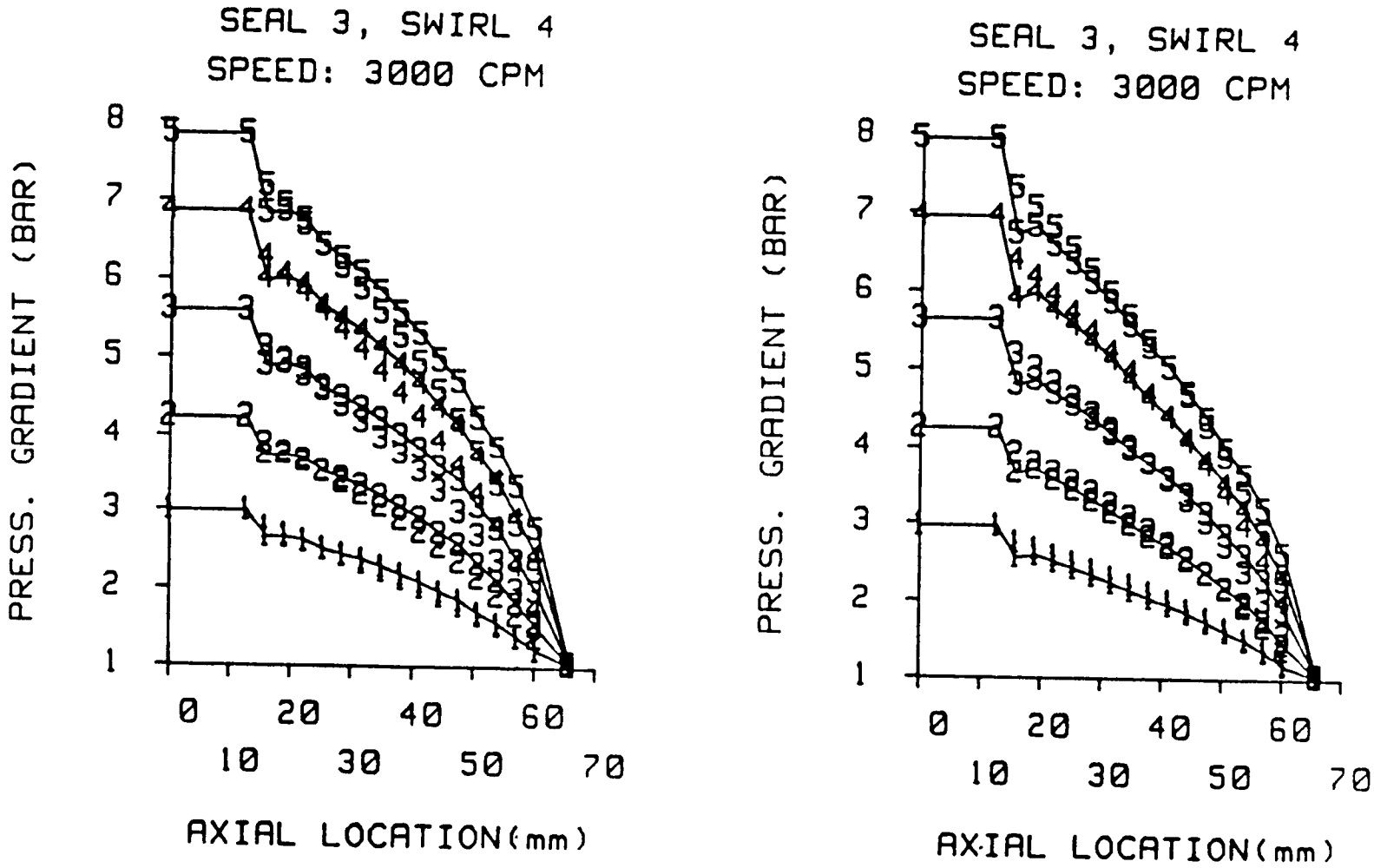

Fig. D23 A comparison of experimental and theoretical pressure gradients of seal 3 for a rotor speed of 3000 cpm and inlet circumferential velocity 4. See table 6 for pressure definitions. Teeth-on-rotor (left), teeth-on-stator (right).

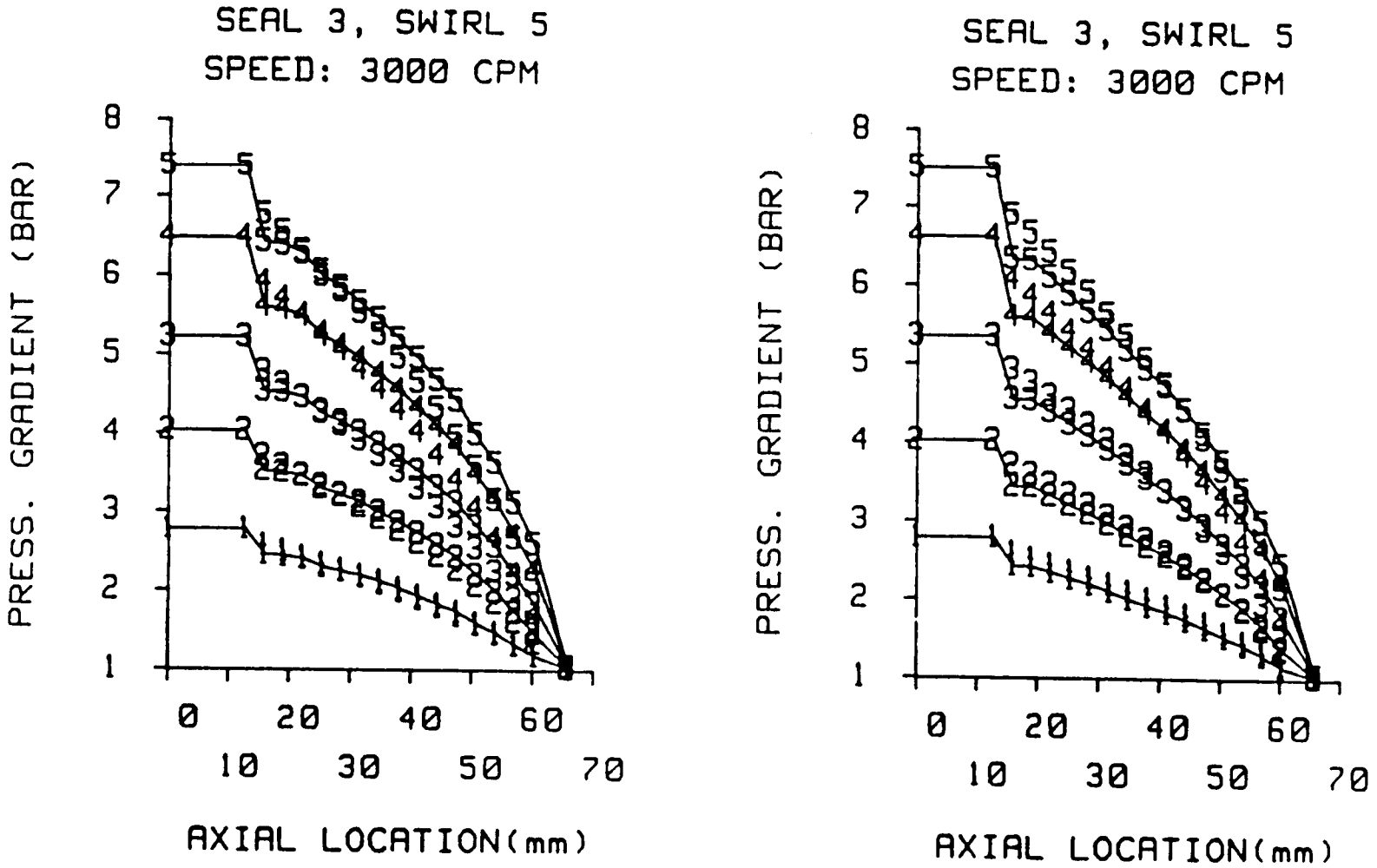

Fig. D24 A comparison of experimental and theoretical pressure gradients of seal 3 for a rotor speed of 3000 cpm and inlet circumferential velocity 5. See table 6 for pressure definitions. Teeth-on-rotor (left), teeth-on-stator (right).